

**Purely Organic Triplet Emitters:  
From Fundamental Molecular Design  
to Performance Amplification in Modern Applications**

by

Wenhao Shao

A dissertation submitted in partial fulfillment  
of the requirements for the degree of  
Doctor of Philosophy  
(Chemistry)  
in the University of Michigan  
2022

Doctoral Committee:

Professor Jinsang Kim, Chair  
Professor Adam J. Matzger  
Professor Jennifer P. Ogilvie  
Professor Paul M. Zimmerman

Wenhao Shao  
whshawn@umich.edu  
ORCID ID 0000-0002-5237-0076

© Wenhao Shao 2022

## ACKNOWLEDGMENTS

I dedicate this dissertation to those who have helped me during this 5-year journey at the University of Michigan.

First let me acknowledge my advisor, Professor Jinsang Kim, who has been the greatest support to my career. I joined the group in a tense situation when the Kim group is my only choice at that time in terms of my future research group, but funding was tight to accommodate another student. Professor Kim recognized my potential after three months' working with him, and accepted me into the group even though we do not have a stable funding source.

In the first year after I joined the group, Professor Kim kept baking me, asking me those very fundamental text-book knowledge in order to strengthen my foundation and prepare me for the upcoming candidacy. Although I did not realize it yet at that time, this foundation I built end up consolidating the connection between theory and application, which is the critical element a material scientist should have. Even though I just joined the group for less than half a year, in the summer of 2018, my workload started to explode since Professor Kim trusted me to carry out a lot of interdisciplinary research topics from our group and from our collaborators. I was able to experience multiple directions of the organic emitter world, and gradually formed a quite comprehensive dissertation plan, leading me towards a successful candidacy. And when I grew senior in the group, Professor Kim trained me extensively on proposal writing, career plan, and gave me a very clear picture of what future faculty should look like piece by piece through each of our regular meetings. None of what I have achieved today could be realized without the mentorship I received from Professor Kim, who always have a clear plan for me.

Apart from research and career, Professor Kim is the most complete person I have ever worked with, not only as a faculty but also regarding his personality. Out of the many lessons he taught me, a recent one is "being generous when giving credits, and being modest when receiving credits". I want to take this opportunity to thank those who have helped me during this journey.

Second, I would like to acknowledge the people whom I have worked with, including Hao, Jie, who have done all the synthesis for the ES IPT manuscript in Chapter II; Jiang, Hanjie and Professor Paul Zimmerman, who are my dearest collaborators and have contributed to the

computational investigations in Chapter II and V, and the proposal we wrote together. Professor Zimmerman has also been a great mentor of mine, who gave me countless inspirations on what computation can realize in emissive materials. Dr. Byeongseop Song was working with me in my OLED project in Chapter IV, who has been very helpful and approachable, even though he graduated and moved out-of-state when I was carrying out the experiments. Dr. Ramin Ansari worked together with me from the first day I joined Kim group. I learned DFT calculation from him and ended up able to carry out my own calculation. We also worked together in the lab on his TADF project, and ended up making a quite valuable publication together. Dr. Zang, Lixin (Mark) was a great mentor of mine when I joined the Kim group, and worked together with me on the encryption study in Chapter III. I definitely should mention Dr. Seong-Jun Yoon here, who is the most excellent and knowledgeable postdoc I have worked with. Dr. Yoon was a lot senior to me in the field of organic emitting materials. He gave me lots of hands-on guidance on organic synthesis when I started, when I was quite nervous about this new field I was about to enter. I should also mention Dr. Da Seul Yang and Jiwon Lim, who has been managing the glovebox with me, and Dr. Yingying Zeng, who has been managing the fluorimeter with me. None of us were experts in the equipment and had to learn from the beginning. I cannot imagine how many obstacles we have figured out together. This list also includes Dr. Dong Ryun Lee and Professor Jun Yeob Lee, Dr. Arkaprabha Konar and Professor Jennifer Ogilvie, and Professor Adam Matzger.

Apart from these whom I have worked with when I was in the Kim group, during my rotation in 2017 I was fortunate to have worked with Professor Mark Banaszak Holl and Dr. Junjie Chen (JJ), both of whom have been my great mentors. JJ at that time as a senior Ph.D. candidate offered me countless suggestions on what I will experience in the upcoming 5 years. One lesson I learned and which I will never forget is, every one of your friends could be a potential collaborator.

I would also like to acknowledge the rest of Kim group, especially Deokwon Seo, Dr. Joonkoo Kang, Mira Diab El Harakeh, Zhang, Shuo, and Zhou, Muru. I'm grateful to share these great memories with you during our chit-chats, group meetings, annual picnics, and new-year dinners at Professor Kim's house. I have received a lot of inspirations from you, which are the privileges I will miss one day.

Last but not least, I could never acknowledge my family and my friends more. My dad - Shao, Yong; my mum - Wen, Xiaohong; my grandma - Shao, Meisheng; my aunt - Shao, Xueqing; my girlfriend - Li, Wenjing; and my cousin - Li, Jiajun. You are the people who will always stand by

my side, and I'm grateful to have your support. My closest friends, Lu, Tieyi and Feng, Weijie, whom I met the first day I entered the Chemistry Department orientation, who has also been my collaborators. We had a meeting together in NCRC in 2018 to present our research and discussing collaborating opportunities. Weijie gave me lots of inspirations when I started. Thank you, my family and friends. I will support you forever, and love you forever.

## TABLE OF CONTENTS

ACKNOWLEDGMENTS .....	ii
LIST OF TABLES .....	ix
LIST OF FIGURES .....	x
ABSTRACT.....	xiv
CHAPTER I - Metal-Free Organic Phosphors towards Fast and Efficient Room-Temperature Phosphorescence.....	1
Abstract.....	1
1.1 Introduction.....	3
1.2. Factors Regulating the Performances of POPs and Insights on Molecular Design.....	4
1.3. Design of Contemporary POPs and POP Systems.....	9
1.4. Application Merits of POPs .....	12
1.5. Design Strategies towards Fast and Efficient POPs.....	15
Publication Information and Author Contribution.....	18
CHAPTER II - Metal-Free Organic Triplet-Emitters with On-Off Switchable Excited State Intramolecular Proton Transfer.....	19
Abstract.....	19
2.1. Introduction.....	20
2.2. Molecular Design and Excited-State Properties .....	21
2.3. Photophysical Properties of BrA-HBI .....	23
2.4. Dissecting the Substitution Effects of Br and Carbonyl .....	25
2.5. On-off Switchable ESIPT Systems in Response to Acid Vapor .....	28
2.6. Photopatterning and Photochromism.....	30
2.7. Conclusions.....	30
Publication Information and Author Contribution.....	31
CHAPTER II. SUPPORTING INFORMATION.....	32
2.8. Additional experimental details .....	32

General.....	32
Physical measurements.....	32
Solvent vapor annealing .....	33
Photopatterning and photochromism.....	33
Synthesis of prototype molecules .....	34
2.9. Computational Details .....	37
2.10. Additional Computational Results .....	38
2.11. Additional Photophysical Analyses.....	42
2.12. Extracting Delayed Emission Quantum Yield .....	47
2.13. Reported ESIPT Molecules with Room Temperature Triplet Emission .....	49
2.14. RAS-SF Frontier Molecular Orbitals of the Prototype Molecules .....	52
CHAPTER III - Photoresponsive Luminescence Switching of Metal-Free Organic Phosphors-Doped Polymer Matrices .....	54
Abstract.....	54
3.1. Introduction.....	55
3.2. UV-induced Phosphorescence Enhancement, Reversibility, and Mechanism .....	56
3.3. Extension of Emission Enhancement Behavior to Other Chromophores .....	60
3.4 Application of UV-Induced Phosphorescence Enhancement in Data-Encryption .....	62
3.5. Conclusions.....	63
Publication Information and Author Contribution .....	64
CHAPTER III. SUPPORTING INFORMATION .....	65
3.6. Experimental Procedures .....	65
Materials .....	65
Methods .....	65
3.7. Phosphorescence decay curves of Br6A/a-PMMA before and after the irradiation .....	66
3.8. Phosphorescence quantum yield measurement data for Br6A in a-PMMA under sealed conditions .....	66
3.9. Br6A/a-PMMA in a glove box before and after irradiation.....	67
3.10 Phosphorescence decay curves of Br6A/a-PMMA film under sealed and unsealed conditions .....	67

3.11. Emission enhancement of Cl6A, I6A and BrPhFlA in a-PMMA and no photochromism from R6G- and Ir(ppy)-doped a-PMMA as well as Br6A in i-PMMA.....	68
3.12. Emission decay curves of Cl6A, I6A, BrPhFlA, and Ir(ppy) <sub>3</sub> as well as Br6A in i-PMMA .....	70
3.13. The deduction of the relationship between the saturation time and the reciprocal of the power density .....	71
3.14. Reversibility study of the photoresponsive behavior.....	72
3.15. Singlet oxygen emission .....	73
CHAPTER IV - Organic Light-Emitting Diode (OLED) Employing Metal-Free Organic Phosphor .....	74
Abstract.....	74
4.1. Introduction.....	75
4.2. Molecular Design and Simulation .....	76
4.3. Photophysical Properties.....	77
4.4. OLEDs analysis .....	80
4.5. Conclusions.....	82
Publication Information and Author Contribution.....	82
CHAPTER IV. SUPPORTING INFORMATION.....	84
4.6. Experimental details.....	84
Synthesis of BrPFL-TFK.....	84
Quantum chemical calculations.....	84
Cyclic voltammetry (CV) measurements .....	85
Photophysical property analysis .....	85
Device Fabrication.....	85
Performance analysis of OLED devices.....	85
4.7. Cyclic voltammetry analysis.....	86
4.8. Additional photophysical analysis .....	87
4.9. NMR and Mass spectra.....	91
CHAPTER V - Heavy Atom Oriented Orbital Angular Momentum Manipulation in Metal-Free Organic Phosphors .....	93
Abstract.....	93



5.1. Introduction.....	94
5.2. Revisiting the theory behind SOC .....	95
5.3. Implementation of HAAM Strategy for Molecular Design.....	96
5.4. Discussion .....	101
Publication Information and Author Contribution .....	102
CHAPTER V. SUPPORTING INFORMATION .....	103
5.5. Additional experimental details .....	103
General.....	103
Physical measurements.....	103
Synthesis of prototype molecules .....	103
5.6. Computational Details .....	111
5.7. Reduced SOCME in the selected orientations .....	112
5.8. Emission and excitation spectra.....	114
5.9. Additional lifetime information .....	122
CHAPTER VI - Conclusions and Perspectives .....	128
6.1. Summary and Outlook .....	129
REFERENCES .....	132

## LIST OF TABLES

Table S2.1. Reported ESIPT molecules with room temperature triplet emission.....	49
Table 3.1. Emission enhancement of several POPs, Ir(ppy) <sub>3</sub> , an organometallic, and R6G a fluorophore in a-PMMA, as well as Br6A in i-PMMA, and their emission lifetime values in air (before long-term irradiation). .....	61
Table S3.1. Measurement data for the phosphorescence QY of Br6A on aPMMA under sealed condition .....	66
Table 5.1. Reduced SOCME in the selected orientations between S <sub>0</sub> and T <sub>1</sub> states.....	98
Table S5.1. Reduced SOCME in the selected orientations between S <sub>0</sub> and T <sub>1</sub> states.....	112
Table S5.2. Reduced SOCME in the selected orientations between S <sub>0</sub> and T <sub>1</sub> states, for Se-N with varying dihedral angle.....	112

## LIST OF FIGURES

Figure 1.1. Illustration of orbital angular momentum change ( $\Delta L$ ) in representative atomic and molecular orbital transitions. ....	6
Figure 1.2. Radiationless decay in POPs: dissecting the effects of collisional quenching ( $kq$ ) and $T_1-S_0$ non-radiative ISC ( $kTS$ ). ....	8
Figure 1.3. Molecular orbitals of carbonyl and tunability of carbonyl derivatives in POPs. ....	9
Figure 1.4. Representative moieties with rich non-bonding electrons and the prototype POPs...	10
Figure 1.5. Matrix engineering strategies to suppress the molecular motion of POPs. ....	11
Figure 1.6. Representative applications of slow and fast POPs. ....	14
Figure 1.7. Illustration of the “Heavy atom oriented orbital angular momentum manipulation” (HAAM) design strategy. ....	16
Figure 1.8. An expanded molecular library of POPs designed by the HAAM concept. ....	17
Figure 2.1. Computational results of HBI (1) and BrA-HBI (2) in their enol or keto forms. ....	22
Figure 2.2. Photophysical properties of BrA-HBI in PMMA or PAA. ....	24
Figure 2.3. Photophysical properties of HBI, Br-HBI, and A-HBI. ....	26
Figure 2.4. Total quantum yield ( $\Phi_{tot}$ ), prompt fluorescence QY ( $\Phi_{PF}$ ), and delayed emission QY ( $\Phi_{delay}$ ) of HBI, A-HBI, Br-HBI, and BrA-HBI. ....	27
Figure 2.5. Solvent vapor annealing results of Br-HBI in P4VP. ....	29
Figure S2.1. Expanded RAS-SF NTO results for HBI (1) and BrA-HBI. ....	38
Figure S2.2. Expanded RAS-SF calculation results for HBI (1) and BrA-HBI (2). ....	39
Figure S2.3. RAS-SF calculation results for keto-form molecules ....	40
Figure S2.4. RAS-SF calculation results for enol-form molecules ....	41
Figure S2.5. Emission spectra v.s. temperature curve for BrA-HBI (2) ....	42
Figure S2.6. Delayed emission lifetime v.s. temperature curve of BrA-HBI (2) ....	43
Figure S2.7. Photophysical analysis of methylated BrA-HBI (2) ....	44
Figure S2.8. Br-HBI (3) in PS ....	44
Figure S2.9. Emissive patterns of Br-HBI (3) in P4VP ....	45

Figure S2.10. Emissive patterns of Br-HBI (3) in PS.....	46
Figure S2.11. Photophysical analysis of emissive patterns .....	46
Figure S2.12. Selected frontier molecular orbitals in the keto form calculated by RAS-SF methods .....	52
Figure S2.13. Selected frontier molecular orbitals in the enol form calculated by RAS-SF methods .....	53
Figure 3.2. Photophysical analysis of Br6A doped a-PMMA films. ....	58
Figure 3.3. Photo-responsive phosphorescence enhancement behavior of Br6A-aPMMA film with camphorquinone additive.....	59
Figure 3.4. Relationship between the saturation time ( $t_s$ ) and the power density ( $P$ ) of the excitation light (LED).....	62
Figure 3.5. Data encryption demonstration.....	63
Figure S3.1. Chemical structures of Cl6A, I6A, BrPhFlA, and 6A.....	65
Figure S3.2. Phosphorescence decay curves of Br6A/aPMMA before and after the irradiation..	66
Figure S3.3. Br6A/a-PMMA in a glove box before and after irradiation. ....	67
Figure S3.4. Phosphorescence decay curves of Br6A/ a-PMMA film under sealed and unsealed conditions.....	67
Figure S3.5. Emission enhancement of Cl6A in a-PMMA.....	68
Figure S3.6. Emission enhancement of I6A in a-PMMA. ....	68
Figure S3.7. Emission enhancement of BrPhFlA in a-PMMA.....	68
Figure S3.8. No emission enhancement of (a) Ir(ppy) <sub>3</sub> and (b) R6G in aPMMA, versus (c) obvious emission enhancement of Br6A in iPMMA before and after the irradiation. ....	69
Figure S3.9. Emission decay curves of (a) Cl6A and (b) I6A in a-PMMA. ....	70
Figure S3.10. Emission decay curves of (a) BrPhFlA and (b) Ir(ppy) <sub>3</sub> in aPMMA. ....	70
Figure S3.11. The phosphorescence decay curve of Br6A in iPMMA.....	70
Figure S3.12. The highest achieved emission intensity in each illumination cycle at various excitation power densities of (a) aPMMA: 1 wt% Br6A drop-casted film and (b) aPMMA: 1 wt% BrPFL-TFK drop-casted film excited by 365 nm LED. ....	72
Figure S3.13. NIR emission spectra of Br6A and BrPFL-TFK in MeOH-d <sub>4</sub> in various concentrations. The singlet oxygen emission is observed at 1270 nm. ....	73

Figure S3.14. NIR emission spectra of Br6A and BrPFL-TFK in MeOH-d4 with two different long-pass filters.....	73
Figure 4.1. Computational results of BrPFL-TFK.....	76
Figure 4.2. Photophysical properties of BrPFL-TFK in optically inert toluene and iPMAA.....	77
Figure 4.3. Photophysical properties of BrPFL-TFK in OLED hosts.....	79
Figure 4.4. Performances of BrPFL-TFK based OLEDs.....	81
Figure S4.1. Cyclic voltammetry (CV) curve of BrPFL-TFK in acetonitrile solution.....	86
Figure S4.2. Comparison of electroluminescence and photoluminescence spectra.....	87
Figure S4.3. UV-Vis absorption spectrum of BrPFL-TFK compared with the steady state (fluorescence emission) of CBP, mCP, and PPT.....	88
Figure S4.4. Temperature-variant steady state emission spectra of BrPFL-TFK doped films with OLED host.....	89
Figure S4.5. <sup>1</sup> H NMR spectrum of BrPFL-TFK in DMSO-d6 with suggested proton assignments.....	91
Figure S6. Mass spectra ( <sup>+</sup> ESI) showing [M+H] <sup>+</sup> peaks for BrPFL-TFK.....	92
Figure 5.1. Contemporary POP design vs POPs designed with the HAAM concept implemented.....	94
Figure 5.2. Computational and experimental results of S-N and Se-N.....	97
Figure 5.3. Computational results of Se-N scanned through the dihedral angle.....	99
Figure 5.4. Computational and experimental results for S/Se-O, S/Se-N, S/Se-B, and S/Se-CO.....	100
Figure S5.1. Reduced SOCME in the selected orientations between S <sub>0</sub> and T <sub>1</sub> states, for Se-N with varying dihedral angle.....	113
Figure S5.2. The emission and excitation spectra of Se-N.....	114
Figure S5.3. The emission and excitation spectra of S-N.....	115
Figure S5.4. The emission and excitation spectra of Se-O.....	116
Figure S5.5. The emission and excitation spectra of S-O.....	117
Figure S5.6. The emission and excitation spectra of Se-B.....	118
Figure S5.7. The emission and excitation spectra of S-B.....	119
Figure S5.8. The emission and excitation spectra of Se-CO.....	120
Figure S5.9. The emission and excitation spectra of S-CO.....	121

Figure S5.10. The experimental intrinsic phosphorescence rate <b><i>kph0</i></b> measured in (a) toluene and (b) in doped PMMA matrix at 78 K, and the <b><i>kph0(Se derivative)/kph0 (S derivative)</i></b> value of each functional group in (c) toluene and (d) in doped PMMA matrix at 78 K.....	122
Figure S5.11. Photoluminescence decay of S-CO, S-B, S-N, and S-O in PMMA matrix measured at 78K.....	124
Figure S5.12. Photoluminescence decay of Se-CO, Se-B, Se-N, and Se-O in PMMA matrix measured at 78K. ....	125
Figure S5.13. Photoluminescence decay of S-CO, S-B, S-N, and S-O in toluene measured at 78K. ....	126
Figure S5.14. Photoluminescence decay of Se-CO, Se-B, Se-N, and Se-O in toluene measured at 78K.....	127

## ABSTRACT

Emissive materials are the essential functional components in many modern and emerging technologies such as organic light-emitting diodes (OLEDs), solid-state lighting, sensors, and data encryption. Metal-free purely organic phosphors (POPs), as a promising novel candidate, have brought milestone evolution to emissive materials in the past decade. Compared to prevailing organo-metallic counterparts, these emitters have various advantages such as large design windows, easy processability, and more environmental friendliness. However, realizing the full capacities of POPs remains challenging due to the limited fundamental understanding of their emission mechanism and the dearth of systematic molecular design blueprint, significantly restricting their overall performance in state-of-the-art emitting systems.

This dissertation research focuses on developing advanced design rules of POPs combining a renovated interpretation of the photophysical laws regularizing their performance and a computation-driven design pipeline. This dissertation begins with reviewing the past developments on POPs and the present challenges towards the design of “fast and efficient” POPs. The molecular design factors affecting the internal and external efficiencies of POPs were summarized by connecting the theoretical descriptors influencing SOC with the molecular orbitals and functional moieties.

Our recent research developments on POPs were discussed from a practical engineering perspective in various modern applications including sensor, imaging, data encryption, display devices, as well as from a fundamental scientific perspective by addressing how molecular level manipulation affects the application merits of POPs. To perform structural expansions on POPs and explore their potential in sensing and patterning systems, purely organic triplet emission is combined with the excited-state intramolecular proton transfer (ESIPT) phenomenon to create dual-emissive “ESIPT triplet emitters” exhibiting up to 50% delayed emission quantum yield ( $\Phi_d$ ). These unique emitters presented tunable triplet emission which could be switched on and off by controlling the matrix acidity. Switchable triplet emission systems controlled by acid vapor annealing as well as photopatterning systems capable of generating facile and high-contrast

emissive patterns have been devised and demonstrated. To explore the potential of POPs in encryption systems, the oxygen quenching characteristic of POPs was adapted to sensitize singlet oxygen species and thus created photo-responsive encoding systems consist of bright green POPs with 19%  $\Phi_d$  and oxygen-permeable polymeric matrix: excitation of POPs leads to area-selective consumption of oxygen in the matrix, leading to localized phosphorescence enhancement and subsequent reversible recording of emissive patterns. Last, to realize POPs' advantages in devices, POP-based OLEDs were constructed with a tailor-designed novel fluorene-based POP with efficient spin-orbit coupling and 24.0%  $\Phi_d$ . Effects of OLED host materials on the phosphor were investigated in terms of color purity, suppression of exciplex emission, and restraint of molecular motion. Bright green phosphorescence emission (1430 cd/m<sup>2</sup> at 100 mA/cm<sup>2</sup>) was realized with 2.5% maximum external quantum efficiency.

Finally, the fundamental molecular design issues of “fast and efficient” POPs were discussed. A novel design concept of “Heavy atom oriented orbital angular momentum manipulation (HAAM)” was presented to address the significance of synergetic interplay between heavy atoms and  $\Delta L$ -satisfying moieties in the promotion of SOC, rather than acting autonomously. Its implementation demonstrated rational creation of milestone molecules with intrinsic SOC efficiencies over 200 cm<sup>-1</sup> and experimental  $\tau_{ph}$  approaching 200  $\mu$ s, while maintaining near-unity room-temperature  $\Phi_{ph}$ . This implies that if a proper SOC manipulation is implemented through the HAAM concept, POPs could potentially have similar ISC and phosphorescence efficiencies to their organometallic counterparts.



**CHAPTER I**  
**Metal-Free Organic Phosphors towards**  
**Fast and Efficient Room-Temperature Phosphorescence**

*Contents in this chapter has been accepted as a review manuscript in Acc. Chem. Res. (manuscript ID: ar-2022-00146q)*

**Abstract**

Metal-free purely organic phosphors (POPs) are promising materials for display technologies, solid-state lighting, and sensors platforms due to their advantageous properties such as large design windows, easy processability, and economic material cost. Unlike inorganic semiconductors, creating the conditions for triplet excitons to produce light in organic materials is a demanding task due to the presence of electron spin configurations that undergo spin-forbidden transitions, which is usually facilitated by spin-orbit coupling (SOC). In the absence of heavy metals, however, the SOC efficiency in POPs remains low, and consequently external non-radiative photophysical processes will also severely affect triplet excitons. Addressing these challenges requires the development of rational molecular design principles to accurately account for how all conceivable structural, electronic, chemical, compositional factors affect materials performance.

This chapter summarizes important molecular design and matrix engineering strategies to tackle the two key challenges for POPs - boosting SOC efficiencies and suppressing non-radiative decays. We start from reviewing the fundamental understanding of internal and external factors affecting the emission efficiencies of POPs, including the theory behind SOC and the origin of non-radiative decays. Subsequently, we discuss the design of contemporary POP systems based on research insights from our group and others, where SOC is mostly promoted by heavy atom effects and the El-Sayed rule: On one hand, non-metal heavy atoms including Br, I, or Se provide the heavy atom effects to boost SOC.

On the other hand, the El Sayed rule addresses the necessity of orbital angular momentum change in SOC and the general utilization of carbonyl, heterocyclic rings, and other moieties with rich non-bonding electrons. Due to the slow-decaying nature of triplet excitons, engineering the matrices of POPs is critical to effectively suppress collisional quenching as the major non-radiative decay route and thus achieving POPs with decent room temperature quantum efficiency. For that purpose, crystalline or rigid amorphous matrices have been implemented along with specific intermolecular forces between POPs and their environment.

Despite the great efforts made in the last decade, the intrinsic SOC efficiencies of POPs remain low, and their emission lifetimes are pinned in the millisecond to second regime. While this is beneficial for POPs with ultralong emission, designing high-SOC POPs with simultaneous fast decay and high quantum efficiencies is particularly advantageous for display systems. Following the design of contemporary POPs, we will discuss molecular design descriptors that could potentially break the current limit to boost internal SOC in purely organic materials. Our recently developed concept of “heavy atom oriented orbital angular momentum manipulation” will be discussed, accompanied by a rich and expanded library of fast and efficient POP molecules, which serves as a steppingstone into the future of this field. We will conclude this chapter by discussing the noteworthy application of POPs in organic light-emitting diodes (OLEDs), solid-state lighting, and sensors, as well as the remaining challenges in the design of fast and efficient POPs.

## 1.1 Introduction

Emissive materials are the functional components in modern technologies such as displays, solid-state lighting, sensors for detection, bio-probes for imaging, and bioelectronics for optical stimulation. Towards these applications, organic semiconductors can produce singlet-exciton-based fluorescence, triplet-exciton-based phosphorescence, or thermally activated delayed fluorescence (TADF). Triplet emitters exhibit long lifetimes due to the presence of electron spin configurations that require spin-forbidden transitions, which should be facilitated by spin-orbit coupling (SOC).<sup>1</sup> Efficient SOC is most commonly achieved by incorporating heavy metal elements to form organometallic phosphors, which have presented significant challenges: besides toxicity and high cost of precious metals, dislocated metal ions in the emitting layer may trap charge carriers and cause color fading,<sup>2,3</sup> jeopardizing device longevity. By comparison, metal-free purely organic phosphors (POPs) have many advantageous properties over inorganic and organometallic counterparts, such as large design windows, readily tunable properties, easy processability, and economic material cost.<sup>4-6</sup> In the absence of heavy metals, however, creating the conditions for triplet excitons to produce light is still a demanding task. Other than the intrinsic low SOC efficiency, external non-radiative photophysical processes also severely affect the light-production of triplet excitons. Addressing these challenges requires rational molecular design principles that accurately account for how all conceivable structural, electronic, chemical, compositional factors affecting materials performance, and allow us to establish blueprints for organic semiconductors with the optimal combination of properties.

During the last decade, various research groups have devised comprehensive molecular design methods to boost the SOC of POPs, mostly through heavy atom effects and the El-Sayed rule.<sup>7</sup> Non-metal heavy atoms including Br,<sup>8</sup> I,<sup>9</sup> or Se<sup>10,11</sup> can provide the heavy atom effects to enhance SOC efficiencies either internally or externally. The El-Sayed rule<sup>7</sup> addresses the necessity of orbital angular momentum change in SOC and the general utilization of carbonyl, heterocyclic rings, and other moieties with rich non-bonding electrons. Due to the slow-decaying nature of triplet excitons, engineering the matrices of POPs is critical to suppressing collisional quenching as the major non-radiative decay route and achieving POPs with decent room temperature quantum efficiencies.<sup>12</sup> For that purpose, crystalline or rigid amorphous matrices have been implemented along with specific intermolecular forces between POPs and their environment.<sup>13-15</sup>

However, current design strategies have inevitably reached their limit. POPs typically possess low intrinsic SOC efficiencies below  $10^1 \text{ cm}^{-1}$  and their emission lifetime were restricted in the millisecond to second regime. The key deficiency in promoting intrinsic SOC efficiencies is the lack of strategies that take into account interactions between design principles. In other words, the heavy atom effect and El-Sayed rule have been discretely exploited, but each alone does not capture the details of how molecular structure leads to angular momentum changes between spin states. In this regard, our recently demonstrated design concept of “heavy atom oriented orbital angular momentum manipulation” (HAAM) addressed the significance of a synergetic relationship in the promotion of SOC between heavy atoms and moieties exerting orbital angular momentum change, rather than acting autonomously. The HAAM strategy envisioned tailor-designed POPs with intrinsic SOC efficiencies over  $10^2 \text{ cm}^{-1}$  and sub-ms phosphorescence lifetime, along with an expanded library of potentially fast and efficient POPs.

This chapter targets at drawing widespread attention on breaking the intrinsic SOC limit of POPs. We will first summarize the fundamental understanding on SOC theory along with the contemporary strategies to create efficient room-temperature phosphorescence (RTP) from POPs. Afterwards, state-of-the-art methods to enhance the SOC of POPs will be discussed.

## 1.2. Factors Regulating the Performances of POPs and Insights on Molecular Design

The most important characteristics of POPs are their room-temperature phosphorescence quantum yield ( $\Phi_{ph}$ ) and lifetime ( $\tau_{ph}$ ). Design strategies for POPs should target at boosting  $\Phi_{ph}$  for bright emission and manipulating  $\tau_{ph}$ : “slow” POPs with large  $\tau_{ph}$  (e.g. “ultralong/persistent” POPs) are ideal for sensor and imaging applications where delayed emission could be easily detected and distinguished from short-lived prompt fluorescence; “fast” POPs with small  $\tau_{ph}$  are suitable for electroluminescence (EL)-generating organic light-emitting diodes (OLEDs) to reduce efficiency “roll-off” caused by accumulation of long-lived triplet excitons.<sup>16</sup>

SOC is the principal quantum physical process regulating the intrinsic performances of POPs, which affects both the population and emission of triplet excitons. In photoluminescence (PL) for instance, triplet excited states are mostly populated by spin-flipped singlet excitons directly-excited from ground state ( $S_0$ ), a process known as inter-system crossing (ISC). The relaxed triplet excitons produce phosphorescence emission through another spin-flip back to  $S_0$

mostly from the lowest triplet states ( $T_1$ ) according to Kasha's rule<sup>17</sup> while in some scenarios higher triplet states are involved.<sup>18</sup>

The underlying theory should be revisited to understand the factors regulating SOC. Under Fermi's golden rule, the transition rate (state 1 to 2) for spin-flipping is given as  $k_{12} \propto |\langle \psi_2 | H_{SO} | \psi_1 \rangle|^2 \rho(E_{12})$ ,<sup>19</sup> where  $\rho(E_{12})$  denotes the joint density of states of the initial and final wavefunctions,  $\psi_1$  and  $\psi_2$ ;  $H_{SO}$  is the transition Hamiltonian, and the term  $\langle \psi_2 | H_{SO} | \psi_1 \rangle$  is the SOC transition matrix element (SOCME). For one-electron systems under relativistic conditions, the main-part of the spin-orbit Hamiltonian,  $H_{SO}$  is  $\frac{Ze^2}{2m^2c^2r^3} \mathbf{L}\mathbf{S}$ ,<sup>20</sup> where  $r$  is the orbital radius,  $\mathbf{L}$  and  $\mathbf{S}$  are the orbital and spin angular momentum, respectively. For many-electron systems, the Hamiltonian is expressed in terms of Breit-Pauli (BP) Hamiltonian<sup>21</sup> as

Equation 1

$$H_{SO} = \alpha^2 \left\{ \sum_n \left[ \sum_i \frac{Z_n}{r_{ni}^3} l_{ni} s_i - \sum_i \sum_{j \neq i} \frac{1}{r_{ni}^3} l_{ni} (s_i + 2s_j) \right] \right\}$$

summation of  $i$  electrons

summation of  $n$  atoms

Effective atomic number for atom ( $n$ )

the spin angular momentum vector for electron ( $i$ ) or ( $j$ )

Fine structure constant ( $\alpha \approx \frac{1}{137}$  if  $l, s, r$  are in atomic units)

the orbital angular momentum vector for electron  $i$  regarding atom  $n$

electron-nuclear distance for electron  $i$  regarding atom  $n$  (the expected value of  $r^{-3}$  operator with the Slater orbitals is proportional to  $Z^3$ )

Notably, SOCME scales with  $Z^4$  in one electron situation since the expectation value of  $r^{-3}$  is proportional to  $Z^3$ . The scaling factor is more complicated in multi-electron systems due to the screening effects of core electrons, but overall, SOCME dramatically increases with heavy elements.

Intuitively, the coupling of electrons' spin and angular momentums in Equation 1 follows the Law of Angular Momentum Conservation - that since spin-flipping implies a change in  $\mathbf{S}$ , the orbital angular momentum,  $\mathbf{L}$ , has to change as well. The rate of "change of  $\mathbf{L}$ " ( $\Delta\mathbf{L}$ ) determines the torque exerted on the electron, which assists spin-flipping.<sup>1</sup> The El-Sayed rule qualitatively summarizes the Law of Angular Momentum Conservation by addressing the necessity to "change orbital types" in SOC-promoting transitions, for instance in a typical case the  $(\pi, \pi^*) - (n, \pi^*)$  transition carries  $\Delta\mathbf{L}$ . Moreover, Equation 1 has also motivated specific molecular design strategies

for “fast and efficient” POPs with considerable SOCME and thus short  $\tau_{ph}$ , which will be discussed in section 1.5.

Although El-Sayed rule has incited various breakthrough in the molecular design of organic phosphors, “orbital type change” does not capture the full picture of  $\Delta L$  manipulation: for instance with a preferential plane-rotation, considerable SOCME could also be observed from  $(\pi, \pi^*) - (\pi, \pi^*)$  transitions (Figure 1.1).<sup>22</sup> More importantly, devising novel molecular design blueprints requires a tangible visualization of angular momentum change in molecular orbitals (MOs) which needs to be substantiated by an expanded library of  $\Delta L$ -satisfying functional groups. The former will be delineated here and the latter in the subsequent sessions.

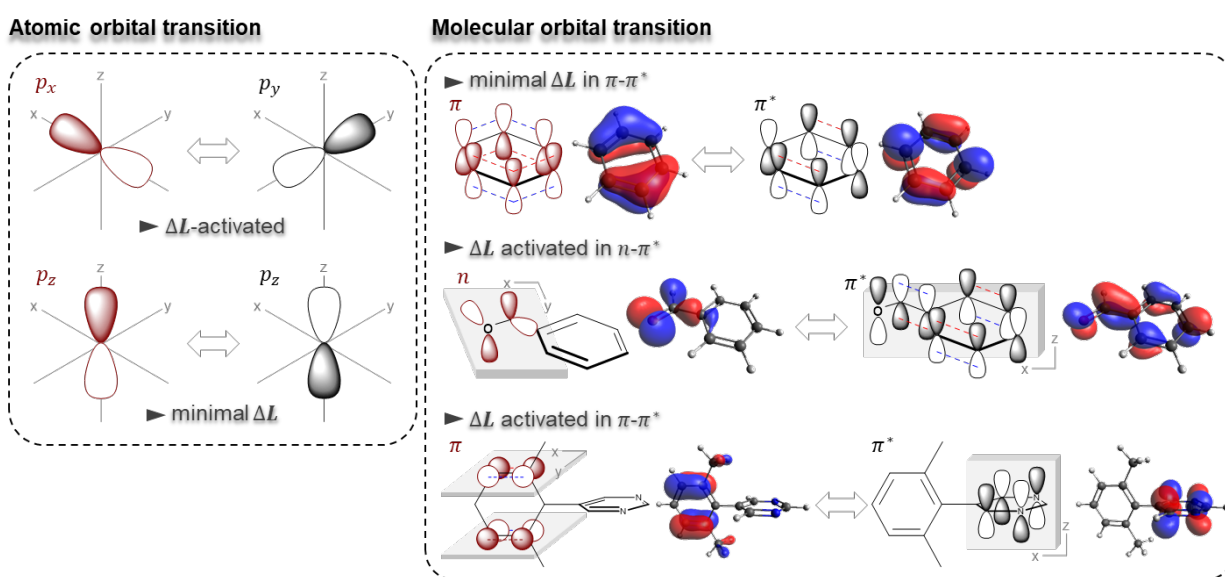


**Figure 1.1. Illustration of orbital angular momentum change ( $\Delta L$ ) in representative atomic and molecular orbital transitions.** Activating  $\Delta L$  requires the transition to exert considerable degree of rotation in the orientation of orbital angular momentums ( $L$ ) involved or the orientation of the planes constructed by individual  $L$ . Left:  $\Delta L$  in atomic orbital transitions including (i)  $p_x$ - $p_y$  transition promoting  $\Delta L$  with  $90^\circ$  rotation in the orientation of  $L$ , and (ii)  $p_z$ - $p_z$  transition impeding  $\Delta L$  with  $180^\circ$   $L$  rotation. Right:  $\Delta L$  in atomic orbital transitions including (i)  $\pi$ - $\pi^*$  transition in benzene impeding  $\Delta L$  with parallelly-aligned planes constructed by each  $L$ , (ii)  $n$ - $\pi^*$  transition in benzaldehyde promoting  $\Delta L$  with vertically-aligned planes constructed by each  $L$ , and (iii)  $\pi$ - $\pi^*$  transition but in twisted phenyl-triazine promoting  $\Delta L$  with vertically-aligned planes constructed by each  $L$ .

Intuitive visualization of  $\Delta L$  in molecular orbitals benefits from simplified atomic orbital systems (Figure 1.1). The  $L$  vector is directed along the axis of rotation of the given electron with its magnitude given by  $|L| = \sqrt{l(l+1)}\hbar$  ( $l$  is quantum number of  $L$ ). Since  $s$  orbitals with  $l = 0$  do not carry any  $L$ ,  $p$  orbitals with  $l = 1$  are involved in  $L$  most often when considering  $\Delta L$  in the frontier molecular orbitals of  $\pi$ -conjugated molecules (i.e. highest occupied and lowest unoccupied molecular orbitals, HOMO and LUMO, and the adjacent orbitals that participates in the lowest energy states). As we know, the magnitude of  $\Delta L$  is related to the cross-product of the

two individual angular momenta while its direction is determined by the right-hand rule. Thus, largest torque is generated when the two atomic orbitals involved are perpendicular to each other while  $\Delta\mathbf{L}$  is diminishing under parallel alignment. For instance, when  $p$  orbitals are concerned,  $p_x - p_y$  transition with  $90^\circ$   $\mathbf{L}$  rotation exerts a large torque facilitating spin-flip, while  $p_z - p_z$  transition falls on the other end.

When  $p$  orbitals form  $\pi$ -conjugated systems, we can still rely on the orientation of planes constructed by  $\mathbf{L}$  of individual atomic orbitals to recognize the general  $\mathbf{L}$  orientation of molecular orbitals. Specifically, transitions between out-of-plane  $\pi$  or  $\pi^*$  orbitals typically carry minimum  $\Delta\mathbf{L}$ . When functional groups with heteroatoms are introduced, their lone-pair  $p$  electrons are partially decoupled from the  $\pi$  system and form non-bonding ( $n$ ) orbitals; the resulted in-plane to out-of-plane rotation between  $n$  and  $\pi$  orbitals exert a large  $\Delta\mathbf{L}$ . In complicate structures with multiple  $\pi$ -conjugated planes, transition between  $\pi$  or  $\pi^*$  orbitals across planes could contribute to  $\Delta\mathbf{L}$  as well and should not be neglected.<sup>22</sup> This turns out to be the major source of  $\Delta\mathbf{L}$  in twisted intramolecular charge transfer when  $n$ -orbital-bearing moieties are not included.<sup>23</sup> Importantly, the discussion here provides a facile visualization of orbital angular momentum and  $\Delta\mathbf{L}$  in metal-free organic molecules, which provides guidelines on the use of functional moieties bearing lone-pair electrons and the construction of sophisticated  $\pi$ -conjugated molecules.

As it comes back to the overall SOC efficiency, internally, the intrinsic  $\Phi_{ph}$  of POPs is directly related to efficient ISC channels for substantial triplet-state population, and the intrinsic  $\tau_{ph}$  is affected by the SOC efficiency of  $T_1$ - $S_0$  transition (Kasha's rule assumed). Although ISC and phosphorescence could ideally be manipulated separately for various purposes, this has scarcely been realized. For instance, while keeping a large SOCME in ISC to ensure a high  $\Phi_{ph}$ , SOCME of  $T_1$ - $S_0$  could be minimized to obtain ultralong POPs.

Externally,  $\Phi_{ph}$  and  $\tau_{ph}$  are complicated by non-radiative decay pathways including quenching through aggregation formation, presence of oxygen, and vibrational quenching from host-guest collisions. Aggregation formation could be effectively prevented by embedding POPs into amorphous matrices,<sup>14</sup> doped crystals,<sup>13</sup> or by attaching bulky side-groups.<sup>24</sup> Due to its triplet ground state ( $^3\Sigma_g^-$ ), Molecular oxygen is a strong phosphorescence quencher. Although this characteristic has incited facile oxygen sensors,<sup>25-27</sup> POPs usually require oxygen-impermeable matrices to prevent oxygen quenching.<sup>8,14</sup>

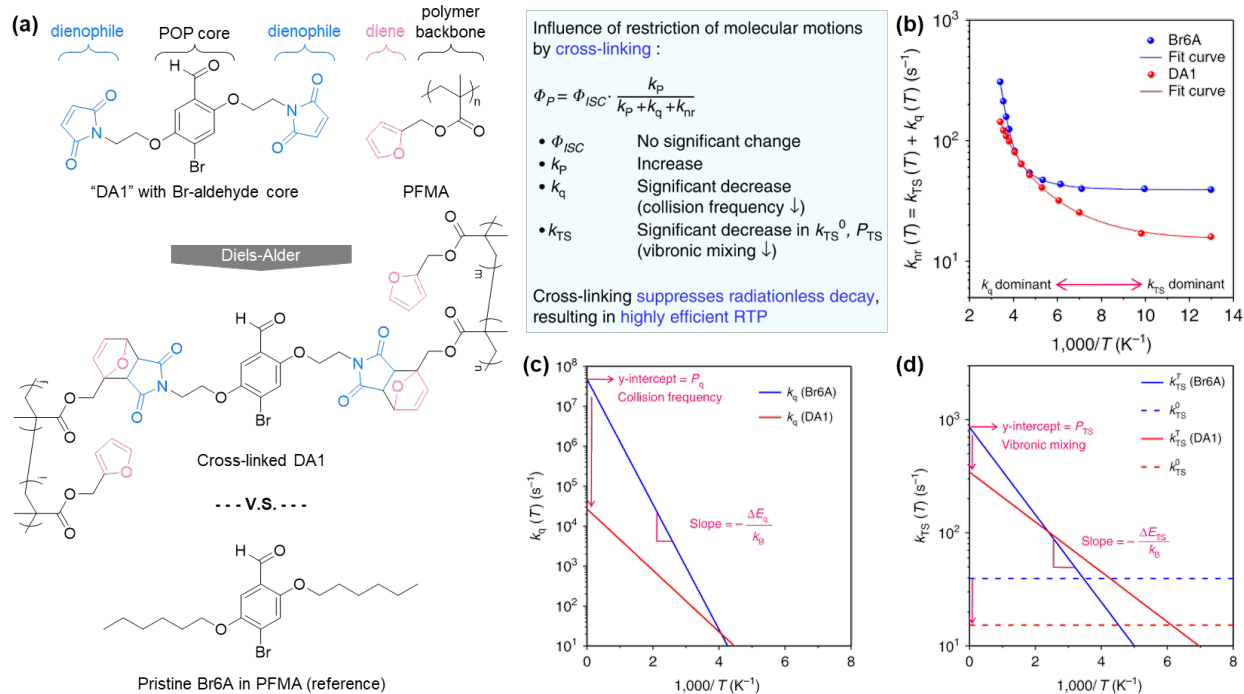


**Figure 1.2. Radiationless decay in POPs: dissecting the effects of collisional quenching ( $k_q$ ) and T<sub>1</sub>-S<sub>0</sub> non-radiative ISC ( $k_{TS}$ ).** Diels-Alder reaction formed covalent linkage between maleimide functionalized POP (DA1) with bromo-aldehyde core and furan functionalized poly(furfuryl methacrylate) (PFMA), which is compared with physically doping non-functionalized Br6A in PFMA. (a) Chemical structures of the compounds involved. (b) non-radiative decay rates ( $k_{nr}$ ) of Br6A-doped (physical blending) and DA1-doped (covalently cross-linked) PFMA films plotted against 1000/temperature ( $T$ ), which revealed two regions with  $k_q$  dominance at higher  $T$  and  $k_{TS}$  dominance at lower  $T$ .  $k_{nr}$  was further deconvoluted into  $k_q$  (c) and  $k_{TS}$  (d) and they were plotted against 1000/ $T$  individually. Dotted lines in (d) represent the  $k_{TS}^0$  values. The slopes are correlated with the activation energy of collisional quenching or vibronic mixing. Figures are reproduced from ref. 12 with permission.

Vibrational quenching is an intricate deactivating process and the underlying kinetics were studied substantially by Kwon et al (Figure 1.2),<sup>12</sup> where the contribution from host-guest interaction and non-radiative ISC between T<sub>1</sub> and S<sub>0</sub> were discussed, both dependent on temperature. Host-guest interaction is normally caused by endothermic Dexter-type energy transfer from triplet states of POPs to those of the surrounding matrix via collisions between the interacting partners.<sup>28</sup> At room temperature, such collisional quenching process is the most prominent source of non-radiative decay after the suppression of oxygen quenching and aggregation formation. At low temperature where molecular motion is suppressed, T<sub>1</sub>-S<sub>0</sub> ISC becomes the dominant deactivating channel which is affected by the degree of vibronic mixing between the states involved. The fundamental understanding on vibrational quenching inspired quantitative comparison of matrices' capabilities to suppress collisional quenching by studying the  $\tau_{ph}$  dropping rate of embedded POPs upon increasing temperature.<sup>22</sup> More importantly, it has



provided principal guideline for matrix engineering strategies to reduce host-guest collisions, which is elaborated in the following session.

### 1.3. Design of Contemporary POPs and POP Systems

Activating efficient RTP from purely organic framework requires the dynamic symbiosis between internal and external factors. In the design of contemporary POPs, intrinsic SOC efficiencies are usually promoted by the aforementioned El-Sayed rule and heavy atom effects. Generally speaking, creating accessible internal channels for  $\Delta L$  and conservation of angular momentum is first and foremost in phosphors, and the key to efficient  $\Delta L$  is the rotation of orbitals. For  $\pi$ -conjugated organic luminescent molecules, relying on  $\pi$  and  $\pi^*$  orbitals from light carbon atoms limits SOC, and thus functional moieties containing heteroatoms are usually introduced to provided de-conjugated  $n$  electrons.

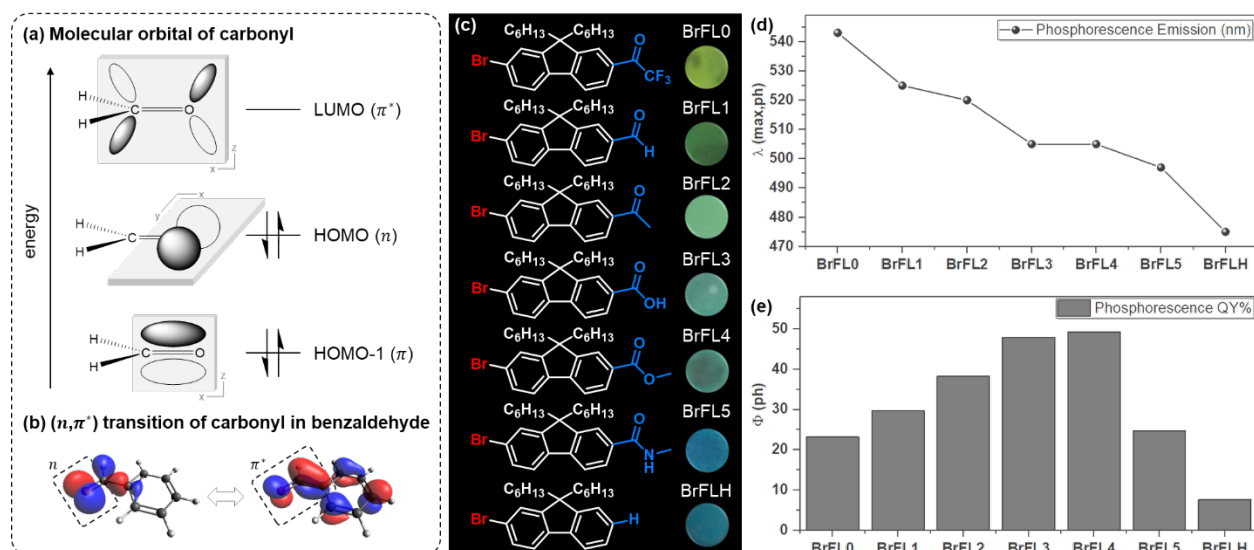


**Figure 1.3. Molecular orbitals of carbonyl and tunability of carbonyl derivatives in POPs.** (a) Selected frontier molecular orbitals of carbonyl (aldehyde): HOMO-1 and LUMO are  $\pi$  and  $\pi^*$  orbitals, respectively, in  $xz$  plane constructed by  $p_z$  orbitals of carbon and oxygen; HOMO is a  $n$  orbital in  $xy$  plane constructed by the  $p_y$  orbital of oxygen. (b) When carbonyl is connected to aromatic systems (e.g. in benzaldehyde), while  $n$  orbital of carbonyl establishes minimal conjugation with the aromatic system,  $\pi^*$  of carbonyl conjugates with the aromatic  $\pi^*$  and forms an extended  $\pi^*$  orbital. Thus,  $L$  rotation is achieved and SOC is activated in the  $n$ - $\pi^*$  transition in benzaldehyde. (c) The energy of carbonyl's MOs is tunable by introducing electron withdrawing and donating moieties. A series of fluorene-based POPs were designed having aldehyde, carboxylic acid, ester, etc. as the carbonyl source, which affected the phosphorescence emission color (c,d) and  $\Phi_{\text{ph}}$  (e). (c-e) are reproduced with permission from ref. <sup>29</sup>.

Carbonyl is a widely explored moiety incorporated in our original design of POPs<sup>8</sup>: since its HOMO consists of the non-bonding electrons from oxygen, when connected to aromatic rings, low-energy ( $n, \pi^*$ ) states are formed by the intramolecular charge transfer from carbonyl to the  $\pi$  system (Figure 1.3a-b). These ( $n, \pi^*$ ) states (either singlet or triplet) create  $\Delta L$ -satisfying ( $n, \pi^*$ ) -

( $\pi, \pi^*$ ) transition channels to assist SOC. Carbonyl could be further decorated with electron withdrawing or donating groups to make aldehyde, ketone, carboxylic acid, ester, etc., which provides tunability on the energy of carbonyls' MOs, the energy of ( $n, \pi^*$ ) states created, and thus phosphorescence emission color along with  $\Phi_{ph}$  (Figure 1.3c-e).<sup>29</sup>

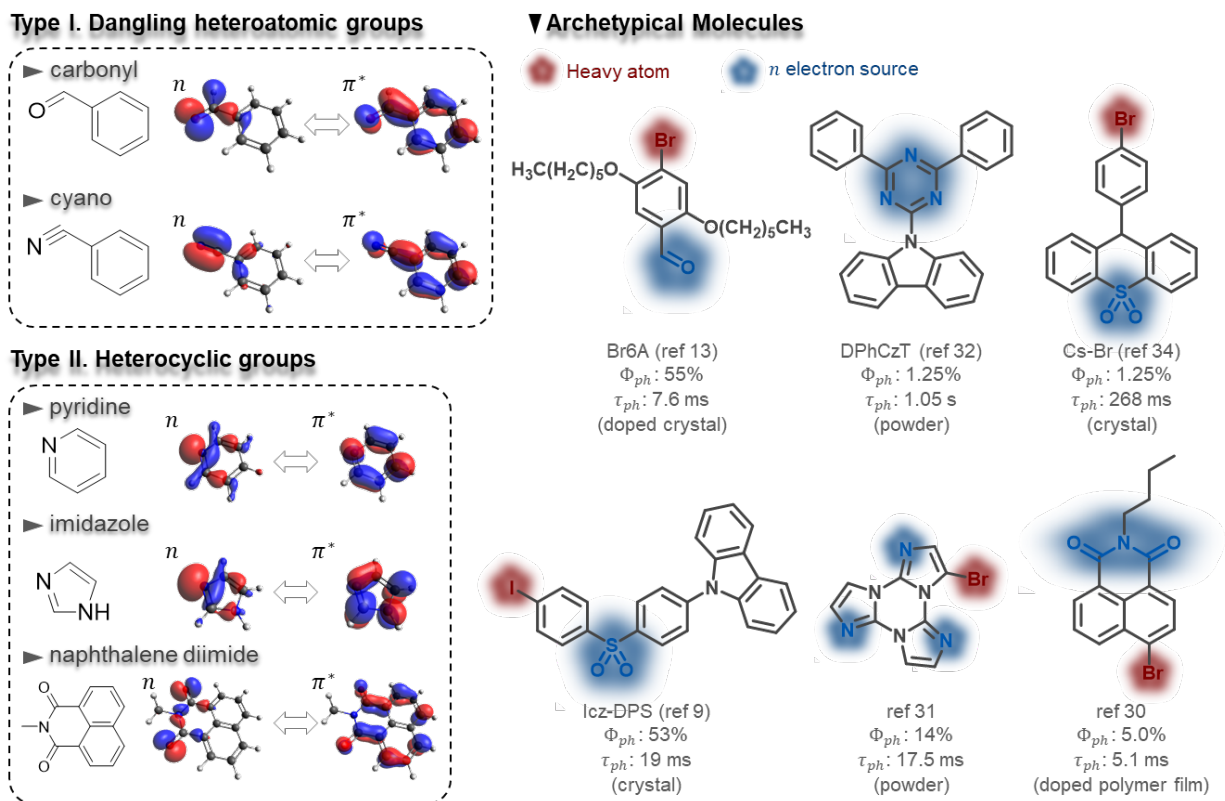


**Figure 1.4. Representative moieties with rich non-bonding electrons and the prototype POPs.** Common moieties with rich  $n$  electrons are generally categorized as Type I - dangling heteroatomic groups and Type II - heterocyclic groups. Their molecular orbitals involved in  $n-\pi^*$  transitions are exhibited. Structures and performances of prototype POPs constructed with these moieties are included with their heavy atoms and/or  $n$  electron sources marked. Since the performance of POPs (i.e.  $\Phi_{ph}$  and  $\tau_{ph}$ ) are sensitive to their environment, the physical state of these representative POPs are included.

Under the similar rationale, other moieties having rich non-bonding electrons are explored extensively and could be generally categorized as Type I - dangling heteroatomic groups and Type II - heterocyclic groups (naphthalene diimide,<sup>30</sup> imidazole,<sup>31</sup> carbazole,<sup>32,33</sup> sulfoxide,<sup>34</sup> etc.). Figure 1.4 illustrates the ( $n, \pi^*$ ) molecular orbital transition of these representative building blocks and the molecular structures of prototype POPs constructed.

On the other hand, heavy atoms could be introduced to boost the overall SOC efficiencies and/or tune the  $\tau_{ph}$  of POPs, either internally by attaching them to the molecular backbone or externally to the matrix.<sup>8</sup> With metals removed, organic heavy atom counterparts are limited. Halogens, mostly bromine ( $Z=35$ ), could be easily attached to aromatic POPs and are thus widely

used from the beginning of POP developments.<sup>8</sup> Iodine ( $Z=53$ ) provides even stronger boosting effects<sup>9,35</sup> and efficient POPs ( $\Phi_{ph} \sim 10^1\%$ ) with  $\tau_{ph}$  in the 1-10  $\mu s$  regime could be obtained occasionally.<sup>36</sup> Recently, chalcogens, mostly selenium ( $Z=34$ ), has been incorporated in POPs. Compared to halogen atoms, chalcogens enabled a larger design window which could be fused in the core of aromatic structures (i.e. benzoselenazole,<sup>37</sup> benzoselenadiazole,<sup>38</sup> selenophene,<sup>38</sup> selenazine,<sup>10,11,39</sup> etc.<sup>40</sup>) or as dangling seleno-ethers.<sup>41,42</sup>

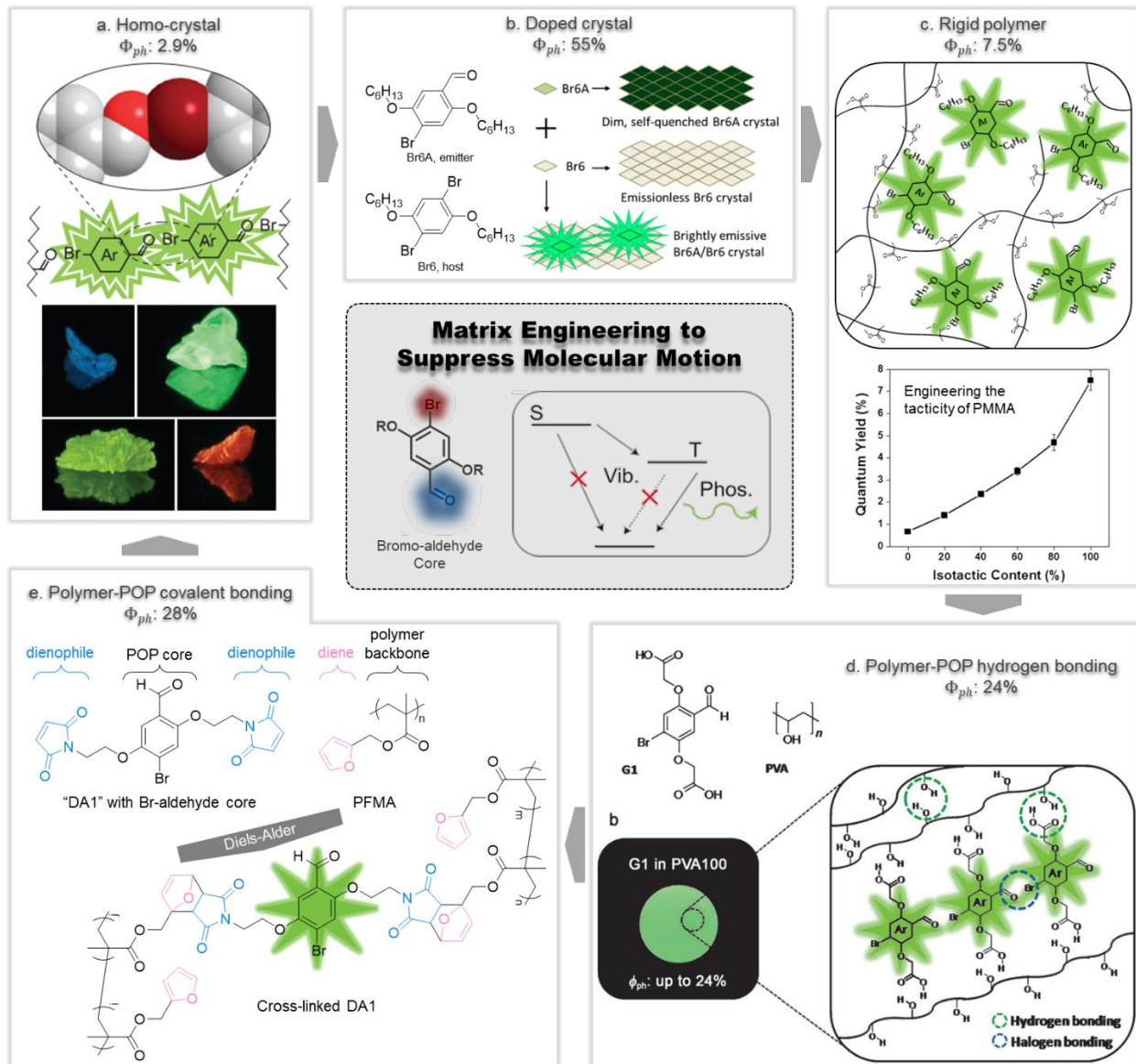


**Figure 1.5. Matrix engineering strategies to suppress the molecular motion of POPs.** All the strategies demonstrated here are based on POPs having bromoaldehyde core. (a) Constructing molecular homo-crystals with rich intermolecular halogen bonding between Br and aldehyde and extract external heavy atom effects,<sup>8</sup> which further evolved into (b) doped crystals systems to prevent aggregation-induced quenching effects.<sup>13</sup> (c) Doping POPs into amorphous poly(methyl methacrylate) (PMMA) and enhancing the polymer rigidity through tacticity engineering.<sup>14</sup> (d) Establishing hydrogen bonding between POPs and polymeric matrix by decorating bromoaldehyde-based POPs with carboxylic acid group and doping them in poly(vinylalcohol) (PVA).<sup>15</sup> (e) Covalently linking POPs with polymeric matrix through Diels-Alder reaction.<sup>12</sup> The figures are reproduced with permission.

Externally in the environment where POPs reside, vibrational quenching effects could be suppressed by matrix engineering strategies as summarized in Figure 1.5. Crystalline matrices were first employed in the initial systematic design of POP systems,<sup>8,13</sup> which provided effective screening against oxygen permeation as well as rigid environment against molecular motion (Figure 1.5a-b). While stringent growth conditions are often needed for organic crystals assembled through  $\pi$ - $\pi$  interactions only, specific intermolecular interactions could be introduced to direct the crystal growth. When halogens are employed, specifically, halogen bonding between slightly electron-accepting  $\sigma$ -holes<sup>43</sup> in halogen atoms and electron-donating  $\Delta L$ -promoting moieties incites additional rigidity and introduces external heavy atom effects, simultaneously.<sup>44</sup> In addition, Coulombic interactions between POPs and organic<sup>45</sup> or inorganic/metallic ions<sup>24,46</sup> are investigated to generate ionic crystals; metal-organic frameworks<sup>47,48</sup> or halide perovskites<sup>49-53</sup> also act as crystalline templates for POPs to provide rigid networks effectively suppressing host-guest vibration and potentially delivering external heavy atom effects. Although metals are involved, these organic-inorganic hybrid systems distinct from organometallic complexes on the fundamental level since the emission originates from robust covalent-linked POPs instead of weaker metal-organic interactions.

Amorphous polymeric matrices are developed to adapt POPs to film-forming amorphous systems more attractive for device fabrication and processing. In this regard, host-guest interactions are suppressed through engineering the intrinsic rigidity of polymers or by introducing additional secondary bonding between polymer and POPs. Intrinsic rigidity of the amorphous host could be roughly estimated by their glass transition temperature ( $T_g$ )<sup>22</sup> under the premise that the solubility parameter between hosts and guests needs to match for POPs to be well embedded in the matrix. Additionally, the tacticity of polymers<sup>14</sup> is manipulated to suppress  $\beta$ -relaxation and subsequent long-range segmental motions occurring at the glass transition temperature of polymers (Figure 1.5c).<sup>54</sup> On the other hand, due to the large design window of polymers, host-guest interactions including hydrogen bonding (Figure 1.5d)<sup>15,55</sup> or direct covalent linkages (Figure 1.5e)<sup>12</sup> are widely explored to anchor POPs in a rigid fashion.

#### 1.4. Application Merits of POPs

Contemporary application of POPs generally explores the characteristics of triplet emission. While bright phosphorescence emission with large  $\Phi_{ph}$  is the universal target, POPs with long and

short  $\tau_{ph}$  are suitable for sensor/imaging<sup>56</sup> and display<sup>57</sup> applications, respectively, as summarized in Figure 1.6. Prolonged  $\tau_{ph}$  makes POPs more susceptible to environmental non-radiative deactivating processes. In this regard, the sensitivity of triplet emission to molecular motion has envisioned solid-state POP-based sensors to organic solvent penetration (Figure 1.6e)<sup>58</sup> and temperature (Figure 1.6f).<sup>14</sup> The sensitivity to oxygen has inspired us to develop dissolved oxygen sensors for oxygen quantification in aqueous environments by embedding hydrophobic POPs in oxygen-permeable water-soluble core-shell nanoparticles (Figure 1.6a),<sup>25</sup> which was further explored in bio-detection platforms with sub-picomolar detection limit by combining lipid-polymer hybrid POP-based nanoparticles with a signal-amplifying enzymatic oxygen scavenging reaction (Figure 1.6b).<sup>59</sup> Phosphorescent bioimaging agents have also been devised to map the hypoxia in tumors<sup>27</sup> (Figure 1.6d) or living tissues.<sup>60</sup> Notably, the oxygen quenching mechanism of POPs could be exploited to sensitize singlet oxygen species and thus create photo-responsive encoding systems: excitation of POPs leads to area-selective consumption of oxygen in the matrix, leading to localized phosphorescence enhancement and subsequent reversible emissive patterns (Figure 1.6c).<sup>61,62</sup>

Prolonged  $\tau_{ph}$  also makes POPs excellent agents for time-resolved sensor and bioimaging platforms.<sup>63</sup> With proper matrix engineering to suppress molecular motion and intentional deactivation of SOC channels,  $\tau_{ph}$  of POPs could be prolonged even further to  $>10^{-1}$  s to generate “ultralong/persistent” RTP<sup>32</sup> easily discernible from the environmental auto-fluorescence,<sup>64</sup> potentially relieving the need for high-end time-resolving imaging devices as demonstrated in persistent POP-based oxygen sensors (Figure 1.6g).<sup>26</sup>

On the other hand, shortened  $\tau_{ph}$  makes POPs promising candidates for EL-generating displays<sup>57</sup> which requires efficient utilization of triplet excitons since carrier recombination is expected to produce singlet and triplet excitons in a 1:3 ratio.<sup>65</sup> In OLEDs, specifically, optically active host materials should be used to ensure efficient energy transfer to POPs. Thus, the selection of host should take into consideration various factors including color purity, charge balance, and the reduction of exciplex formed between host and guest (Figure 1.6h),<sup>22</sup> which makes the choice of host limited. In this regard, strategies to suppress molecular motion have not been well implemented in OLED hosts and is oftentimes limited to  $\pi$ - $\pi$  interaction along with introducing hosts with high  $T_g$ ,<sup>22</sup> instead of exploring specific interactions between host and POPs.

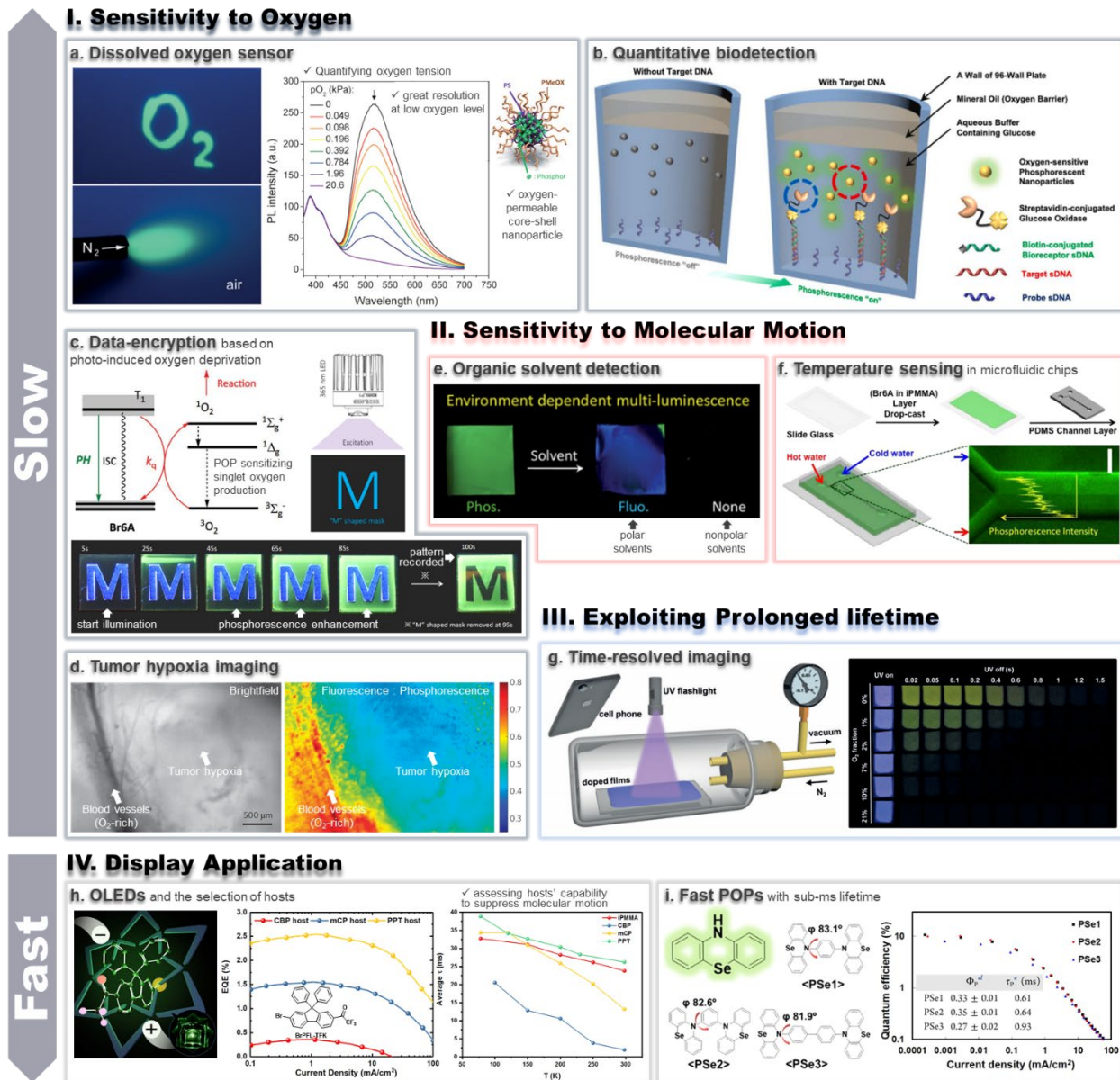


**Figure 1.6. Representative applications of slow and fast POPs.** Slow POPs with prolonged  $\tau_{ph}$  are promising in sensor and imaging platforms: I, the sensitivity to oxygen has been explored in (a) dissolved oxygen sensors capable of quantifying oxygen tension with great sensitivity in super-low oxygen levels, which were made by embedding POP molecules in oxygen-permeable core-shell nanoparticles,<sup>25</sup> (b) quantitative biodetection platforms coupling the oxygen responsiveness of POP-based lipid-polymer nanoparticles with a signal-amplifying enzymatic oxygen scavenging reaction to achieve sequence-specific detection of biomarkers,<sup>59</sup> (c) data-encryption systems based on photo-responsive phosphorescence enhancement phenomenon activated through POP-sensitized singlet oxygen production and subsequent local oxygen consumption by the matrix,<sup>62</sup> and (d) tumor hypoxia imaging coupling local oxygen tension with fluorescence/phosphorescence ratio;<sup>27</sup> II, the sensitivity to molecular motion has been explored in (e) temperature sensors<sup>14</sup> and (f) organic solvent detection;<sup>58</sup> III, the long lifetime has inspired (g) time-resolved imaging platforms using low-end detection devices based on POPs with ultralong lifetime.<sup>26</sup> IV, Fast POPs with shortened  $\tau_{ph}$  are suitable for display applications and the need to address (g) proper selection of hosts to suppress molecular motion in OLEDs<sup>22</sup> and (h) utilizing fast POPs with sub-ms lifetime to suppress efficiency roll-off.<sup>10</sup> The figures are reproduced with permission.

The long-lived nature of triplet excitons turns out to be a blessing and a curse as it limits POPs' merits in displays: the best contemporary strategies could not shorten their  $\tau_{ph}$

systematically below the *ms* regime. However, fast and efficient POPs are required in OLEDs since one critical issue frequently observed is that the external quantum efficiencies (EQE) significantly decrease at high current densities. Primary cause of this “efficiency roll-off” is the accumulation of long-lived triplet excitons, resulted in triplet-triplet annihilation.<sup>16</sup> Recently, a series of efficient POPs having selenium heavy atoms were employed in OLEDs and suggested unprecedentedly high intrinsic SOC efficiency over  $10^2 \text{ cm}^{-1}$ , short  $\tau_{ph}$  in the  $10^2 \mu\text{s}$  regime, and maximum EQE over 10% with the potential to relieve the efficiency roll-off (Figure 1.6i).<sup>10</sup> The unexpected results from this study suggested that a revised molecular design strategy is needed specifically for fast and efficient POPs.

### 1.5. Design Strategies towards Fast and Efficient POPs

Current design strategies have reached their limit to create fast and efficient POPs; thus, POPs typically possess low intrinsic SOC efficiencies below  $10^1 \text{ cm}^{-1}$  and their emission lifetime were restricted in the millisecond to second regime. The key deficiency is the lack of strategies that take into account interplay between design principles. That is, the heavy atom effect and  $\Delta L$ -satisfying moieties (i.e. functional groups exerting orbital angular momentum change) have been discretely exploited. In other words, heavy atoms are not rationally positioned in a way that their orbitals closely interact with the orbitals undergoing angular momentum change. The most important message from Equation 1 is that the orbital and spin angular momentums of electrons are coupled through the interaction with effective atomic number.<sup>1</sup> According to Equation 1, the heavy atom must be in close proximity with the orbital angular momentum migration, otherwise the effective  $Z$  from that atom is suppressed by the  $r^{-3}$  dependence of  $H_{SO}$ .

This new design strategy for fast and efficient POPs, named as “*Heavy atom oriented orbital angular momentum manipulation*” (*HAAM*),<sup>11</sup> addressed the significance of a synergetic relationship between heavy atoms and  $\Delta L$ -satisfying moieties in the promotion of SOC, rather than acting autonomously. The HAAM strategy was recently verified and benchmarked both computationally and experimentally using a series of selenium-based POPs (Figure 1.7).<sup>10,11</sup> Its implementation demonstrated rational creation of milestone molecules with intrinsic SOC efficiencies over  $200 \text{ cm}^{-1}$  and experimental  $\tau_{ph}$  approaching  $200 \mu\text{s}$ , while maintaining near-unity room-temperature  $\Phi_{ph}$ . This implies that if a proper SOC manipulation is implemented through the HAAM concept, POPs could potentially have similar ISC and phosphorescence efficiencies to

their organometallic counterparts. In Chapter V, we will discuss the benchmark and verification of the HAAM concept in detail through the design of a series of prototype POPs.

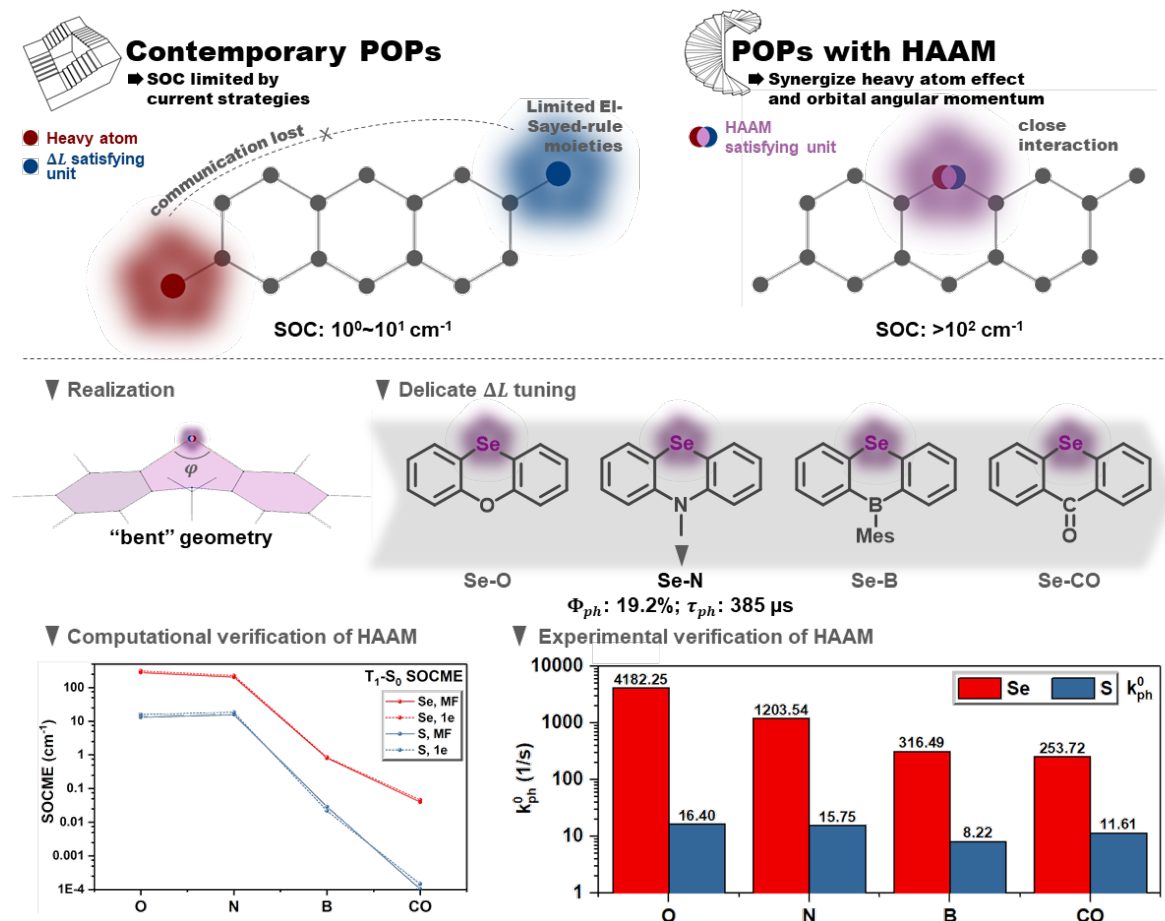


**Figure 1.7.** Illustration of the “Heavy atom oriented orbital angular momentum manipulation” (HAAM) design strategy. In contemporary POPs, heavy atom and  $\Delta L$ -satisfying moieties are acting autonomously while HAAM address the contribution of heavy atom orbitals in the orbitals carrying out  $\Delta L$ . HAAM was benchmarked in a series of selenium-based POPs with bent geometry and was verified both computationally and experimentally where selective tunability of heavy atom effect and the magnitude of  $\Delta L$  was achieved. Reproduced with permission from ref. <sup>11</sup>.

The HAAM concept projects an expanded molecular library of fast and efficient POPs as the key to maximizing SOC in POPs is activating the contribution of heavy atom orbitals in  $\Delta L$ , and the central to activating efficient  $\Delta L$  channels is utilizing non-bonding electrons of heavy atoms. In an exemplary phenoselenazine structure (Figure 1.8), selenium’s  $p$  electrons are partially decoupled from the aromatic system and thus the  $p_{x/y} - p_z$  transition, exerting large  $\Delta L$ , promotes the SOC of phosphorescence emission and a few vital ISC channels. Under the similar concept, an expanded HAAM-activated molecular library is proposed in this chapter (Figure 1.8).



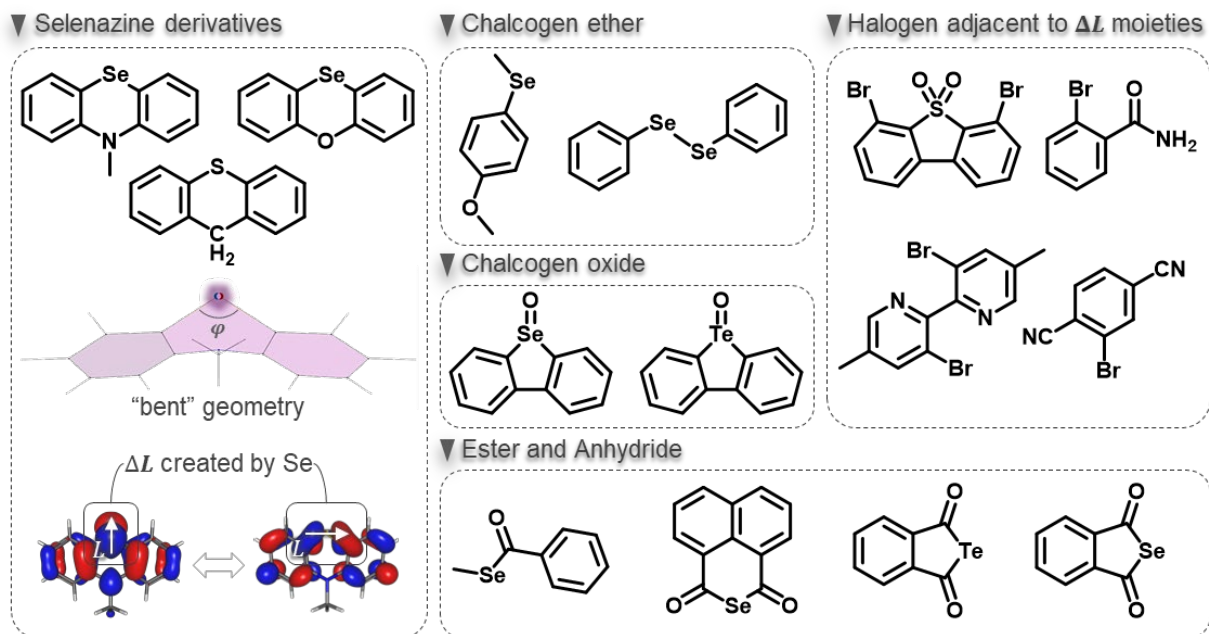


**Figure 1.8.** An expanded molecular library of POPs designed by the HAAM concept. The inset box shows the bent geometry of the phenoselenazine derivatives, where  $\Delta L$  is created by selenium through an in-plane to out-of-plane  $p$  orbital rotation.

The unique feature of chalcogens over halogens is their ability to be incorporated in the aromatic backbone instead of as dangling side groups. In this regard, leaving chalcogens' lone-pair  $p$  electrons "unprotected" in the selenazine or selenophene structure makes heavy atom orbitals most accessible in  $\Delta L$ -activating. However, these lone-pair  $p$  electrons should get decoupled from the aromatic  $\pi$  conjugation as observed in the bent phenoselenazine structure<sup>10,11</sup> to increase their energy and participate in the frontier molecular orbitals. Similarly, chalcogen-ether structure could be envisioned where chalcogen atoms are no longer fused in a ring system, opening various structural possibilities. "Protecting" the lone-pair  $p$  electrons using chalcogen oxide moieties reduces their contribution in  $\Delta L$  as a method to control the SOC efficiency.

A larger design window is opened using traditional light-element based  $\Delta L$ -satisfying units, like carbonyl, and placing heavy atoms in adjacent positions so that their non-bonding electrons could participate in the  $(\pi, \pi^*) - (n, \pi^*)$  type  $\Delta L$ . Chalcogen ester and anhydride structures could be anticipated. Moreover, this design rationale employs halogen-containing POPs<sup>66</sup> since halogen only has one available bonding site and could not create efficient  $\Delta L$  channels on their own.

### **Publication Information and Author Contribution**

*Contents in this chapter has been submitted as a review manuscript to Acc. Chem. Res. (manuscript ID: ar-2022-00146q)*

Shao, W.; Kim, J. “Metal-Free Organic Phosphors towards Fast and Efficient Room-Temperature Phosphorescence”

### **Author Contribution**

W.S. designed and composed the manuscript; J.K. provided supervision and revised the manuscript.

**CHAPTER II**  
**Metal-Free Organic Triplet-Emitters with**  
**On-Off Switchable Excited State Intramolecular Proton Transfer**

*Contents in this chapter has been accepted to publish in Adv. Funct. Mater. (manuscript ID: adfm.202201256)*

**Abstract**

Metal-free organic triplet emitters are an emerging class of organic semiconducting material. Among them, molecules with tunable emission responsive to environmental stimuli have shown great potentials in solid state lighting, sensors, and anticounterfeiting systems. Here, a novel excited-state intramolecular proton transfer (ESIPT) system is proposed showing the activation of thermally activated delayed fluorescence (TADF) or room-temperature phosphorescence (RTP) simultaneously from both keto and enol tautomers. The prototype ESIPT triplet emitters exhibited up to 50% delayed emission quantum yield. Their enol-keto tautomerization can be switched by controlling the matrix acidity in doped polymer films. Taking advantage of these unique properties, we have devised “on-off” switchable triplet emission systems controlled by acid vapor annealing, as well as photopatterning systems capable of generating facile and high-contrast emissive patterns.

## 2.1. Introduction

Metal-free purely organic triplet emitters utilizing room-temperature phosphorescence (RTP)<sup>8</sup> or thermally activated delayed fluorescence (TADF)<sup>67</sup> are the functional components in modern technologies. Among purely organic triplet emitters, those with tunable emission that can respond to environmental stimuli have attracted widespread attention.<sup>68</sup> In conventional fluorescence emitters, one way to achieve tunable emission is through excited-state intramolecular proton transfer (ESIPT), which is a unique four-level photophysical process - while chromophores originally reside in their enol ground state (E), upon excitation to the excited enol form (E\*), they undergo rapid tautomerization to an energetically lower excited keto configuration (K\*), followed by emission to the keto ground state (K).<sup>69</sup> Importantly, the transient proton transfer process is highly sensitive to environmental stimuli, and frustrated proton transfer is widely observed in protic or polar environment.<sup>70-72</sup> With fine tuning of the structure and matrix, partially frustrated proton transfer has led to dual and triple ESIPT emitters<sup>73</sup> and even single molecule white emitters.<sup>74-77</sup>

This intriguing four-level photocycle and its unique sensitivity to environmental stimuli have inspired us to devise ESIPT-based triplet emitters and create stimuli-responsive systems with tunable triplet emission activated both in enol and keto forms. Harvesting triplet excitons from ESIPT chromophores is a generally overlooked field due to the insufficient molecular design blueprint. Table S2.1 listed out the reported ESIPT materials with room-temperature triplet emission. As TADF and RTP materials received wide attention in the past decade, recently, the intrinsic intramolecular charge transfer of ESIPT structures has been utilized to activate TADF in organic light-emitting devices,<sup>78-80</sup> followed by a few photophysical and computational study of their excited state dynamics.<sup>81-83</sup> On the other hand, however, activating RTP from ESIPT molecules is much less explored<sup>84,85</sup> while most photophysical studies focus on low-temperature phosphorescence properties.<sup>86,87</sup> Moreover, as these pioneering works explored the keto-form properties of ESIPT triplet emitters, molecular engineering pathways to harvest triplet energy from the enol tautomer is missing.

In this report, we created a series of organic triplet emitters having ESIPT properties in which efficient TADF or RTP with is activated both in enol and keto forms with a record-high delayed emission quantum yield up to 50%. Considering the complicated four-level photocycle involved, the simplest (2'-hydroxyphenyl)benzimidazole (HBI, **1**) scaffold is chosen with subsequent

attachment of Br to induce intramolecular heavy atom effect<sup>88</sup> and aromatic carbonyl as the El-Sayed-rule-satisfying unit<sup>7</sup> to create channels for orbital angular momentum migration.<sup>1,11</sup> This strategy is universally applicable to activating efficient triplet population from various ESIPT structures. A thorough photophysical study on the prototype molecules was conducted to elucidate the substitution effects of Br and carbonyl. We believe that future developments of triplet-activated ESIPT molecules would benefit from the outcome of this work.

Furthermore, the application merit of dual-form ESIPT triplet emitters was explored in the spirit of their sensitivity to acidity in the solid state matrices. These prototype materials exhibited “on-off” switchable enol-keto tautomerization in poly(4-vinylpyridine) (P4VP) with acid vapor annealing. Photo-reaction capabilities of the hydroxyl groups were also exploited to generate high-contrast emissive patterns utilizing the keto-enol photochromism.

## 2.2. Molecular Design and Excited-State Properties

In our design strategy, the key to triplet state activation of ESIPT molecules is creating transition channels between  $(\pi, \pi^*)$  and  $(n, \pi^*)$  states both in keto and enol forms, which potentially carry large spin-orbit coupling matrix elements (SOCMEs).<sup>7</sup> A computational study using the restricted active space - spin flip (RAS-SF) method<sup>89-93</sup> was performed to characterize the model compound HBI and determine the accessibility of these channels. RAS-SF is a wave function theory that is well-suited for treating electronically excited states.<sup>94,95</sup> Recent work has enabled RAS-SF to predict accurate SOC elements,<sup>11</sup> making it particularly useful to investigate the prototype ESIPT compounds.

Examination of the electronic transitions of HBI, as seen in the natural transition orbitals (NTO) (Figure S2.2), indicated that most low-energy excited states have primarily  $(\pi, \pi^*)$  character in both enol and keto forms. This is reflected in Figure 2.1a-b, where HBI molecules tend to show relatively low SOC constants, more specifically  $\sim 1.0 \text{ cm}^{-1}$  for 1-enol and 1-keto, due to a lack of heavy atoms in singlet-triplet transitions. The  $T_2$  state of 1-keto has significant  $(n, \pi^*)$  character and therefore moderate SOCME ( $\sim 10 \text{ cm}^{-1}$ ) is expected in the  $S_1$ - $T_2$  transition, but the  $T_2$  state is also significantly higher in energy than  $S_1$  and therefore inaccessible.

To overcome the insufficient SOC in HBI, a carbonyl group was introduced to provide low energy  $(n, \pi^*)$  excited states and thus create accessible  $(\pi, \pi^*)$  -  $(n, \pi^*)$  transition channels exerting in-plane to out-of-plane orbital angular momentum rotation to facilitate SOC,<sup>96,97</sup> and Br

was also introduced to elevate the overall SOCMEs. Specifically, Br is attached adjacent to carbonyl where its non-bonding electrons could participate in the carbonyl-centered  $n-\pi^*$  transition. This proximity results in much better utilization of the heavy atom effect compared to isolated Br and carbonyl,<sup>66</sup> in concordance with the heavy atom oriented orbital angular momentum manipulation effect (HAAM) we recently studied.<sup>11</sup>

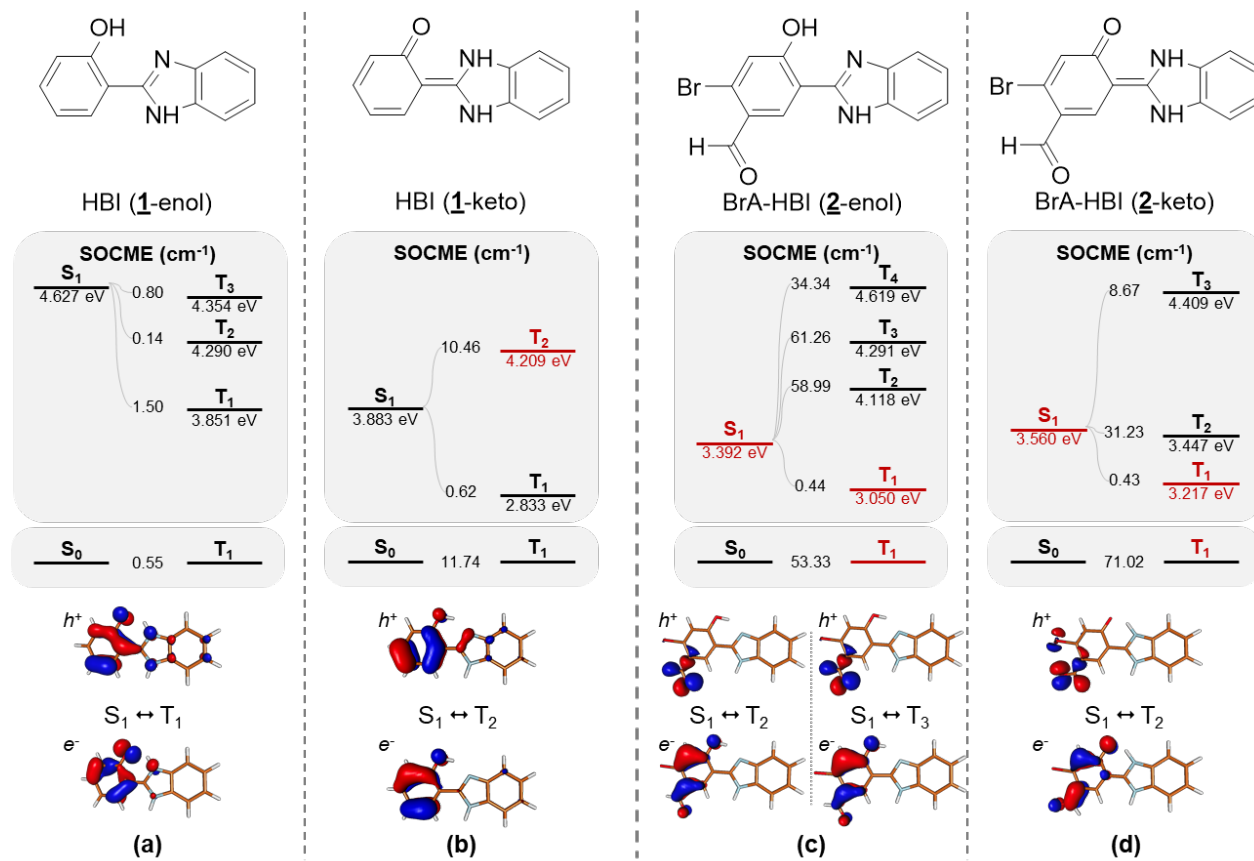


**Figure 2.1. Computational results of HBI (1) and BrA-HBI (2) in their enol or keto forms.** RAS-SF calculation results for the selected excited states (black denotes  $\pi, \pi^*$  while red denotes  $n, \pi^*$  states), their energies, and SOCMEs between S<sub>1</sub> and triplet states as well as that between S<sub>0</sub> and T<sub>1</sub>. RAS-SF NTOs of selected S-T transitions are displayed. An expanded NTO table is shown in Figure S2.1. The orbital configuration of each state is shown in Figure S2.2.

The strategically created BrA-HBI (Figure 2.1c-d) with qualitatively distinct low-lying states compared to HBI, where the former's S<sub>1</sub> and T<sub>1</sub> states show considerable ( $n, \pi^*$ ) character. In addition, the S<sub>1</sub> states of BrA-HBI have much lower excitation energy compared to that of HBI, corresponding to transitions between the non-bonding ( $n$ ) and  $\pi^*$  orbitals (see NTOs in Figure S2.1), given that lone-pair electron orbitals of aldehyde are higher in energy than electrons in the bonding  $\pi$  orbitals. Due to the low orbital overlap between the non-bonding and anti-bonding  $\pi^*$  orbitals, BrA-HBI have relatively small S<sub>1</sub>-T<sub>1</sub> energy gaps, where  $\Delta E_{S_1-T_1} \cong 0.34$  eV in both 2-enol and 2-keto, according to the energy diagram shown in Figure 2.1c-d.

While potential triplet emission channels are created by the aldehyde group, the plausibility of populating the  $T_n$  states still depends on additional factors. In 2-enol, the  $S_1$ - $T_1$  SOCME is low (Figure 2.1c) since  $S_1$  and  $T_1$  each has  $(n, \pi^*)$  character, and the  $T_2$  state of 2-enol has a high excitation energy that makes it inaccessible. The keto tautomer, 2-keto, exhibits a lower-energy  $T_2$  state than the enol tautomer, mainly due to the intrinsic C=O double bond that stabilizes the  $\pi^*$  orbital, which further lowers the transition energies between  $S_1$  and  $T_2$  states. This intrinsic carbonyl of the keto form helps create the efficient  $S_1$ - $T_2$  ISC channel with a high SOCME of  $31.2 \text{ cm}^{-1}$  that bears  $n$  to  $\pi$  orbital angular momentum variation (see the NTOs of BrA-HBI in Figure S2.1), which helps promote triplet population; and similarly significant  $T_1$ - $S_0$  SOC, stimulating triplet emission.

With these computational prediction and insights in hand, we conducted a series of photophysical studies to further validate the capabilities of the BrA-HBI.

### 2.3. Photophysical Properties of BrA-HBI

In a diluted solution, BrA-HBI displayed characteristic keto emission with large Stokes shift ( $>60 \text{ nm}$  from the onsets, Figure 2.2b). The emission peak was hypsochromically shifted upon increasing the solvent polarity. However, the ES IPT processes were efficient enough to prevent enol emission even in protic ethanol.

Triplet state properties of BrA-HBI in solid state were studied by doping it in poly(methyl methacrylate) (PMMA) and poly(acrylic acid) (PAA) separately. PMMA was chosen as a neutral host for the keto tautomer and PAA as an acidic host with the potential to hinder proton transfer process and unveil enol emission. As shown in Figure 2.2d, BrA-HBI in PMMA exhibited characteristic steady state emission in its keto form with a large Stokes shift. The total quantum yield ( $\Phi_{tot}$ ) rose from 9.8 % to 31 % from air to anoxic condition, which was accompanied by an increased delayed emission lifetime ( $\tau_d$ ) to  $1.90 \text{ ms}$  (Figure 2.2c), indicating considerable contribution from triplet excitons. Unexpectedly, the delayed and steady-state emission profile almost coincide with each other, suggesting potential TADF emission character but with a rather slow room-temperature lifetime in the  $ms$  regime.

Temperature-variant experiments were then performed to study the origin of the emission. As the temperature dropped to  $78 \text{ K}$ , a new lower-energy peak emerged near  $508 \text{ nm}$  while the emission band at ca.  $450 \text{ nm}$  gradually faded (Figure 2.2d, S2.5). The new emission peak near

508 nm could be characterized as phosphorescence emission while the original emission band at higher temperature could be assigned to a mixture of prompt fluorescence and TADF emission. Besides, the  $\tau_d$  v.s. T curve were also recorded in Figure S2.5 which suggested the migration between two lifetime species (i.e. TADF and phosphorescence). These verifications strongly supported the TADF nature of the emission at room temperature with a  $\Delta E_{ST}$  of 0.31 eV (from the emission peak, or  $\lambda_{max}$  at 78 K).

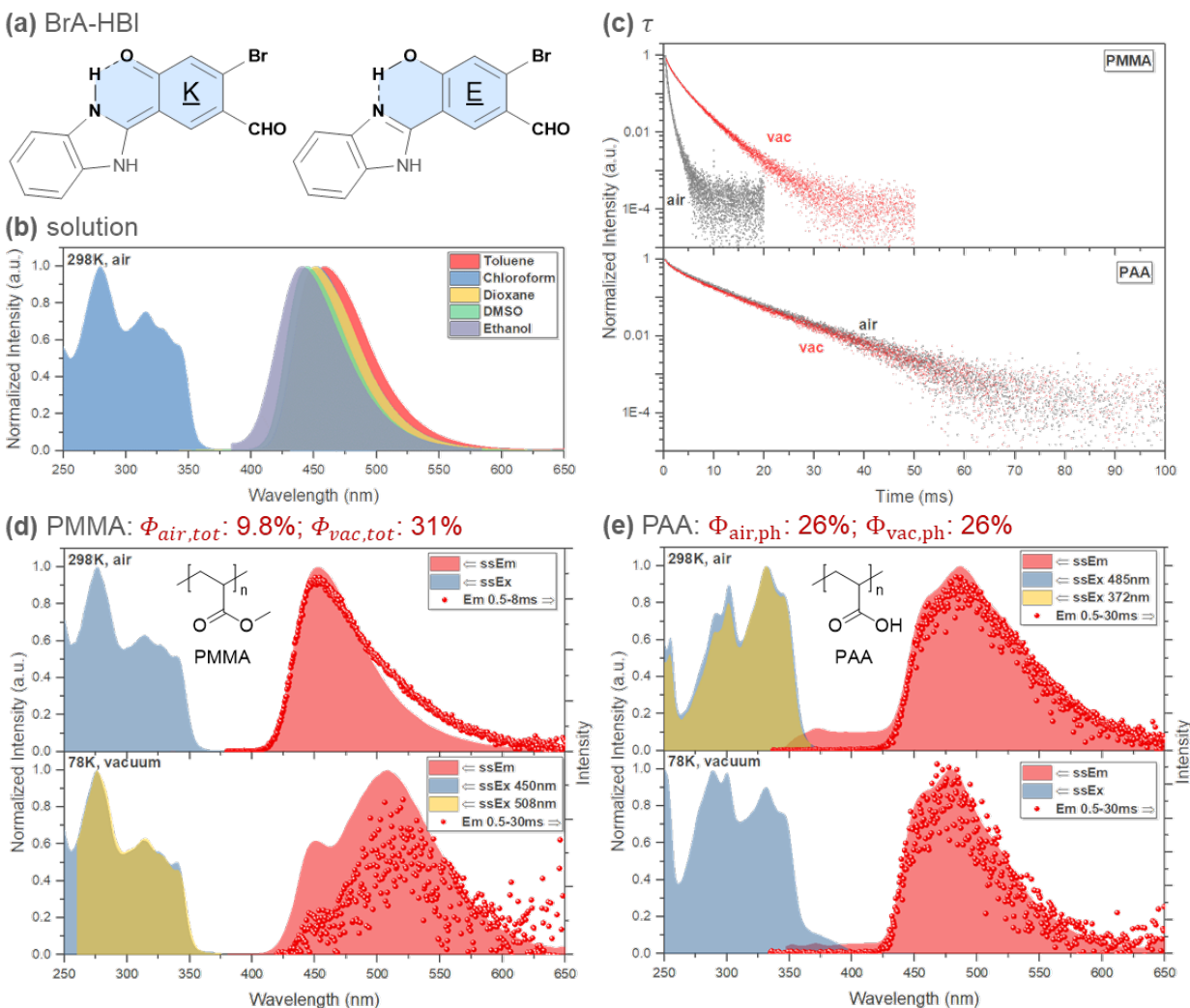


**Figure 2.2. Photophysical properties of BrA-HBI in PMMA or PAA.** (a) Chemical structure of BrA-HBI in its enol (E) and keto (K) form; steady state excitation (filled), emission spectra (filled), and delayed emission spectra (dots) of BrA-HBI in (b) various solvents (OD~0.1) at 298 K, spin-coated (d) PMMA or (e) PAA films with 1 wt% doping concentration measured at 298 K (top) and 78 K (bottom); (c) emission decay curves of BrA-HBI in PMMA (top) or PAA (bottom) measured at 298 K in air or in vacuum, which were measured from 200  $\mu$ s.

Computational results (Figure 2.1) provide a plausible explanation for the emission mechanism. Although carbonyl attachment has created a new  $S_1/T_1$  pair with ( $n, \pi^*$ ) and thus mild charge transfer (CT) character, the gap (0.34 eV) is large, not to mention the low  $S_1$ - $T_1$  SOCME



of ca.  $0.2 \text{ cm}^{-1}$ . However, we suspect that the up-conversion of triplet excitons may be assisted by the  $T_2$  state and the  $S_1$ - $T_2$  ISC channel with considerable SOCME, possibly through the spin-vibronic coupling pathway<sup>98-102</sup> as demonstrated in some blue TADF emitters.<sup>103</sup>

Interestingly in the doped PAA system (Figure 2.2e), we observed a completely different emission profile with a new higher-energy fluorescence band below  $400 \text{ nm}$ , which overlaps with the excitation spectrum, indicating a small Stokes shift typically seen in the enol tautomer. The room temperature delayed emission spectrum displayed a structured profile and maintained its shape at  $78 \text{ K}$  with only a small hypsochromic shift. Together with the single-component decay profile of  $\tau_d$  v.s.  $T$  curve (Figure S2.6), this indicates that BrA-HBI in PAA exhibited phosphorescence emission character instead, in sharp contrast to its TADF character in PMMA matrix.

To confirm the enol emission in PAA, we permanently blocked ESIPT through methylation on the hydroxyl group of BrA-HBI. When the resulting molecule was doped into PMMA and PAA, both systems displayed a similar emission profile to that of BrA-HBI@PAA system with a fluorescence band below  $400 \text{ nm}$  and a phosphorescence band at ca.  $520 \text{ nm}$  (Figure S2.7). Thus, we confirmed the blocked ESIPT of BrA-HBI in PAA matrix, most likely due to the strong solid-state intermolecular H-bond interaction between PAA and the phenolic ESIPT donor on BrA-HBI.

#### 2.4. Dissecting the Substitution Effects of Br and Carbonyl

In general, carbonyl substitution is considered essential to generate low-energy non-bonding electrons that assist in the orbital angular momentum shift,<sup>1</sup> in line with the El-Sayed rule;<sup>7</sup> meanwhile, Br is used to boost the overall SOC efficiencies. Further verification of their effects under our molecular scaffold was conducted by comparing the photophysical properties of BrA-HBI to those of mono-functionalized Br-HBI (with Br only) and A-HBI (with aldehyde only), as well as the non-functionalized HBI. Their properties in PMMA or PAA matrices are separately discussed as follows.

In PMMA (Figure 2.3a-c), non-functionalized HBI itself displayed classical keto emission without any delayed contents. Triplet emission was spotted in the form of TADF with aldehyde attachment. On the other hand, Br mono-substituted Br-HBI displayed three peaks in its delayed emission profile. While the other two ( $486$  and  $530 \text{ nm}$ ) could be assigned to phosphorescence emission from  $T_1$  state, the one at the higher energy ( $460 \text{ nm}$ ) likely originated from  $T_2$

phosphorescence and contained minimal TADF character since its intensity relative to  $T_1$  phosphorescence does not decrease even at 78 K.

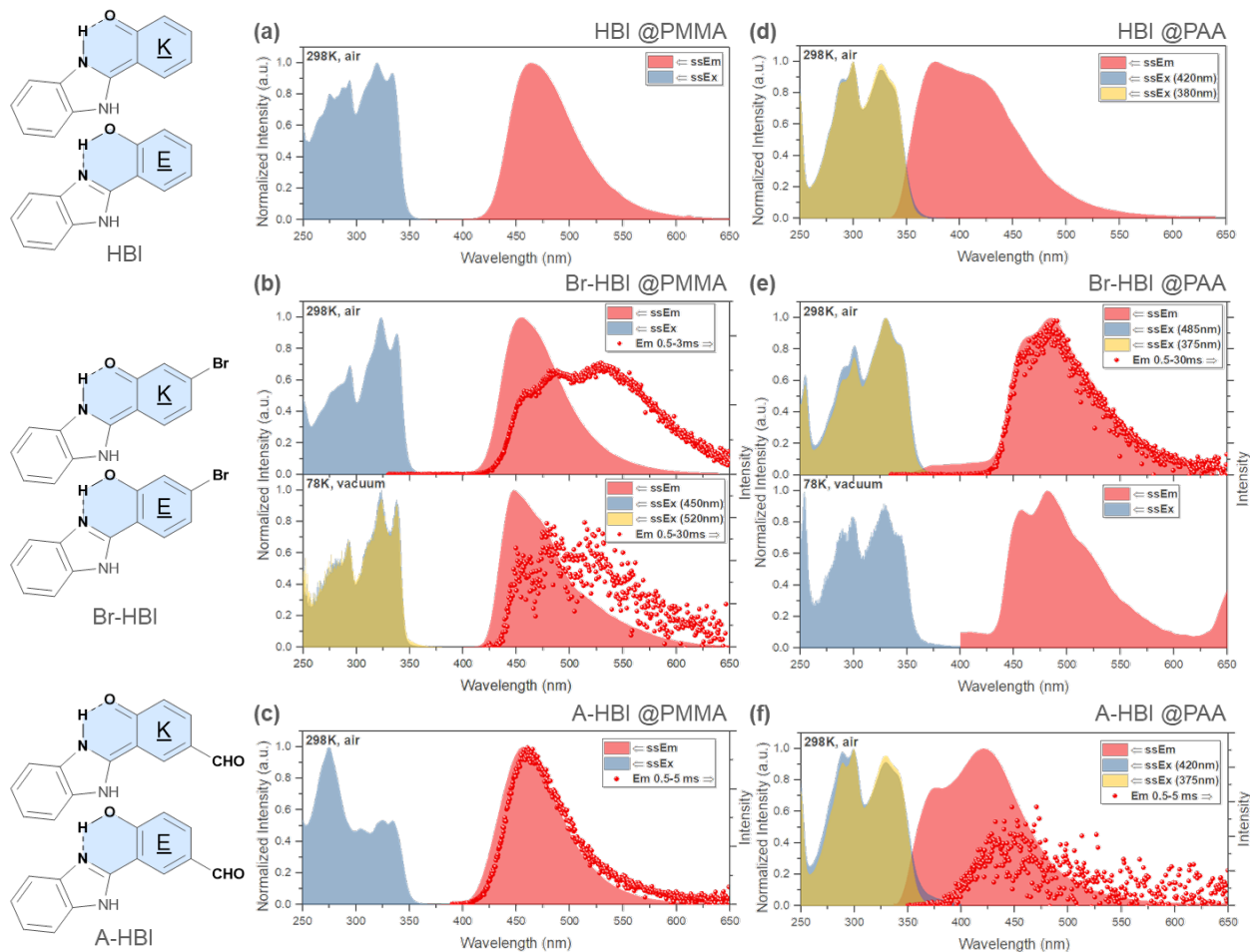


**Figure 2.3. Photophysical properties of HBI, Br-HBI, and A-HBI.** Steady state excitation (filled), emission spectra (filled), and delayed emission spectra (dots) of HBI, Br-HBI, and A-HBI in spin-coated (a-c) PMMA or (d-f) PAA films with 1 wt% doping concentration measured at 298 K or 78 K (indicated in each figure).

However, Br attachment alone in the absence of aldehyde is not sufficient to upconvert triplet excitons to singlet domains; thus, its delayed spectrum mostly consists of phosphorescence emission as the emission  $\lambda_{max}$  is independent of temperature change. To achieve quantitative comparison, we then deconvoluted the total quantum yield of each emitter into prompt and delayed portions. While the delayed and steady-state profile couldn't be spectrally separated, we managed to extract the delayed contents by analyzing the lifetime and steady state emission profiles in air vs. anoxic conditions (see section 2.12 for details).

As shown in Figure 2.4a, aldehyde substituted A-HBI dramatically enhanced the delayed QY to 14%, while Br substituted Br-HBI only displayed 6%  $\Phi_{delay}$ . These results are expected from the calculated keto-form energy state and SOCME profile (Figure S2.3): aldehyde substitution

alone could create new  $S_1$  and  $T_1$  states with  $(n, \pi^*)$  character and thus efficient  $(n, \pi^*) - (\pi, \pi^*)$  ISC channels for triplet population, while Br-HBI, despite its globally enhanced SOC, lacks efficient down-converting ISC channels due to its significantly large  $S_1$ - $T_1$  energy gap and inefficient SOCMEs. However, additional Br attachment on top of aldehyde substitution enhanced further the overall SOC efficiency (as calculated) as well as  $\Phi_{delay}$  (14 to 26%).

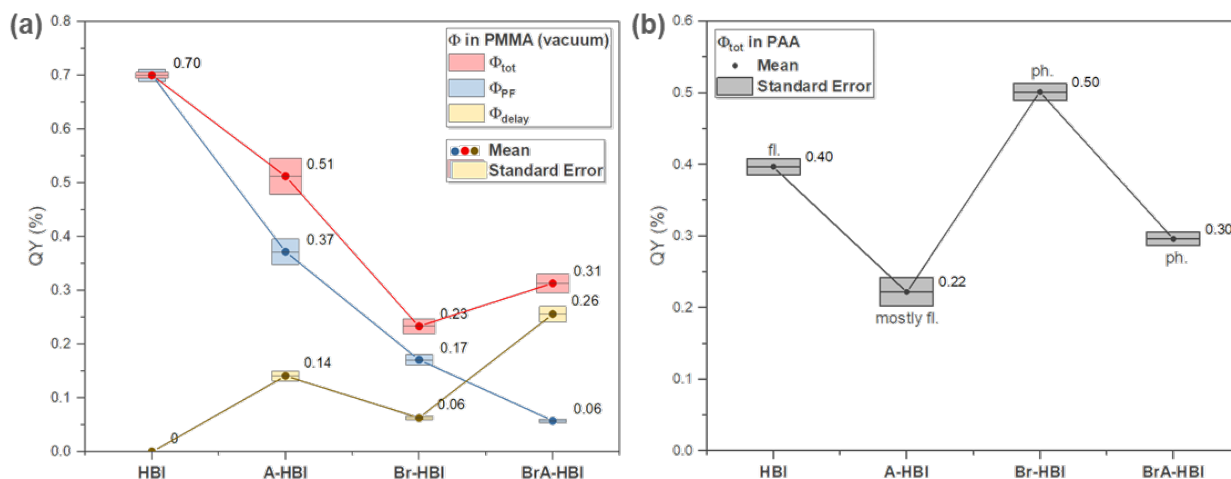


**Figure 2.4.** Total quantum yield ( $\Phi_{tot}$ ), prompt fluorescence QY ( $\Phi_{PF}$ ), and delayed emission QY ( $\Phi_{delay}$ ) of HBI, A-HBI, Br-HBI, and BrA-HBI measured in (a) PMMA and (b) PAA.

On the other hand, prompt fluorescence QY ( $\Phi_{PF}$ ) dropped dramatically from HBI (as high as 70%) through A/Br-HBI to BrA-HBI (6%). Although aldehyde attachment in A-HBI incited large  $\Phi_{delay}$ , the total QY ( $\Phi_{tot}$ ), compared to unsubstituted HBI, still dropped to 53% likely due to increased non-radiative decay from long-lived triplet excitons. It is surprising that, potentially due to efficient triplet population, Br attachment alone would lead to large drop in  $\Phi_{tot}$  to 23%, which was eventually recovered to 31% in fully-armed BrA-HBI. Interpreted from the computational results (Figure S2.3), adequate  $S_1$ - $T_2$  exciton up-conversion may be activated in Br-HBI, but the large  $\Delta E_{T_2-T_1}$  may not be favorable for the relaxation of high-energy triplet excitons. As a result, some  $T_2$  excitons could directly relax to ground state as the spectrum indicated (Figure 2.3b), and a few percent of  $T_2$  electrons survived to  $T_1$  state and emitted regular phosphorescence according to Kasha's rule.<sup>17</sup>

In PAA, while all four emitters displayed characteristic enol emission (Figure 2.3d-f), Br substitution played critical role to induce large phosphorescence yield ( $\Phi_{ph}$ , Figure 2.4b). Predicted from the calculation results for the enol-form (Figure S2.4), all four emitters were not expected to exhibit large triplet population: efficient SOC channel is missing in HBI and Br-HBI since the lowest energy states have pure  $(\pi, \pi^*)$  character; despite having new  $(n, \pi^*)$   $S_1$  and  $T_1$

states, the aldehyde-equipped A-HBI and BrA-HBI still lack an efficient SOC channel due to the higher lying  $^3(\pi, \pi^*)$  T<sub>2</sub> states (ca. 4.1 eV) v.s. S<sub>1</sub> states (ca. 3.4 eV). This is reflected in the emission profile of HBI and A-HBI where except for the weak delayed emission in A-HBI, both emitters displayed mostly prompt fluorescence in PAA. However, Br attachment brought up major discrepancy: while almost pure phosphorescence was achieved in the BrA-HBI@PAA system with a high  $\Phi_{ph}$  of 30%, Br attachment alone reached an even higher  $\Phi_{ph}$  of 50% in PAA (Figure 2.4b).

The exact origin of this unexpectedly high  $\Phi_{ph}$  is unknown but may shine light on the benefit of PAA as a great yet overlooked matrix for triplet emitters: 1) due to the large density of H-bonds in PAA, it serves as a good oxygen barrier. In PAA,  $\tau_{ph}$  in air is almost the same as that in anoxic conditions, which is quite the opposite in PMMA (Figure 2.2c); 2) PAA could establish multiple H-bonds with our ESIPT molecules, which helps prevent triplet excitons from decaying non-radiatively – a strategy widely used in organic RTP emitters;<sup>12,15,104</sup> 3) The presented results suggest a potential synergic effect between Br and PAA with the enol form only. We are currently reviewing the origin of this effect.

In short, we systematically analyzed the substituent effects of Br and aldehyde in promoting triplet population and delayed emission in this section through discussing the photophysical properties of HBI, Br-HBI, and A-HBI in PMMA and PAA. The results in PMMA are in good agreement with prediction: carbonyl is used to create channels for orbital angular momentum change during SOC, while Br is used to boost the overall SOC efficiencies. In PAA, however, Br is critically important to induce efficient triplet emission due to promising external effects from the PAA matrix.

## 2.5. On-off Switchable ESIPT Systems in Response to Acid Vapor

The switchable ESIPT process in PMMA vs. PAA instigated us to develop smart responsive systems. Poly(4-vinylpyridine) (P4VP) was selected since, despite being neutral, it is readily protonated upon acid doping<sup>105</sup> and serves as an acidic matrix. As for the ESIPT chromophore, we selected Br-HBI instead of BrA-HBI since its emissive species is easily distinguishable due to very high  $\Phi_{ph}$  in its enol form but very low triplet yield in its keto form.

The Br-HBI@P4VP film was subjected to solvent vapor annealing (SVA) with concentrated HCl. As shown in Figure 2.5a, keto emission was detected from the pristine film which well resembled that from PMMA. Upon acid treatment, P4VP was protonated, and the emission profile

shifted to the enol species with a rising high energy (<400 nm) fluorescence band, similar to that in PAA. Furthermore, original keto emission was recovered when the films were baked, possibly due to the evaporation of HCl<sup>105</sup> and consequent deprotonation of P4VP. These results indicate certain reversibility in our system.

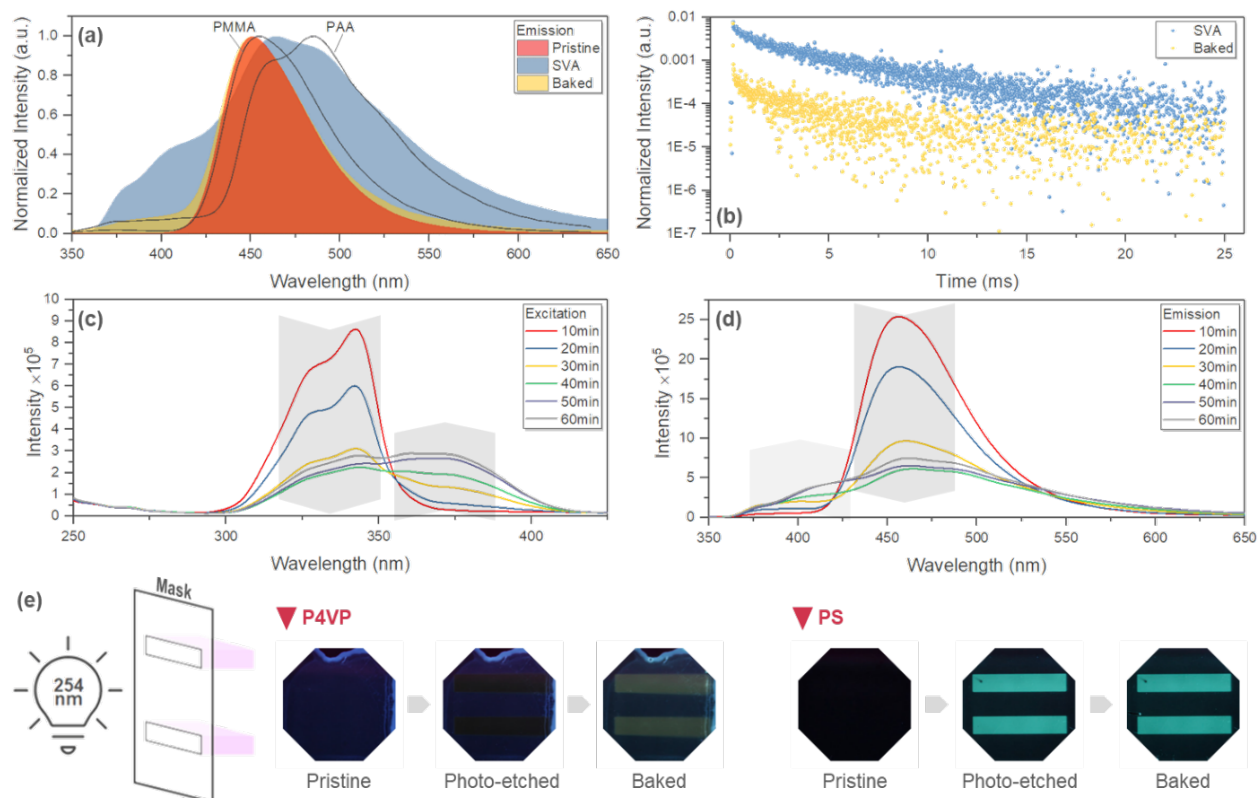


**Figure 2.5. Solvent vapor annealing results of Br-HBI in P4VP.** (a) Normalized steady state emission spectra (filled) and (b) emission decay curves (dots) of Br-HBI in P4VP (spin-coated, 1 wt% doping) upon solvent vapor annealing (SVA) with concentrated HCl and subsequent baking. Emission spectra in PMMA and in PAA (line) are included in for reference. The decay curves were measured from 0 ms. (c) excitation spectra and (d) steady state emission as SVA progressed. (e) Emissive patterns of Br-HBI in P4VP or PS under 365 nm illumination created by photo-etching with 254 nm UV lamp and a mask, followed by baking at 150 °C (P4VP) or 60 °C (PS).

As expected, in the protonated P4VP, Br-HBI exhibited much longer-lived phosphorescence (Figure 2.5b), indicating strong host-guest interactions in the protonated film, which can effectively suppress the non-radiative decay. Additionally, Figure 2.5c-d show the gradual keto-enol migration of the active emissive species upon the acid vapor treatment, during which an unexpected new excitation band emerged at a lower energy (ca. 370 nm). Although we cannot clearly identify the new excitation species, it could originate from the strong host-guest interaction.

Furthermore, the keto-enol switching in P4VP indeed originated from matrix acidity variation instead of direct protonation of the ESIPT molecule, which is supported by the SVA performance

in the inert polystyrene (PS) matrix (Figure S2.8). Only mild intensity drop was observed in the emission profile of PS film upon acid vapor annealing, and the emission stays in the keto form.

## 2.6. Photopatterning and Photochromism

Triplet emission chromism during enol-keto exchange has inspired us to explore their photopatterning applications. It turns out that keto-to-enol tautomerization is directly achievable upon photochemical etching with 254 nm UV, which is capable of generating phenoxy radicals from the hydroxyl moieties in the ESIPT molecules,<sup>106</sup> which then react with the polymer backbone and block the proton transfer processes. This is accompanied by a distinct emission color change from blue to yellowish-green under 365 nm UV excitation.

As shown in Figure 2.5e and S2.9-2.10, Br-HBI was doped in P4VP or PS and the resulting thin films were subjected to 254 nm photochemical etching under a mask. In P4VP, the irradiated area displayed faint yellow-green color which became much brighter after subsequent baking. The pattern was stable after long-term storage. In PS, under the same fabrication conditions, much brighter green emission pattern was revealed after UV irradiation but additional thermal annealing had minimal effect. Photophysical analysis exhibited considerable triplet emission character from the treated areas (Figure S2.11), indicating enol emission since keto-form Br-HBI could not emit long-lived photons in the yellowish-green regime. Under 365 nm excitation, the generated photopatterns displayed high contrast to non-treated areas, which benefited from the fact that a new excitation band emerged past 365 nm in the treated sample while the pristine film has minimum absorption at 365 nm (Figure S2.11).

## 2.7. Conclusions

ESIPT molecules have intriguing four-level photophysical states, but they have been rarely used as triplet emitters. The acid sensitivity of proton transfer process has inspired us to develop ESIPT based metal-free organic triplet emitters exhibiting switchable dual-form emission. We started from the simplest HBI structure and successfully activated bright room-temperature triplet emission both in the keto and enol tautomers by incorporating aldehyde to generate efficient  $(n, \pi^*) - (\pi, \pi^*)$  SOC channels and Br to elevate the overall SOC efficiencies. Interestingly, the developed BrA-HBI is capable of emitting blue delayed fluorescence in its keto form with a high  $\Phi_d$  of 31% in PMMA, while enol-related green phosphorescence is detected in PAA with 26%

$\Phi_{ph}$ . We further investigated the effect of Br and aldehyde, separately, on triplet population and triplet emission. Results highlighted unexpected external boosting effects of PAA host on the phosphorescence efficiency of brominated ESIPT chromophores. Surprisingly, enol-form Br-HBI exhibited 50%  $\Phi_{ph}$  in PAA matrix. To our best knowledge, BrA-HBI and Br-HBI were among the brightest ESIPT triplet emitters designed so far (SI).

Application merits of the prototype ESIPT triplet emitters were explored in the spirit of the keto-enol tautomerization. We have developed on-off switchable system that is responsive to acid vapor by utilizing reversibly protonation of P4VP matrix. Upon switching the matrix acidity, ESIPT triplet emitters could undergo switching between their enol and keto forms. Secondly, photo-patterning systems were developed by taking advantage of the triplet emission chromism of ESIPT chromophores. Bright yellowish-green emissive patterns were generated with high contrast.

In summary, we activated bright triplet emission from conventional ESIPT chromophores and exploited the enol-keto “on-off” switchability in various materials systems. The simplicity of our material design and the comprehensive photophysical investigation may allow for the future developments of ESIPT triplet emitters and their advances in solid-state lighting, information encryption, and solid-state sensors.

### **Publication Information and Author Contribution**

*Contents in this chapter has been accepted to publish in Adv. Funct. Mater. (manuscript ID: adfm.202201256)*

Wenhao Shao, Jie Hao, Hanjie Jiang, Paul M. Zimmerman, Jinsang Kim\*, “Metal-Free Organic Triplet-Emitters with On-Off Switchable Excited State Intramolecular Proton Transfer”

### **Author Contribution**

W.S. designed this manuscript. Preliminary calculation was conducted by W.S.. RAS-SF calculation was conducted by H.J.. Computational results were analyzed by W.S. and H.J.. Synthetic route of the molecules studied was desined by W.S. and J.H.; J.H. synthesized Br-HBI, BrA-HBI, A-HBI, while W.S. conducted the methylation of BrA-HBI. The rest of the experiments, including photophysical analyses, SVA, and photopatterning, was conducted by W.S.. P.M.Z. supervised the computational investigation. J.K. supervised the the overall manuscript.

## CHAPTER II. SUPPORTING INFORMATION

### 2.8. Additional experimental details

#### General

All chemicals used were purchased from Millipore Sigma or Fisher Scientific and used without further purification unless specified. 4-bromo-2-hydroxybenzaldehyde was purchased from TCI America and ChemScene. Deuterated solvents for NMR spectroscopy (nuclear magnetic resonance) were purchased from Cambridge Isotope Laboratories or Millipore Sigma. Poly(methyl methacrylate) (PMMA) was purchased from Aldrich Chemical Co. ( $M_w \sim 350,000$ ). Poly(acrylic acid) (PAA) was purchased from Aldrich Chemical Co. (lot # MKBR9922V,  $M_w \sim 450,000$ ). Poly(4-vinylpyridine), linear (P4VP) was purchased from Scientific Polymer Products Inc. (lot # 401116018,  $M_w \sim 50,000$ ). Polystyrene (PS) was purchased from Aldrich Chemical Co. (lot # 15902CI,  $M_w \sim 280,000$ ).

#### Physical measurements

- Nuclear Magnetic Resonance (NMR) spectra were collected on Varian Vnmrs 500 (500 MHz) spectrometer.
- Mass Spectrometry and High Resolution Mass Spectrometry (HRMS) were conducted on Agilent Q-TOF HPLC-MS. Compounds were dissolved in Milli-Q water/acetonitrile (LC/MS grade) (9:1) with a concentration of  $10 \mu\text{M}$  and  $10 \mu\text{L}$  of the solution was injected into the spectrometer. Blank mixed solvent was used as the background. Mass spectra reported in section VIII were obtained by subtracting the background spectra from the sample spectra.
- Photoluminescence spectra were collected on a Photon Technologies International (PTI) QuantaMaster spectrofluorometer (QM-400) equipped with an integrating sphere (K-Sphere) and a cryostat.
- The emitters were doped in PMMA or PAA for solid-state measurements: quartz substrates ( $1.5 \times 2.5 \text{ cm}$ ) were prepared and cleaned by sonication consecutively in soap, deionized water, acetone, isopropyl alcohol, and then proceeded to UV-ozone treatment for 30 min. THF/chloroform (1:1 vol.:vol.) solution containing emitter (1 wt% to polymer) and 2.5 wt% PMMA, or ethanol solution containing emitter (1 wt% to polymer) and 2.5 wt% PAA were prepared and spin-coated on the cleaned quartz substrates (500 rpm for 5 min). Last, the films were transferred into a glovebox filled with  $\text{N}_2$  and baked at  $120 \text{ }^\circ\text{C}$  for 30 min. Films were stored in the glovebox except during measurements.



- For absolute quantum yield measurements, blank PMMA or PAA films were used as background.

### **Solvent vapor annealing**

The emitters were doped in P4VP or PS for solvent vapor annealing and photophysical measurements: quartz (1.5\*2.5 cm) or glass (1.5\*1.5 cm) substrates were prepared and cleaned by sonication consecutively in soap, deionized water, acetone, isopropyl alcohol, and then proceeded to UV-ozone treatment for 30 min. Chloroform solution containing Br-HBI (1 wt% to polymer) and 1.25 wt% polymer were prepared and spin-coated on the cleaned substrates (500 rpm for 5 min). The prepared films were dried under vacuum for at least 20 minutes to ensure complete evaporation of solvent. Solvent vapor annealing was carried out in an empty vacuum desiccator: the sample and a 25 mL beaker containing concentrated HCl (10 mL) were placed in a petri-dish at the center of the metal plate. The chamber was closed and vacuumed for an initial 2 minutes for the stabilization of HCl vapor. Then, the stop cock connected with the vacuum was closed and the vacuum in the desiccator was maintained for an additional 8 minutes.

### **Photopatterning and photochromism**

The emitters were doped in P4VP or PS on cleaned glass substrates following the same procedure. The samples were transferred to a N<sub>2</sub>-filled glovebox and were covered with a photomask made of Molybdenum by Towne Technologies, Inc. A 254 nm hand-held UV lamp (purchased from Fisher Scientific) with a low power density of 2.4 mW/cm<sup>2</sup> was used to generate the photopattern. The samples were subsequently baked on a hot plate at various temperatures selected. Note that samples were placed upside-down (polymer film in contact with the hot plate) during the baking process to prevent bubble formation. A Canon EOS 550d camera was used to record the emission of the films illuminated with a 365 nm hand-held UV lamp, before photopatterning, directly after photopatterning, and after baking.

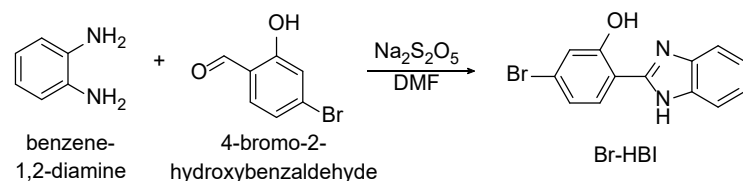
## Synthesis of prototype molecules

Purity of the compounds synthesized were confirmed by NMR and MS/HRMS, as documented in section VII and VIII.

### ▪ (HBI, 1) 2-(1*H*-benzo[*d*]imidazol-2-yl)phenol

HBI was purchased from Millipore Sigma and used without further purification.

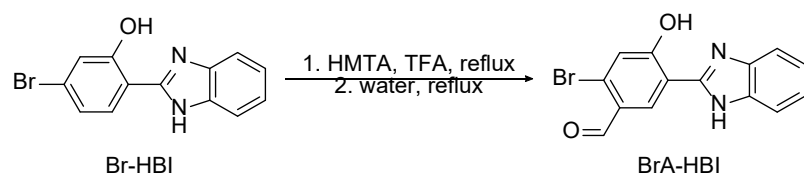
### ▪ (Br-HBI, 3) 2-(1*H*-benzo[*d*]imidazol-2-yl)-5-bromophenol



To a single-neck 500 mL round bottom flask with a stirring solution of benzene-1,2-diamine (9.95 mmol, 1 equiv.) and 4-bromo-2-hydroxybenzaldehyde (9.95 mmol, 1 equiv.) in DMF (200 mL, ~0.05 mL/mmol benzaldehyde), sodium metabisulfite (1.99 mmol, 0.2 equiv.) was added. The mixture was stirred for 6–8 h at 110 °C. Color of the mixture turned gradually to green and dark brown at the end. After the reaction was completed, the mixture was poured into cold DI water under stirring. The resulting solid (pink/red) was further purified by column chromatography on silica gel (eluent: hexane/ethyl acetate, 30:1 to 4:1) to afford a pale yellow solid (1.7g, 60%).

- <sup>1</sup>H NMR (500 MHz, DMSO-*d*<sub>6</sub>) δ 13.41 (s), 8.00 (d, *J* = 8.4 Hz, 1H), 7.67 (s, 2H), 7.30 (dt, *J* = 6.1, 3.6 Hz, 2H), 7.27 (d, *J* = 2.0 Hz, 1H), 7.24 (dd, *J* = 8.4, 2.0 Hz, 1H).
- <sup>13</sup>C NMR (126 MHz, DMSO-*d*<sub>6</sub>) δ 159.27, 151.32, 128.27, 124.70, 122.65, 120.34, 112.59.
- HRMS [M+H]<sup>+</sup>
  - Predicted *m/z*: 289.00 (100.0%), 291.00 (98.5%), 290.00 (14.2%), 292.00 (13.8%), 293.00 (1.2%)
  - Found *m/z*: 288.9968 (100%), 290.9949 (97.7%), 288.9998 (14.5%), 291.9977 (14.4%)

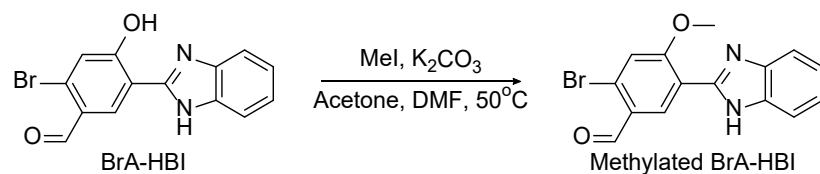
### ▪ (BrA-HBI, 2) 5-(1*H*-benzo[*d*]imidazol-2-yl)-2-bromo-4-hydroxybenzaldehyde



In a 100 mL double-neck round bottom flask, the previously synthesized Br-HBI (3.35 mmol, 1 equiv.) and hexamethylenetetramine (HMTA, 33.5 mmol, 10 equiv.) were added followed by the addition of trifluoroacetic acid (TFA, 35 mL). After degassing the mixture with Ar, it was heated at reflux for 5 h, during which the initial white slurry turned into clear yellow solution. Prolonged reaction time had no obvious side effects and might help increase the yield of para aldehyde-substituted products v.s. ortho products. 2. Afterwards, DI water (~ 30 mL) was added and the mixture was refluxed for another 1 h. Then the reaction was stopped and left in the refrigerator overnight. The solid precipitate formed was filtered and washed with water. The obtained crude product was purified by column chromatography on silica gel (dry-loading, eluent: hexane/ethylacetate, 20:1 to 1:1; product was obtained near 9:1-6:1) to afford a pale yellow solid (93 mg).

- $^1\text{H NMR}$  (500 MHz, DMSO- $d_6$ )  $\delta$  10.12 (s, 1H), 8.67 (s, 1H), 7.70 (dd,  $J = 6.0, 3.2$  Hz, 2H), 7.41 (s, 1H), 7.34 (dd,  $J = 6.0, 3.1$  Hz, 2H).
- $^{13}\text{C NMR}$  (126 MHz, DMSO- $d_6$ )  $\delta$  190.16, 164.56, 150.34, 129.44, 129.02, 125.08, 123.97, 122.64, 115.38, 113.20.
- HRMS  $[\text{M}+\text{H}]^+$ 
  - Predicted  $m/z$ : 316.99 (100.0%), 318.99 (97.4%), 319.99 (15.5%), 318.00 (15.3%), 319.00 (1.5%), 321.00 (1.1%)
  - Found  $m/z$ : 316.9916 (100%), 318.9898 (97.6%), 317.9940 (15.3%), 319.9926 (15.7%)

#### ▪ Methylation of BrA-HBI

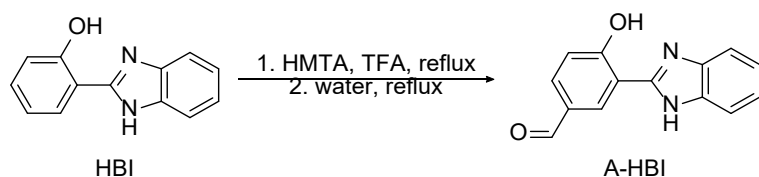


In a 10 mL round bottom flask, the mixture of BrA-HBI (4.337 mg, 13.68  $\mu\text{mol}$ ), powdered  $\text{K}_2\text{CO}_3$  (5.900 mg, 3.121 equiv.), and methyl iodide (MeI, a few drops, in excess) in acetone (3 mL)

+ DMF (1 mL) mixed solvent (DMF could be used solely) was stirred at 60°C under Ar atmosphere for several days. The reaction was slow due to the low reactivity of BrA-HBI. K<sub>2</sub>CO<sub>3</sub> (5.9 mg) and MeI (a few drops) were added in the middle of the reaction to fully convert the unreacted BrA-HBI to the product. When the starting material disappeared on TLC, the solution was poured into water to obtain the crude product, which was further purified by multiple reprecipitations in water/methanol mixture to obtain the pure product as a white powder (0.99 mg).

- <sup>1</sup>H NMR (400 MHz, DMSO-d<sub>6</sub>) δ 12.29 (s, 1H), 10.18 (s, 1H), 8.81 (s, 1H), 7.71 – 7.67 (m, 1H), 7.66 (s, 1H), 7.62 (dd, J = 6.7, 1.7 Hz, 1H), 7.27 – 7.19 (m, 2H), 4.17 (s, 3H).
- HRMS [M+H]<sup>+</sup>
  - Predicted m/z: 331.01 (100.0%), 333.01 (99.0%), 332.01 (17.2%), 334.01 (16.0%), 335.01 (1.7%)
  - Found m/z: 331.0075 (100%), 333.0056 (98.9%), 332.0102 (16.9%), 334.0084 (16.5%)

▪ (A-HBI, 4) 3-(1*H*-benzo[*d*]imidazol-2-yl)-4-hydroxybenzaldehyde



A-HBI was synthesized from HBI using the same procedure as BrA-HBI. Yield: 100 mg, 12.6%.

- <sup>1</sup>H NMR (500 MHz, DMSO-d<sub>6</sub>) δ 13.88 (s), 9.93 (s, 1H), 8.69 (d, J = 1.6 Hz, 1H), 7.95 (dd, J = 8.5, 1.6 Hz, 1H), 7.70 (dd, J = 5.4, 3.3 Hz, 2H), 7.32 (dd, J = 6.0, 3.1 Hz, 2H), 7.23 (d, J = 8.5 Hz, 1H).
- <sup>13</sup>C NMR (126 MHz, DMSO-d<sub>6</sub>) δ 191.30, 163.68, 151.05, 133.98, 128.80, 128.77, 123.69, 118.45, 113.67.
- HRMS [M+H]<sup>+</sup>
  - Predicted m/z: 239.08 (100.0%), 240.09 (15.3%), 241.09 (1.5%)
  - Found m/z: 239.0815 (100%), 240.0841 (15.8%)

## 2.9. Computational Details

The RAS-SF method is programmed in the Q-Chem 5.4 software package<sup>107</sup>, and the SOC computations are implemented in a development version of Q-Chem. All RAS-SF calculations were performed with the 6-31G\* basis set<sup>108</sup> and the RIMP2-cc-pVDZ auxiliary basis<sup>109</sup>. RAS-SF hole, particle calculations with 8 electron in 8 orbital active spaces were carried out with RAS1 and RAS3 subspaces including all occupied and virtual orbitals, respectively. Unless otherwise stated, the core electrons were kept frozen. Reference orbitals for RAS-SF were obtained from restricted open-shell density functional theory (RODFT) using the B3LYP functional in the nonet state. Geometries of the molecules were optimized at the ground state using  $\omega$ B97X-D functional<sup>110</sup> and the def2-TZVP basis set<sup>111</sup>. Calculations of SOC constants utilize general libraries developed for SOC calculations within EOM-CC<sup>112</sup>. Spin-orbit NTOs were computed and analyzed using the libwfa library<sup>113</sup>. The NTOs with the largest singular values, for each compound, were plotted using Molden program<sup>114</sup>.

## 2.10. Additional Computational Results

	 HBI (1-enol)	 HBI (1-keto)	 BrA-HBI (2-enol)	 BrA-HBI (2-keto)
$S_0 \leftrightarrow T_1$ SOCME	 $(\pi, \pi^*)$ 0.57	 $(\pi, \pi^*)$ 11.74	 $(n, \pi^*)$ 53.33	 $(n, \pi^*)$ 71.43
$S_1 \leftrightarrow T_1$ SOCME	 $(\pi, \pi^*)$ 1.50	 $(\pi, \pi^*)$ 0.62	 $(n, n)$ 0.44	 $(\pi, \pi^*)$ 0.43
$S_1 \leftrightarrow T_2$ SOCME	 $(\pi, \pi^*)$ 0.14	 $(\pi, \pi^*)$ $(n, \pi^*)$ 10.46	 $(n, \pi^*)$ 58.99	 $(\pi, \pi^*)$ 31.23

**Figure S2.1. Expanded RAS-SF NTO results for HBI (1) and BrA-HBI (2).** Relevant orbitals of HBI and BrA-HBI in their enol or keto forms; RAS-SF natural transition orbitals of significant S-T transitions are displayed, along with their SOC constants (units in  $cm^{-1}$ ) and the corresponding transition characters.

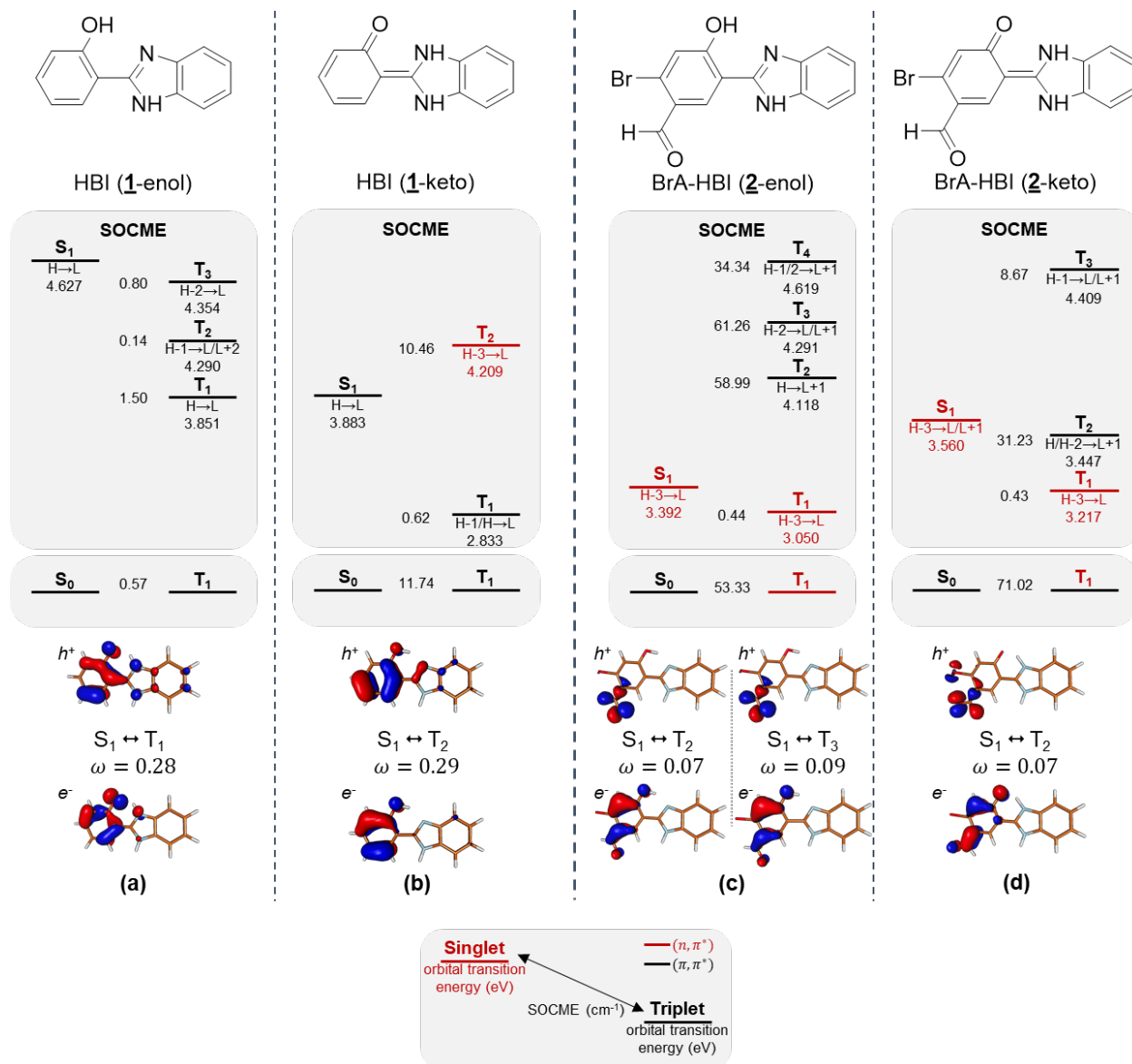


**Figure S2.2.** Expanded RAS-SF calculation results for HBI (1) and BrA-HBI (2) showing the orbital configurations: Chemical structures of HBI and BrA-HBI in their enol or keto forms; RAS-SF calculation results for the selected excited states, their energies (units in eV), transition character, and SOCMEs (units in  $cm^{-1}$ ) between S1 and triplet states (see the legend for details). RAS-SF natural transition orbitals of the S-T transitions with largest SOCME are displayed.  $\omega$  represents the singular values of the transitions shown in the NTO pairs, indicating the significance of the specified orbital transitions. Selected frontier molecular orbitals were attached in section 2.14.

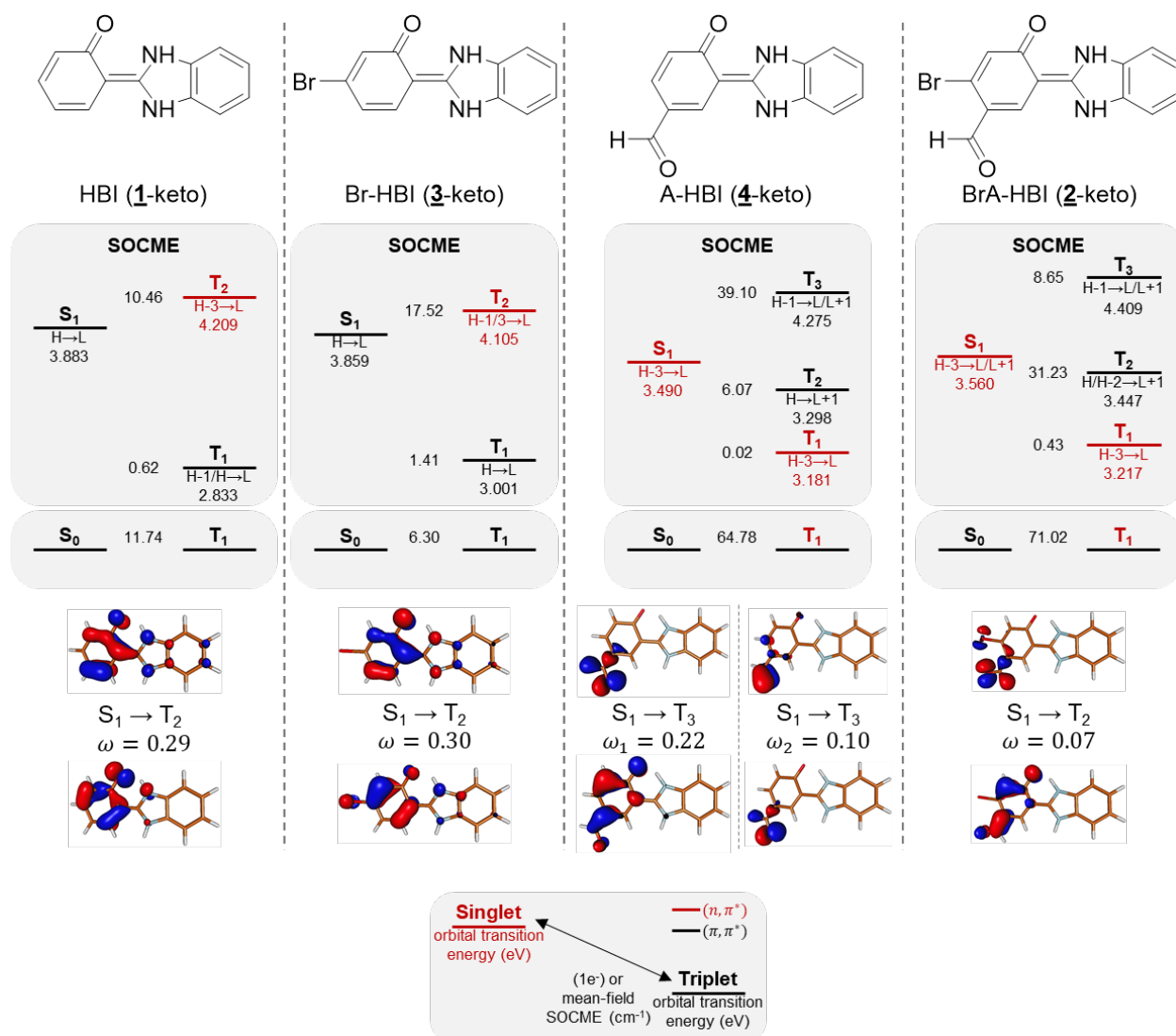


**Figure S2.3. RAS-SF calculation results for keto-form molecules.** Chemically structures of HBI, Br-HBI, A-HBI, and BrA-HBI in their keto form; RAS-SF calculation results for the selected excited states, their energies, transition character, SOCMEs between  $S_1$  and triplet states, and SOCMEs between  $T_1$  and  $S_0$  (see the legend for details). RAS-SF natural transition orbitals of the S-T transitions with largest SOCME are displayed.  $\omega$  represents the singular values of the transitions shown in the NTO pairs, indicating the significance of the specified orbital transitions. In some cases (A-HBI), two NTO pairs are shown, both having large  $\omega$  values. Selected frontier molecular orbitals were attached in section 2.14.



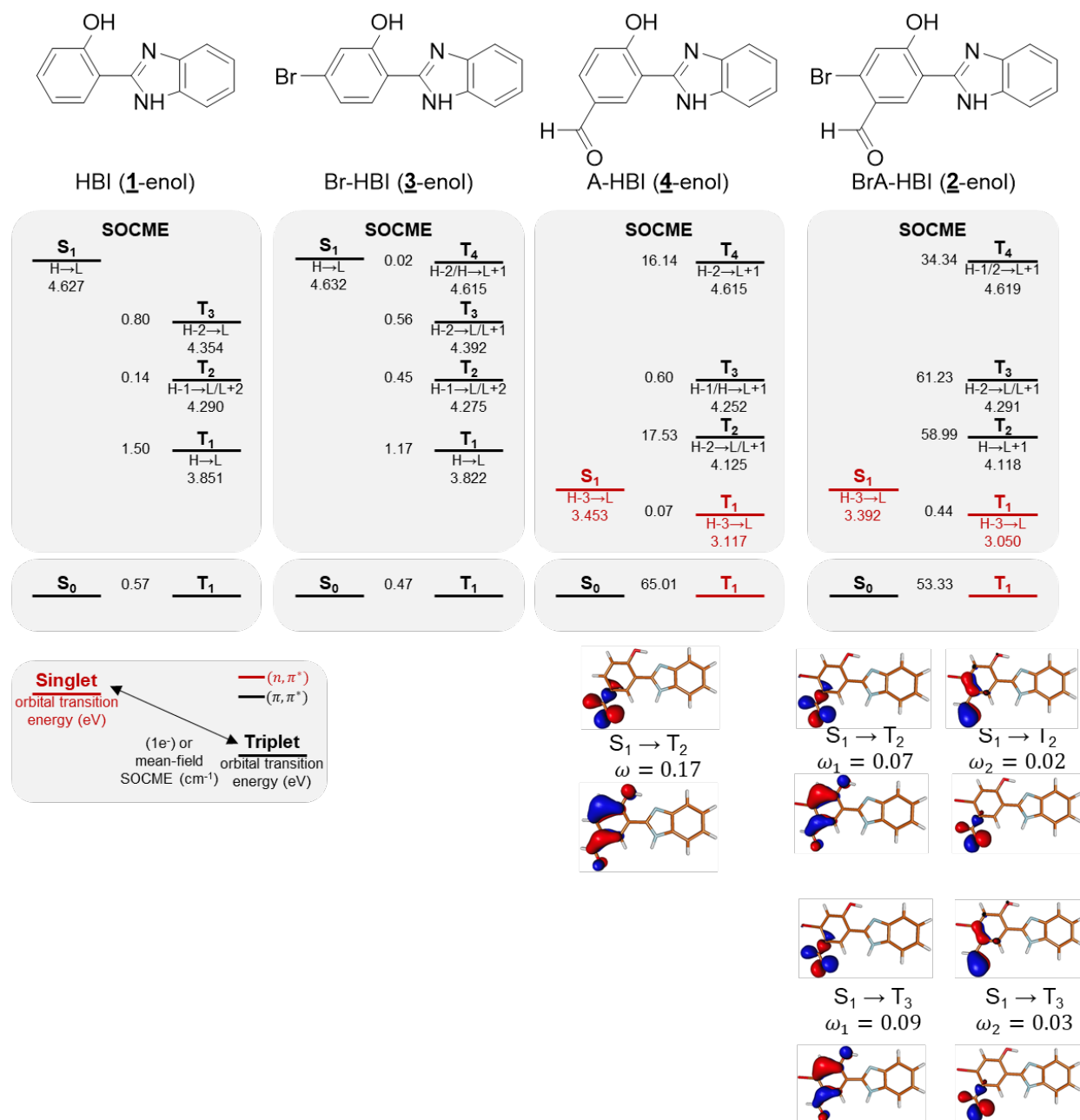


**Figure S2.4. RAS-SF calculation results for enol-form molecules.** Chemically structures of HBI, Br-HBI, A-HBI, and BrA-HBI in their enol form; RAS-SF calculation results for the selected excited states, their energies, transition character, SOCMEs between  $S_1$  and triplet states, and SOCMEs between  $T_1$  and  $S_0$  (see the legend for details). RAS-SF natural transition orbitals of the S-T transitions with largest SOCME are displayed.  $\omega$  represents the singular values of the transitions shown in the NTO pairs, indicating the significance of the specified orbital transitions. In some cases (BrA-HBI), two NTO pairs under the same transition are shown, both having large  $\omega$  values. Selected frontier molecular orbitals were attached in section 2.14.

## 2.11. Additional Photophysical Analyses

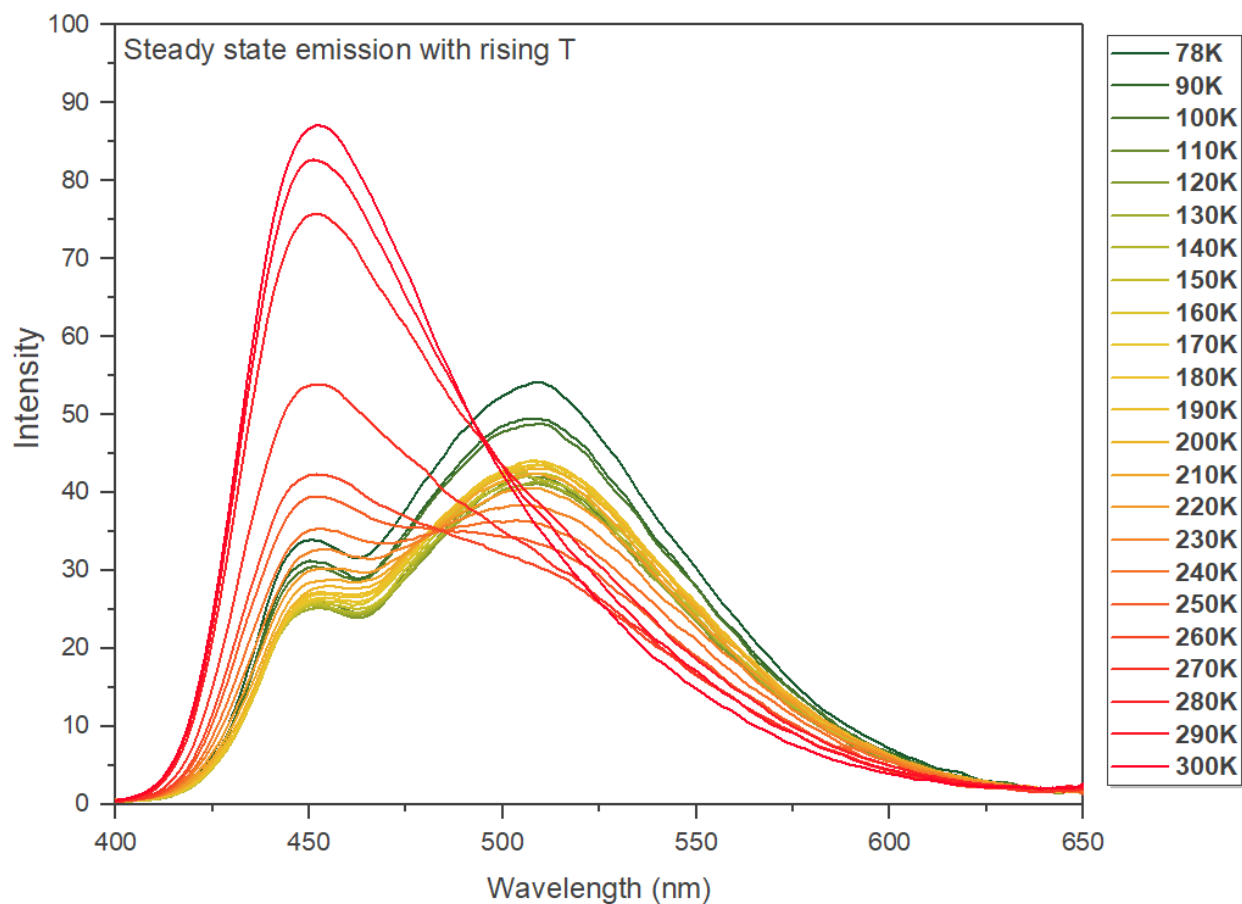


**Figure S2.5. Emission spectra v.s. temperature curve for BrA-HBI (2).** Steady state emission spectra of BrA-HBI in spin-coated PMMA film with 1 wt% doping concentration, measured in vacuum with rising temperature.

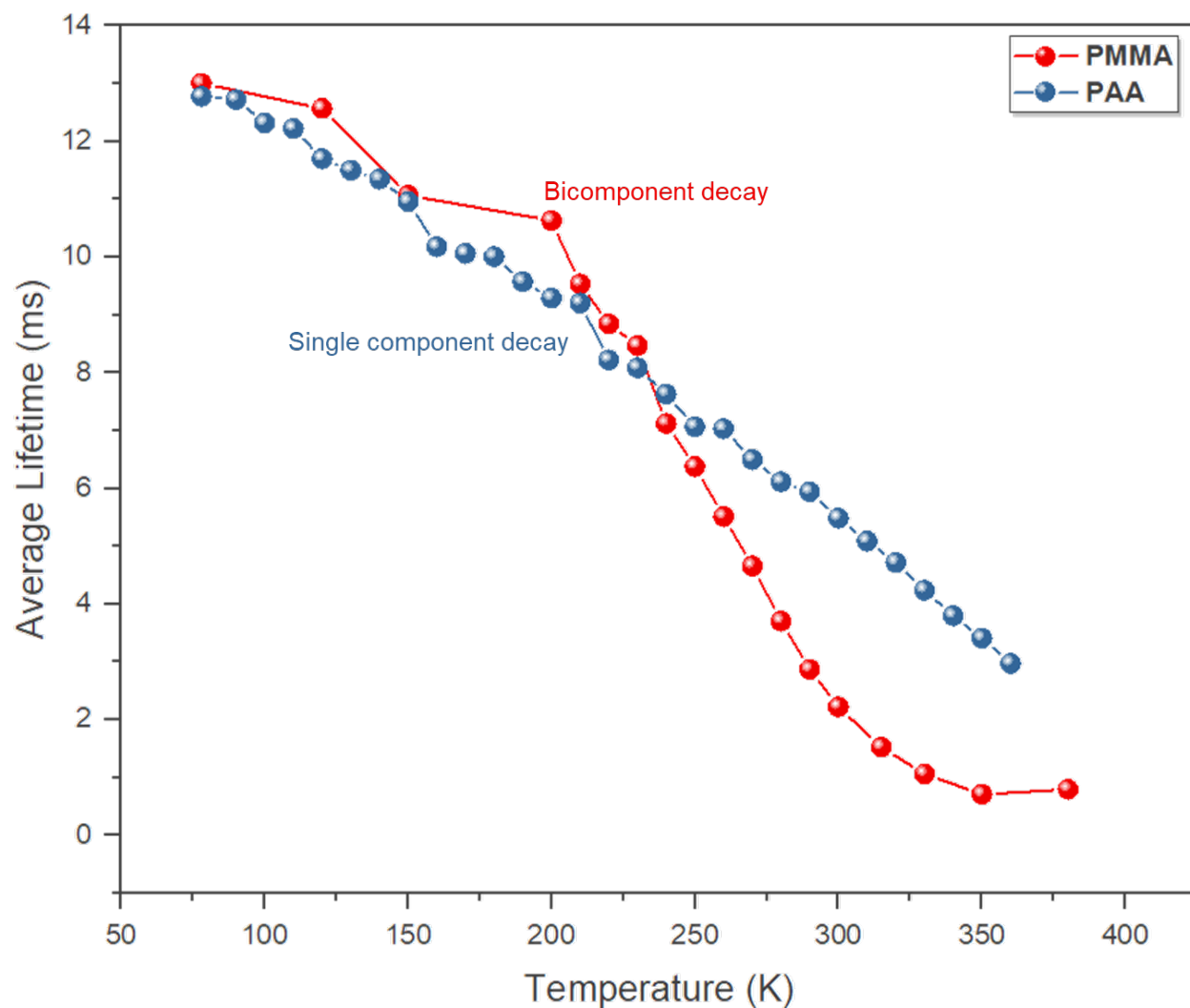


**Figure S2.6. Delayed emission lifetime v.s. temperature curve of BrA-HBI (2) in spin-coated PMMA or PAA film with 1 wt% doping concentration, measured in vacuum with rising temperature.**

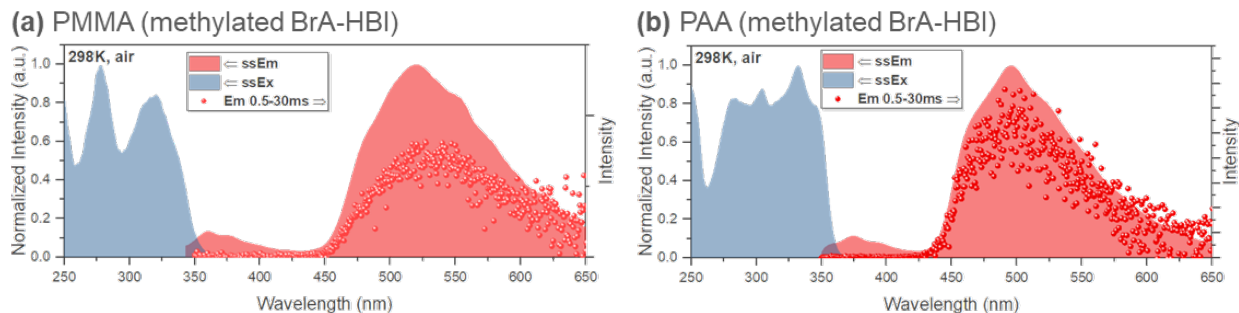


**Figure S2.7. Photophysical analysis of methylated BrA-HBI (2).** Steady state excitation (filled), emission spectra (filled), and delayed emission spectra (dots) of methylated BrA-HBI in spin-coated (a) PMMA or (b) PAA films with 1 wt% doping concentration measured at 298K.

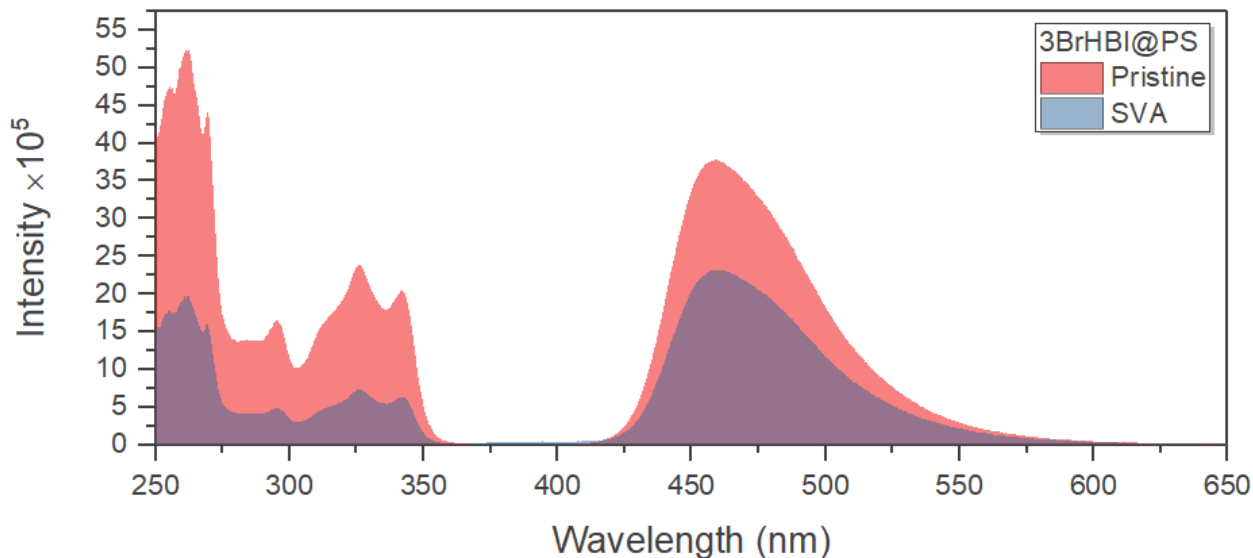


**Figure S2.8. Br-HBI (3) in PS.** Steady state emission spectra of Br-HBI in PS (spin-coated, 1 wt% doping) upon solvent vapor annealing (SVA) with concentrated HCl.

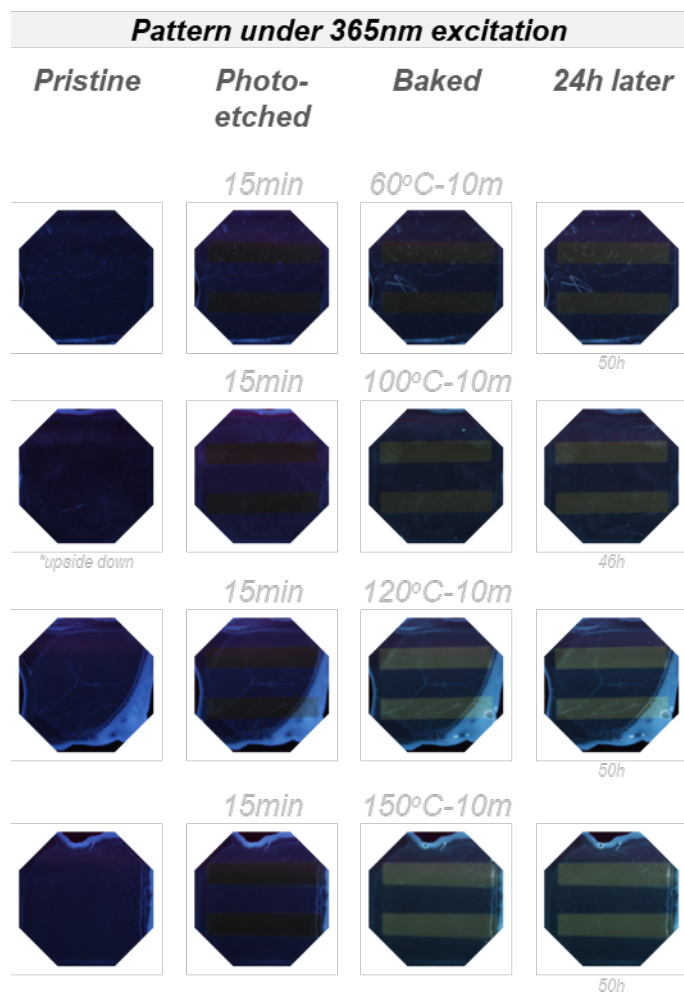


**Figure S2.9. Emissive patterns of Br-HBI (3) in P4VP under 365 nm illumination created by i) photo-etching with 254 nm UV lamp and a mask for 15 minutes, followed by ii) baking at various temperatures for 10 minutes.**

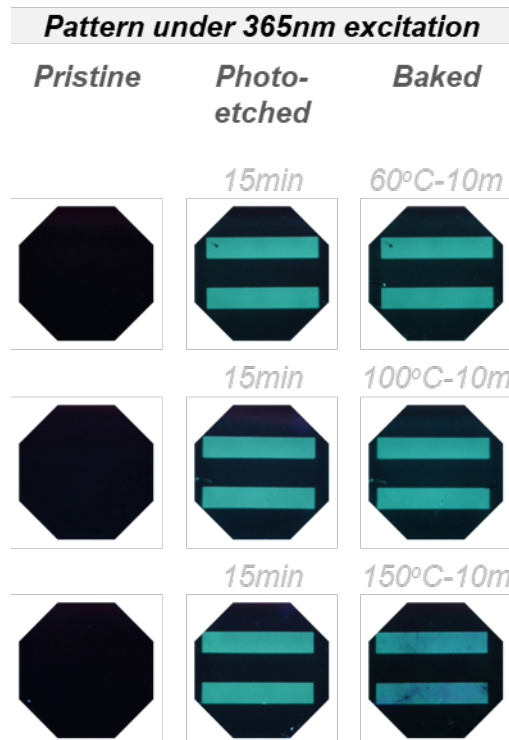


**Figure S2.10. Emissive patterns of Br-HBI (3) in PS under 365 nm illumination created by i) photo-etching with 254 nm UV lamp and a mask for 15 minutes, followed by ii) baking at various temperatures for 10 minutes.**

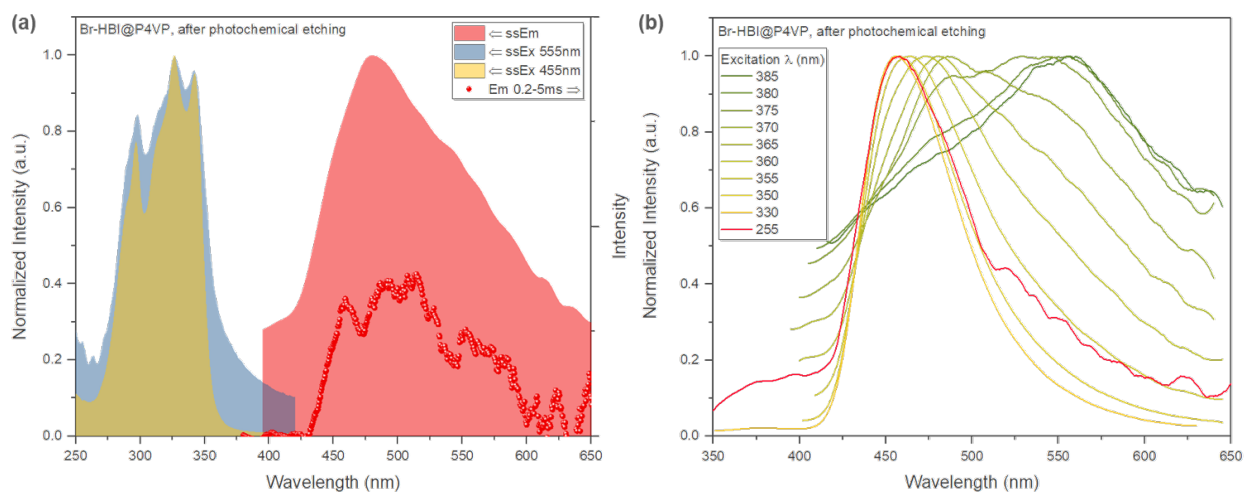


**Figure S2.11. Photophysical analysis of emissive patterns.** (a) Steady state excitation (filled), emission spectra (filled), and delayed emission spectra (dots) of Br-HBI in P4VP (spin-coated, 1 wt% doping) after photo-etching with 254 nm UV lamp for 15 minutes; panel (b) displays the steady state emission spectra with various excitation wavelengths.

## 2.12. Extracting Delayed Emission Quantum Yield from Total Quantum Yield

In this section, we will explain how to deconvolute the total quantum yield ( $\Phi_{tot}$ ) into prompt fluorescence ( $\Phi_{PF}$ ) and delayed emission quantum yield ( $\Phi_{delay}$ ) as shown in Figure 2.4.

For HBI, A-HBI, Br-HBI, and BrA-HBI in PAA matrix, deconvolution could be simply done from the steady state emission spectra since prompt fluorescence and delayed emission, in the form of phosphorescence, could be easily distinguished.

In the PMMA matrix at room temperature, the steady state emission spectra were complicated by prompt and delayed emission, which overlapped with each other. However, we could use the steady state emission intensity in air v.s. in vacuum, assisted by the delayed emission intensity in air v.s. in vacuum, to deconvolute  $\Phi_{delay}$  from  $\Phi_{tot}$ . The procedure is documented as follows:

### 1) Data acquisition

First, the steady state and delayed emission spectra in air and in vacuum are obtained as well as the delayed emission decay curve in air and in vacuum. Steady state emission spectra of a blank PMMA film fabrication under the same procedure was measured as the background. Delayed emission spectra didn't need additional background information since PMMA was optically inert in our excitation range and scattered incident light has been gated. and Spin-coated PMMA thin films were quite susceptible to oxygen permeation, and thus deprivation of oxygen under vacuum would restore the total emission profile, both in the steady state and delayed regime.

### 2) Integration of emission intensity

After subtracting the background spectra from blank PMMA films, the steady state emission spectra in air and in vacuum were integrated to obtain  $I_{ss,air}$  and  $I_{ss,vac}$ . Using the same integration range, delayed emission spectra were integrated without background subtraction to obtain  $I'_{d,air}$  and  $I'_{d,vac}$ . Since a gated time range was applied during delayed emission measurement (e.g. 0.2-10 ms),  $I'_{d,air}$  and  $I'_{d,vac}$  were not the total delayed emission intensity and therefore not comparable and needed to be corrected using the fitted decay curve.

### 3) Decay fitting and extrapolation

The decay curves in air and in vacuum were fitted using the embedded multi-exponent fitting module of QuantaMaster (data acquisition and analysis software from PTI). Using the fitting parameters, the original decay curves were extrapolated to 1  $\mu$ s and 1 s, assuming that this range would cover most of the delayed contents and make  $I_{d,air}$  and  $I_{d,vac}$  comparable. The tail of the decay curves (1 s) could be easily fitted with various softwares (QuantaMaster, OriginalPro, etc.);

however, extra discretion was needed to fit the head ( $1 \mu\text{s}$ ) of the decay curve in air, which usually exhibit multi-exponent profile in contrast to the decay curve in vacuum. Misleading short decay species ( $\tau < 20 \mu\text{s}$ ) could exist in the final fitting results even though the measured time range (usually 0.2-10 ms) couldn't cover these short decay species.

As a result, the fitted decay curves could be integrated with the time range chosen for delayed emission spectra measurement (e.g. 0.2-10 ms) and the "full intensity range" ( $1 \mu\text{s} - 1 \text{s}$ ). The ratio,  $I_{1\mu\text{s}-1\text{s}}/I_{0.2-10\text{ms}}$  was used to correct the delayed emission intensity,  $I'_{d,\text{air}}$  and  $I'_{d,\text{vac}}$ . In other words,

$$I_{d,\text{air}} = I'_{d,\text{air}} \frac{I_{1\mu\text{s}-1\text{s}}}{I_{0.2-10\text{ms}}}, I_{d,\text{vac}} = I'_{d,\text{vac}} \frac{I_{1\mu\text{s}-1\text{s}}}{I_{0.2-10\text{ms}}}$$

where  $I_{d,\text{air}}$  and  $I_{d,\text{vac}}$  are the corrected delayed emission intensity.

#### 4) Extracing $\Phi_{\text{delay}}$ and $\Phi_{\text{PF}}$

We assume that prompt fluorescence intensity,  $I_{\text{PF}}$ , didn't change from air to vacuum. Thus,

$$I_{\text{SS},\text{vac}} = I_{d,\text{vac}}^* + I_{\text{PF}}$$

$$I_{\text{SS},\text{air}} = I_{d,\text{air}}^* + I_{\text{PF}}$$

Note that we used  $I_{d,\text{air}}^*$  and  $I_{d,\text{vac}}^*$  here to be distinguished from  $I_{d,\text{air}}$  and  $I_{d,\text{vac}}$  since steady state and delayed emission were measured using different detectors. Thus, we could derive

$$\frac{I_{\text{SS},\text{vac}} - I_{\text{SS},\text{air}}}{I_{d,\text{vac}}^*} = \frac{I_{d,\text{vac}}^* - I_{d,\text{air}}^*}{I_{d,\text{vac}}^*} = \frac{I_{d,\text{vac}} - I_{d,\text{air}}}{I_{d,\text{vac}}}$$

Therefore,

$$\Phi_{\text{delay},\text{vac}} = \Phi_{\text{tot},\text{vac}} \frac{I_{d,\text{vac}}^*}{I_{\text{SS},\text{vac}}}$$

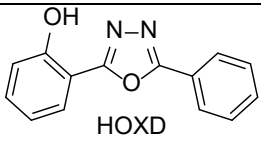
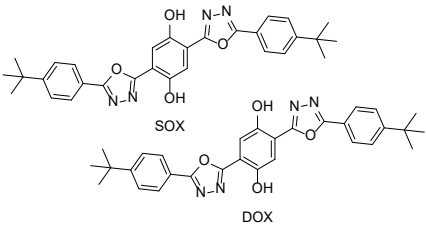
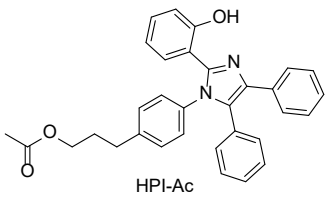
$$\Phi_{\text{PF}} = \Phi_{\text{tot}} - \Phi_{\text{delay}}$$

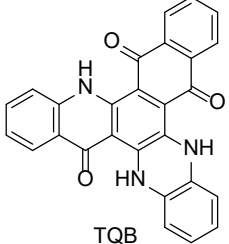
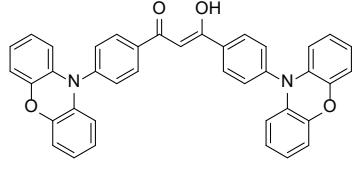
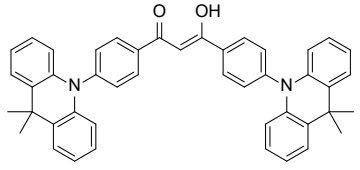
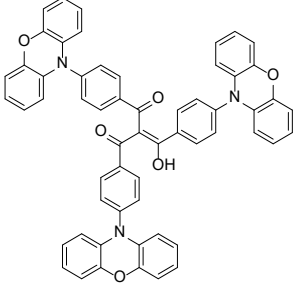
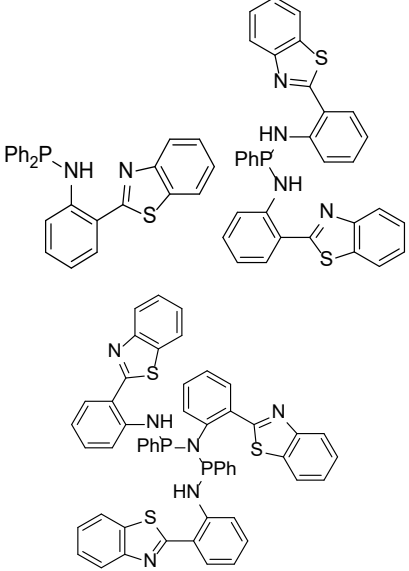


### 2.13. Reported ESIPT Molecules with Room Temperature Triplet Emission

Table S2.1 listed the contemporary ESIPT emitters that exhibited triplet emission potential. As shown here, room-temperature triplet emission, either in the form of room-temperature phosphorescence (RTP) or thermal assisted delayed fluorescence (TADF) were very rarely observed prior to 2017, nor were their photophysical properties systematically studied. The first tailor-designed ESIPT TADF emitter was made by Adachi group in 2017,<sup>79</sup> but the photoluminescence quantum yield of the delayed emission did not exceed 10% due to insufficient reverse intersystem crossing. Since then, study of ESIPT TADF emitters mushroomed and the delayed emission quantum yield was pushed to 42%.<sup>78</sup> However, all of these pioneer studies are based on the keto form of ESIPT molecules, and no reports on activating triplet emission from enol form is reported to the best of our knowledge. In addition, activating efficient RTP from ESIPT emitters is rarely explored.

**Table S2.1. Reported ESIPT molecules with room temperature triplet emission**

	Compound	Type of emission	$\Phi_{delayed}$	Year ref.
1	 HOXD	RTP	Unreported	2002 115
2	 SOX DOX	RTP	Unreported	2007 116
3	 HPI-Ac	TADF	Unreported	2007 117

4	 <p>TQB</p>	TADF	9.5% <sup>a</sup>	2017 79
5	 <p>PXZPDO</p>	TADF	36% <sup>b</sup>	2018 78
6	 <p>DMACPDO</p>	TADF	42% <sup>b</sup>	2018 78
7	 <p>TPXZBM</p>	TADF	4.5% <sup>b</sup>	2021 80
8		RTP	<1% <sup>c</sup>	2021 84

<sup>a</sup>Measured at 300K, doped in bis[2-(diphenyl- phosphino)phenyl]ether oxide (DPEPO) host.

<sup>b</sup>Measured at 300K, doped in 4,4'-di(9H-carbazol-9-yl)-1,1'-biphenyl (CBP) host.  $\Phi_{delayed}$  was calculated using the total PLQY ( $\Phi_{PL}$ ) and delayed fluorescence weight factor ( $R_d$ ) provided in the original reports.

<sup>c</sup>Measured at 300K in undoped crystals.

## 2.14. RAS-SF Frontier Molecular Orbitals of the Prototype Molecules

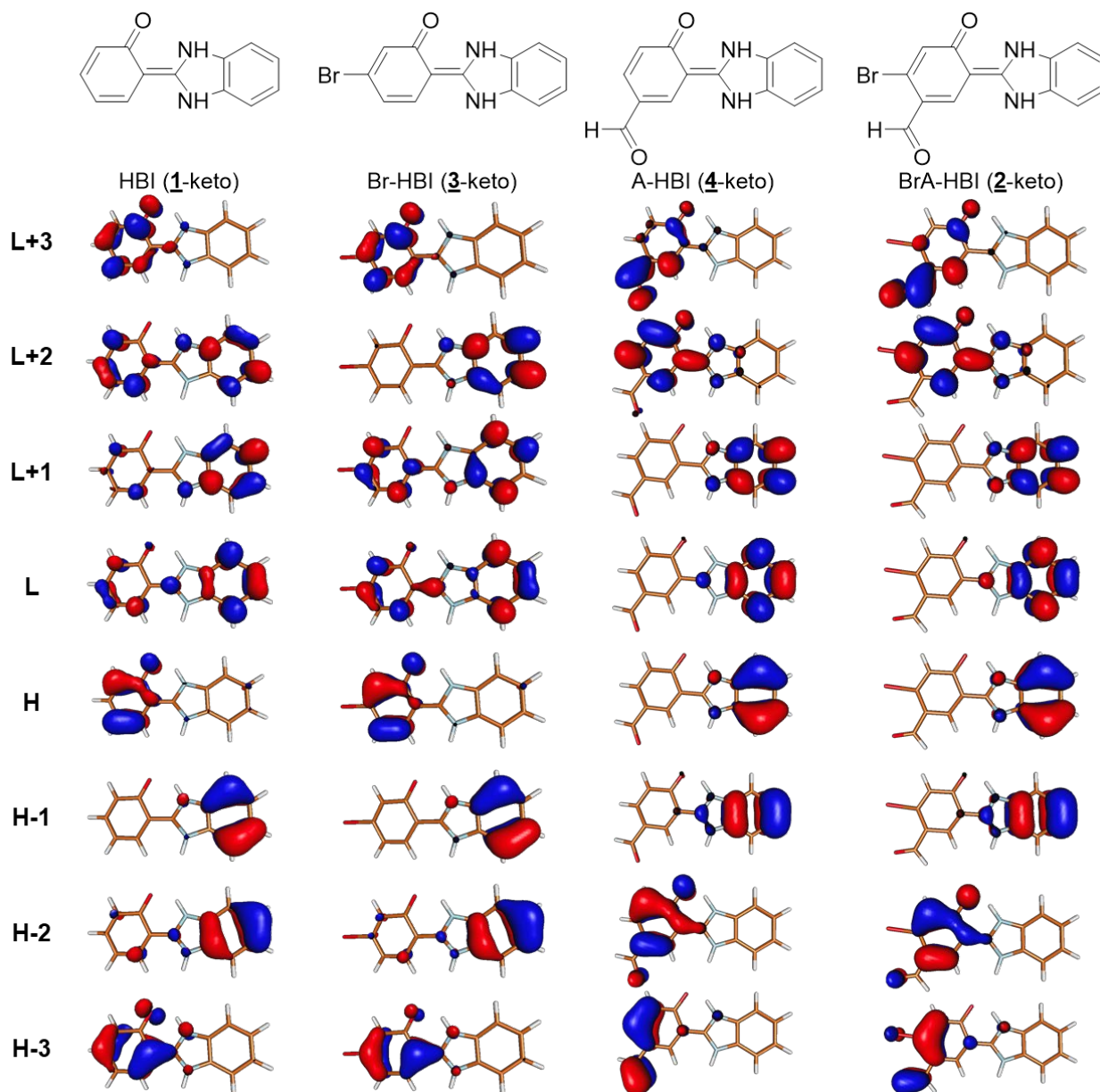
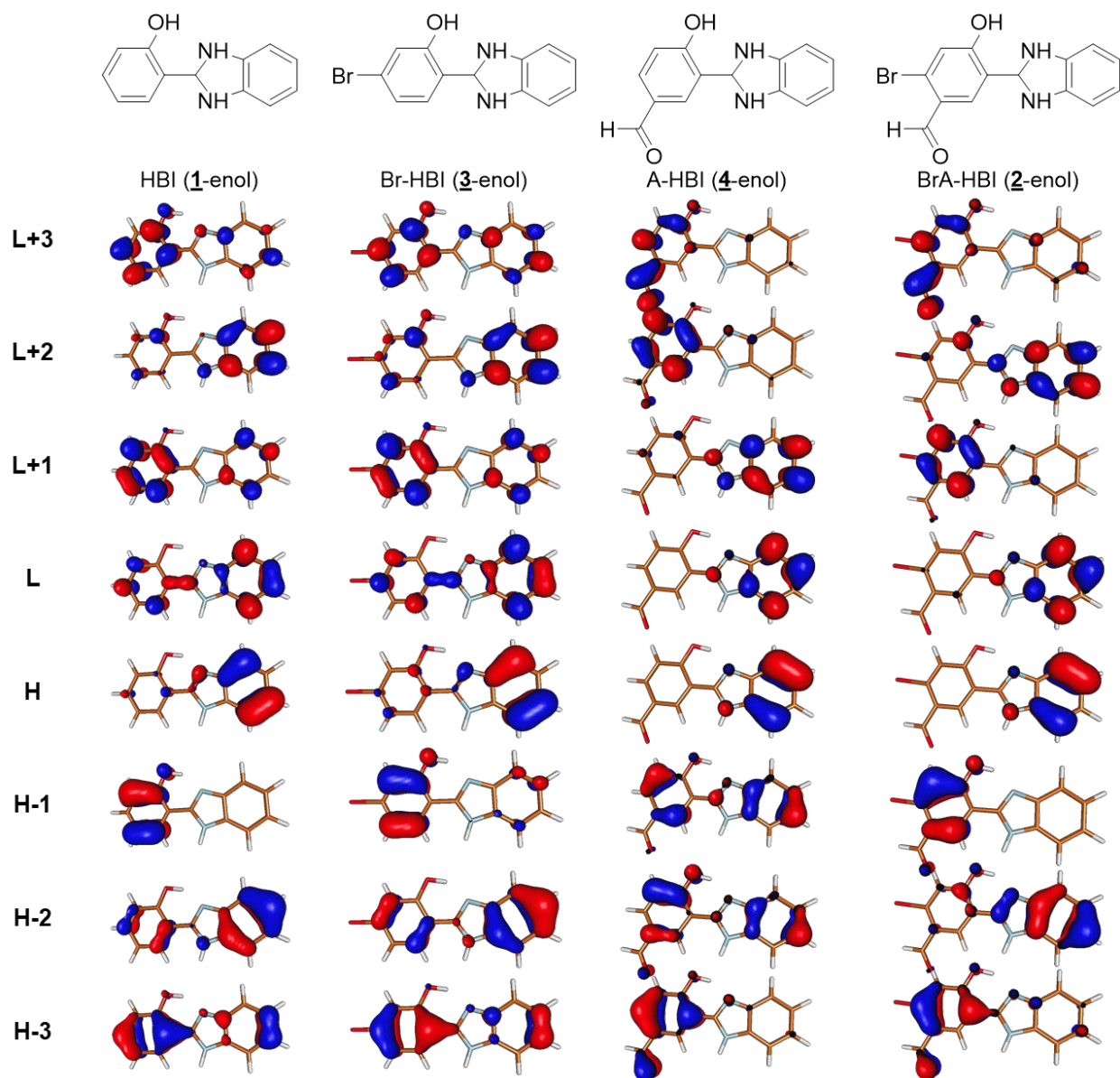


Figure S2.12. Selected frontier molecular orbitals in the keto form calculated by RAS-SF methods. H: HOMO, L: LUMO.



**Figure S2.13.** Selected frontier molecular orbitals in the enol form calculated by RAS-SF methods. H: HOMO, L: LUMO.

**CHAPTER III**  
**Photoresponsive Luminescence Switching of**  
**Metal-Free Organic Phosphors-Doped Polymer Matrices**

*Contents in this chapter has been published as follows:*

Zang, L., Shao, W., Kwon, M. S., Zhang, Z. & Kim, J. Photoresponsive Luminescence Switching of Metal-Free Organic Phosphors Doped Polymer Matrices. *Adv. Opt. Mater.* **2020**, 8, 2000654.

**Abstract**

A new type of luminescence switching behavior based on phosphorescence enhancement from a series of metal-free organic phosphors doped polymers by UV-irradiation was investigated. This phenomenon is observed only from pairs of organic phosphors and polymer matrices having a combination of appropriate triplet exciton lifetime and oxygen permeability. Systematic investigation revealed that the luminescence switching behavior of organic phosphors embedded in a specific polymeric matrix stems from the conversion of triplet oxygens to singlet oxygens by UV-irradiation, leading to the unique phosphorescence enhancement of organic phosphors. Visualization of latent information by UV-irradiation was demonstrated toward novel secure information communication applications.

### 3.1. Introduction

Switching of optical properties of materials in response to light has been an intriguing topic owing to its importance in the application of molecular switches, imaging devices, transmission glasses, and smart windows.<sup>118</sup> Photoresponsive switching in materials' optical properties is devised most commonly from reversible transformation between two chemical isomers (i.e. photoisomerism) having different absorption characteristics by photoirradiation.<sup>119</sup> Photo-induced reversible ring opening and closing reactions and cis/trans isomerizations observed in diarylethenes, azobenzenes, and spiropyrans<sup>119,120</sup> can alter the effective conjugation length of the photochromic molecules which can also turn on and off intramolecular and intermolecular energy transfers, leading to chromatic transition.<sup>121</sup> Photoresponsive luminescence switching can be commonly achieved by either reversible conversion between the non-emissive and emissive states of photochromic compounds, or by the control of energy transfer between a photochromic donor molecule and an emitting acceptor. While luminescence switching responding to light has been developed mostly from fluorophores,<sup>121</sup> phosphorescence switching have some unique advantages such as freedom from the interference of background emission due to their much longer emission lifetime.<sup>122</sup>

Most phosphors are organometallic by nature and accordingly, photoresponsive phosphorescence switching has also been limited to organometallic complexes having a photochromic moiety as a ligand.<sup>123,124</sup> Even though, metal-free purely organic phosphors (POP) have a much longer triplet lifetime<sup>125,126</sup> than their organometallic counterparts due to the absence of heavy metal atoms promoting spin-orbit coupling (SOC), photoinduced phosphorescence switching has rarely been reported from POP.<sup>32,61,127,128</sup>

To design photoresponsive phosphorescence switching from POP, we first consider the oxygen sensitivity of POP as phosphorescence is originated from triplet states and the phosphorescence lifetime of POP is in a millisecond or longer regime.<sup>25,27,129–131</sup> In fact, oxygen-induced phosphorescence quenching is the major non-radiative decay process of POP. On the other hand, the energy transfer from the lowest triplet state ( $T_1$ ) of phosphorescence emitters to triplet oxygens can generate singlet oxygens that are highly reactive and often result in chemical reactions (e.g. photodynamic therapy of triplet photosensitizers).<sup>132</sup> Considering this fact, we envisioned that the conversion of triplet oxygens to singlet oxygens by photo-irradiation would result in triplet

oxygen consumption and thereby potentially enhance phosphorescence of POP, rendering a new type of phosphorescence switching behavior.

Here, we report UV-induced phosphorescence enhancement of POP-doped polymers. To investigate the underlying mechanism of this phenomenon, fluorophores and organometallic phosphors having a shorter emission lifetime are compared with POP. We also studied the effect of oxygen permeability of matrix polymers by using a series of polymer matrices having different oxygen diffusion rates. We found that distinctive light-responsive luminescence switching is observed only in the combination of POP with a long phosphorescence lifetime and atactic poly(methyl methacrylate) (*a*-PMMA). Our studies revealed that the phosphorescence switching behavior of POP-doped *a*-PMMA films is originated from the conversion of triplet to singlet oxygen mediated by photoexcitation of POP, which leads to the phosphorescence enhancement. Visualization of latent information by UV-irradiation was demonstrated toward novel secure communication applications.

### 3.2. UV-induced Phosphorescence Enhancement, Reversibility, and Mechanism

2,5-dihexyloxy-4-bromobenzaldehyde (Br6A) is a metal-free purely organic phosphor having its triplet lifetime in a millisecond regime.<sup>8,12,13,15</sup> The bromo-benzaldehyde moiety of Br6A greatly enhances intersystem crossing (ISC) via the El-Sayed rule-satisfying aromatic aldehyde combined with the heavy atom effect of bromine.<sup>8</sup> As we previously reported, Br6A-doped *a*-PMMA film showed negligible phosphorescence because *a*-PMMA has substantial oxygen permeability and  $\beta$ -relaxation, and thus phosphorescence is quenched by oxygen.<sup>14,133</sup> Based on that, we recently devised oxygen-sniffing core-shell nanoparticles by incorporating a covalently crosslinked Br6A derivative into an oxygen permeable polystyrene core.<sup>25</sup>

Figure 3.1 illustrates the photoresponsive phosphorescence switching of a Br6A doped *a*-PMMA film. Interestingly, the emission of Br6A is significantly enhanced upon continuous 365 nm UV-irradiation as shown in Figure 3.1b. To better visualize this phenomenon, a M-shaped card was placed on and later removed from the film surface to enable comparison between the emission intensities of the covered and uncovered areas during the UV-irradiation. When the M-shaped card was removed after 95 s of the UV irradiation, the uncovered region appeared much brighter than the covered region, clearly demonstrating the emission enhancement. Further irradiation of the film after removing the M-shaped card showed that the formerly dark character



M region was brightened. Notable phosphorescence enhancement was observed in this process from almost no emission to bright green emission. To quantitatively investigate this phenomenon, the photoluminescence spectra and decay curves of the 1 wt% Br6A doped *a*-PMMA film before and after the exposure to UV light were recorded (Figure S3.2). Figure 3.1c shows the gated emission spectra of the film before and after 30 s irradiation by LED (28.21 mW/cm<sup>2</sup>), revealing a ca. 6.5-fold intensity enhancement.

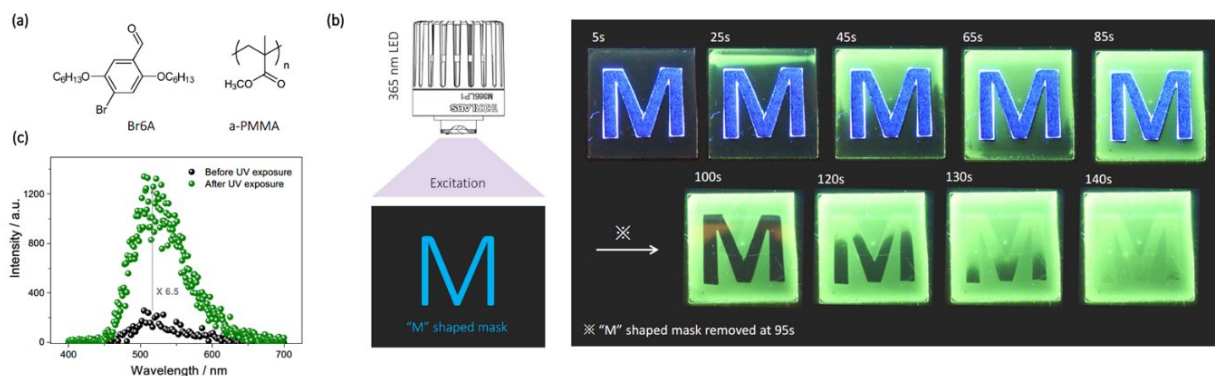


**Figure 3.1. Photo-responsive emission enhancement phenomenon from Br6A doped *a*-PMMA films.** (a) Chemical structures of Br6A, a metal-free organic phosphor, and *a*-PMMA (b) Images taken from the video recording 1 wt% Br6A doped *a*-PMMA (Br6A/*a*-PMMA) irradiated by a UV lamp (1.06 mW/cm<sup>2</sup>) (c) Gated PL spectra of the Br6A/*a*-PMMA before and after the UV exposure.

It is well known that oxygen level can greatly affect the phosphorescence intensity of POP. Thus, to examine the effect of oxygen on the UV-induced phosphorescence enhancement behavior of POP, we first carried out the same UV-irradiation experiment in a glove box in which the oxygen level is maintained below 3 ppm. As shown in Figure S3.3, no emission enhancement is observed even after 30 s continuous UV-irradiation, and thus the covered and uncovered regions are indistinguishable, implying that the luminescence switching behavior is closely related to the existence of oxygen. To further confirm that phosphorescence enhancement is related to the oxygen level in the polymer matrix, the phosphorescence spectra, decay curves, and phosphorescence quantum yield ( $\Phi_p$ ) of an epoxy-sealed 1 wt% Br6A doped *a*-PMMA film (sealed in the glove box to exclude oxygen entrapping) were obtained (Figure 3.2 and Figure S3.4). As shown in Figure 3.2a, the emission of the sealed sample ( $\Phi_p = 19\%$ ) is 20-fold brighter than that of the unsealed sample, clearly indicating that the phosphorescence enhancement is related to oxygen level in the polymer.

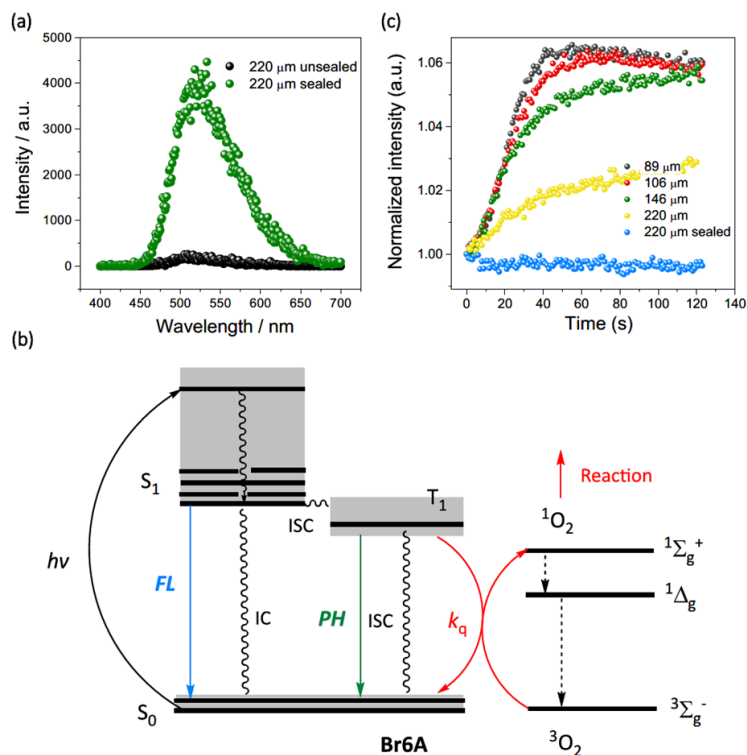


**Figure 3.2. Photophysical analysis of Br6A doped a-PMMA films.** (a) The emission spectra of 1 wt% Br6A doped a-PMMA films under unsealed and sealed conditions; (b) The energy diagram of a possible enhancement mechanism; (c) The relative phosphorescence intensity of 1 wt% Br6A doped a-PMMA films with different thicknesses compared to the initial value upon UV irradiation. As one can see, the enhancement in Figure 3.2c is not as significant as Figure 3.1c because the light source used for Figure 3.2c is a xenoflash lamp integrated in a fluorescence/phosphorescence spectrophotometer, whose power intensity is much lower than that of the UV lamp for the experiment shown in Figure 3.1c.

We next investigated the reversibility of the observed photoswitching behavior. Because the depleted triplet oxygen level can be replenished as oxygen penetrates through the polymer matrix when the UV-irradiation is halted, the enhanced phosphorescence intensity should drop down. As we expected, the photoswitching behavior is reversible through repeated cycles of turn-on and -off the UV-irradiation as demonstrated in Video S1. However, a certain level of photobleaching is inevitable when Br6A is used as the chromophore, especially at higher light intensity (Section 2.8 in SI and Figure S3.12) since it is well known that aromatic aldehyde is prone to photo-oxidation.<sup>56</sup> In fact, photobleaching was substantially reduced when the aldehyde was replaced by trifluoroacetyl group, as demonstrated by our recently developed metal-free organic phosphor, BrPFL-TFK (Figure S3.12).<sup>22</sup>

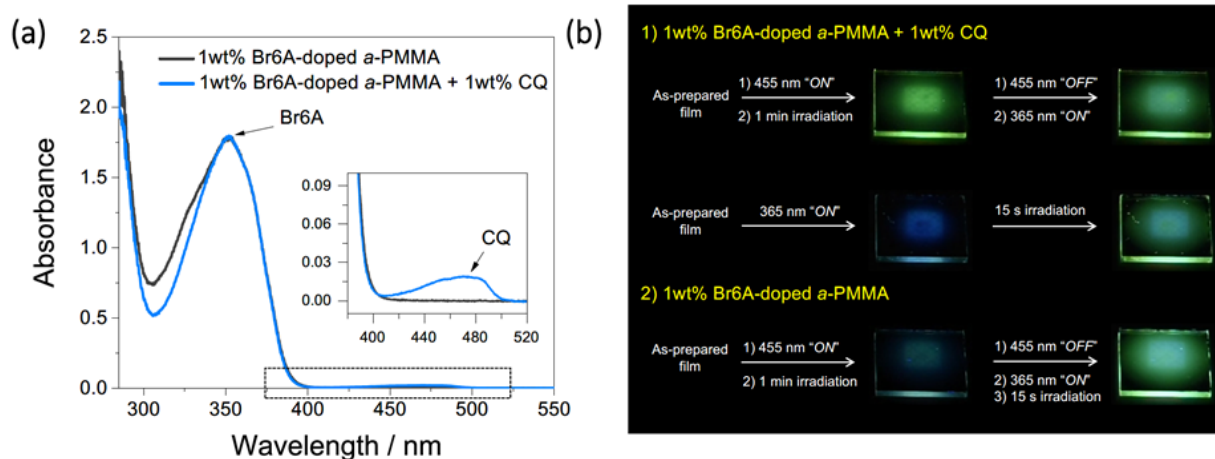


**Figure 3.3. Photo-responsive phosphorescence enhancement behavior of Br6A-aPMMA film with camphorquinone additive.** (a) UV-vis absorption spectra of 1 wt% Br6A in aPMMA and 1 wt% Br6A / 1wt% ( $\pm$ )camphorquinone (CQ) in aPMMA; (b) Photoresponsive luminescence switching study with and without CQ in the aPMMA: Br6A system.

To verify the suggested triplet oxygen consumption-based phosphorescence enhancement mechanism, we prepared methanol solutions of Br6A and BrPFL-TFK at various concentrations and studied singlet oxygen generation upon 365 nm and 345 nm UV irradiation, respectively. As shown in Figure S3.13 the singlet oxygen emission spectra at 1270 nm were observed. To further investigate the phosphorescence enhancement mechanism by preparing a camphorquinone-doped Br6A/a-PMMA film. Camphorquinone is known to generate triplet excitons upon photoexcitation at around 460 nm where Br6A is barely excited.<sup>134</sup> As demonstrated in Video S2 and Figure 3.3, strong phosphorescence was observed from the camphorquinone-doped Br6A/a-PMMA film after 1 min of 455 nm LED irradiation due to the conversion of triplet oxygen to singlet oxygen by the triplet excitons of camphorquinone, which is commonly used for photopolymerization of dental resins. Further phosphorescence enhancement was negligible when 365 nm lamp was turned on. On the contrary, without camphorquinone, phosphorescence from Br6A/a-PMMA film was not brightened by 455 nm irradiation but sharp emission enhancement was clearly observed by 365 nm irradiation. These results strongly support that the observed phosphorescence enhancement originates from the triplet oxygen conversion to singlet oxygen by photoexcited POP.

Based on these results, a phosphorescence emission enhancement mechanism through triplet oxygen consumption is proposed as follows (Figure 3.2b). Upon excitation, Br6A is excited from its ground state to the singlet excited state, and quickly undergoes ISC to the triplet state. Then the triplet energy is transferred to surrounding oxygen molecules in the ground state (i.e.  $^3\Sigma_g^-$ ).<sup>25</sup> This process might be efficient due to the sufficiently long triplet exciton lifetime of Br6A (0.21 ms).

As a result, highly reactive singlet oxygen is generated<sup>135</sup> and, subsequently, consumed through reactions with chemical species around the polymer matrices (e.g. oxidation of PMMA).<sup>136</sup> However, considering the reversible feature of the observed photoswitching, oxidation of PMMA is reasonably ruled out as the origin of the photoresponsive phenomenon. Moreover, PMMA does not absorb 365 nm. Therefore, the energy transfer of transient PMMA radical species cannot be the origin of the photoswitching either.<sup>137,138</sup> The rate of oxygen consumption inside the *a*-PMMA matrix should be faster than the oxygen permeation rate into the polymer matrix. Consequently, the triplet oxygen consumption by UV-irradiation leads to the phosphorescence enhancement of Br6A in the *a*-PMMA matrix.

It is worth noting that the emission intensity difference between the sealed and unsealed samples (i.e. 20-fold) is much larger than the enhancement produced by UV-irradiation (6.5 fold). This is likely because even though oxygens are consumed inside the polymer matrix, due to the oxygen permeation into the polymer matrix, in steady-state, oxygen concentration in the *a*-PMMA matrix cannot be as low as in the sealed sample.<sup>133</sup> Another possible reason is that oxygen in the deep bottom of the polymer film close to the glass substrate cannot be fully consumed because of the limited UV penetration depth. In fact, it is well-known that light has a certain penetration depth depending on its wavelength: e.g., blue photons can only penetrate less than 1 mm.<sup>139</sup> To further investigate the penetration limit issue, the effect of film thickness on the phosphorescence enhancement was studied. Figure 3.2c shows the normalized PL enhancement of the Br6A/*a*-PMMA films having different thicknesses along the UV irradiation by a xenoflash lamp integrated in a fluorimeter. The phosphorescence intensity increased gradually with the irradiation time, except for the sealed sample, consistent with the visual observation by using the LED lamp shown in Figure 3.1. However, one can see in Figure 3.2c, the achievable maximum emission enhancement was reduced upon increasing the film thickness, denoting the limit of UV penetration depth. Hence, oxygens cannot be completely consumed by UV irradiation and consequently the enhancement by UV irradiation is not as significant as the sealed sample.

### 3.3. Extension of Emission Enhancement Behavior to Other Chromophores

We observed the same emission enhancement from several other POPs including 4-chloro-2,5-dihexyloxybenzaldehyde (Cl6A), 2,5-dihexyloxy-4-iodobenzaldehyde (I6A), and 7-Bromo-9,9-diphenyl-9H-fluorene-2-carbaldehyde (BrPhF1A), which clearly supports the suggested mechanism. Chemical structures of Cl6A, I6A, and BrPhF1A are provided in the SI. Photos

showing the enhancement properties of Cl6A, I6A, and BrPhFLA can be found in the SI (Figure S3.5-S3.7). However, we were unable to observe any notable UV-induced luminescence switching from Rhodamine 6G (R6G)- and Ir(ppy)<sub>3</sub>-doped *a*-PMMA films (Figure S3.8a-b). We reasoned that the negligible emission enhancement in the R6G- and Ir(ppy)<sub>3</sub>-doped *a*-PMMA films is because the emitting state of R6G is a singlet state and Ir(ppy)<sub>3</sub> has a rather short phosphorescence lifetime (i.e. 3 μs) and thus it is much less sensitive to oxygen compared to POP. In fact, singlet excitons are usually not quenched by triplet oxygen and the short triplet lifetimes of organometallic phosphors do not allow enough time for efficient energy migration to triplet oxygen.<sup>140</sup> According to Stern-Volmer equation ( $I_0/I_p = 1 + K_{sv}[O_2] = 1+k_q\tau_0[O_2]$ , here,  $I_0$  and  $I_p$  are the emission intensity without oxygen and at a given oxygen concentration ( $[O_2]$ ), respectively;  $K_{sv}$  is the Stern-Volmer rate constant;  $k_q$  is the bimolecular quenching rate constant, and  $\tau_0$  is the emission lifetime without oxygen),<sup>140</sup> the sensitivity of phosphorescence to oxygen depends on  $\tau_0$ . Thus, the sensitivity of organometallic phosphors to oxygen is much lower because their  $\tau_0$  is approximately three orders of magnitude shorter than that of POPs. These results indicate that the observed UV-induced luminescence switching is a unique property of POP.

**Table 3.1. Emission enhancement of several POPs, Ir(ppy)<sub>3</sub>, an organometallic, and R6G a fluorophore in *a*-PMMA, as well as Br6A in *i*-PMMA, and their emission lifetime values in air (before long-term irradiation).**

Emitter	Polymer	Photochromism	Type	Lifetime
Cl6A	<i>a</i> -PMMA	Yes	POP	540 μs
Br6A	<i>a</i> -PMMA	Yes	POP	210 μs
Br6A	<i>i</i> -PMMA	Yes	POP	310 μs
I6A	<i>a</i> -PMMA	Yes	POP	285 μs
BrPhFLA	<i>a</i> -PMMA	Yes	POP	2006 μs
Ir(ppy) <sub>3</sub>	<i>a</i> -PMMA	No	Organometallic	3 μs
R6G	<i>a</i> -PMMA	No	Fluorophore	4 ns <sup>25,135</sup>

We further examined the phosphorescence switching of Br6A in isotactic PMMA (*i*-PMMA). Figure S3.8c shows the photos of Br6A in *i*-PMMA before and after the UV irradiation. Luminescence switching is weak because the initial phosphorescence intensity is already high due to both the poor oxygen permeability and the absence of  $\beta$ -transition of *i*-PMMA. It has been reported that  $\Phi_p$  of Br6A in *i*-PMMA (7.5%) is much higher than that in *a*-PMMA (0.7%) at ambient conditions.<sup>14</sup> Table 3.1 summarizes the behaviors of several POPs, the organometallic phosphor Ir(ppy)<sub>3</sub>, and a fluorophore R6G in *a*-PMMA, as well as Br6A in *i*-PMMA, and their

emission lifetime values.<sup>141,142</sup> The decay curves of Cl6A, I6A, BrPhFlA, and Ir(ppy)<sub>3</sub> in *a*-PMMA, as well as Br6A in *i*-PMMA are provided in Figure S3.9-S3.11.

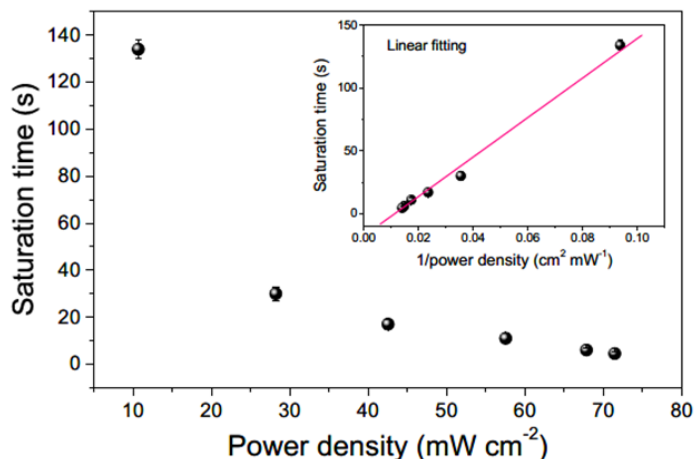


**Figure 3.4.** Relationship between the saturation time ( $t_s$ ) and the power density ( $P$ ) of the excitation light (LED); inset, a linear correlation between the saturation time and  $(\text{power density})^{-1}$ .

Effect of the UV-power on the enhancement was also investigated.<sup>135</sup> The emission enhancements at different excitation power densities ( $P$ ) for the same samples were recorded. The time required to reach the saturation was defined as the saturation time ( $t_s$ ), and could be obtained from the video recordings. Figure 3.4 shows the relationship between  $t_s$  and  $P$ . The  $t_s$  decreases as  $P$  increases. Considering the reaction kinetics between singlet oxygens and the substance in the polymer that are oxidized by singlet oxygen<sup>143</sup> and the Stern-Volmer equation,<sup>144</sup> we deduce an inverse linear correlation between  $t_s$  and  $P$  (shown in the inset of Figure 3.4 and the detailed derivations are provided in the SI). As predicted, the obtained data show a linear inverse proportionality between  $t_s$  and  $P$ , supporting that the observed enhancement is related to the triplet oxygen consumption by UV.

### 3.4 Application of UV-Induced Phosphorescence Enhancement in Data-Encryption

We applied the UV-induced phosphorescence enhancement to a secure information communication. Figure 3.5 shows photographs (captured from the video in the SI) of a sample excited by the 365 nm LED having a power density of 57.53 mW/cm<sup>2</sup> for (a) 1 s and (b) after 10 s of irradiation. In the square patterns, only the sections for “UM1817” are printed with Br6A/*a*-PMMA dissolved in chloroform as the ink, and the remaining characters are printed with a secondary ink containing a “non-phosphorescent” derivative of Br6A, 2,5-Dihexyloxybenzaldehyde (6A, chemical structure in Figure S3.1) with similar fluorescence characteristics as Br6A. Upon excitation at 365 nm, the latent information UM1817 is

indistinguishable because there is essentially no phosphorescence emission from Br6A in the presence of oxygen and its fluorescence intensity is similar to that of 6A. The encrypted “UM1817” is clearly revealed after 10s of UV irradiation owing to the triplet oxygen consumption by UV light and the consequent phosphorescence enhancement. This unique photoresponsive luminescence switching from a specific combination of organic phosphors and a proper polymer matrix can also render their potential use in detecting harmful UV-light or monitoring oxygen levels in various processes.

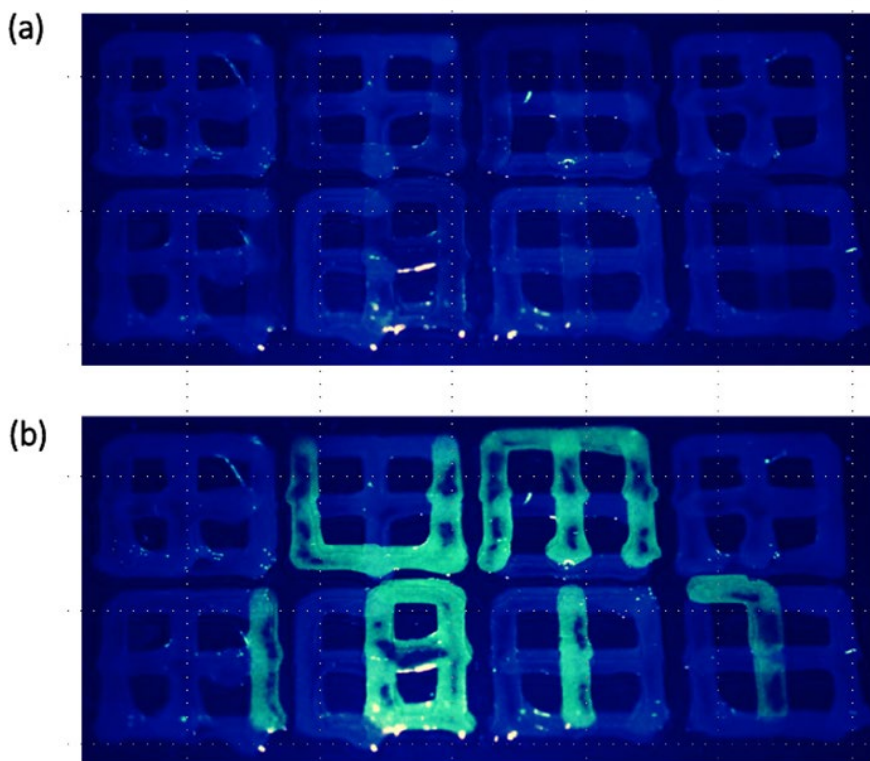


**Figure 3.5. Data encryption demonstration.** (a) Photograph of a sample excited for 1 s by a 365 nm LED having a power density of  $57.53 \text{ mW}/\text{cm}^2$ . (b) Photograph of the sample after 10 s of UV exposure.

### 3.5. Conclusions

In summary, a new type of light-induced luminescence switching was devised based on the triplet oxygen consumption by UV-light and consequent phosphorescence enhancement of metal-free organic phosphors embedded in a-PMMA. The phosphorescence intensity is greatly enhanced by the UV-light exposure in the presence of oxygen but this enhancement could not be observed in an oxygen-free environment. The photoresponsive luminescence switching was not observed in fluorescent dyes or organometallic phosphors having a fast emission lifetime. i-PMMA having a better oxygen barrier property than a-PMMA cannot induce the notable luminescence change

either. Conversion ground-state triplet oxygen to singlet oxygen mediated by UV-excited POP was proposed as the origin of the photoresponsive luminescence switching of the organic phosphor. Therefore, the observed light-responsive phosphorescence enhancement is a unique phenomenon pertinent to purely organic phosphors having a long emission lifetime when they are embedded in a polymer matrix having proper oxygen permeability. Visualization of concealed information on such organic phosphor films by UV-irradiation was demonstrated toward novel secure information communication applications.

### **Publication Information and Author Contribution**

*Contents in this chapter has been published as follows:*

Zang, L., Shao, W., Kwon, M. S., Zhang, Z. & Kim, J. Photoresponsive Luminescence Switching of Metal-Free Organic Phosphors Doped Polymer Matrices. *Adv. Opt. Mater.* **2020**, 8, 2000654.

### **Author Contribution**

Zang, L. and Kwon, M. S. designed this manuscript. Kwon, M. S. carried out the preliminary experimental investigation on the photochromism phenomenon. Zang, L. conducted thorough investigation and wrote the initial manuscript. Shao, W. conducted singlet oxygen emission measurements and camphorquinone related experiments, and revised the manuscript. Zhang, Z. provided supervision to Zang, L.. Kim, J. provided general supervision, obtained funding, and revised the manuscript.



## CHAPTER III. SUPPORTING INFORMATION

### 3.6. Experimental Procedures

#### Materials

All reagents were purchased from Sigma-Aldrich and used as purchased without additional purification. Deuterated solvents were purchased from Cambridge Isotope Laboratories. Br6A, 4-chloro-2,5-dihexyloxybenzaldehyde (Cl6A), and 2,5-dihexyloxy-4-iodobenzaldehyde (I6A) were synthesized following the method described in our previous work.<sup>13</sup> 7-Bromo-9,9-diphenyl-9H-fluorene-2-carbaldehyde (BrPhFlA) was synthesized according to a published method.<sup>145</sup> 2,5-Dihexyloxybenzaldehyde (6A) was synthesized as described previously.<sup>146</sup>

Figure S3.1 shows the chemical structures of them. <sup>1</sup>H NMR (300 MHz, CDCl<sub>3</sub>) for 6A: δ10.50 (1H), 7.30 (1H), 7.15 (1H), 6.85 (1H), 4.10 (2H), 3.90 (2H), 1.80 (4H), 1.43 (4H), 1.35 (8H), 0.88 (6H). <sup>1</sup>H NMR (300 MHz, CDCl<sub>3</sub>) for BrPhFlA: δ10.00 (1H), 7.92 (3H), 7.73 (1H), 7.60 (2H), 7.30 (6H), 7.18 (4H). An optimum phosphor concentration of 1 wt% versus polymer mass was used. A mixture of the phosphor and polymer was dissolved in chloroform at a concentration of 1 mg/mL for the phosphor (roughly, 1 mg Br6A and 100 mg a-PMMA in 1 mL chloroform). The solution was drop-cast on an unmodified glass substrate followed by annealing at 60 °C for 30 min in a glove box having the oxygen level of 1 ppm.

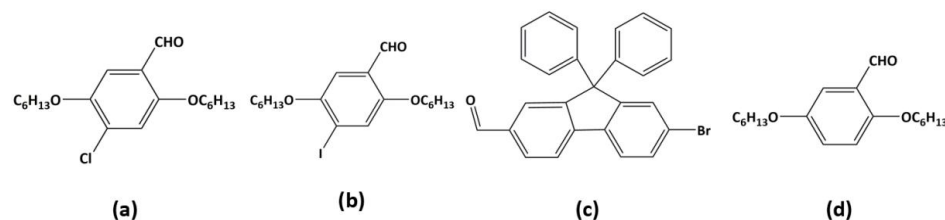


**Figure S3.1. Chemical structures of Cl6A, I6A, BrPhFlA, and 6A.**

#### Methods

Photoluminescence emission spectra, as well as quantum yields, were collected on a Photon Technologies International (PTI) QuantaMaster spectrofluorometer equipped with an integrating sphere. The gated emission and phosphorescence lifetime data were collected using a PTI LaserStrobe system equipped with a Xenoflash lamp. For these measurement, drop-cast samples were prepared. Singlet oxygen emission spectra were collected from an InGaAs NIR detector equipped on the PTI spectrofluorometer. For the video clips, the samples were excited by a 365

nm LED (Thorlab) at various power densities and responses were filmed with a digital camera (Nikon D7200).

### 3.7. Phosphorescence decay curves of Br6A/a-PMMA before and after the irradiation

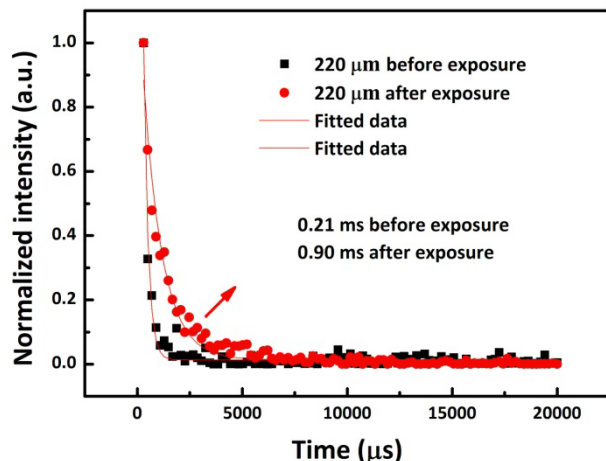


Figure S3.2. Phosphorescence decay curves of Br6A/aPMMA before and after the irradiation.

### 3.8. Phosphorescence quantum yield measurement data for Br6A in a-PMMA under sealed conditions

Table S3.1. Measurement data for the phosphorescence QY of Br6A on aPMMA under sealed condition

	Excitation (a.u.)	Emission (a.u)	QY (%)
1	1970430	411603	20.9
2	2955200	556892	18.8
3	5396980	977145	18.1
4	2870400	524968	18.3
Average			19.0

### 3.9. Br6A/a-PMMA in a glove box before and after irradiation

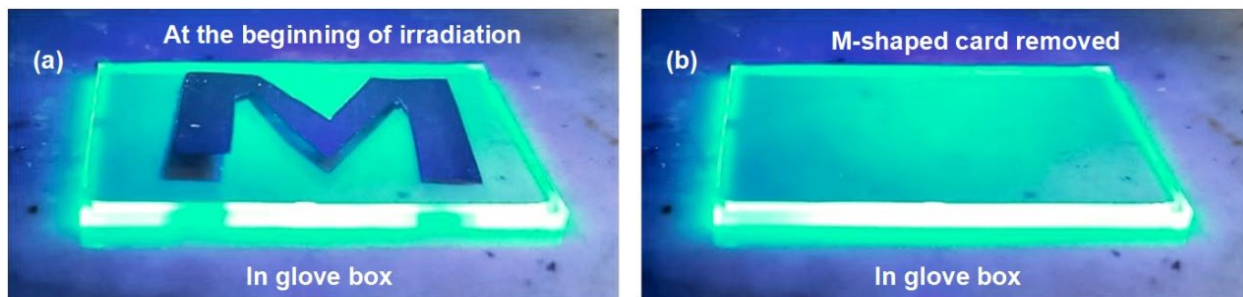


**Figure S3.3. Br6A/a-PMMA in a glove box before and after irradiation.** 1 wt% Br6A in aPMMA film excited by a 365 nm LED for 1 s and (b) after 30 s irradiation and followed by the removal of the M-shaped card in a glove box with the oxygen level below 1 ppm. No contrast is observed.

### 3.10 Phosphorescence decay curves of Br6A/a-PMMA film under sealed and unsealed conditions

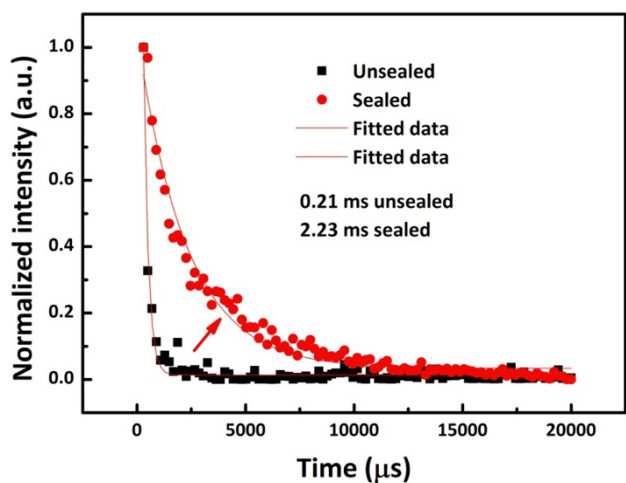


**Figure S3.4. Phosphorescence decay curves of Br6A/ a-PMMA film under sealed and unsealed conditions.**

**3.11. Emission enhancement of Cl6A, I6A and BrPhFIA in a-PMMA and no photochromism from R6G- and Ir(ppy)-doped a-PMMA as well as Br6A in i-PMMA**

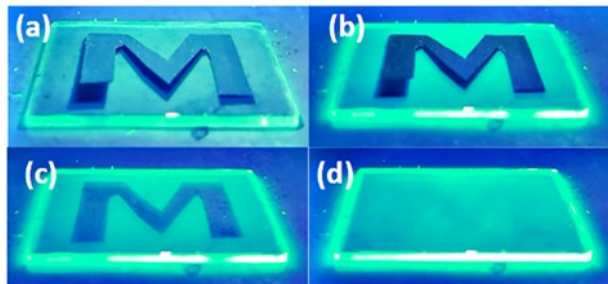


**Figure S3.5. Emission enhancement of Cl6A in a-PMMA.** (a) at the start of illumination, mask on; (b) after illumination for a while, mask on; (c) taking off the mask, photochromism behaviour was obvious; (d) kept illuminating for a while, phosphorescence from the masked area was recovered.

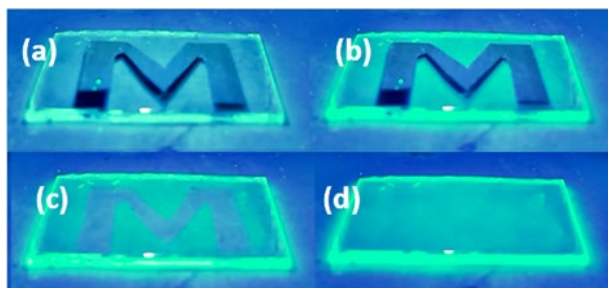


**Figure S3.6. Emission enhancement of I6A in a-PMMA.** (a) at the start of illumination, mask on; (b) after illumination for a while, mask on; (c) taking off the mask, photochromism behaviour was obvious; (d) kept illuminating for a while, phosphorescence from the masked area was recovered.

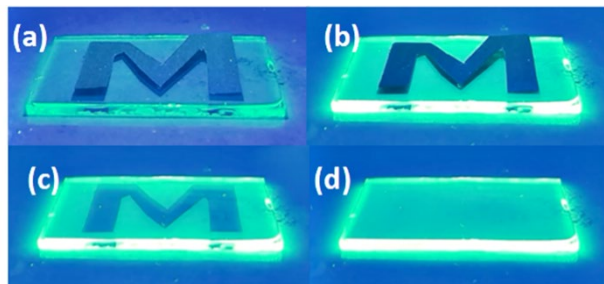


**Figure S3.7. Emission enhancement of BrPhFIA in a-PMMA.** (a) at the start of illumination, mask on; (b) after illumination for a while, mask on; (c) taking off the mask, photochromism behaviour was obvious; (d) kept illuminating for a while, phosphorescence from the masked area was recovered.

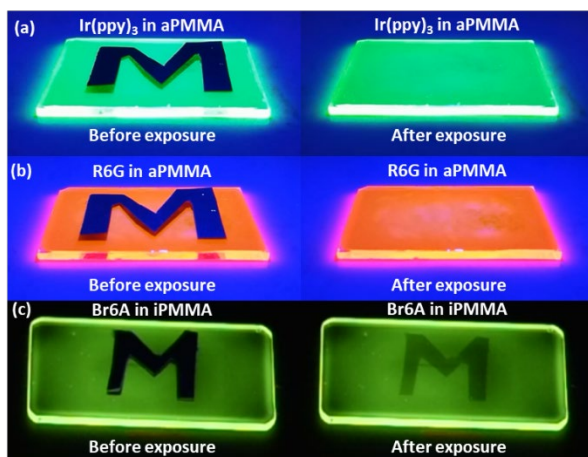


**Figure S3.8. No emission enhancement of (a) Ir(ppy)<sub>3</sub> and (b) R6G in aPMMA, versus (c) obvious emission enhancement of Br6A in iPMMMA before and after the irradiation.**

### 3.12. Emission decay curves of Cl6A, I6A, BrPhFIA, and Ir(ppy)<sub>3</sub> as well as Br6A in i-PMMA

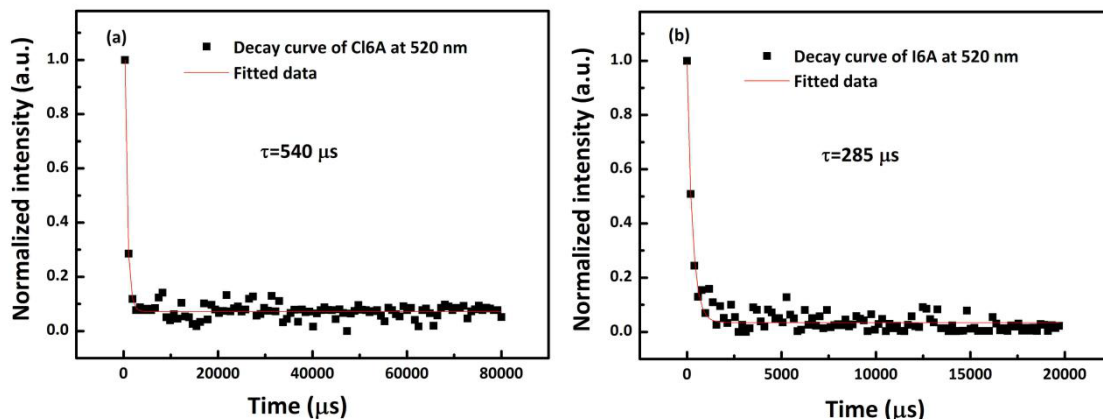


Figure S3.9. Emission decay curves of (a) Cl6A and (b) I6A in a-PMMA.

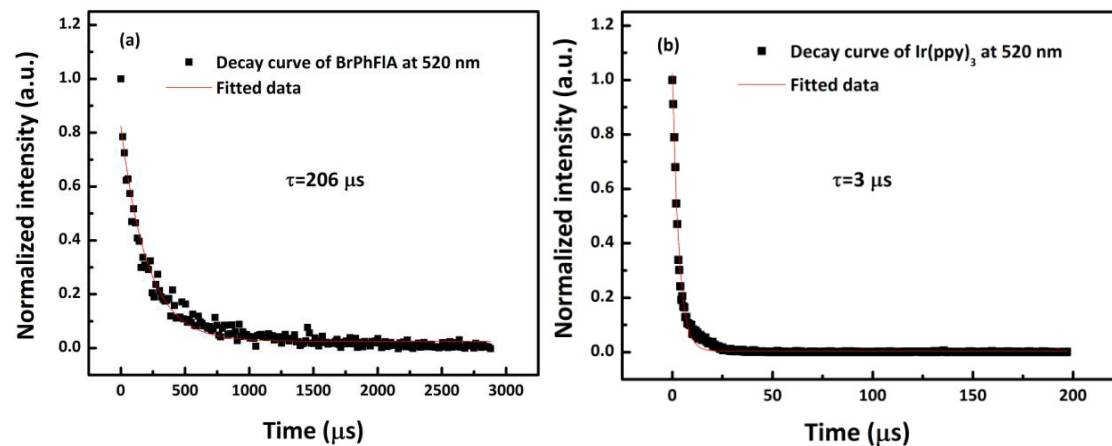


Figure S3.10. Emission decay curves of (a) BrPhFIA and (b) Ir(ppy)<sub>3</sub> in aPMMA.

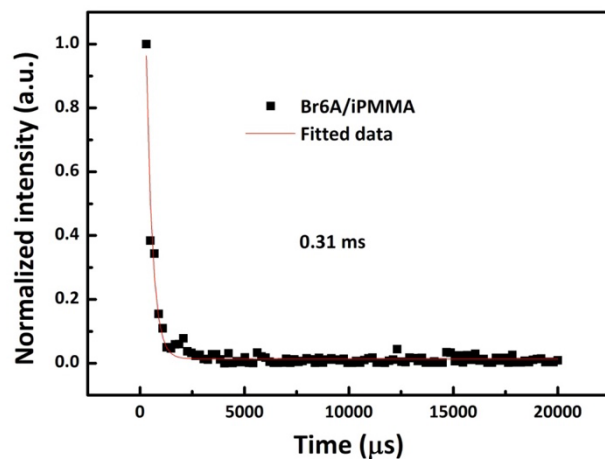


Figure S3.11. The phosphorescence decay curve of Br6A in iPMMA.

### 3.13. The deduction of the relationship between the saturation time and the reciprocal of the power density

Considering the reaction kinetics between singlet oxygen and the substance in the polymer that can be oxidized by singlet oxygen, the concentration of the substance ( $[C]$ ) versus irradiation time ( $t$ ) should follow the first-order kinetic equation,<sup>143</sup>

$$[C] = [C]_0 \exp(-kPt) \quad (S1)$$

where  $[C]_0$  is the initial concentration of the substance,  $P$  is the power density of the excitation source,  $k$  is the photodegradation rate constant of the substance. Thus, the reacted concentration of the substance can be expressed as,

$$[C]_{reacted} = [C]_0 - [C] = [C]_0[1 - \exp(-kPt)] \quad (S2)$$

We assume that the concentration of the reacted substance is the same as the produced singlet oxygen concentration by UV irradiation. Then, the concentration of the singlet oxygen produced by UV irradiation ( $[O_2^1]$ ) can be written as,

$$[O_2^1] = [C]_{reacted} = [C]_0[1 - \exp(-kPt)] \quad (S3)$$

Then, the concentration of the remaining triplet oxygen ( $[O_2^1]$ ) can be expressed as,

$$[O_2] = [O_2]_0 - [O_2^1] = [O_2]_0 - [C]_0[1 - \exp(-kPt)] \quad (S4)$$

With this expression for the oxygen concentration, we can write the Stern-Volmer equation ( $I_0/I_P = 1 + K_{SV}[O_2]$ , here,  $I_0$  is the emission intensity when oxygen cannot be consumed further. We assume that this is the same emission intensity in the absence of oxygen.  $I_P$  is the intensity at a given oxygen concentration, and  $K_{SV}$  is the Stern-Volmer rate constant<sup>144</sup>) for the irradiation process as,

$$I_0/I_P = 1 + K_{SV}\{[O_2]_0 - [C]_0[1 - \exp(-kPt)]\} = A_1 + A_2 \exp(-kPt) \quad (S5)$$

Here,  $A_1 = 1 + K_{SV}[O_2]_0 + K_{SV}[C]_0$  and  $A_2 = K_{SV}[C]_0$ , which are both constant. Based on the result shown in Figure 3.3, when the intensity reaches the saturation,  $I_0/I_P$  becomes the same for any power density. Let's say that value of  $I_0/I_P = a$ , then,

$$A_1 + A_2 \exp(-kPt) = a \quad (S6)$$

Then, we can get  $t = b/P$ . Here  $b = \ln[(A_1 - a)/A_2]/k$ . Therefore, the relationship between the saturation time and  $1/P$  should be linear.

### 3.14. Reversibility study of the photoresponsive behavior

We studied the reversibility of the photoresponsive switching behavior of our system in order to discern whether the possible oxidation of matrix polymer by singlet oxygen could be the origin of the photoswitching. Directly after the films were fabricated, the achievable peak emission intensity of Br6A or BrPFL-TFK was tracked after one minute of 365 nm irradiation. After the emission intensity measurement, the film was left in ambient atmosphere for 3 minutes to ensure complete oxygen backfill before the subsequent cycle of measurement. Data were collected over 5 illumination cycles. Figure S3.12 shows the emission enhancement by UV irradiation is reversible even though the highest intensity reached in each cycle decreases over time due to photodegradation.

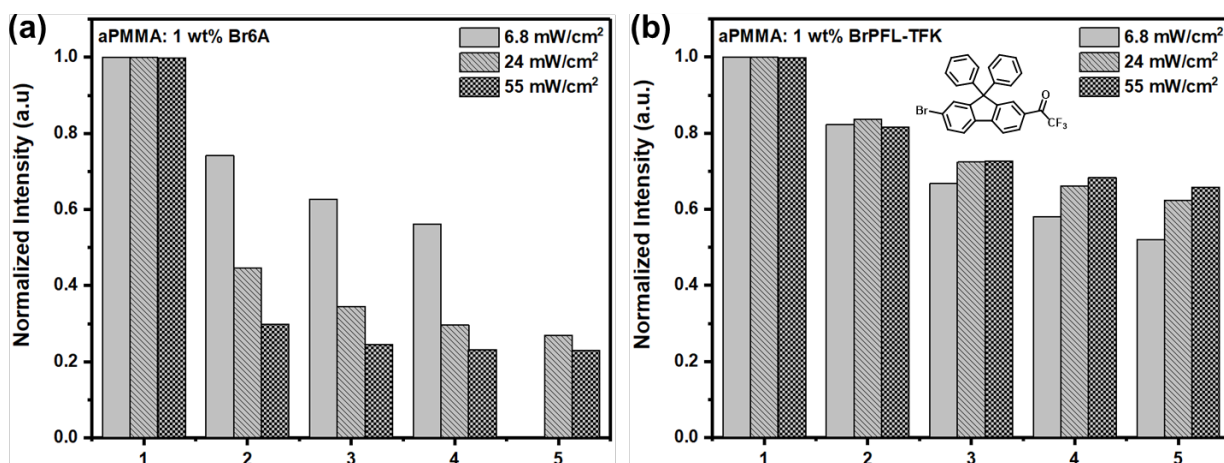


**Figure S3.12.** The highest achieved emission intensity in each illumination cycle at various excitation power densities of (a) aPMMA: 1 wt% Br6A drop-casted film and (b) aPMMA: 1 wt% BrPFL-TFK drop-casted film excited by 365 nm LED.



### 3.15. Singlet oxygen emission

Methanol solutions of Br6A and BrPFL-TFK in various concentration were prepared. Singlet oxygen emission was measured after 365 nm (for Br6A) or 345 nm (for BrPFL-TFK) UV irradiation.

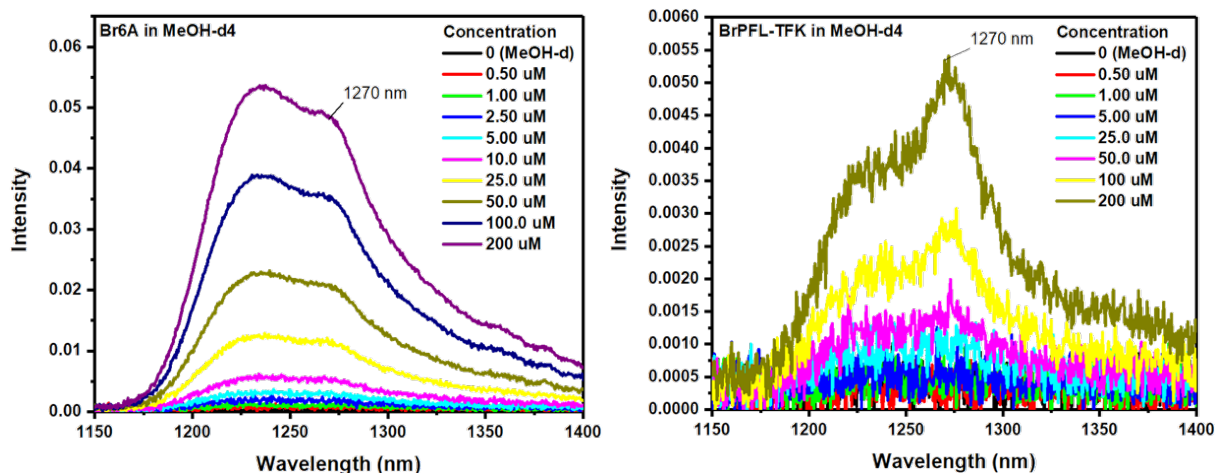


**Figure S3.13. NIR emission spectra of Br6A and BrPFL-TFK in MeOH-d4 in various concentrations.** The singlet oxygen emission is observed at 1270 nm.

The additional peak at around 1230 nm came from the second-order signal of the residual tail the 600 nm long-pass filter could not remove. We confirmed this by using a 560 nm filter. When the 560 nm filter was used, the location of the artifact moved to  $\sim 1140$  nm.

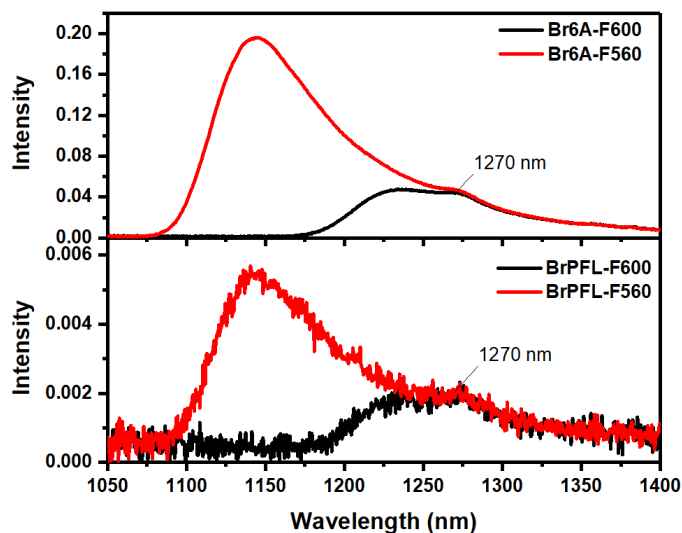


**Figure S3.14. NIR emission spectra of Br6A and BrPFL-TFK in MeOH-d4 with two different long-pass filters (F600: 600 nm filter; F560: 560 nm Filter).** The singlet oxygen emission peak at 1270 nm is marked.

**CHAPTER IV**  
**Organic Light-Emitting Diode (OLED)**  
**Employing Metal-Free Organic Phosphor**

*Contents in this chapter has been published as follows:*

Song, B.<sup>α</sup>, Shao, W.<sup>α</sup>, Jung, J., Yoon, S. J. & Kim, J. Organic Light-Emitting Diode Employing Metal-Free Organic Phosphor. *ACS Appl. Mater. Interfaces* **2020**, *12*, 6137–6143. <sup>α</sup> equal contribution first author.

**Abstract**

Metal-free organic phosphorescent materials are promising alternatives to the organometallic counterparts predominantly adopted in organic light-emitting diodes due to their low-cost, chemical stability, and large molecular design window. However, only few report on OLED devices incorporating metal-free organic phosphors has been presented due to the lack of understanding on material properties, device physics, and device fabrication process. Here, we report a tailor-designed novel fluorene-based organic phosphor with efficient spin-orbit coupling activated by bromine, aromatic carbonyl, and spiro-annulated phenyl moieties. 24.0% photoluminescence quantum yield was achieved when doped in optically inert amorphous polymer hosts. Effects of OLED host materials on the phosphor were investigated in terms of color purity, suppression of exciplex emission, and restraint of molecular motion. Bright green phosphorescence emission (1430 cd/m<sup>2</sup> at 100 mA/cm<sup>2</sup>) was realized with 2.5% maximum external quantum efficiency at 1 mA/cm<sup>2</sup>.

## 4.1. Introduction

Organic light-emitting diode (OLED), as an emerging high-end display, has been rapidly replacing liquid crystal displays (LCD).<sup>147</sup> A significant improvement in the efficiency of OLED was achieved by the development and incorporation of phosphorescent organometallic compounds, which enables efficient intersystem-crossing (ISC) between singlet and triplet states.<sup>148,149</sup> The strong spin-orbit coupling promoted by the heavy-metal atom at the center of the organometallic phosphors allows otherwise forbidden radiative ISC from the triplet excited states to the ground state.<sup>150</sup> However, the organometallic phosphors, particularly blue-light-emitting compounds are known to suffer from the metal-ligand bond-breakage during the OLED operation and the high cost of rare-earth metals.<sup>2,3,151</sup> Room-temperature phosphorescence (RTP) from metal-free organic materials has gained much attention since they are composed of more stable covalent bonds and have a large molecular design window for property tuning.<sup>4</sup> Due to the absence of the heavy metal in the molecular structure, various molecular design strategies to achieve efficient phosphorescence must be implemented, such as, efficient spin-orbit coupling,<sup>8,145,152</sup> the heavy-atom effect by halogen bonding in molecular crystals,<sup>8,153</sup> and effective suppression of molecular vibration.<sup>14,145</sup> Even though many such novel metal-free organic phosphors have been investigated in the literature, few report on OLED devices incorporating metal-free organic phosphors has been presented<sup>57</sup> due to the lack of understanding on material properties, device physics, and device fabrication process.<sup>154</sup>

In this work, we report phosphorescence OLEDs employing a metal-free organic phosphor, 1-(7-bromo-9,9-diphenyl-9H-fluorene-2-yl)-2,2,2-trifluoroethan-1-one (BrPFL-TFK). Rigid fluorene moiety was adopted as the core, which was previously reported to have low sensitivity to molecular vibration and exhibit efficient RTP in solution.<sup>145</sup> Efficient spin-orbit coupling (SOC) routes are activated in BrPFL-TFK with bromine to induce heavy atom effect,<sup>8</sup> aromatic carbonyl to introduce low-energy  $n,\pi^*$  triplet states,<sup>1,155,156</sup> and spiro-annulated phenyl moieties to promote additional orbital angular momentum change ( $\Delta L$ ).<sup>1,23,157,158</sup> 24.0% photoluminescence quantum yield (PLQY) was achieved when BrPFL-TFK was doped in optically inert amorphous polymer hosts. Due to the prevailing collisional quenching of metal-free organic phosphors with a relatively-long triplet lifetime ( $\sim$ ms),<sup>8,12-14</sup> a more careful consideration should be given to the host material in the emissive layer (EML) of OLEDs. N,N'-dicarbazolyl-4,4'-biphenyl (CBP), N,N'-dicarbazolyl-3,5-benzene (mCP), and 2,8-bis(diphenylphosphoryl)dibenzo[b,d]thiophene (PPT)

were investigated as the host materials, among which PPT exhibited the best performance regarding color purity, suppression of molecular motion, and reduction of host-guest exciplex formation. Bright green phosphorescence emission ( $1430 \text{ cd/m}^2$  at  $100 \text{ mA/cm}^2$ ) was achieved from the PPT: BrPFL-TFK electroluminescence devices. The maximum external quantum efficiency (EQE) of the OLEDs with the PPT host was 2.5% at  $1 \text{ mA/cm}^2$  compared to 0.4%, 1.6% at  $1 \text{ mA/cm}^2$  of the OLEDs with the CBP, mCP host, respectively.

## 4.2. Molecular Design and Simulation

Figure 4.1a shows the synthetic scheme of BrPFL-TFK. The spiro-annulated phenyl moieties introduce excellent thermal stability owing to the large steric hindrance.<sup>159</sup> Density functional theory (DFT) and its time-dependent version (TDDFT) are employed to investigate the molecular orbitals and excited state profile of BrPFL-TFK. The calculated highest occupied molecular orbital (HOMO) energy level of BrPFL-TFK is -6.54 eV, which is comparable to -6.34 eV obtained from a cyclic voltammetry measurement (Figure S4.1). The origin of this deep HOMO is the electron-withdrawing fluorine and carbonyl moieties. TDDFT study of BrPFL-TFK revealed three triplet energy states below its first singlet excited state ( $S_1$ ).

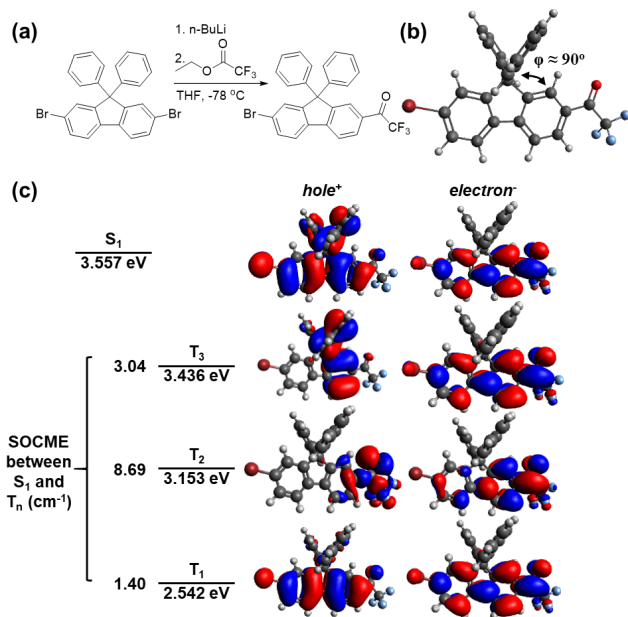


**Figure 4.1. Computational results of BrPFL-TFK.** (a) Synthetic scheme of BrPFL-TFK. (b) Molecular structure of BrPFL-TFK optimized at the B3LYP/cc-pVDZ level. Dihedral angle ( $\varphi$ ) between fluorene plane and spiro-annulated phenyl planes is marked. (c) Natural transition orbitals of the lowest four excited energy states calculated with the optimized ground state structure, energy level of each state, and the spin orbit coupling matrix element between  $S_1$  and  $T_1$ - $T_3$ . Calculation done at the B3LYP/cc-pVDZ level.

To identify the potential ISC channels, spin-orbit coupling matrix elements (SOCMEs) between  $S_1$  and the lowest three triplet excited states were calculated (Figure 4.1c). While  $S_1$ ,  $T_1$ , and  $T_3$  were contributed by  $\pi,\pi^*$  transition,  $T_2$  bears  $n,\pi^*$  transition characteristic from the carbonyl moiety; thus, large SOCME ( $8.69\text{ cm}^{-1}$ ) was achieved between  $S_1$  and  $T_2$ .

Unexpectedly, SOCME between  $S_1$  and  $T_3$  ( $3.04\text{ cm}^{-1}$ ) fell into the same order of magnitude as that between  $S_1$  and  $T_2$  despite their mutual  $\pi,\pi^*$  transition characters, which might be introduced by the two spiro-annulated phenyl moieties. As their natural transition orbitals (NTO) have shown, the ISC between  $S_1$  and  $T_3$  involved certain charge migration between spiro-annulated phenyl and the fluorene moieties in their hole orbitals despite the relatively similar electron population in their electron orbitals. Such charge migration would carry large change in orbital angular momentum due to the large dihedral angle ( $\approx 90^\circ$ ) between phenyl and fluorene moieties (Figure 4.1b), which is critical to induce efficient SOC.<sup>1,23,157,158</sup> Similarly, due to charge migration between spiro-annulated phenyl and the fluorene moieties in their hole orbitals, considerable SOCME between  $S_1$  and  $T_1$  ( $1.40\text{ cm}^{-1}$ ) was identified. In short, efficient ISC was expected from the synergic effect of the El-Sayed's rule-satisfying aromatic carbonyl, spiro-annulated phenyl moieties, and the heavy atom effect from bromine.

### 4.3. Photophysical Properties

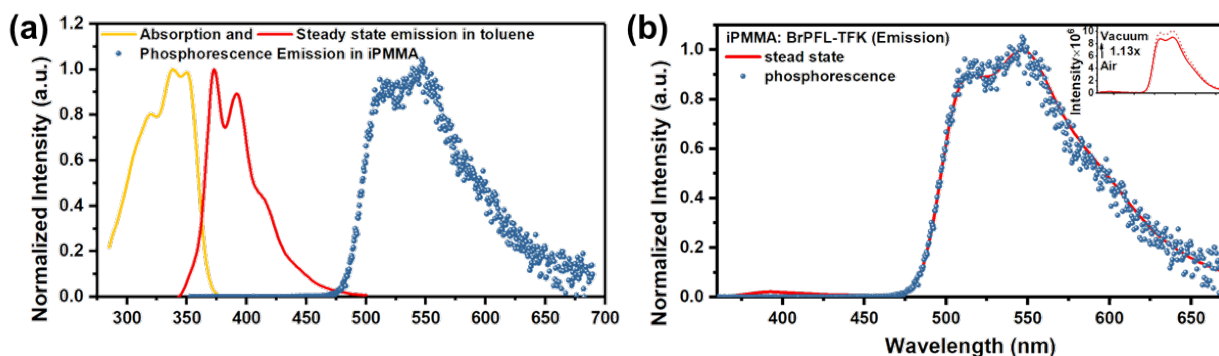


**Figure 4.2. Photophysical properties of BrPFL-TFK in optically inert toluene and iPMMMA.** (a) Normalized UV-vis absorption and steady state emission spectra of BrPFL-TFK in toluene ( $10\ \mu\text{M}$ ), and phosphorescence emission in iPMMMA integrated from 0.2-9.9 ms after excitation. All traces were measured at 298 K (b) steady state emission spectrum of iPMMMA thin film doped with 1 wt% BrPFL-TFK and its phosphorescence emission integrated from 0.2-9.9 ms after excitation measured in air at 298 K. Inset showed the steady state emission measured in air (solid line) and in vacuum (dotted line).

The absorption and emission properties of BrPFL-TFK in toluene are summarized in Figure 4.2a. Solid state photophysical properties of BrPFL-TFK were analyzed by doping it in rigid and optically inert isotactic PMMA (iPMMA). The lowest unoccupied molecular orbital

(LUMO) energy level of -3.25 eV was calculated from the difference between the HOMO energy level (-6.34 eV) and the optical band gap (3.09 eV). BrPFL-TFK emitted only weak fluorescence in solution under ambient conditions. However, strong phosphorescence emission was observed from the 1 wt% doped BrPFL-TFK in iPMA film with 21.2% PLQY and 5.28 ms average phosphorescence lifetime ( $\bar{\tau}_{ph}$ ) in air at room temperature whereas only negligible fluorescence was detected (Figure 4.2b); phosphorescence intensity was further increased upon oxygen depletion (PLQY = 24.0%,  $\bar{\tau}_{ph}$  = 23.8 ms; Figure 4.2b inset). The triplet exciton energy (assuming  $T_1$ ) of BrPFL-TFK was calculated to be 2.56 eV from the onset of the phosphorescence spectrum.

The effects of OLED host materials on the photophysical properties of BrPFL-TFK were studied with 50 nm CBP, mCP, and PPT thin films doped with 2 volume % BrPFL-TFK. Measurements were initially carried out under ambient conditions to identify the origin of the emission before vacuuming to best simulate the operation conditions of OLEDs (Figure 4.3). Fluorescence emissions of host materials were also measured as a reference. As marked in Figure 4.3a-c, fluorescence from hosts or BrPFL-TFK existed in the doped films. The small shifts of the host or guest fluorescence in the doped films relative to those in solution likely stem from environmental factors. However, an unexpected fluorescent emission peak existed in doped CBP or mCP films (ca. 470 or 450 nm, respectively), which were likely originated from the exciplex between BrPFL-TFK and hosts since the HOMO of CBP (-5.90 eV) or mCP (-6.10 eV) is shallower than that of BrPFL-TFK (-6.34 eV, Figure 4.4a). The calculated energy difference between the LUMO of BrPFL-TFK and HOMOs of CBP and mCP are 2.63 eV (471 nm) and 2.83 eV (438 nm), respectively, which are comparable to their exciplex emission  $\lambda_{max}$  in the doped films. On the other hand, PPT cannot form exciplex with BrPFL-TFK due to its deeper HOMO and shallower LUMO (Figure 4.4a).

Furthermore, PL performance of the host-guest films was evaluated in oxygen-free atmosphere, where phosphorescence from BrPFL-TFK was dramatically increased (Figure 4.3a-c inset) while fluorescence intensity stayed similar. Because triplet emission of metal-free organic phosphors is quenched by oxygen,<sup>25</sup> aggregation formation, or endothermic Dexter energy transfer (ET) to host molecule,<sup>28,160</sup> we thus hypothesized that Dexter-type ET through host-dopant collisions mainly affected the phosphorescence properties of the only 2 vol. % BrPFL-TFK films in oxygen-free condition.

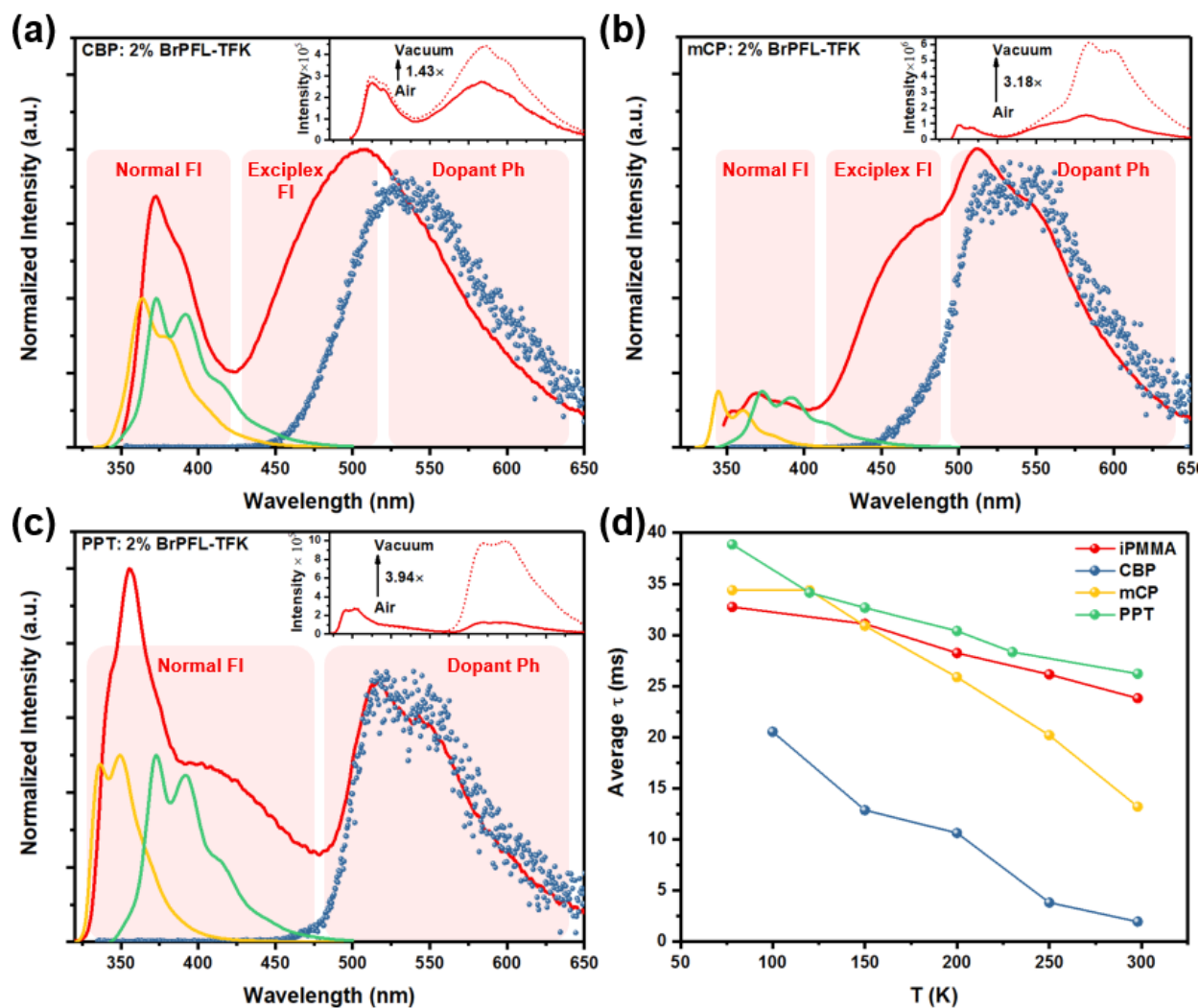


**Figure 4.3. Photophysical properties of BrPFL-TFK in OLED hosts.** (a-c) steady state emission of CBP (a), mCP (b), and PPT (c) films doped with 2 vol% BrPFL PFK (red); phosphorescence emission of doped films integrated from 0.2-0.9 ms (CBP), 0.2-1.9 ms (mCP), or 0.2-4.9 ms (PPT) after excitation (blue dots); steady state (fluorescence) emission of BrPFL-TFK in toluene (green), and steady state (fluorescence) emission of CBP (a), mCP (b), and PPT (c) in toluene (10  $\mu$ M) (yellow); All spectra were measured in air at 298 K; Inset showed the steady state emission of doped films in air (solid line) and in vacuum (dotted line). (d) Phosphorescence lifetime of doped iPMMA, CBP, mCP, and PPT films v.s. temperature measured in vacuum.

As suggested by Kwon, et. al.,<sup>12</sup> the collisional quenching could be qualitatively evaluated by the decrease in phosphorescence lifetime upon elevating temperature (Figure 4.3d). As temperature increased,  $\bar{\tau}_{ph}$  of BrPFL-TFK exhibited a dropping rate of 101  $\mu$ s/K in mCP host and 93.4  $\mu$ s/K in CBP host compared to only 55.2  $\mu$ s/K in PPT hosts, indicating much better suppression of molecular collisions when PPT was adopted as the host material. The rigidity of PPT host comes from its high Tg (100  $^{\circ}$ C)<sup>161</sup> compared to mCP (55  $^{\circ}$ C)<sup>162</sup> and CBP (62  $^{\circ}$ C)<sup>163</sup> The efficient suppression of molecular motion of PPT was similar to that of the well-known rigid host iPMMA, which exhibited a  $\bar{\tau}_{ph}$  dropping rate of 51.8  $\mu$ s/K from 78 to 295 K when BrPFL-TFK was

embedded. However, such advantage of PPT host could not be well realized in air due to its high oxygen permeability. Interestingly, the lifetime of BrPFL-TFK is much lower in CBP than that in mCP. We hypothesize that the internal phosphorescence lifetime of BrPFL-TFK might be affected by exciplex formation. Even though exciplex was observed in both doped CBP and mCP films, exciplex formation in doped CBP films had more impact on the phosphorescence properties of BrPFL-TFK.

In short, PPT host allowed the best PL performance of BrPFL-TFK among the three hosts discussed here in terms of color purity, suppression of exciplex formation, and restraint of molecular motion. These advantages in PPT host would benefit the performance of BrPFL-TFK in electroluminescent devices. Even though photophysical properties of host-dopant films cannot be exactly realized in OLEDs since triplet excitons must be produced from ISC processes in photoluminescence while 75 % triplet excitons are directly produced upon injection of uncorrelated electrons and holes in electroluminescence, we anticipated that the advantage of PPT in suppressing molecular motion would be more evident in OLEDs owing to the larger triplet exciton population.

#### 4.4. OLEDs analysis

An energy level diagram of the materials used in this study is shown in Figure 4.4a. For all devices, CBP, mCP, or PPT was used as a host material in the emissive layer at 2 % doping concentration. We doped MoO<sub>3</sub> in the hole-injection layer (HIL) of CBP or mCP to increase the hole conductivity.<sup>164</sup> For the electron-transporting layer (ETL), 1,3,5-tri(1-phenyl-1H-benzo[d]imidazol-2-yl)phenyl (TPBi), 3,5,3',5'-tetra(m-pyrid-3-yl)phenyl[1,1]biphenyl (BP4mPy) or PPT was used depending on host materials used. A thin layer of BrPFL-TFK was added since HOMO of PPT is very deep (-6.69 eV), hole transport directly from mCP, whose HOMO is -6.10eV, to EML is not energetically favorable. EL spectrum of 2% BrPFL-TFK doped CBP (D1), mCP (D2), and PPT (D3) devices are compared in Figure 4.4b. Excellent color purity of BrPFL-TFK phosphorescence emission was observed in D3, while fluorescence emission peaks (either host or guest fluorescence or exciplex fluorescence) hampered the color purity when CBP or mCP was adopted as hosts. A comparison of EL spectra and the relevant PL spectra of the doped films are presented in Figure S4.2.



We noticed that fluorescence emission from host or guest was dramatically reduced in D3. Such difference between EL and PL might indicate a higher initial triplet yield and improved host-to-dopant charge transfer in OLEDs. However, similar considerations did not result in reduced exciplex fluorescence in D2. In D1, considerable host or dopant fluorescence still existed, indicating insufficient energy transfer from CBP to BrPFL-TFK resulted from the smaller spectral overlap between the fluorescence emission of CBP and the absorption of BrPFL-TFK compared to the overlaps in cases of mCP and PPT (Figure S4.3). Even though direct comparison between metal-free organic phosphors and organometallic phosphors is difficult, a similar result was found in the CBP-Europium organometallic host-guest system.<sup>165</sup>

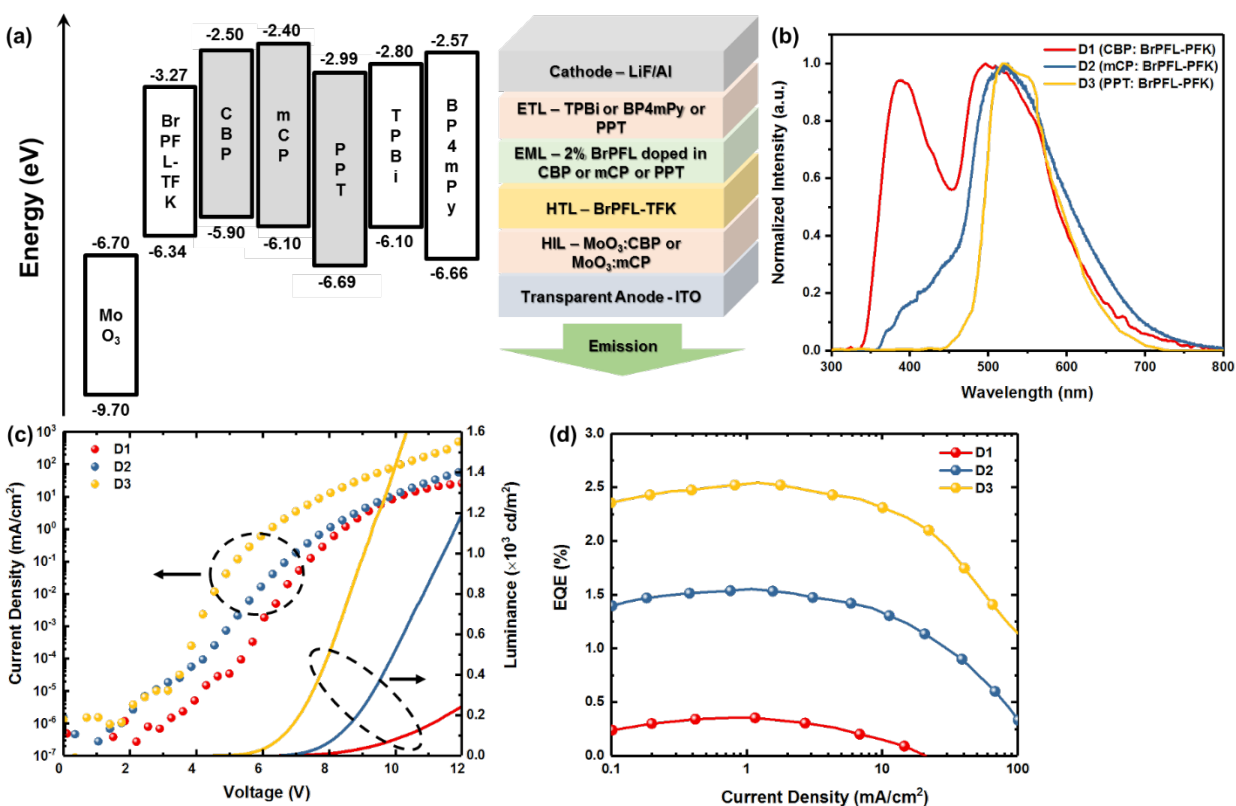


**Figure 4.4. Performances of BrPFL-TFK based OLEDs.** (a) (left) Energy level diagram of materials used in organic light emitting-diode (OLED) devices. HOMO and LUMO levels of each material are indicated. Shaded materials indicate host materials used for the emissive layer of the devices. (right) Simplified diagram of full OLED device structure. (b) Electroluminescent spectra of OLED devices. For D1, CBP: 15 vol% MoO<sub>3</sub> (20 nm), BrPFL-TFK (5nm), CBP: 2 vol% BrPFL-TFK (30 nm), TPBi (60 nm) were used as HIL, HTL, EML, and ETL, respectively; For D2, mCP: 15 vol% MoO<sub>3</sub> (20 nm), BrPFL-TFK (5nm), mCP: 2 vol% BrPFL-TFK (30 nm), and BP4mPy (40 nm) were used as HIL, HTL, EML, and ETL, respectively; For D3, mCP: 15 vol% MoO<sub>3</sub> (20 nm), BrPFL-TFK (5nm), PPT: 2 vol% BrPFL-TFK (30 nm), and PPT (40 nm) were used as HIL, HTL, EML, and ETL, respectively. (c) Current density-voltage-luminescence (J-V-L) characteristics of OLED devices (d) External quantum efficiency-current density (EQE-J) plot of the three devices.

Current density-voltage-luminescence (J-V-L) characteristics and external quantum efficiency (EQE) of the devices are summarized in Figure 4.4c&d. The devices of BrPFL-TFK

doped in PPT host (D3) exhibited the brightness of 1430 cd/m<sup>2</sup> at 100 mA/cm<sup>2</sup> and EQE<sub>max</sub> of 2.5 % at 1 mA/cm<sup>2</sup>. The turn-on voltage of D3 is much lower (~2 V) than the devices made of CBP host (D1) or mCP host (D2) due to the deeper LUMO level of PPT ETL compared to the level of BP4mPy and TPBi. Therefore, electron injection from cathode to PPT ETL would be much more efficient owing to the smaller electron injection barrier. Figure 4.4d showed significant EQE drops when the current density is higher than 10 mA/cm<sup>2</sup> for all devices. Even though we tried to minimize triplet-triplet annihilation (TTA) by keeping a low doping concentration (2%) of BrPFL-TFK, TTA was unavoidable because the triplet lifetime of BrPFL-TFK is in the range of millisecond.

#### 4.5. Conclusions

In summary, we successfully demonstrated phosphorescent OLEDs employing a metal-free organic phosphor, BrPFL-TFK. The aromatic carbonyl, spiro-annulated phenyl moieties, and heavy atom effect from bromine in BrPFL-TFK synergistically facilitate efficient ISC, allowing bright phosphorescence emission. PPT was identified as the suitable OLED host material for BrPFL-TFK compared to CBP or mCP due to its suppression of exciplex formation and restriction of molecular motion, rendering good color purity and high phosphorescence yield. OLEDs incorporating BrPFL-TFK and PPT host exhibited 2.5 % maximum EQE at 1 mA/cm<sup>2</sup>. Significant EQE roll-off behavior, however, was observed at the current density higher than 10 mA/cm<sup>2</sup>. The long triplet lifetime (~ms) of BrPFL-TFK is the primary reason of the EQE roll-off. Triplet lifetime of metal-free organic phosphors should be reduced by further enhancing SOC efficiency with heavy atom effects or other molecular design features to increase orbital angular momentum change during SOC.

#### Publication Information and Author Contribution

*Contents in this chapter has been published as follows:*

Song, B.<sup>α</sup>, Shao, W.<sup>α</sup>, Jung, J., Yoon, S. J. & Kim, J. Organic Light-Emitting Diode Employing Metal-Free Organic Phosphor. *ACS Appl. Mater. Interfaces* **2020**, *12*, 6137–6143. <sup>α</sup> equal contribution first author.

#### Author Contribution

Song, B. conducted device fabrication and characterization, designed and wrote the initial manuscript. Shao, W. conducted all the photophysical analysis, quantum chemical investigation, part of the device fabrication and characterization, and designed and wrote the final manuscript. Jung, J. and Yoon, S. J. synthesized the compound BrPFL-TFK. Jung, J. also conducted initial photophysical analysis. Kim, J. supervised this study, obtained funding, and revised the manuscript.

## CHAPTER IV. SUPPORTING INFORMATION

### 4.6. Experimental details

All chemicals used were purchased from Millipore-Sigma and used without further purification. Isotactic poly(methyl methacrylate) (iPMMA) has a tacticity of >80% isotactic. Deuterated solvents for NMR (nuclear magnetic resonance) were purchased from Cambridge Isotope Laboratories.

#### Synthesis of BrPFL-TFK

2,7-Dibromo-9,9-diphenyl-9H-fluorene was synthesized as the starting material described in the literature.<sup>159</sup> The synthesized 2,7-Dibromo-9,9-diphenyl-9H-fluorene (1g, 2.1mmol) was placed into a flame-dried reaction flask under argon purging. Anhydrous tetrahydrofuran was added (20 ml) and the reaction flask was cooled to -78 °C. n-BuLi (2.5 M solution in hexane) (0.84ml, 2.1mmol) was added dropwise and the reaction flask was stirred for 1 hr, followed by the addition of ethyl trifluoroacetate (0.6g, 4.2mmol). After 1 hr of stirring, the resulting mixture was let warm up to room temperature and stirred overnight. The reaction was quenched carefully with NH<sub>4</sub>Cl and extracted with ethyl acetate. The extracted organic layer was dried over MgSO<sub>4</sub> with cycles of filtering and evaporation under vacuum at ~10<sup>-2</sup> torr. The reaction product was purified by silica column chromatography with dichloromethane and hexane, yielding 0.5g (48%) as a white powder. <sup>1</sup>H NMR (400 MHz, DMSO-d<sub>6</sub>): δ 8.25 (d, J = 8.2 Hz, 1H), 8.09 (d, J = 8.2 Hz, 2H), 7.91 (s, 1H), 7.73 – 7.67 (m, 2H), 7.32 – 7.22 (m, 6H), 7.10 (dd, J = 7.9, 1.6 Hz, 4H). MS (+ESI) *m/z* [M+H]<sup>+</sup> calcd for C<sub>27</sub>H<sub>17</sub>BrF<sub>3</sub>O<sup>+</sup> 493.0409; observed 493.0407. <sup>1</sup>H NMR spectrum was recorded by a Varian, MR 400 (400 MHz). Chemical shift values were recorded as parts per million relative to tetramethylsilane as an internal standard. Mass spectra were carried out with Agilent 6230 TOF HPLC-MS.

#### Quantum chemical calculations

Geometry optimization and vertical excitation energy calculations of BrPFL-TFK have been carried out by means of Density function theory (DFT) and time-dependent density functional theory (TD-DFT) as implemented in the Gaussian 09 package<sup>166</sup> using the B3LYP<sup>167,168</sup> functional and cc-pVDZ<sup>169</sup> basis set in vacuum. Spin-orbit coupling was studied in the Dalton 2016<sup>170</sup> package under the same functional/basis set in vacuum based on the ground state geometry optimized in Gaussian 09.

### **Cyclic voltammetry (CV) measurements**

CV were performed on CH instruments electrochemical analyzer. Glassy carbon electrode, Pt wire, and Ag/AgCl electrode were used as working, counter, and reference electrodes, respectively. A ferrocene/ferrocenium (Fc/Fc<sup>+</sup>) redox couple was used as the internal standard which is assumed to have an absolute energy level of -4.8 eV.<sup>171</sup>

### **Photophysical property analysis**

Thin films of BrPFL-TFK doped in iPMA were prepared through drop casing of 400  $\mu$ L chloroform solution containing 1 wt% iPMA and 0.01 wt% BrPFL-TFK onto quartz substrates. After evaporation, the film was annealed at 120 °C for 30 minutes. 50 nm CBP, mCP, and PPT thin films doped BrPFL-TFK were fabricated by co-evaporating BrPFL-TFK and host materials at 0.04A/s and 1.96 A/s, respectively, resulting in 2 % by vol. of BrPFL-TFK in the mixed layer. UV-vis absorption spectra were recorded with a Varian Cary 50 Bio spectrometer. Photoluminescence (PL) emission spectra were obtained with a Horiba-PTI Quantmaster 400 system. Phosphorescent lifetime data were collected with a xenon flashlamp. Quantum yields were obtained using an integrating sphere (K-Sphere).

### **Device Fabrication**

The glass/ITO substrate were sonicated with detergent, DI water, acetone, isopropanol for >5 min, respectively. Substrates were subsequently treated with ultraviolet (UV)-ozone for 15 minutes to remove surface-contaminant and lower the work-function of ITO. Substrates were loaded into an ultra-high purity (<1 ppm of O<sub>2</sub>, H<sub>2</sub>O) glovebox system integrated with a vacuum thermal evaporation chamber. All layers were grown inside the chamber with the base pressure of  $2 \times 10^{-7}$  torr. Prior to LiF and Al depositions, a molybdenum shadow mask with 2 mm diameter circles (3.14 mm<sup>2</sup> area opening) was placed on the sample surface to define the area of the devices.

### **Performance analysis of OLED devices**

The current density-voltage-luminance (J-V-L) was measured by a HP 4156a semiconductor parameter analyzer attached with a FDS1010 calibrated photodiode from Thorlab, following the standard procedure of OLED measurement.<sup>172</sup> Electroluminescent spectra were recorded with a HR2000+ES from Ocean Optics coupled to the OLED devices via a 300  $\mu$ m-diameter optical fiber.

#### 4.7. Cyclic voltammetry analysis

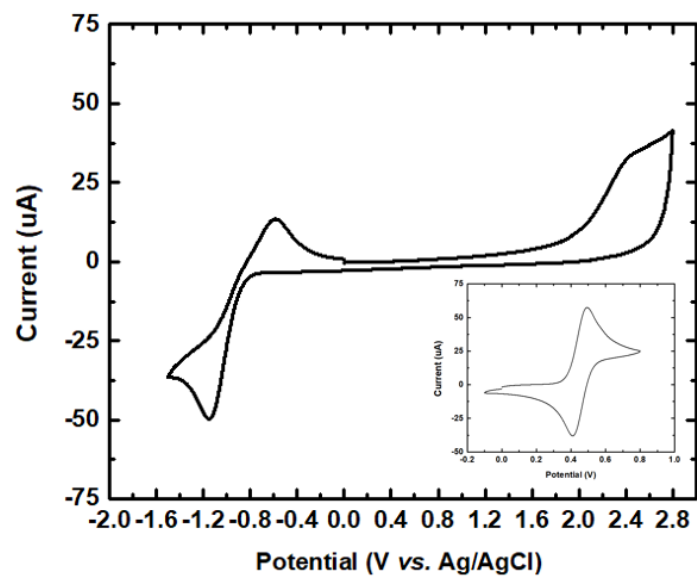


**Figure S4.1. Cyclic voltammetry (CV) curve of BrPFL-TFK in acetonitrile solution.** The inset is the CV curve of ferrocene as a standard reference at a scan rate of 50 mV/s.

#### 4.8. Additional photophysical analysis

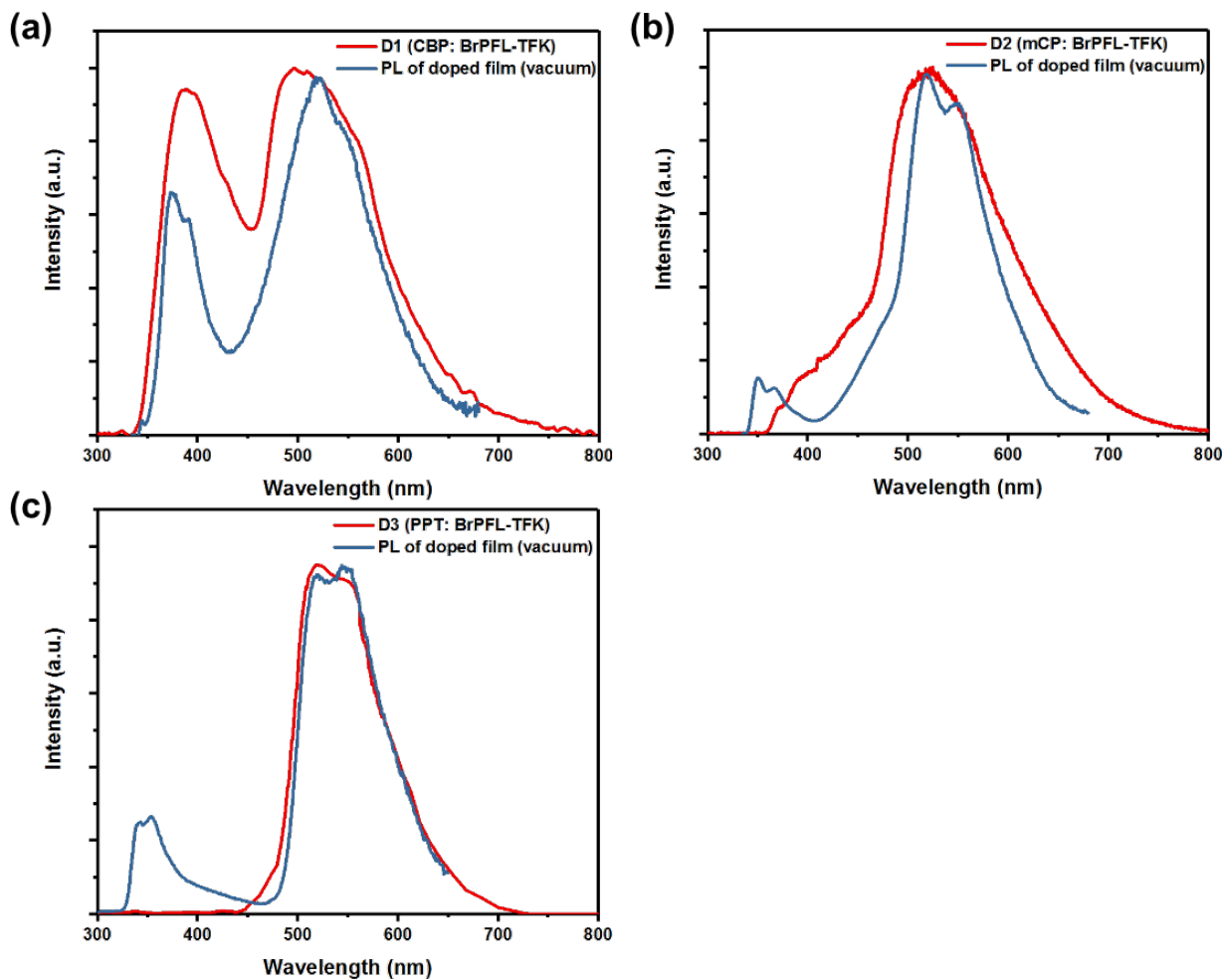


**Figure S4.2. Comparison of electroluminescence and photoluminescence spectra.** Comparison of electroluminescence spectra (red) and thin film steady state emission spectra of BrPFL-TFK doped in each host (blue). (a) CBP based D1 and related films; (b) mCP based D2 and related films; (c) PPT based D3 and related films.

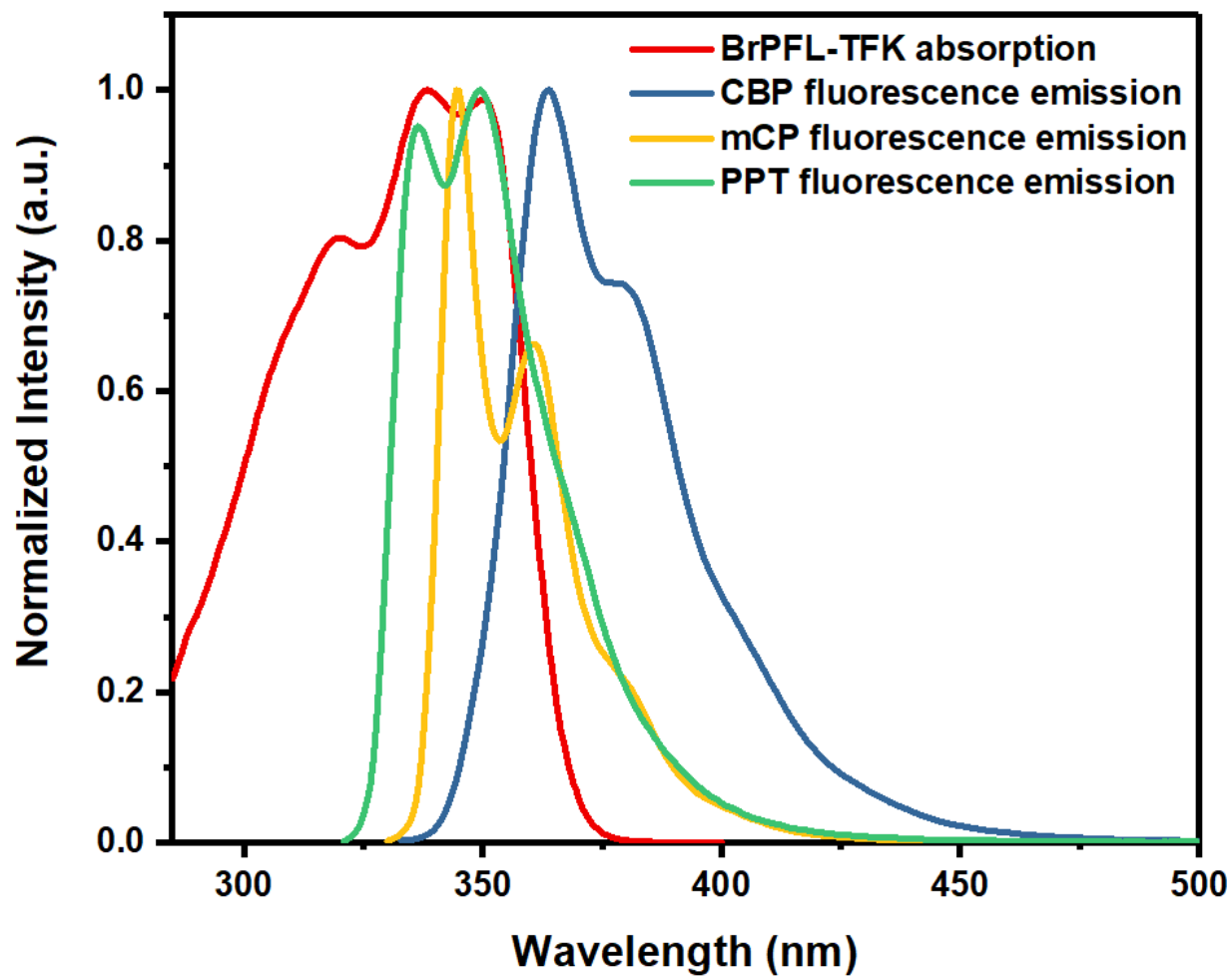
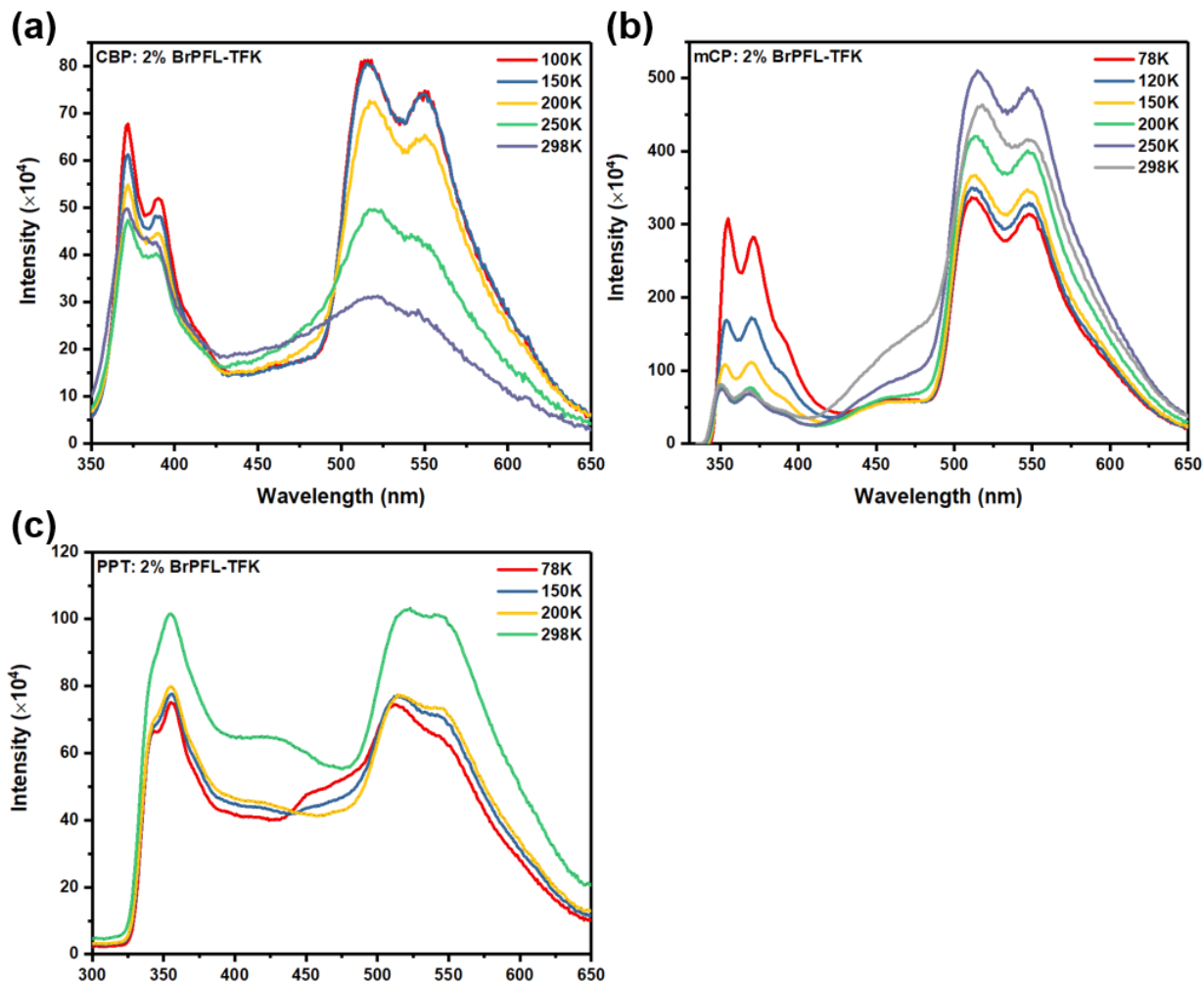


Figure S4.3. UV-Vis absorption spectrum of BrPFL-TFK compared with the steady state (fluorescence emission) of CBP, mCP, and PPT. Measurements were conducted in toluene at 298 K.





**Figure S4.4. Temperature-variant steady state emission spectra of BrPFL-TFK doped films with OLED host.** Steady state emission of CBP (a), mCP (b), and PPT (c) films doped with 2 vol% BrPFL-TFK at different temperatures. Measurements were carried out under vacuum and spectra were recorded in the order of low to high temperature.

Please notice that the spectral shape or relative peak intensity within the same spectrum is not well-trustable due to the following reasons: 1) Photostability of 50 nm vacuum deposited host-guest films studied here is not good, and thus spectral shape or relative peak intensity might have changed from one trace to another even when all other measurement conditions are the same; 2) Film degradation might have happened during storage even under nitrogen atmosphere and the data in Figure S4.4 were not recorded directly after the fabrication of films. However, PL traces in **Figure S4.2** or **Figure 4.3a-c** were recorded directly after the films were fabricated without any addition photoirradiation processes on the films in between.

Nevertheless, it's shown here that for doped CBP films, phosphorescence emission intensity has decreased, while the exciplex emission intensity has increased with rising temperature. On the

other hand, for doped mCP films, with 298 K as the exception, both phosphorescence and exciplex emission intensity has increased while normal fluorescence intensity has decreased with rising temperature. Such trends were difficult to understand but might shine the light on temperature dependency of host-to-guest energy transfer or exciplex formation process.

Because of the reasons stated above, we did not study the temperature dependency of phosphorescence emission. Generally speaking, phosphorescence emission intensity or lifetime would decrease with increasing temperature due to the emerging non-radiative decay processes. However, the complicated photophysical processes here in the host-guest systems have imposed difficulty in extracting such dependency from emission intensity. On the other hand, through the dependency of phosphorescence lifetime on temperature, a clear picture regarding host-dependent non-radiative decay has been demonstrated in **Figure 4.3d**.

## 4.9. NMR and Mass spectra

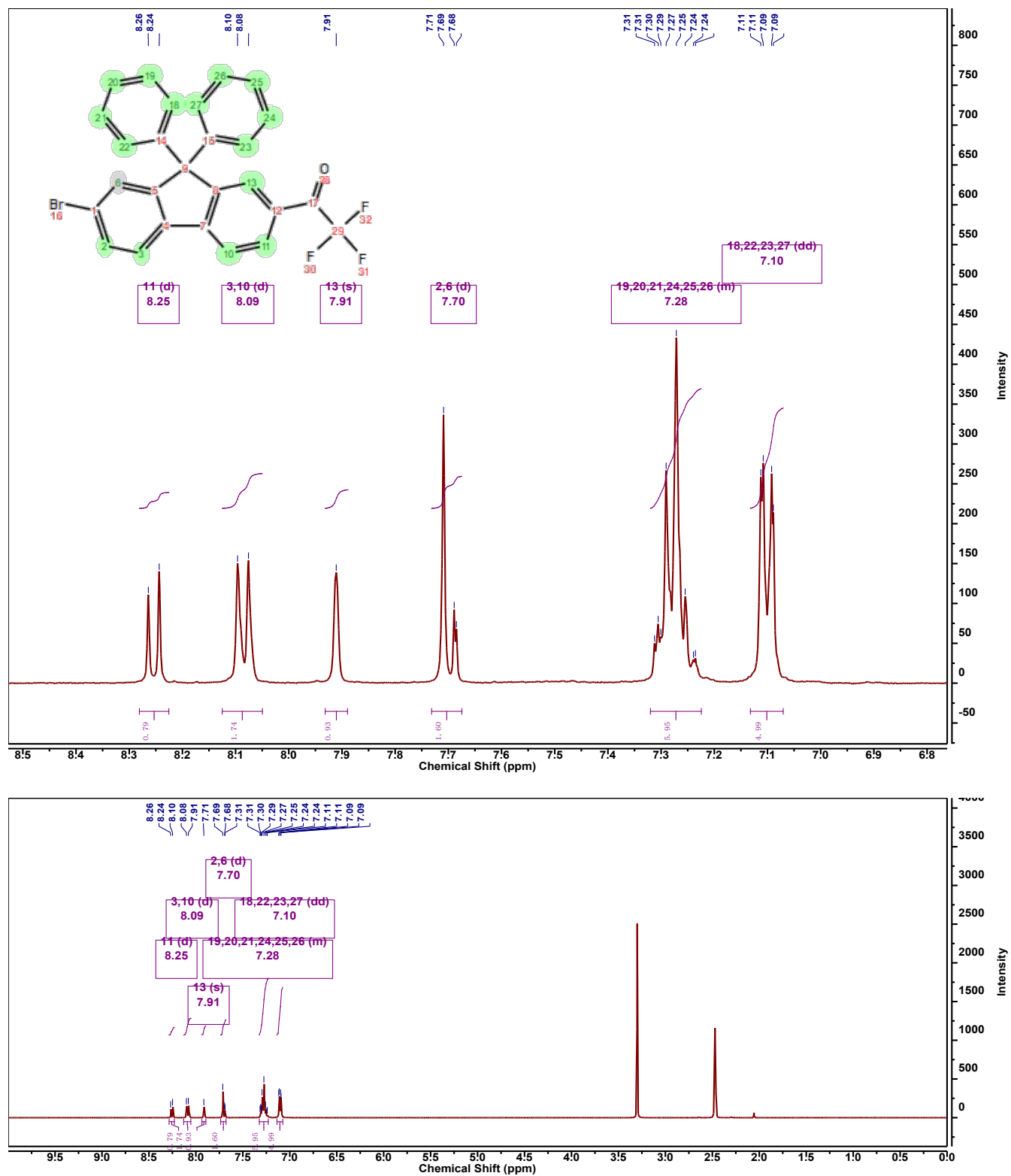
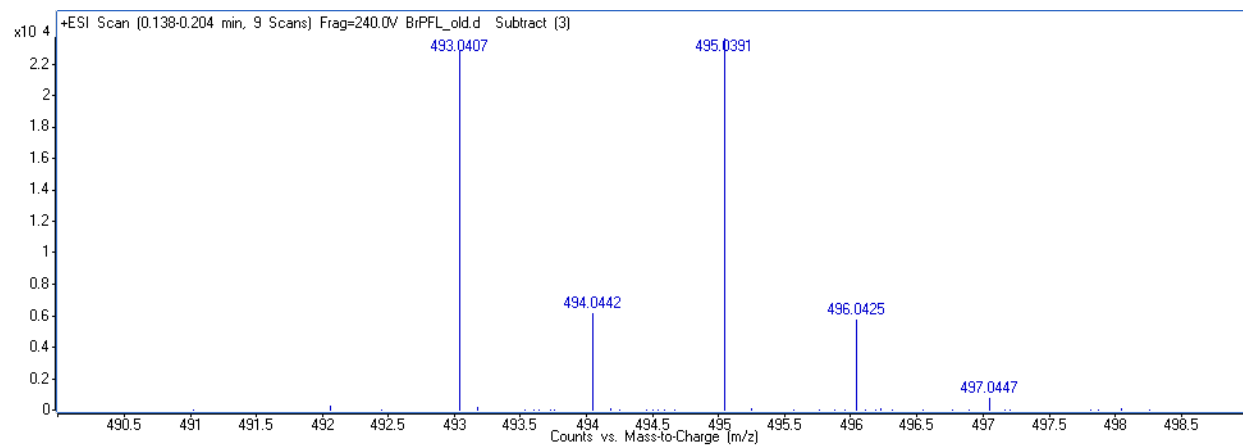


Figure S4.5. <sup>1</sup>H NMR spectrum of BrPFL-TFK in DMSO-d<sub>6</sub> with suggested proton assignments.



**Figure S6. Mass spectra (<sup>+</sup>ESI) showing [M+H]<sup>+</sup> peaks for BrPFL-TFK.**

## CHAPTER V

### Heavy Atom Oriented Orbital Angular Momentum Manipulation in Metal-Free Organic Phosphors

*Contents in this chapter has been published as follows:*

Shao, W., Jiang, H., Ansari, R., Zimmerman, P., Kim, J. Heavy Atom Oriented Orbital Angular Momentum Manipulation in Metal-Free Organic Phosphors. *Chem. Sci.* **2022**, *13*, 789–797.

#### **Abstract**

Metal-free purely organic phosphors (POPs) are emerging materials for display technologies, solid-state lighting, and chemical sensors. However, due to limitations in contemporary design strategies, the intrinsic spin-orbit coupling (SOC) efficiency of POPs remains low and their emission lifetime is pinned in the millisecond regime. Here, we present a design concept for POPs where the two main factors that control SOC—the heavy atom effect and orbital angular momentum—are tightly coupled to maximize SOC. This strategy is bolstered by novel natural-transition-orbital-based computational methods to visualize and quantify angular momentum descriptors for molecular design. To demonstrate the effectiveness of this strategy, prototype POPs were created having efficient room-temperature phosphorescence with lifetimes pushed below the millisecond regime, which were enabled by boosted SOC efficiencies beyond  $10^2 \text{ cm}^{-1}$  and achieved record-high efficiencies in POPs. Electronic structure analysis shows how discrete tuning of heavy atom effects and orbital angular momentum is possible within the proposed design strategy, leading to a strong degree of control over the resulting POP properties.

## 5.1. Introduction

In chapter I, we have thoroughly reviewed the design strategies of contemporary POPs, their advantages, and uprising limitations. SOC is the central photophysical process promoting the spin-forbidden transition from singlet to triplet states. As a brief summary, in the design of contemporary POPs, SOC is promoted mostly by heavy atom effects and the El-Sayed rule. Figure 5.1 listed a few representative POPs with halogen or chalcogen heavy atoms: Br<sup>31,173–184</sup>, I<sup>9,185,186</sup>, or Se<sup>10,187–191</sup>. The El-Sayed rule explains the necessity of orbital angular momentum change in promoting SOC<sup>7</sup>, and the utilization of carbonyl<sup>14,62,173,174,176–178,180</sup>, heterocyclic rings<sup>192–194</sup> (e.g. triazine in DPhCzT<sup>192</sup>), and other moieties having rich non-bonding electrons (e.g. sulfoxide in Cs-Br<sup>195</sup>) to stimulate low energy ( $n, \pi^*$ ) states and thus create ( $\pi, \pi^*$ )-( $n, \pi^*$ ) transition channels.

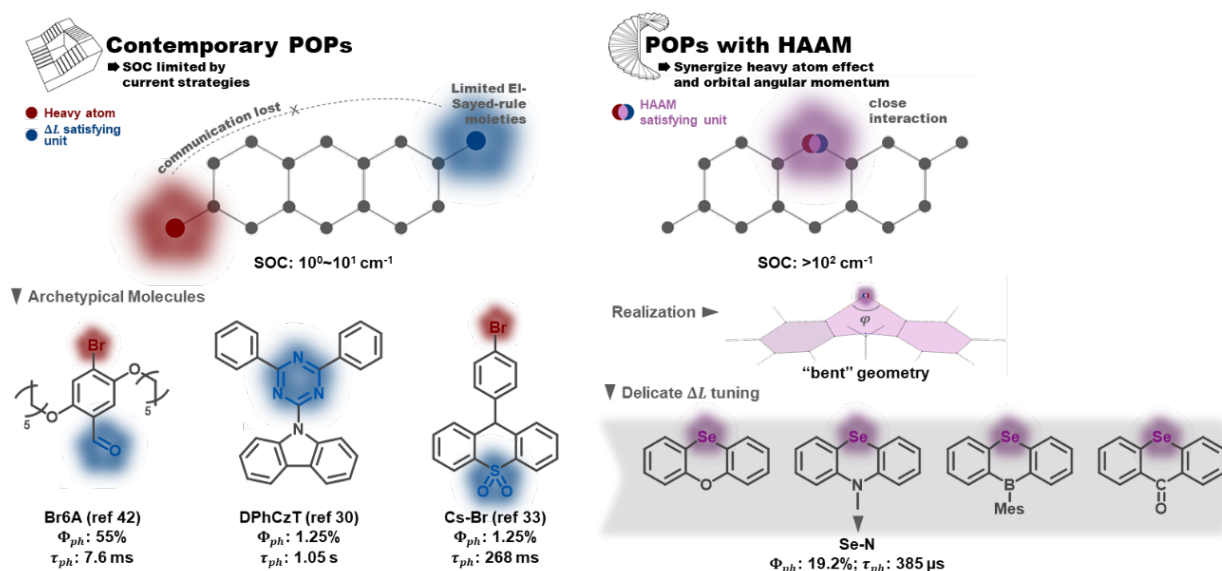


Figure 5.1. Contemporary POP design vs POPs designed with the HAAM concept implemented.

However, current design strategies have reached their limit. The intrinsic SOC efficiencies of POPs remain low (e.g.  $T_1\text{-}S_0$  SOC is usually  $10^0\text{--}10^1 \text{ cm}^{-1}$ ) with their emission lifetime stuck in the millisecond to second regime. The lack of synergistic interactions between the SOC-promoting components is the major deficiency of contemporary design strategies. On one hand, the El-Sayed rule hasn't been fully exploited to capture the detailed picture of molecular features leading to angular momentum changes between spin states. On the other hand, the interplay between the heavy atom effect and orbital angular momentum is missing, i.e., heavy atoms are not rationally positioned in such a way that their orbitals strongly interact with those undergoing angular momentum change. Such delicate manipulations are not required in organometallic complexes,

where the angular momentum changes are centered on the metal atom. In POPs, however, this connection is not trivial to achieve but could have a great impact on increasing SOC. An additional factor that has hindered creation of better design strategies is that contemporary computational tools—while able to quantify SOC—have provided little insight into the electronic origins of the SOC within chromophores.

In this chapter, we report a novel molecular design concept to manipulate SOC in POPs that synergistically uses the heavy atom effect in close connection with orbital angular momentum to overcome SOC limits of organic phosphors. Subsequently, we discuss the verification and benchmark of this new design rule in a series of prototype POPs. To emphasize the core of our design concept that uses heavy atoms to directly stimulate  $\Delta L$ , we named it “*Heavy atom oriented orbital angular momentum manipulation*” (HAAM) (see Figure 5.1). This rational design strategy enhances SOC to over  $10^2 \text{ cm}^{-1}$  and pushes the lifetime limit of organic phosphors to below ms regime, as demonstrated in a series of prototype POPs using chalcogen heavy atoms. HAAM is confirmed to be operational through a novel natural transition orbital (NTO)-based computational method to visualize the molecular orbital origins of SOC. In total, this work introduces the HAAM design concept and tests its relevance using theory, computation, and experiment.

## 5.2. Revisiting the theory behind SOC

The theory behind SOC has been thoroughly discussed in Chapter I, section 1.2, which was centered at the Breit-Pauli SOC Hamiltonian<sup>21</sup>. The most important message concerning the HAAM concept from Equation 1 is that orbital and spin angular momenta are coupled through the interaction with atomic number. Importantly, due to the form of Equation 1, the heavy atom must be in close proximity with the spin orbital transition, otherwise the effective  $Z$  from that atom is suppressed by the  $r^{-3}$  dependence of  $H_{SO}$ . While our discussion here makes these principles transparent, in practice the combination of heavy atom effects with orbital angular momentum change has rarely been addressed in the design of POPs. For instance, Sarkar and Hendrickson et al.<sup>66</sup> examined benzaldehydes with Br substitution at various positions and revealed extraordinarily boosted SOC when Br is at the *para* position relative to aldehyde. However, the orbital angular momentum influence was not discussed although it was clear from their results that Br’s contribution to  $\Delta L$  was drastically enhanced at the *para* position. In our recent reports<sup>10,196</sup>, we elucidated the origin of efficient SOC from the perspective of  $\Delta L$  and expanded the  $\Delta L$ -

promoting mechanism beyond traditional  $(\pi, \pi^*) - (n, \pi^*)$  transitions, but the interaction of heavy atom with  $\Delta L$  was not reviewed. In short, the HAAM strategy hasn't been well established in the systematic molecular design of POPs, which gives an open design space to explore the HAAM method for creating novel, tunable organic triplet emitters.

To help instantiate the HAAM strategy, *ab initio* simulations can provide insight into proposed chromophore designs by revealing their specific electronic structures and SOC elements. In particular, the restricted active space – spin flip (RAS-SF) method<sup>89–93</sup> is a wave function theory that is well-suited for treating electronically excited states<sup>94,95</sup> of photoactive molecular systems. RAS-SF has been shown to accurately treat a variety of challenging electronic structure problems, including polyradicals, singlet fission mechanisms, and charge transfer processes.<sup>197–201</sup> Recent work has enabled RAS-SF to predict accurate SOC elements, making it particularly useful to complement the HAAM design concept. Furthermore and vital to instantiating the HAAM strategy, RAS-SF can produce natural transition orbitals (NTO) that couple pairs of spin states, revealing the specific changes in electronic structure that give rise to spin-orbit interactions. In this work, RAS-SF will show how the HAAM concept applies in practice to novel organic phosphors. This study therefore provides quantitative predictions of SOC and direct visualization of the interactions leading to SOC.

### 5.3. Implementation of HAAM Strategy for Molecular Design

Increasing the involvement of heavy atoms in  $\Delta L$  is critical to the HAAM concept, and the best amplification should be achieved where heavy atom orbitals are involved in the electronic transition of interest. Thus, the utilization of non-bonding electrons from heavy atoms is critically important. Chalcogen was selected as the heavy atom since, unlike halogens, it could be incorporated in the core of POPs to activate  $\Delta L$  channels on its own, as shown in our previous work<sup>10</sup>. To access non-bonding  $p$  electrons from Se, we designed N-methylated phenylselenazine (Se-N) carrying a bent geometry enabled by  $sp^3$  hybridization at the nitrogen (Figure 5.2a). Accordingly,  $p$  electrons from Se are expected to be partially decoupled from the surrounding  $\pi$ -conjugated system and the non-bonding electrons could participate in  $\Delta L$ .



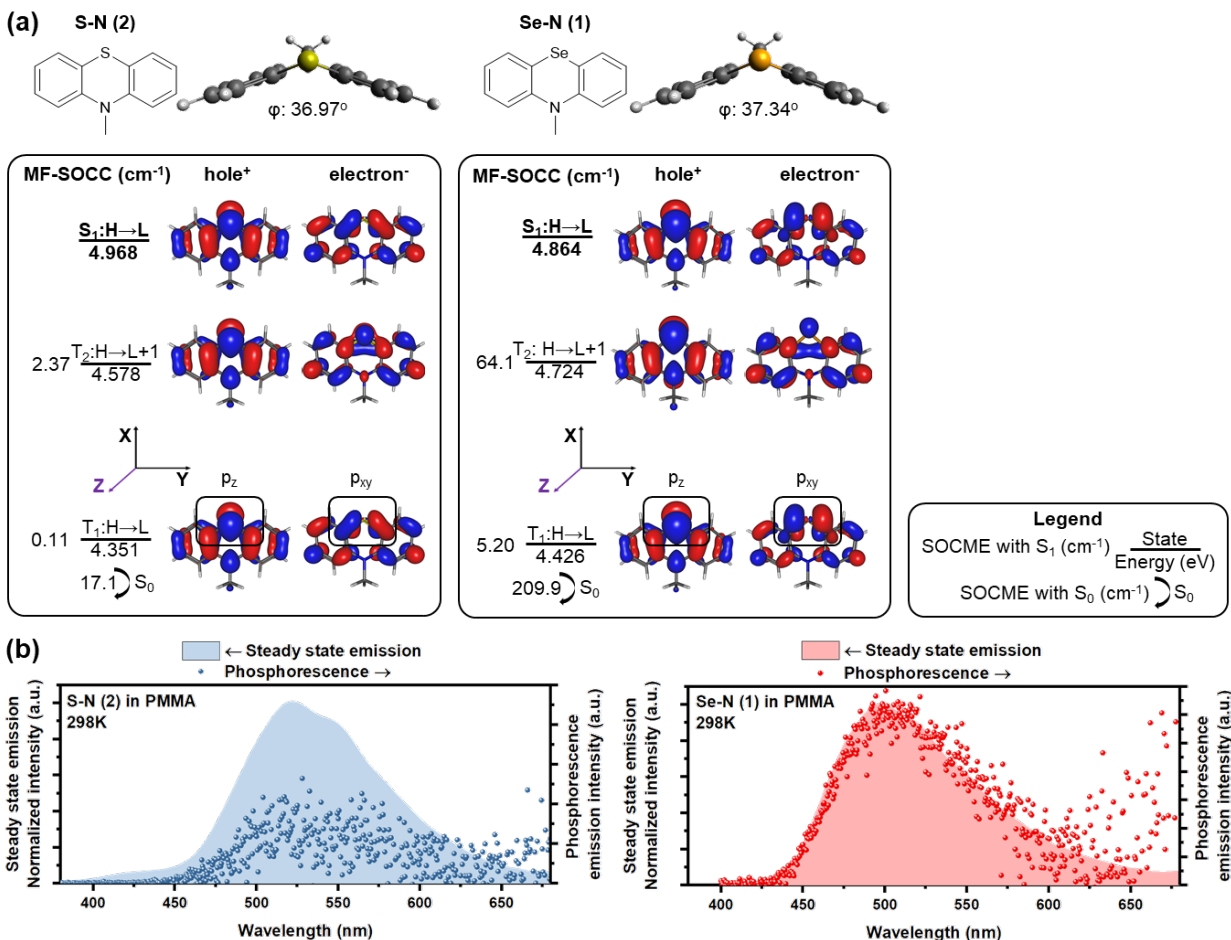


**Figure 5.2. Computational and experimental results of S-N and Se-N.** (a) Chemical structures of S-N and Se-N. Electronic structure results from RAS-SF showing the ground state optimized structure with bent geometry and dihedral angle and the NTOs of  $S_1$ ,  $T_1$ ,  $T_2$  states. Energy of each state and the selected mean field SOCMEs are shown as well. (b) Steady state emission spectra (filled graph, left axis) and gated phosphorescence emission spectra (dot, right axis, 0.5-5 ms for Se-N and 0.5-20 ms for S-N) of the two emitters doped in atactic PMMA (1 wt%, spin-cast) measured at room temperature in vacuum.

RAS-SF calculations of Se-N showed a large SOCME of  $209.9 \text{ cm}^{-1}$  between  $T_1$  and the ground state  $S_0$ , which is the critical transition affecting phosphorescence rate. A  $64.1 \text{ cm}^{-1}$  SOCME for the  $S_1$ - $T_2$  transition was also calculated, for the critical ISC process to populate triplet excitons. A detailed analysis on the NTOs of Se-N was performed to elucidate the high SOC efficiency of Se-N and its connections with the HAAM concept. As shown in Figure 5.2a,  $p_z$  electrons of Se populated the hole orbital of  $T_1$  while  $p_{xy}$  (linear combination of  $p_x$  and  $p_y$ , denoting orbitals in the  $xy$  plane in general) populated the electron orbital. Since orbital angular momentum rotates  $90^\circ$  between  $p_z$  and  $p_{xy}$  orbitals, electron migration between the hole and electron orbitals of  $T_1$  would carry a large “heavy atom oriented”  $\Delta L$ , enabled by the heavy Se atom. In other words, the  $T_1$ - $S_0$  transition of Se-N follows the HAAM concept, leading to its large SOCME. Similarly, HAAM is also manifested in the  $S_1$ - $T_2$  SOC: the transition occurs through the

excited electron orbitals of the S<sub>1</sub> and T<sub>2</sub> states, which are populated by  $p_{xy}$  and  $p_z$  electrons of Se, respectively.

To further test the novel design principle, Se-N was synthesized and embedded in polymeric matrixes (see methods for details). In anoxic environment, fast room-temperature phosphorescence decay was observed (Figure 5.2b), with measured  $\tau_{ph}$  of 385  $\mu$ s and  $\Phi_{ph}$  of 19.2%. *These results are consistent with the computed SOCME of  $10^2 \text{ cm}^{-1}$ , which is a record-high in POPs,<sup>4</sup> and is comparable to that of some organometallic phosphors.<sup>202-204</sup> This large SOCME enabled by the HAAM concept shows that POPs can have similar emissive properties compared to their organometallic counterparts, where SOCMEs are typically in the range of  $10^2$ - $10^3 \text{ cm}^{-1}$ .*<sup>202-204</sup>

While the NTO analyses above provide qualitative visualization for how non-bonding  $p$ -electrons of Se directs  $\Delta\mathbf{L}$ , this phenomenon could also be quantified. Intuitively, if  $\Delta\mathbf{L}$  is dominated by a  $p_z$ - $p_{xy}$  transition, by using the right-hand rule,  $\Delta\mathbf{L}$  should be parallel to the  $xy$  plane. In other words, if we reduce the angular momentum change operator  $\hat{L}$  using cartesian coordinates into  $\hat{L}_{x/y}$  (i.e.  $\hat{L}_x$  or  $\hat{L}_y$ ) and  $\hat{L}_z$ , SOC efficiency will be more pronounced with the  $\hat{L}_{x/y}$  operator, since the  $\hat{L}_z$  operator only performs an orbital rotation around the  $z$  axis.

**Table 5.1. Reduced SOCME in the selected orientations between S<sub>0</sub> and T<sub>1</sub> states**

Orientation	S-N	Se-N
$L_x$ or $L_-$	-10.50-6.02i	-137.56+0.01i
$L_z$ or $L_0$	0.00	-78.77i
$L_y$ or $L_+$	-10.50+6.02i	-137.56-0.01i

RAS-SF based NTO analyses not only produce accurate representation of SOC mechanism, but also provide insights on the reduced SOCME in selected orientations, which reveal the contributions of each angular momentum operator.<sup>202</sup> In practice, according to the matrix representation of the angular momentum in the basis of  $p$ -orbitals, Se  $p_z$ - $p_{xy}$  transition in T<sub>1</sub>-S<sub>0</sub> of Se-N should produce a considerable  $\langle p_z | \hat{L}_{x/y} | p_{xy} \rangle$  matrix element compared to that from the  $\langle p_z | \hat{L}_z | p_{xy} \rangle$  operator. This is confirmed by RAS-SF results (Table 5.1) showing major contributions to SOC from the reduced components in  $L_- (L_x)$  and  $L_+ (L_y)$  orientations. Most importantly, the HAAM concept is directly supported since the majority of SOC is facilitated by  $\Delta\mathbf{L}$  on Se heavy atom. The benefit from RAS-SF methods is substantial in our discussion.

The HAAM strategy was further examined by discretely tuning the heavy atom effect and  $\Delta\mathbf{L}$ . First, heavy atom effect was measured by replacing Se in Se-N with S while keeping  $\Delta\mathbf{L}$

relatively consistent. Frontier excited states of the designed molecule, S-N, have similar NTOs to those of Se-N, suggesting similar  $\Delta\mathbf{L}$  is present in the relevant electronic transitions. As expected, the SOCMEs of S-N were much smaller than those of the Se counterpart (e.g., 17.1 vs 209.9  $\text{cm}^{-1}$   $T_1$ - $S_0$  SOCME). Table 5.1 also indicates largely reduced SOCME of S-N for the reduced components in all three orientations.

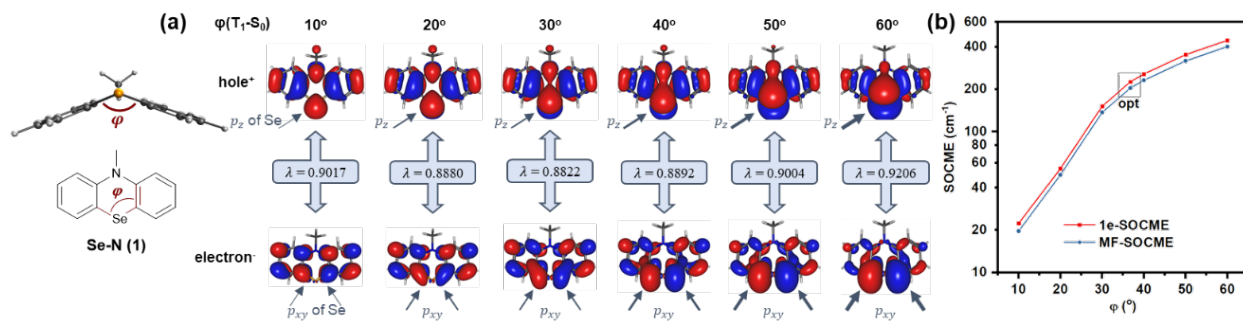


**Figure 5.3. Computational results of Se-N scanned through the dihedral angle.** (a)  $T_1$ - $S_0$  NTOs of Se-N optimized with dihedral angle ( $\phi$ ) fixed;  $\lambda$  represents the contribution of the NTO pair in SOC (max. 1). (b) RAS-SF one-electron and mean-field SOCMEs of  $T_1$ - $S_0$  transition v.s. dihedral angle,  $\phi$  ( $^\circ$ ).

Secondly, Se was reintroduced and the contribution of heavy atom orbitals in  $\Delta\mathbf{L}$  was examined over a range of angular momentum changes. This was achieved via simulation by measuring the SOC for  $T_1 - S_0$  along various bending angles (Figure 5.3a). The contribution of Se  $p_{xy}$  orbitals in the  $T_1$  state gradually increased as the bending angle was enlarged from  $10$  to  $60^\circ$  since  $p_{xy}$  electrons are gradually decoupled from the  $\pi$ -conjugated system, leading to the increased  $\Delta\mathbf{L}$  and  $T_1$ - $S_0$  SOCME (Figure 5.3b). Similar trends also exist in the reduced SOCMEs in  $L_-$ ,  $L_0$ , and  $L_+$  orientations (Figure S5.1, Table S5.1).

To probe the dihedral degree of freedom via experiment, the functional group opposite to Se provides a possible handle. Thus, a series of molecules was designed where the nitrogen in Se-N is replaced by oxygen, boron, or carbonyl (Figure 5.4a). With these substitutions, the dihedral angle was reduced from  $\sim 37^\circ$  to  $0^\circ$  (Figure 5.4d) due to a change in orbital hybridization from  $sp^3$  (N) to  $sp^2$  (CO). Accordingly,  $\Delta\mathbf{L}$  is expected to decrease since non-bonding electrons of Se experience a higher degree of conjugation with the nearby ring system. Since Se is a much heavier atom than oxygen, boron, or carbonyl, the heavy atom effect should remain approximately constant. In line with expectations, the calculated  $T_1$ - $S_0$  SOCMEs show a decreasing trend upon reducing the bending angle from Se-N through Se-B to Se-CO (Figure 5.4b,d). A similar trend is observed in the primary SOCME component in the  $L_\pm$  direction (Figure 5.4c, Table S5.1). Besides the bending angle, which affects the rotation of  $\mathbf{L}$ , the induction effect of the substituents controls

the electron density on Se and consequently the absolute value of  $L$ . This could explain the larger  $T_1$ - $S_0$  SOCME value of Se-O than that of Se-N, despite its smaller dihedral angle.

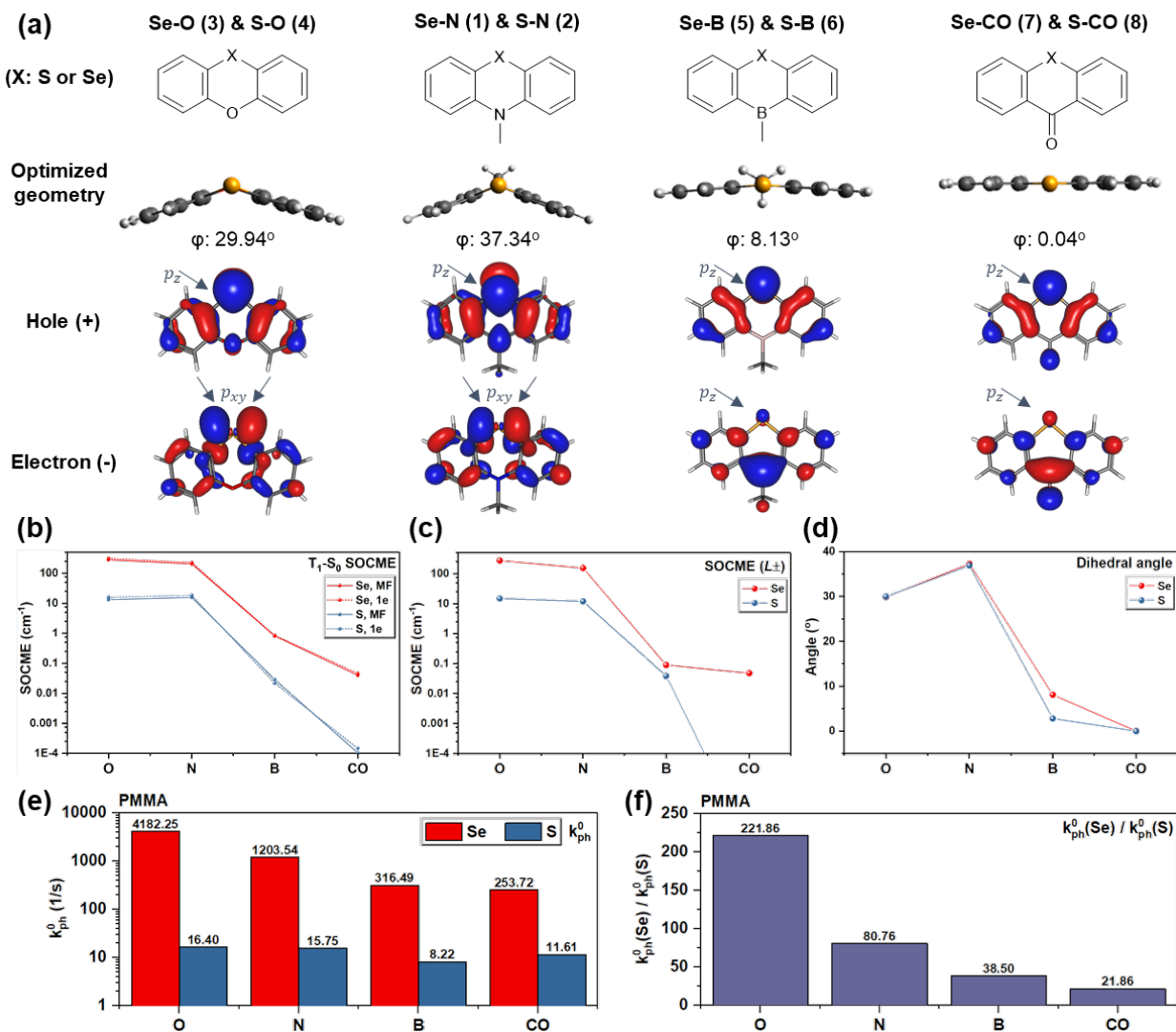


**Figure 5.4. Computational and experimental results for S/Se-O, S/Se-N, S/Se-B, and S/Se-CO.** (a) Molecular structures of the oxygen, nitrogen, boron, and carbonyl derivatives (X = S or Se), their optimized ground state geometries and dihedral angles, and RAS-SF NTOs of  $T_1$  states with Se  $p_z$  and  $p_{xy}$  orbitals marked; (b) RAS SF one-electron (1e) and mean-field (MF) SOCMEs of  $T_1$ - $S_0$  transition, (c) the reduced 1e SOCME in  $L_-$  or  $L_+$  orientations (modulus) v.s. functional groups; (d) the dihedral angles of molecules studied v.s. their functional groups; (e) the experimental intrinsic phosphorescence rate  $k_{ph}^0$  measured in doped PMMA matrix at 78 K in vacuum, and (f) the  $k_{ph}^0(\text{Se derivative})/k_{ph}^0(\text{S derivative})$  value of each functional group.

The computational results along with the molecular design rationale were experimentally checked by analyzing the intrinsic phosphorescence rate ( $k_{ph}^0$ ) measured at 78 K. As expected,  $k_{ph}^0$  decreased dramatically as the dihedral flattens in the series from Se-O to Se-CO (Figure 5.4e). However, this observation alone only indirectly supports that the dihedral angle, or  $\Delta L$  variation, leads to  $k_{ph}^0$  variation. To gain further insight,  $k_{ph}^0$  of each Se compound is compared with its S

counterpart (e.g. Se-N v.s. S-N). The experimental  $k_{ph}^0$  of the S compounds doesn't experience a sharp decreasing trend from S-O to S-CO, but generally follows the prediction except for S-CO. We hypothesize that inevitable non-radiative decay for such long-lived triplet excitons in the sulfur compounds, as well as small mismatch between predicted and experimental dihedral angle could lead to unexpectedly larger  $k_{ph}^0$  in the S compounds (see section 5.9 in the supporting information for details).

Generally, while all four derivatives showed remarkable enhancement in  $k_{ph}^0$  by replacing S with Se in the same molecular frame (Figure 5.4e), the degree of  $k_{ph}^0$  “boost”, characterized by  $k_{ph}^0(\text{Se-derivative})/k_{ph}^0(\text{S-derivative})$ , varies with each molecular frame. It is worth addressing that the degree of  $k_{ph}^0$  boost follows the dihedral angle, since a larger  $\Delta L$  would enhance the contribution of heavy atom orbitals, and thus lead to more prominent heavy atom effects. Experimental results suggested the same trend (Figure 5.4f) in the degree of  $k_{ph}^0$  boost, which increased from Se-CO (ca. 22-fold), through Se-B, Se-N, to Se-O (a remarkable ca. 222-fold), strongly implying the beneficial effect of the increased dihedral angle and  $T_1$ - $S_0$   $\Delta L$ . These experimental results therefore demonstrate that the “heavy atom oriented”  $\Delta L$  can be effective in practice, as motivated and expected by the HAAM concept.

#### 5.4. Discussion

The analysis above implements the “Heavy Atom Oriented Orbital Angular Momentum Manipulation” (HAAM) as a novel design feature for POPs and tested the concept using simulations and experiments. This HAAM strategy enables a powerful use of SOC theory in molecular design, and shows the potential to give control over SOC in triplet emitters. Highly efficient POPs with fast emission were realized with this strategy, having  $k_{ph}^0$  over  $10^3 \text{ s}^{-1}$  and promising room-temperature phosphorescence (RTP) properties.

This advance was supported by a novel computational method, RAS-SF, which can accurately quantify SOC in triplet emitters. RAS-SF also provides detailed NTO analysis to provide direct computational supports for the HAAM concept by revealing the electronic changes from triplet to singlet state that come with SOC. Importantly, the connection between experimental findings and systematic RAS-SF-assisted molecular design gave strong evidence that the tuning of heavy atom effects and orbital angular momentum—in synergy—is vital to increasing SOC in POPs. In other

words, the combined quantitative and qualitative aspects of RAS-SF allowed the HAAM concept to be successfully translated from theory to practice for the design of POPs.

This combination of HAAM strategy with the RAS-SF SOC method can be extended to other organic triplet-based emitter scaffolds. Whereas the HAAM concept is enacted in practice to the Se series in this work, the key to efficient HAAM-based POPs is activating the contribution of heavy atom orbitals in  $\Delta L$ , and the key to activate efficient  $\Delta L$  channels is utilizing non-bonding electrons of heavy atoms. The “bent geometry” investigated here is expected to be just one efficient molecular scaffold to fulfill this task. A related, but less powerful method is to place heavy atoms adjacent to conventional El-Sayed rule satisfying moieties, so that they could participate in the  $(\pi, \pi^*) - (n, \pi^*)$  type  $\Delta L$ . This design rationale employs halogen-containing POPs,<sup>66,196</sup> since halogen only has one available bonding site and could not create efficient  $\Delta L$  channels on their own.

In addition, while the fused-ring motif of the presented article appears to efficiently utilize the HAAM concept by connecting the heavy atom within the  $\Delta L$ -producing channel, heavy chalcogen atoms could also be placed in attachable pendent groups to create  $\Delta L$  channels, such as coupling them with ester or anhydride groups, or directly replace the oxygen in carbonyl with heavier chalcogens. However, these moieties haven't been systematically explored yet.

Further exploration of the HAAM strategy will focus on expanding the library of HAAM-based POPs in order to further break the SOC limits of POPs. Another promising direction is to create new OLEDs that outperform their metal-organic counterparts.

## **Publication Information and Author Contribution**

*Contents in this chapter has been published as follows:*

Shao, W., Jiang, H., Ansari, R., Zimmerman, P., Kim, J. Heavy Atom Oriented Orbital Angular Momentum Manipulation in Metal-Free Organic Phosphors. *Chem. Sci.* **2022**, *13*, 789–797.

## **Author Contribution**

W.S. synthesized the materials and conducted the photophysical analyses, and wrote the manuscript; H. J. performed all computation analyses and contributed to the computation sections of the article; R.A. provided the selenium precursor for the compound Se-N; J.K. and P.M.Z. supervised the research and revised this article.

## CHAPTER V. SUPPORTING INFORMATION

### 5.5. Additional experimental details

#### General

All chemicals used were purchased from Millipore Sigma or Fisher Scientific unless specified and used without further purification. (2-Bromophenyl)hydrazine was purchased from Oakwood Products, Inc.. Deuterated solvents for NMR spectroscopy (nuclear magnetic resonance) were purchased from Cambridge Isotope Laboratories. Phenoxathiine (S-O, 98.0+%) and 9H-thioxanthen-9-one (S-CO, 98.0+%) were purchased from TCI America and used without further purification. 9H-selenoxanthen-9-one (Se-CO) was purchased from Millipore Sigma and used without purification.

#### Physical measurements

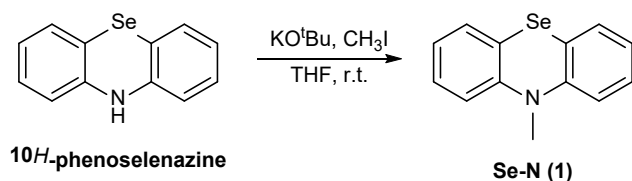
Nuclear Magnetic Resonance (NMR) spectra were collected on Varian MR400 (400 MHz), Varian Vnmrs 500 (500 MHz), or Varian Vnmrs 700 (700 MHz) spectrometer as indicated. Photoluminescence spectra were collected on a Photon Technologies International (PTI) QuantaMaster spectrofluorometer (QM-400) equipped with an integrating sphere (K-Sphere) and a cryostat. The emitters were doped in atactic PMMA matrix for solid-state measurements: quartz substrates (1.5\*2.5 cm) were prepared and cleaned by sonication consecutively in soap, deionized water, acetone, isopropyl alcohol, and then proceeded to UV-ozone treatment for 30 min. Chloroform solution containing 0.025 wt% emitter and 2.5 wt% PMMA was prepared and spin-coated on the cleaned quartz substrates (500 rpm for 5 min). Last, the films were transferred into a glovebox filled with N<sub>2</sub> and baked at 120 °C for 30 min.

#### Synthesis of prototype molecules

We've designed a series of molecules in this report to provide systematic experimental support for the HAAM concept, as well as to demonstrate the capability of the HAAM concept in creating highly efficient POPs. The synthetic scheme of 10-methyl-10*H*-phenothiazine (S-N) and 10-methyl-10*H*-phenoselenazine (Se-N) were adopted and modified from ref <sup>205</sup>. The scheme of 10-mesityl-10*H*-dibenzo[*b,e*][1,4]thiaborinine (S-B) and 10-mesityl-10*H*-dibenzo[*b,e*][1,4]selenaborinine (Se-B) were adopted and modified from ref <sup>206</sup>. The scheme of phenoxaselenine (Se-O) was adopted from ref <sup>207</sup>. Phenoxathiine (S-O, 98.0+%) and 9H-

thioxanthen-9-one (S-CO, 98.0+%) were purchased from TCI America and used without further purification. 9H-selenoxanthen-9-one (Se-CO) was purchased from Millipore Sigma and used without purification.

▪ **(Se-N, 1) 10-methyl-10H-phenoselenazine**

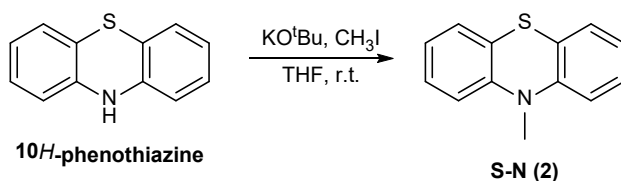


The synthetic procedure for 10H-phenoselenazine was described in ref<sup>208</sup>.

10H-phenoselenazine (98 mg, 0.4 mmol, 1 eq.) and potassium tert-butoxide (67 mg, 0.6 mmol, 1.5 eq.) were dissolved in anhydrous THF (3 mL) at 0 °C. After stirring for 20 min, methyl iodide (142 mg, 1 mmol, 2.5 eq.) was added to the solution. The mixture was stirred at room temperature overnight. Then, the reaction was quenched with water and the resulting mixture was extracted with CH<sub>2</sub>Cl<sub>2</sub>. The combined organic layers were washed with brine, dried over Na<sub>2</sub>SO<sub>4</sub>, filtered and evaporated to dryness under vacuum. The crude product was further purified with flash column chromatography (Hexane/CH<sub>2</sub>Cl<sub>2</sub>) to afford 10-methyl-10H-phenoselenazine (Se-N, 1) as a white solid (17.0 mg, 16.4% yield).

- <sup>1</sup>H NMR (500 MHz, Chloroform-d) δ 7.32 (dd, J = 7.5, 1.4 Hz, 2H), 7.22 (td, J = 8.2, 1.4 Hz, 2H), 6.97 – 6.90 (m, 4H), 3.44 (s, 3H).
- <sup>1</sup>H NMR (500 MHz, DMSO-d<sub>6</sub>) δ 7.34 (dd, J = 7.5, 1.3 Hz, 2H), 7.29 – 7.23 (m, 2H), 7.03 (d, J = 8.1 Hz, 2H), 7.00 – 6.94 (m, 2H), 3.36 (s, 3H).
- <sup>13</sup>C NMR (126 MHz, DMSO-d<sub>6</sub>) δ 145.86, 129.89, 128.37, 123.40, 119.30, 116.20, 37.12.
- <sup>77</sup>Se NMR (134 MHz, DMSO-d<sub>6</sub>) δ 278.89.

▪ **(S-N, 2) 10-methyl-10H-phenothiazine**



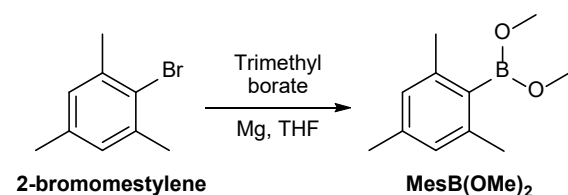
10H-phenothiazine (1 g, 5 mmol, 1 eq.) and potassium tert-butoxide (0.845 g, 7.5 mmol, 1.5 eq.) were dissolved in anhydrous THF (10 mL) at 0 °C. After stirring for 20 min, methyl iodide



(0.623 mL or 1.42 g, 10 mmol, 2 eq.) was added to the solution. The mixture was stirred at room temperature overnight. Then, the reaction was quenched with water, and the resulting mixture was extracted with CH<sub>2</sub>Cl<sub>2</sub>. The combined organic layers were washed with brine, dried over Na<sub>2</sub>SO<sub>4</sub>, filtered and evaporated to dryness under vacuum. The crude product was further purified with flash column chromatography (Hexane/CH<sub>2</sub>Cl<sub>2</sub>) to afford the pure 10-methyl-10*H*-phenothiazine (S-N, **2**) as a white solid (992.2 mg, 92.69% yield).

- <sup>1</sup>H NMR (401 MHz, Chloroform-d) δ 7.21 – 7.10 (m, 4H), 6.98 – 6.88 (m, 2H), 6.82 (d, J = 8.1 Hz, 2H), 3.38 (s, 3H).
- <sup>1</sup>H NMR (500 MHz, DMSO-d<sub>6</sub>) δ 7.24 – 7.19 (m, 2H), 7.15 (dd, J = 7.8, 1.0 Hz, 2H), 6.96 (t, J = 7.3 Hz, 4H), 3.30 (s, 3H).
- <sup>13</sup>C NMR (126 MHz, DMSO-d<sub>6</sub>) δ 145.78, 128.21, 127.22, 122.92, 122.53, 115.05, 35.56.

▪ **Dimethyl mesitylboronate, or MesB(OMe)<sub>2</sub>**

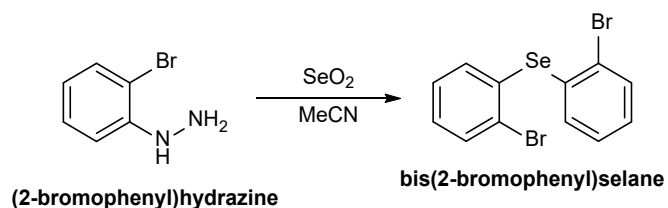


(adopted and modified from ref<sup>209,210</sup>.)

Mesityl magnesium bromide was prepared from 2-bromomesitylene (10.0 g, 50.23 mmol), magnesium turnings (1.343 g, 55.25 mmol, 1.1 eq.), and a small iodine crystal (127 mg, 0.5023 mmol, 0.01 eq.) in anhydrous THF (100 mL). After cloudiness appeared from the original clear solution, the mixture was refluxed for 2 hours at 80 °C or until all the magnesium disappeared, air-cooled to room temperature, and then slowly cooled to -78 °C using a liquid nitrogen/ethyl acetate bath. Trimethyl borate (6.440 mL, 57.76 mmol, 1.15 eq.) was added quickly and the solution was slowly warmed to room temperature overnight. Afterwards, solvent was removed in vacuo and the residue was extracted with Ar-degassed hexanes. Solvent was completely removed from the crude mixture under reduced pressure to get an opaque oil which was distilled in vacuo (10<sup>-3</sup> mbar, 130-200 °C) to obtain MesB(OMe)<sub>2</sub> as a colorless, transparent oil (4.069 g, 42.2% yield), which was stored in a desiccator in vacuum.

- <sup>1</sup>H NMR (400 MHz, Chloroform-d) δ 6.81 (s, 2H), 3.56 (s, 5H), 2.32 – 2.20 (m, 9H).
- <sup>11</sup>B NMR (128 MHz, Chloroform-d) δ 31.30.

▪ **Bis(2-bromophenyl)selane**

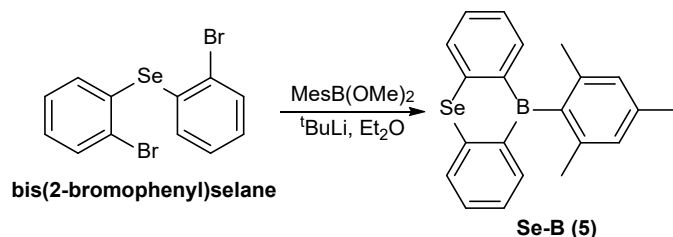


(adopted and modified from ref<sup>211</sup>.)

2-bromophenyl)hydrazine (2 g, 10.69 mmol, 1 eq.) was dissolved in acetonitrile (25 mL) and added to a stirred suspension of selenium dioxide (1.78 g, 16.04 mmol, 1.5 eq.) in acetonitrile (25 mL). The suspension turned orange and then orange-red after bubble formation, and was then stirred at 60 °C for 1 h. Desired product was observed on TLC after 1 h and the resulting mixture was extracted with hexane to afford a red solution. After concentration under reduced pressure, the crude product was further purified with flash column chromatography (hexane) to afford bis(2-bromophenyl)selane as a yellow-orange solid (344.2 mg, 16.5% yield).

- <sup>1</sup>H NMR (500 MHz, Chloroform-d) δ 7.63 (dd, J = 7.6, 1.6 Hz, 2H), 7.25 (dd, J = 7.6, 1.9 Hz, 2H), 7.23 – 7.13 (m, 4H).
- <sup>13</sup>C NMR (126 MHz, DMSO-d<sub>6</sub>) δ 134.44, 133.78, 132.71, 130.45, 129.44, 126.61.
- <sup>77</sup>Se NMR (95 MHz, Chloroform-d) δ 462.71.

▪ **(Se-B, 5) 10-mesityl-10H-dibenzo[*b,e*][1,4]selenaborinine**

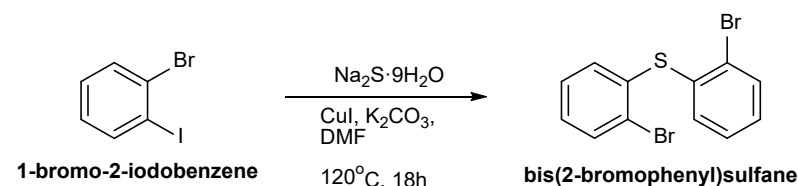


<sup>t</sup>BuLi (1.9M pentane solution, 0.303 mL, 0.5766 mmol, 4.42 eq.) was added to a solution of bis(2-bromophenyl)selane (51 mg, 0.1304 mmol, 1 eq.) in diethyl ether (3 mL) at -78 °C. After stirring for 30 min at -78 °C, MesB(OMe)<sub>2</sub> (37.58 mg, 0.1957 μmol, 1.40 eq.) in diethyl ether (1.5 mL) was added to the reaction mixture. The mixture was warmed up to room temperature and stirred overnight before quenched with water. The organic layer was extracted with CHCl<sub>3</sub> and dried over anhydrous Na<sub>2</sub>SO<sub>4</sub>. After removal of the solvent under reduced pressure, the residue

was purified with flash column chromatography (hexane) to afford 10-mesityl-10*H*-dibenzo[*b,e*][1,4]selenaborinine (Se-B, **5**) as a yellow solid (19.85 mg, 42.1% yield).

- <sup>1</sup>H NMR (500 MHz, Chloroform-*d*) δ 7.92 – 7.87 (m, 1H), 7.84 (d, *J* = 7.9 Hz, 1H), 7.57 – 7.51 (m, 1H), 7.29 (t, *J* = 7.4 Hz, 1H), 6.94 (s, 1H), 2.41 (s, 2H), 1.93 (s, 3H).
- <sup>1</sup>H NMR (401 MHz, DMSO-*d*<sub>6</sub>) δ 8.01 (d, *J* = 7.6 Hz, 1H), 7.72 (dd, *J* = 7.7, 1.3 Hz, 1H), 7.69 – 7.61 (m, 1H), 7.41 – 7.34 (m, 1H), 6.92 (s, 1H), 2.33 (s, 2H), 1.83 (s, 3H).
- <sup>13</sup>C NMR (126 MHz, DMSO-*d*<sub>6</sub>) δ 143.74, 140.39, 137.46, 136.11, 134.96, 132.75, 127.86, 127.07, 125.71, 118.06, 22.50, 20.85.
- <sup>11</sup>B NMR (128 MHz, Chloroform-*d*) δ 61.79.
- <sup>77</sup>Se NMR (95 MHz, Chloroform-*d*) δ 409.75.

#### ▪ Bis(2-bromophenyl)sulfane

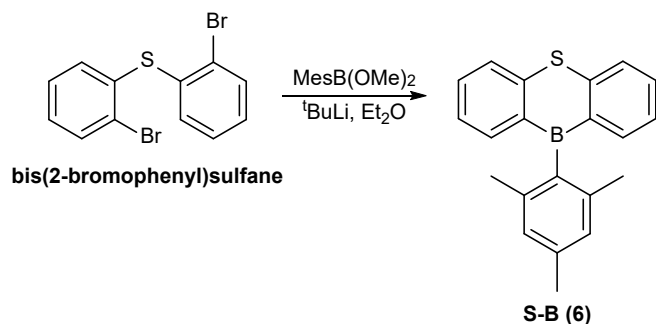


(adopted and modified from ref<sup>212</sup>.)

CuI (38.5 mg, 0.202 mmol, 0.2 eq.), K<sub>2</sub>CO<sub>3</sub> (279 mg, 2.02 mmol, 2 eq.), Na<sub>2</sub>S (291 mg, 1.21 mmol, 1.2 eq.) and 1-bromo-2-iodobenzene (572 mg, 2.02 mmol, 2 eq.) were mixed in DMF (4 mL). The mixture was heated at 120°C overnight and allowed to cool to room temperature. The resulting mixture was extracted with ethyl acetate. The combined organic layers were dried over Na<sub>2</sub>SO<sub>4</sub> and then concentrated under reduced pressure. The crude product was purified with flash column chromatography (hexane) to afford bis(2-bromophenyl)sulfane as white powder (126.4 mg, 36.3% yield).

- <sup>1</sup>H NMR (401 MHz, Chloroform-*d*) δ 7.65 (dd, *J* = 7.8, 1.2 Hz, 2H), 7.24 (dd, *J* = 7.6, 1.4 Hz, 2H), 7.18 – 7.11 (m, 4H).
- <sup>1</sup>H NMR (500 MHz, DMSO-*d*<sub>6</sub>) δ 7.79 – 7.75 (m, 2H), 7.42 – 7.38 (m, 2H), 7.30 (td, *J* = 7.6, 1.3 Hz, 2H), 7.13 (dd, *J* = 7.8, 1.4 Hz, 2H).
- <sup>13</sup>C NMR (126 MHz, DMSO-*d*<sub>6</sub>) δ 134.81, 134.02, 132.68, 130.13, 129.43, 125.35.

▪ (S-B, 6) 10-mesityl-10*H*-dibenzo[*b,e*][1,4]thiaborinine

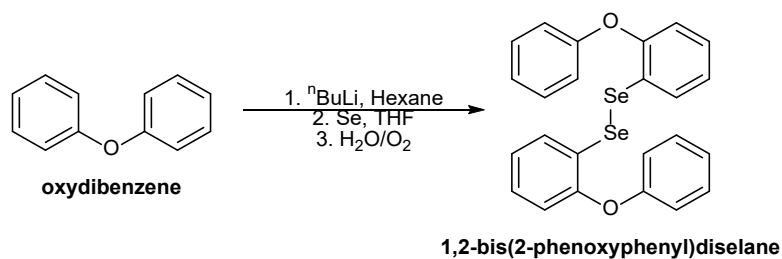


<sup>t</sup>BuLi (1.9m pentane solution, 0.667 mL, 1.267mmol, 4.36 eq.) was added to a solution of bis(2-bromophenyl)sulfane (100mg, 0.2906 mmol, 1 eq.) in Et<sub>2</sub>O (2 mL) at -78°C. After stirring for 30 min at -78°C, MesB(OMe)<sub>2</sub> (77mg, 0.4011mmol, 1.38 eq.) in Et<sub>2</sub>O (3 mL) was added to the reaction mixture. The reaction mixture was stirred at r.t. overnight and the reaction was quenched with water.

The organic layer was extracted with CHCl<sub>3</sub> and dried over anhydrous Na<sub>2</sub>SO<sub>4</sub>. After removal of the solvent under reduced pressure, the residue was purified with flash column chromatography (hexane) to afford 10-mesityl-10*H*-dibenzo[*b,e*][1,4]thiaborinine (S-B, 6) as a pale yellow solid (45.67 mg, 43.51% yield).

- <sup>1</sup>H NMR (400 MHz, Chloroform-*d*) δ 7.88 (d, *J* = 7.7 Hz, 1H), 7.78 (d, *J* = 8.1 Hz, 1H), 7.62 (t, *J* = 7.5 Hz, 1H), 7.30 (t, *J* = 7.4 Hz, 1H), 6.95 (s, 1H), 2.41 (s, 2H), 1.93 (s, 3H).
- <sup>1</sup>H NMR (500 MHz, DMSO-*d*<sub>6</sub>) δ 7.94 (d, *J* = 8.1 Hz, 2H), 7.79 – 7.70 (m, 5H), 7.42 (t, *J* = 7.4 Hz, 2H), 6.94 (s, 2H), 2.34 (s, 3H), 1.83 (s, 6H).
- <sup>13</sup>C NMR (126 MHz, DMSO-*d*<sub>6</sub>) δ 143.90, 139.28, 138.10, 136.71, 133.42, 127.50, 126.04, 125.68, 23.00, 21.33.

▪ 1,2-bis(2-phenoxyphenyl)diselane



(adopted and modified from ref<sup>207</sup>.)

1. To a solution of oxydibenzene (1.532 g, 9 mmol, 1eq.) in anhydrous hexane (25 mL), a 2.5 M solution of n-BuLi (9 mmol, 3.7 mL) in hexane was added dropwise at 0 °C and the reaction mixture was kept at this temperature for about 3 h with stirring. The reaction mixture was slowly warmed up to room temperature and it was left under stirring overnight.

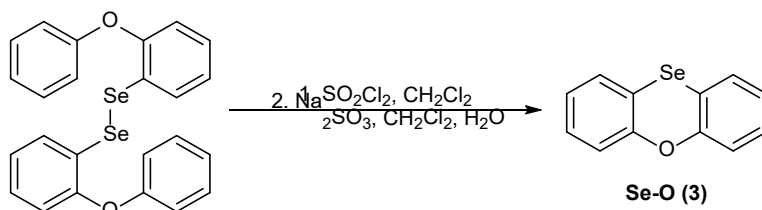
2. The solvent was removed in vacuum and the remaining oil was dissolved in THF (20 mL). Afterwards, the stoichiometric amount of Se (710.64 mg, 9 mmol, 1eq.) was added and the solution became deep brown.

3. The reaction mixture was stirred for additional 2 h and then water was added (under argon) and subsequently the solution was exposed to air. The solvent was removed in vacuo and the remaining solid was dissolved in DCM (25 mL). The organic phase was washed with water and dried over anhydrous Na<sub>2</sub>SO<sub>4</sub> to afford 1,2-bis(2-phenoxyphenyl)diselane as a red oil which turned into a solid after storage in freezer (2.076 g, 92.93% yield).

○ <sup>1</sup>H NMR (700 MHz, Chloroform-d) δ 7.69 (d, J = 7.9 Hz, 2H), 7.34 (t, J = 7.5 Hz, 4H), 7.18 (t, J = 7.7 Hz, 2H), 7.12 (t, J = 7.4 Hz, 2H), 7.02 (dd, J = 21.5, 8.0 Hz, 6H), 6.83 (d, J = 8.1 Hz, 2H).

○ <sup>77</sup>Se NMR (134 MHz, Chloroform-d) δ 354.66.

#### ▪ (Se-O, 3) Phenoxaselenine



**1,2-bis(2-phenoxyphenyl)diselane**

(adopted and modified from ref<sup>207</sup>.)

1. To a solution of 1,2-bis(2-phenoxyphenyl)diselane (0.335 g, 0.675 mmol) in anhydrous DCM (10 mL), a 1 M solution of SO<sub>2</sub>Cl<sub>2</sub> in CH<sub>2</sub>Cl<sub>2</sub> (0.675 mL, 0.675 mmol) was added dropwise and the solution grew from light yellow to brown. The solution was left stirred for 2 days, and the color gradually changed back to yellow. After removal of all volatiles at reduced pressure, the remaining intermediate solid was washed with anhydrous hexane and dried.

2. To a solution of the intermediate in DCM (15 mL), Na<sub>2</sub>SO<sub>3</sub> (0.0206 g, 0.16 mmol) in H<sub>2</sub>O (15 mL) was added. The solution was stirred for 3 h. The organic phase was separated and dried over

anhydrous Na<sub>2</sub>SO<sub>4</sub>, filtered, and concentrated at reduced pressure to afford phenoxaselenine (Se-O, **3**) as a white solid (135 mg, 31.5% yield).

- <sup>1</sup>H NMR (500 MHz, Chloroform-d) δ 7.30 (d, J = 7.6 Hz, 2H), 7.20 (t, J = 7.7 Hz, 2H), 7.12 (d, J = 8.0 Hz, 2H), 7.04 (t, J = 7.4 Hz, 2H).
- <sup>1</sup>H NMR (500 MHz, DMSO-d<sub>6</sub>) δ 7.47 (dd, J = 7.7, 1.4 Hz, 1H), 7.30 – 7.24 (m, 1H), 7.18 (dd, J = 8.1, 1.1 Hz, 1H), 7.12 (td, J = 7.5, 1.2 Hz, 1H).
- <sup>13</sup>C NMR (126 MHz, DMSO-d<sub>6</sub>) δ 152.68, 130.24, 129.11, 125.87, 118.96, 116.33.
- <sup>77</sup>Se NMR (134 MHz, Chloroform-d) δ 256.69.

## 5.6. Computational Details

The RAS-SF method is programmed in the Q-Chem 5.0 software package,<sup>213</sup> and the SOC computations are implemented in a development version of Q-Chem. All RAS-SF calculations were performed with the polarized, triple-zeta def2-TZVP basis set<sup>111,214</sup> and the RIMP2-cc-pVTZ auxiliary basis.<sup>111</sup> RAS-SF hole, particle calculations with 4 electron in 4 orbital active spaces were carried out with RAS1 and RAS3 subspaces including all occupied and virtual orbitals, respectively. Unless otherwise stated, the core electrons were kept frozen. Reference orbitals for RAS-SF were obtained from restricted open-shell density functional theory (RODFT) using the B3LYP functional in the triplet state. Geometries of the molecules were optimized at the ground state using  $\omega$ B97X-D functional<sup>215,216</sup> and the def2-TZVP basis set<sup>111,214</sup>. Calculations of SOC constants utilize general libraries developed for SOC calculations within EOM-CC.<sup>112</sup> Spin-orbit NTOs were computed and analyzed using the libwfa library.<sup>113</sup> The NTOs with the largest singular values, for each compound, were plotted using Gabedit program.<sup>217</sup>

## 5.7. Reduced SOCME in the selected orientations

**Table S5.1. Reduced SOCME in the selected orientations between  $S_0$  and  $T_1$  states**

Orientation	$L_x$ or $L_-$	$L_z$ or $L_0$	$L_y$ or $L_+$
S-O	14.8229+2.0238i	0.00	14.8229-2.0238i
Se-O	272.7789+45.2145i	0.00	272.7789-45.2145i
S-N	-10.50-6.02i	0.00	-10.50+6.02i
Se-N	-137.56+0.01i	-78.77i	-137.56-0.01i
S-B	-0.0390i	0.00	0.0399i
Se-B	-0.0002+0.0908i	0.00	-0.0002-0.0908i
S-CO	0.00	0.0001i	0.00
Se-CO	0.0001+0.0485i	0.00	0.0001-0.0485i

**Table S5.2. Reduced SOCME in the selected orientations between  $S_0$  and  $T_1$  states, for Se-N with varying dihedral angle**

Orientation	$L_x$ or $L_-$	$L_z$ or $L_0$	$L_y$ or $L_+$
10°	18.2431+0.0069i	3.8320i	18.2431-0.0069i
20°	-37.2080+0.2711i	13.2820i	-37.2080-0.2711i
30°	-105.4036-0.0016i	-38.6745i	-105.4036+0.0016i
40°	173.2978-0.0001i	113.4250i	173.2978+0.0001i
50°	229.5948-0.0089i	223.7239i	229.5948+0.0089i
60°	-264.4984+0.0081i	-372.0783i	-264.4984-0.0081i



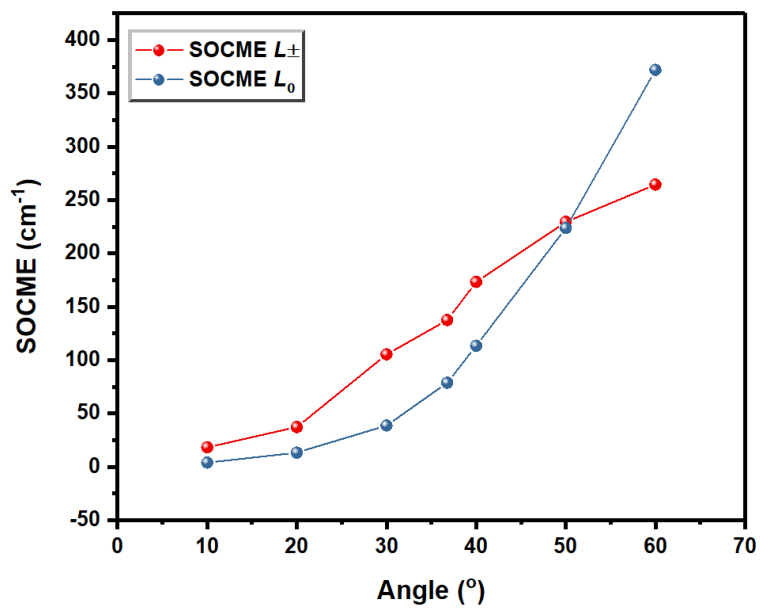


**Figure S5.1. Reduced SOCME in the selected orientations between  $S_0$  and  $T_1$  states, for Se-N with varying dihedral angle (showing the modulus).**

## 5.8. Emission and excitation spectra

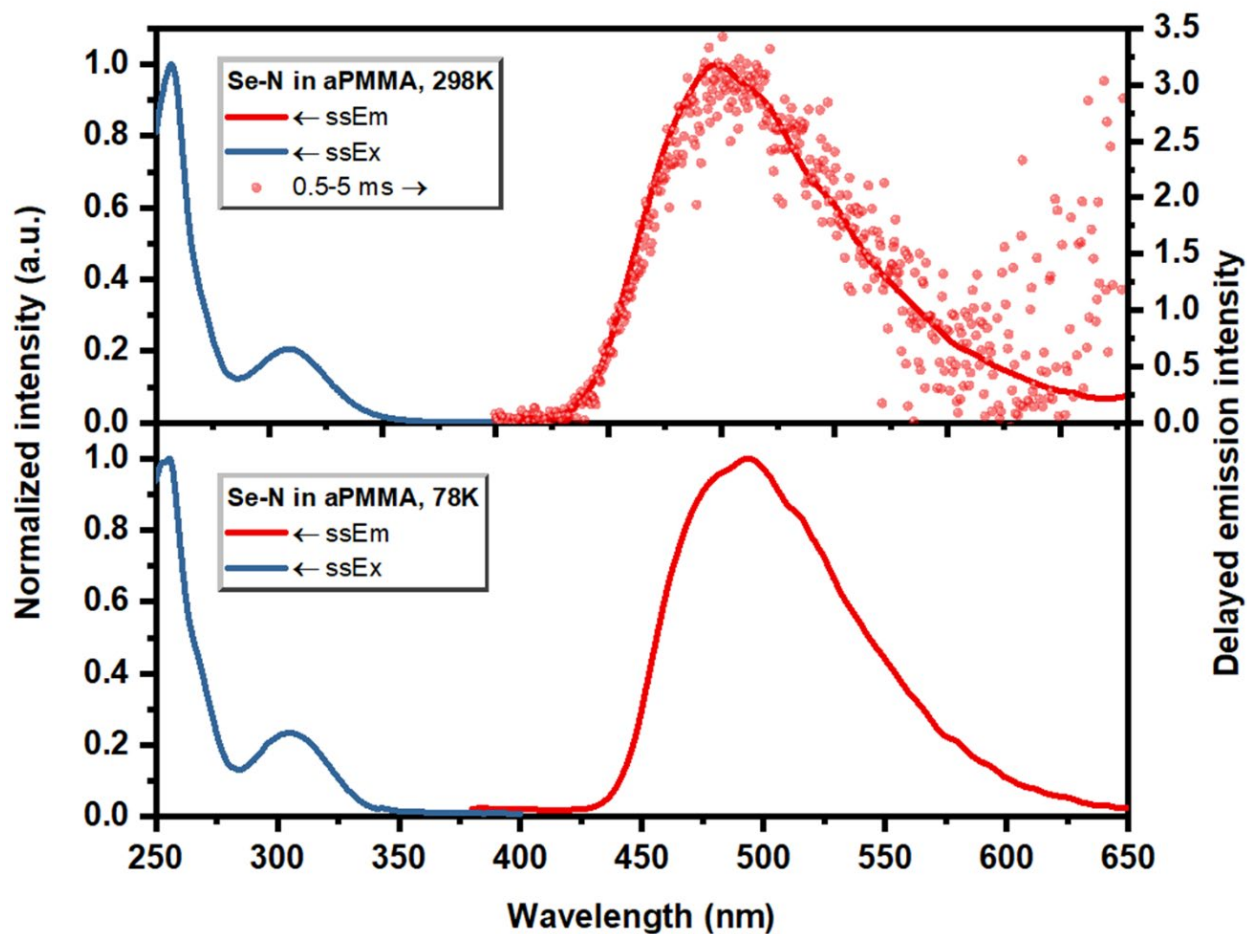


**Figure S5.2.** The emission and excitation spectra of Se-N (1 wt% in atactic PMMA matrix) at 298 K and 78 K measured in vacuum: steady state emission (red line), steady state excitation (blue line), and delayed emission (0.5-5 ms, red dot).

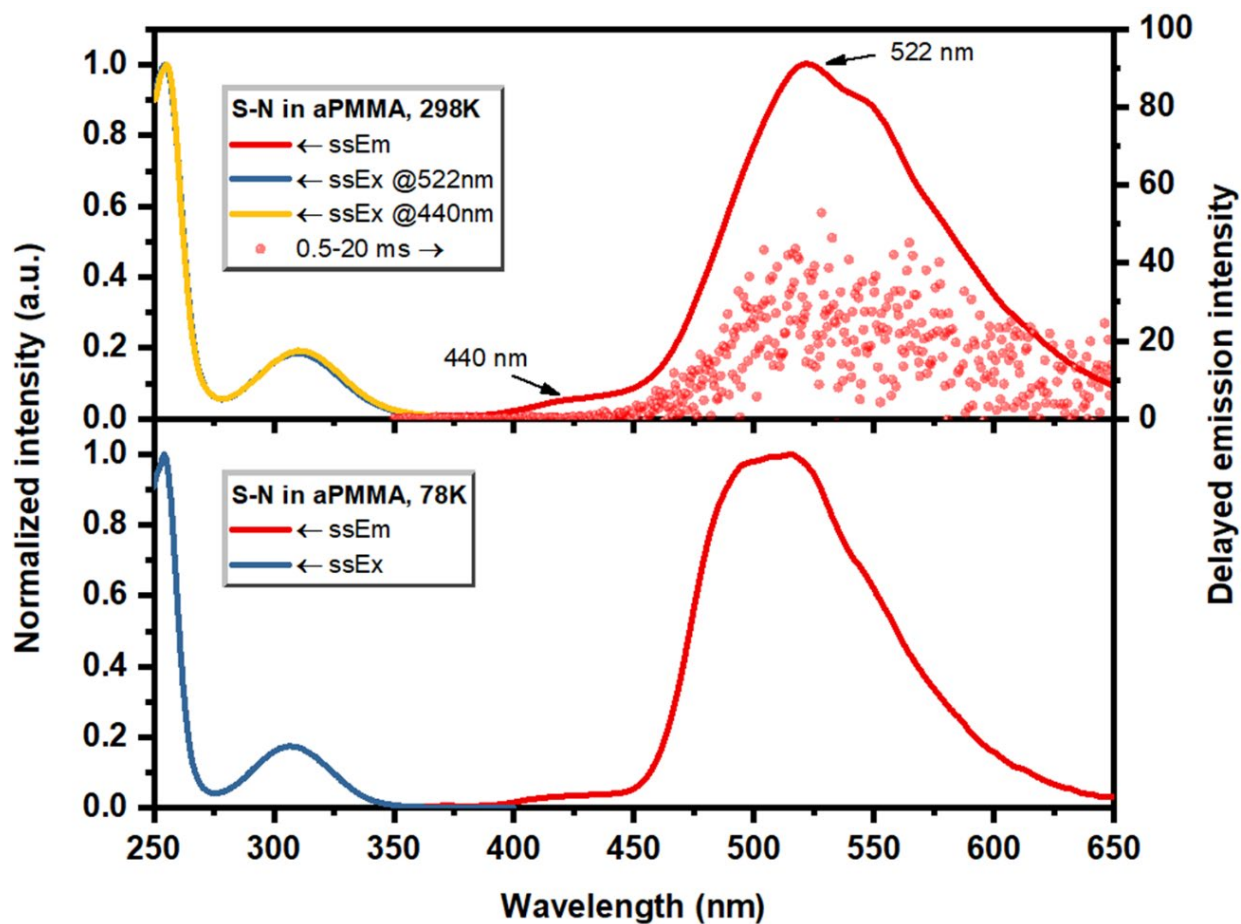


**Figure S5.3.** The emission and excitation spectra of S-N (1 wt% in atactic PMMA matrix) at 298 K and 78 K measured in vacuum: steady state emission (red line), steady state excitation (blue & yellow line), and delayed emission (0.5-5 ms, red dot).

The emission peak at 440 nm could either come from prompt fluorescence or delayed fluorescence.

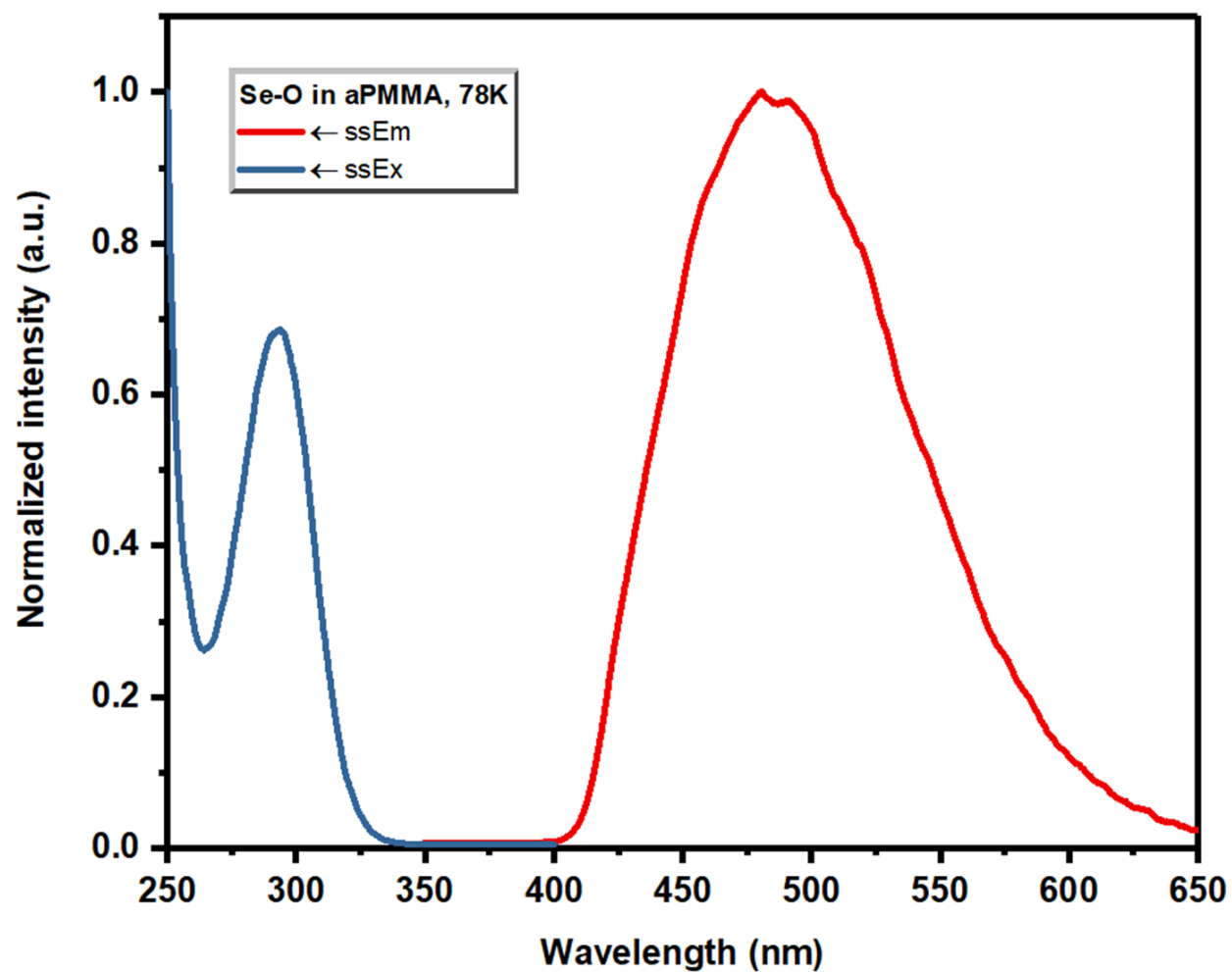


**Figure S5.4.** The emission and excitation spectra of Se-O (1 wt% in atactic PMMA matrix) at 78 K measured in vacuum: steady state emission (red line) and steady state excitation (blue line). The emission at 298 K was very weak, and thus it wasn't shown here.

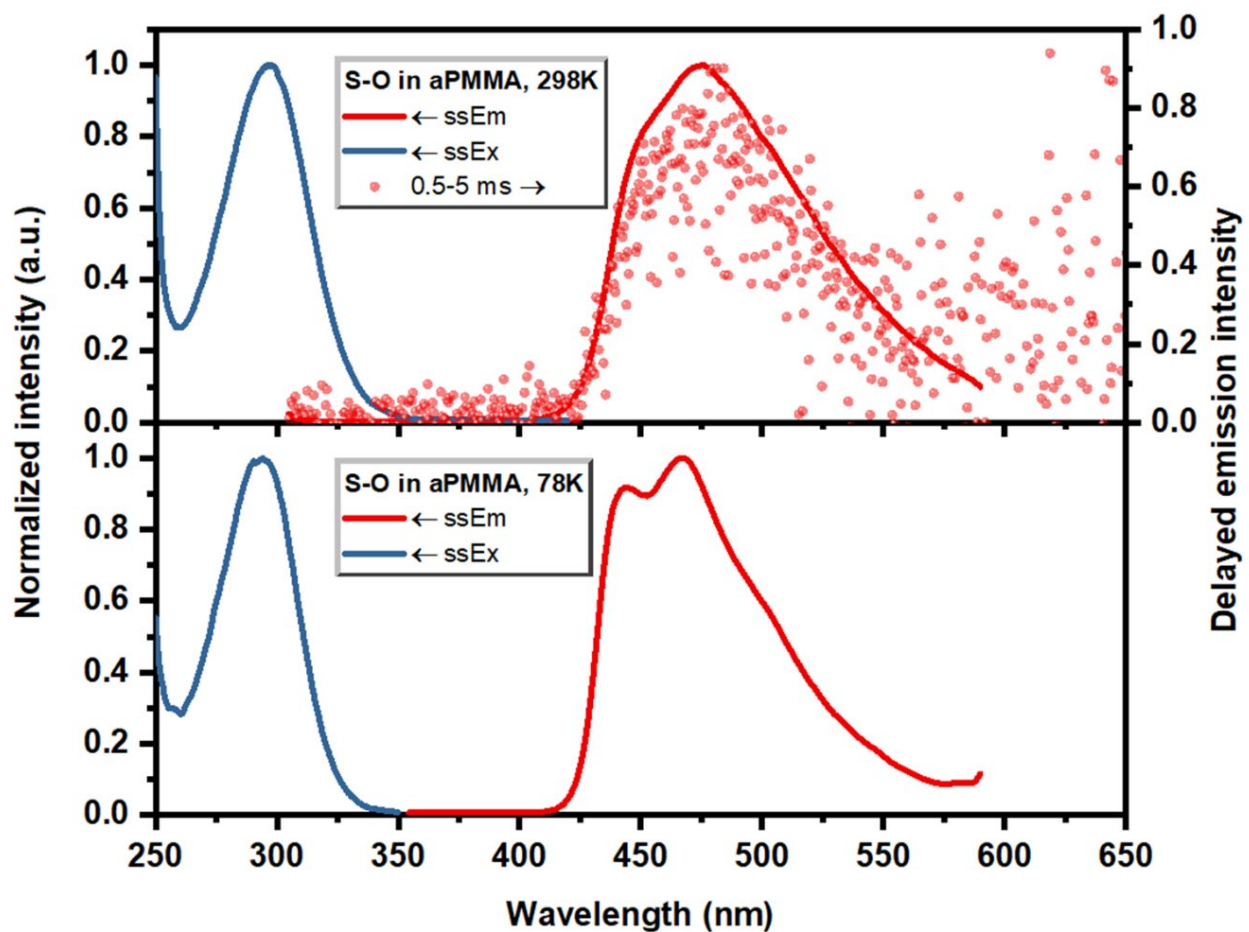


**Figure S5.5.** The emission and excitation spectra of S-O (1 wt% in atactic PMMA matrix) at 298 K and 78 K measured in vacuum: steady state emission (red line), steady state excitation (blue line), and delayed emission (0.5-5 ms, red dot).

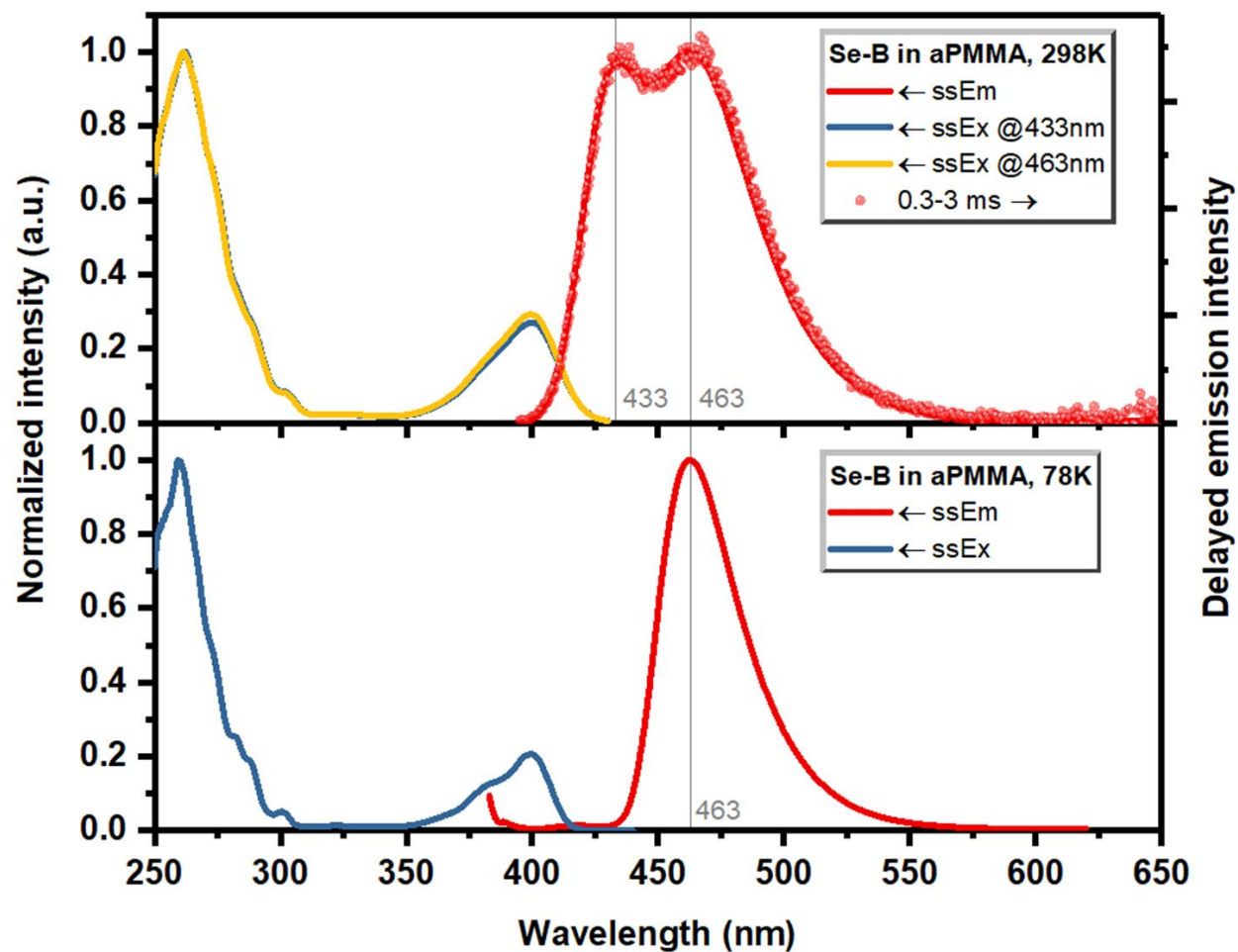


**Figure S5.6.** The emission and excitation spectra of Se-B (1 wt% in atactic PMMA matrix) at 298 K and 78 K measured in vacuum: steady state emission (red line), steady state excitation (blue & yellow line), and delayed emission (0.5-5 ms, red dot).

The emission peak at 433 nm (298 K) is from delayed fluorescence since it stayed the same relative intensity in the delayed spectrum, and disappeared at 78 K.

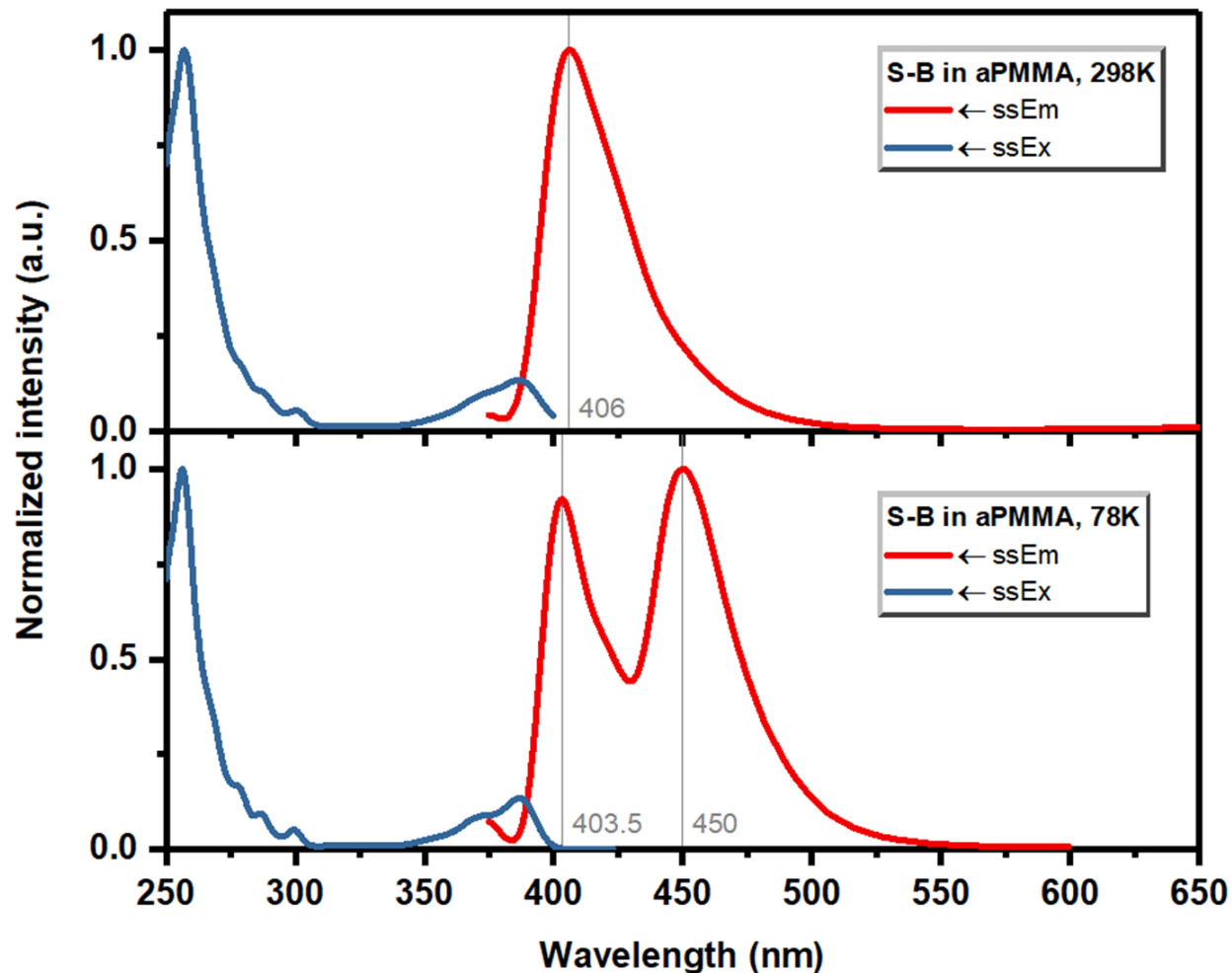


**Figure S5.7.** The emission and excitation spectra of S-B (1 wt% in atactic PMMA matrix) at 298 K and 78 K measured in vacuum: steady state emission (red line) and steady state excitation (blue line).

The emission peak at 406 nm (298 K) or 403.5 nm (78K) should have certain delayed fluorescence character.

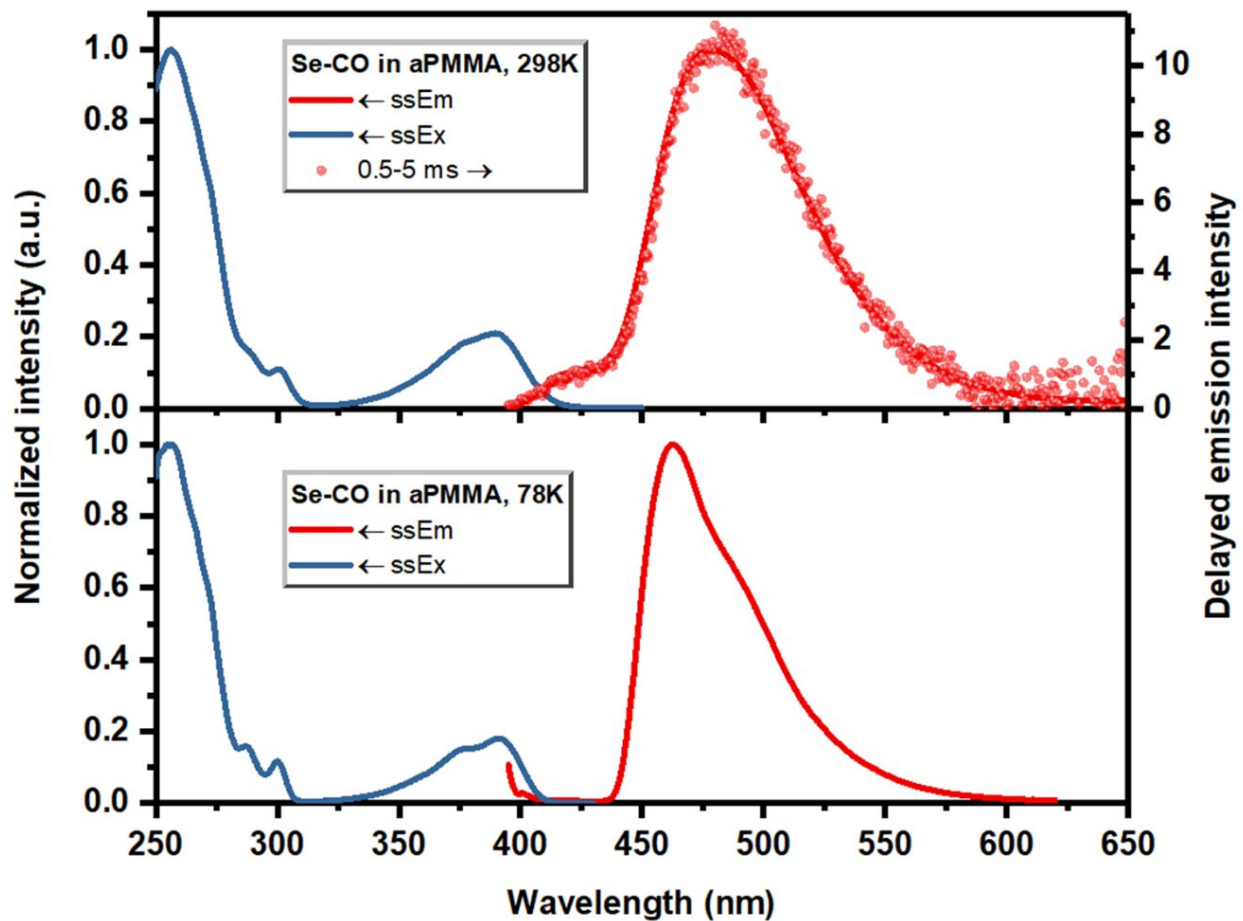


**Figure S5.8.** The emission and excitation spectra of Se-CO (1 wt% in atactic PMMA matrix) at 298 K and 78 K measured in vacuum: steady state emission (red line), steady state excitation (blue line), and delayed emission (0.5-5 ms, red dot).



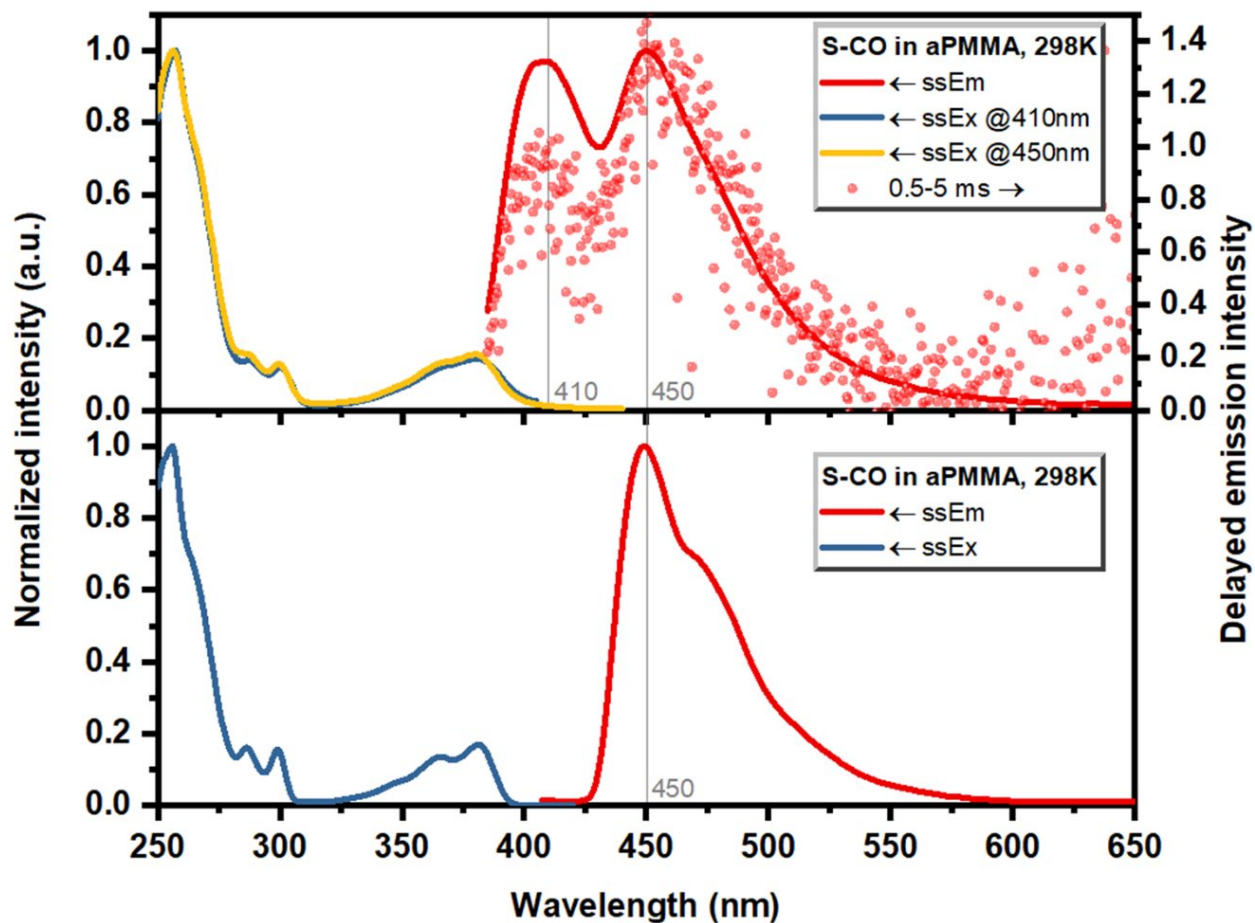


**Figure S5.9.** The emission and excitation spectra of S-CO (1 wt% in atactic PMMA matrix) at 298 K and 78 K measured in vacuum: steady state emission (red line), steady state excitation (blue & yellow line), and delayed emission (0.5-5 ms, red dot).

The emission peak at 410 nm (298 K) should have certain delayed fluorescence character since it stayed the same relative intensity in the delayed spectrum, and disappeared at 78 K.

## 5.9. Additional lifetime information

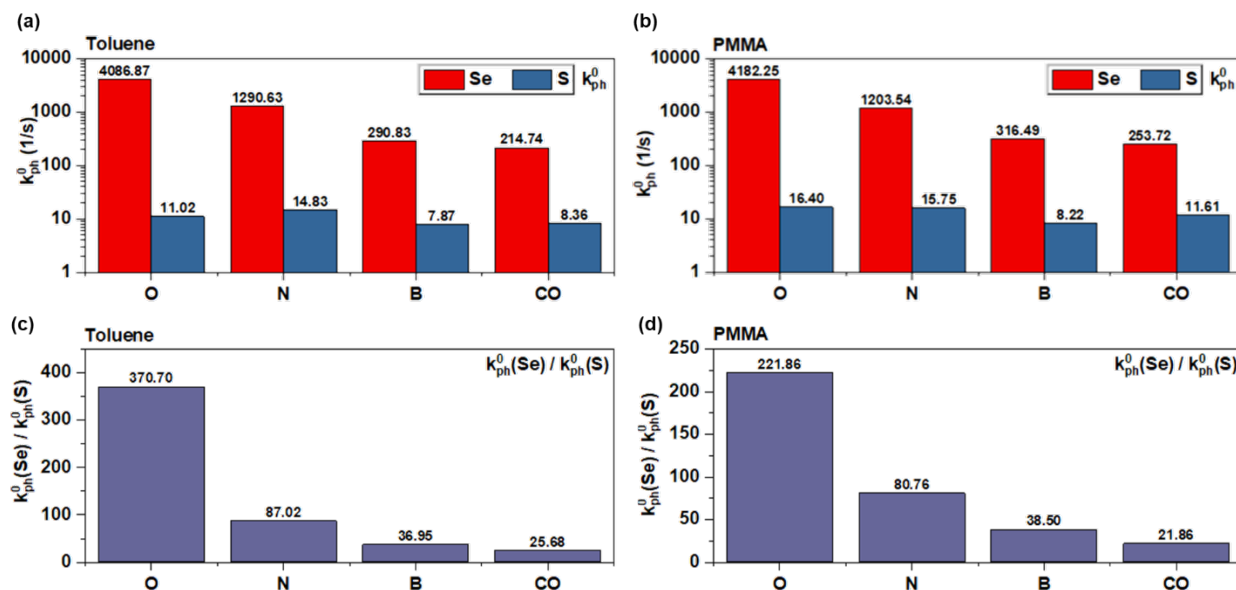


**Figure S5.10.** The experimental intrinsic phosphorescence rate  $k_{ph}^0$  measured in (a) toluene and (b) in doped PMMA matrix at 78 K, and the  $k_{ph}^0(\text{Se derivative})/k_{ph}^0(\text{S derivative})$  value of each functional group in (c) toluene and (d) in doped PMMA matrix at 78 K.

The general trend where  $k_{ph}^0$  or SOCMEs decrease with decreasing dihedral angle is clearly observed in the Se compounds. In the sulfur series, the general trend in  $k_{ph}^0$  still follows prediction in that a sharp drop in dihedral angle from Se-O/N to Se-B/CO has led to obvious reduction in  $k_{ph}^0$ . This leaves just one case, the  $k_{ph}^0$  of S-CO, which is higher than that of S-B and therefore does not fit the trend.

We presume two plausible reasons. First, sulfur is not a heavy atom and due to the intrinsically lower SOCME, S derivatives will be more prone to non-radiative decay than their Se counterparts. This deactivation pathway comes from both the compound itself and its interaction with the matrices. Thus, the varying non-radiative decay rate from S-O, S-N to S-B and S-CO could lead to the deviation from the predicted  $T_1$ - $S_0$  SOCME trend.

Second, experimental dihedral angles of the two CO compounds are likely shifted from their calculated value. This is very important particularly for planar molecules since a little distortion from complete planarity could lead to large gain in  $T_1$ - $S_0$  SOCME. For instance, the predicted  $T_1$ - $S_0$  SOCME for Se-CO is  $0.046 \text{ cm}^{-1}$  and  $1.04e^{-4} \text{ cm}^{-1}$  for S-CO, which should both lead to very long intrinsic phosphorescence lifetime or very low  $k_{ph}^0$ . However, the experimental results in

PMMA at 78K suggested otherwise. For instance, Se-CO has a fast-than-predicted  $\tau_{ph}^0$  of 4.09 ms. Thus, we hypothesized that the experimental dihedral angle or more precisely,  $\Delta L$  in the CO series is non-negligible. Hence, the actual phosphorescence rate should be larger than the predicted value. To demonstrate these in experiments, we've compared the lifetimes of 8 compounds studied in dilute toluene solution with those in PMMA at 78K.

According to Figure S5.10, changing the matrix has inevitably changed the lifetime at 78K. This change is extremely large for S-CO which had  $k_{ph}^{78K}$  of 8.36 1/s in toluene v.s. 11.61 1/s in PMMA. S-CO and S-B now have similar lifetimes in toluene. We suspect that either non-radiative decay or dihedral angle change both due to interaction with the matrix may have led to the great lifetime change. Due to similar reasons, surprisingly, S-O presented similar large  $k_{ph}^{78K}$  change from PMMA to toluene. However, the overall lifetime trend is very obvious as predicted in the Se compounds, and hence the decreasing  $k_{ph}^0(\text{Se derivative})/k_{ph}^0(\text{S derivative})$  as shown in Figure S5.10c-d. It is less pronounced in the S compounds, but follows the general reducing trend from S-N/O to S-B/CO.

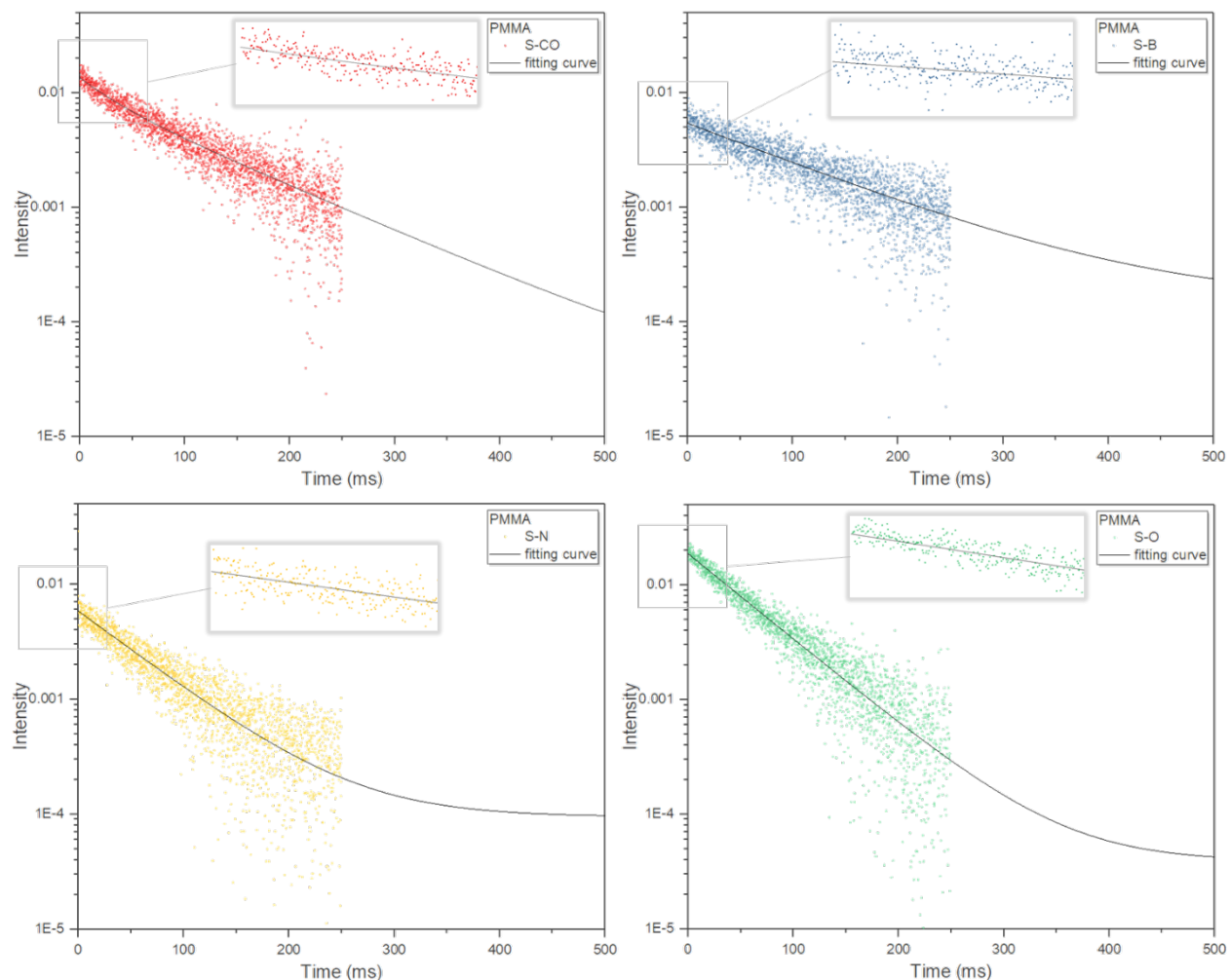


**Figure S5.11. Photoluminescence decay of S-CO, S-B, S-N, and S-O in PMMA matrix measured at 78K.** The fitting curve was included, which was done by Origin Lab software with its built-in exponential decay function. The raw decay data was recorded from 0 to 250 ms, while fitting was done using the data from 10 to 250 ms. The insets show the fitting in the head (1-30 ms). The head, body, and tail of the decay were all well-fitted, indicating good fitting quality.

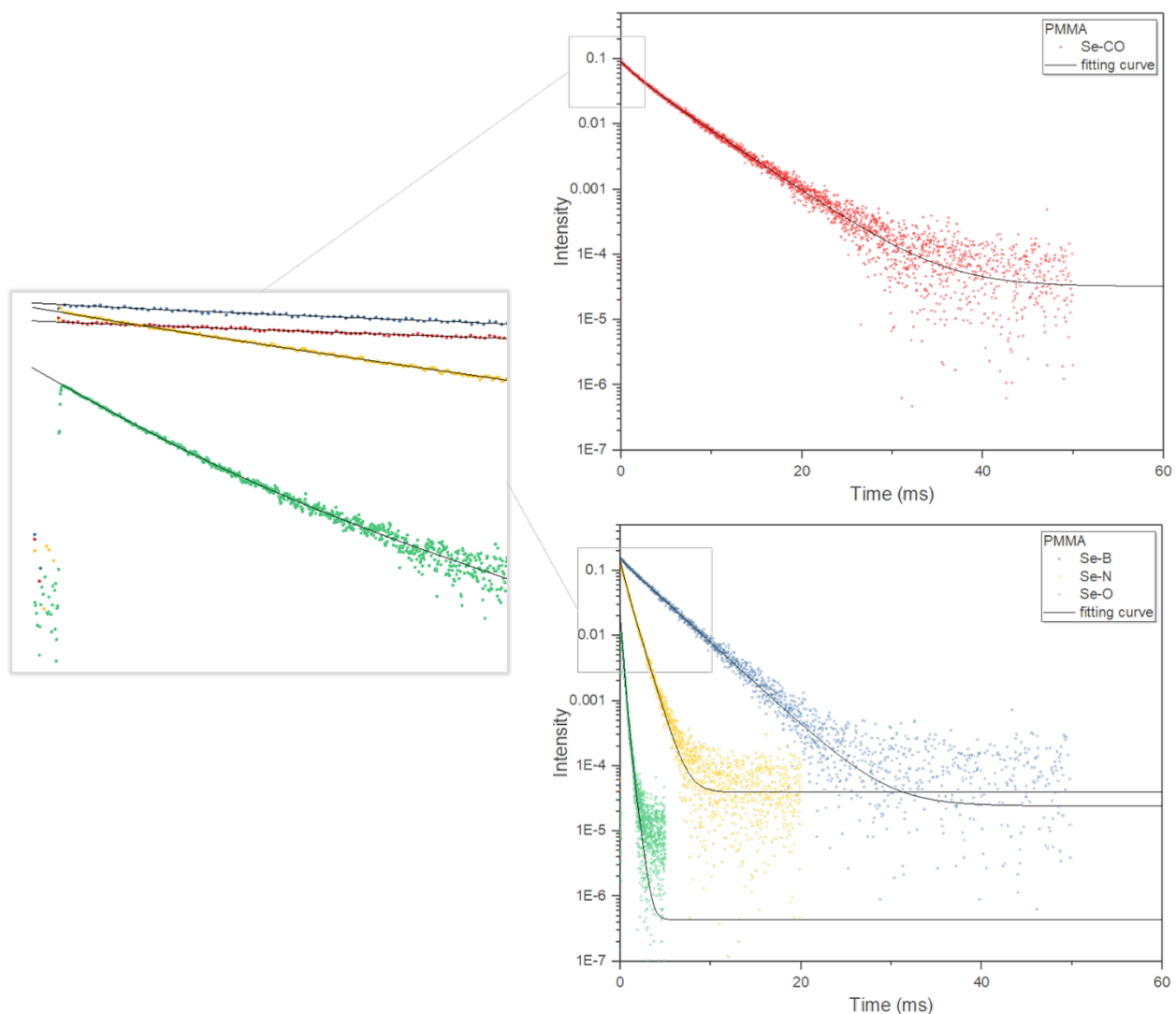


**Figure S5.12. Photoluminescence decay of Se-CO, Se-B, Se-N, and Se-O in PMMA matrix measured at 78K.** The fitting curve was included, which was done by Origin Lab software with its built-in exponential decay function. The raw decay data was recorded from 0 ms, while fitting was done using the data from 0.2 ms. The insets show the fitting in the head (0-2 ms). The head, body, and tail of the decay were all well-fitted, indicating good fitting quality.

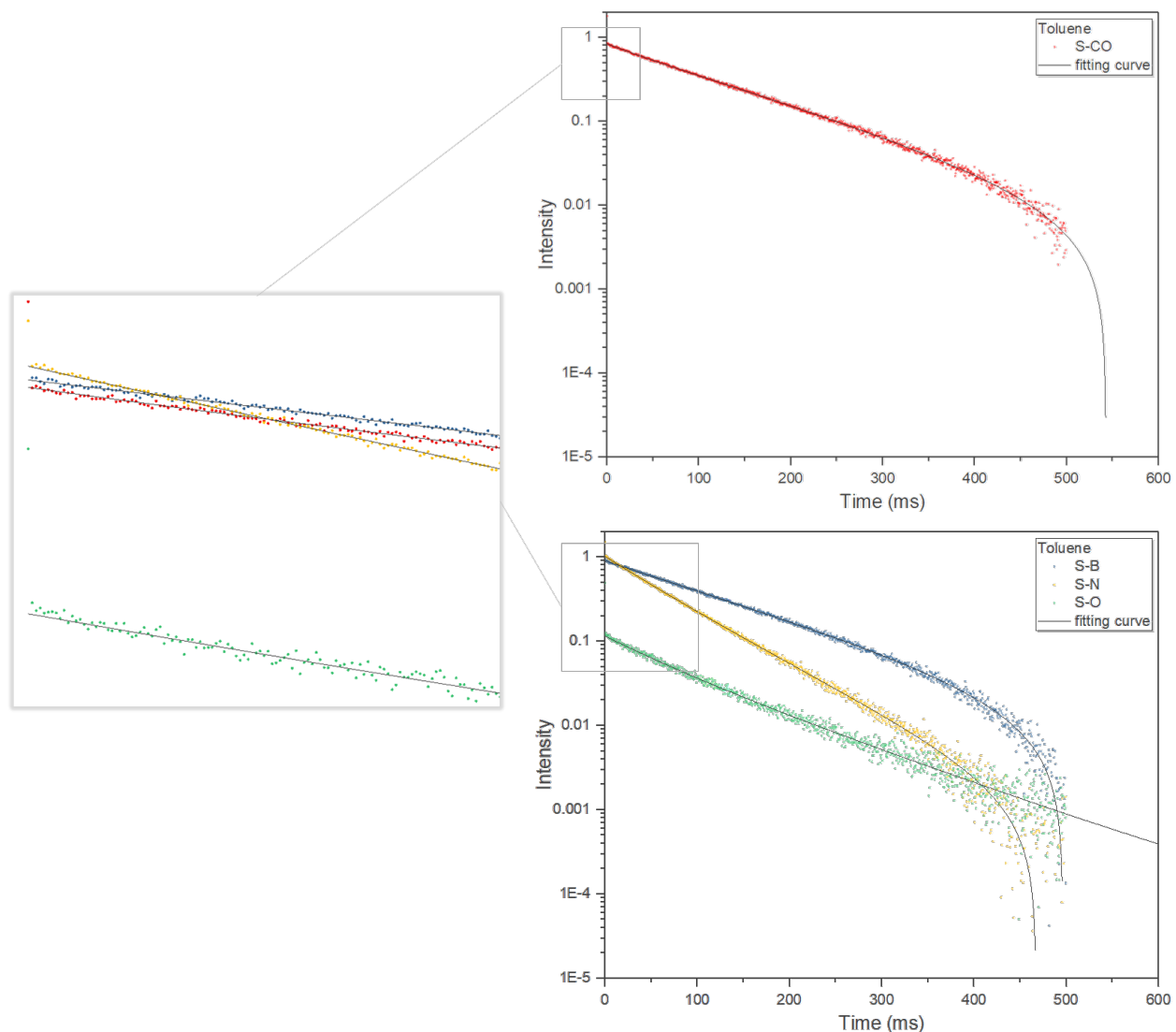


**Figure S5.13. Photoluminescence decay of S-CO, S-B, S-N, and S-O in toluene measured at 78K.** The fitting curve was included, which was done by Origin Lab software with its built-in exponential decay function. The raw decay data was recorded from 0-500 ms, while fitting was done using the data from 10 ms. The insets show the fitting in the head (0-60 ms). The head, body, and tail of the decay were all well-fitted, indicating good fitting quality.

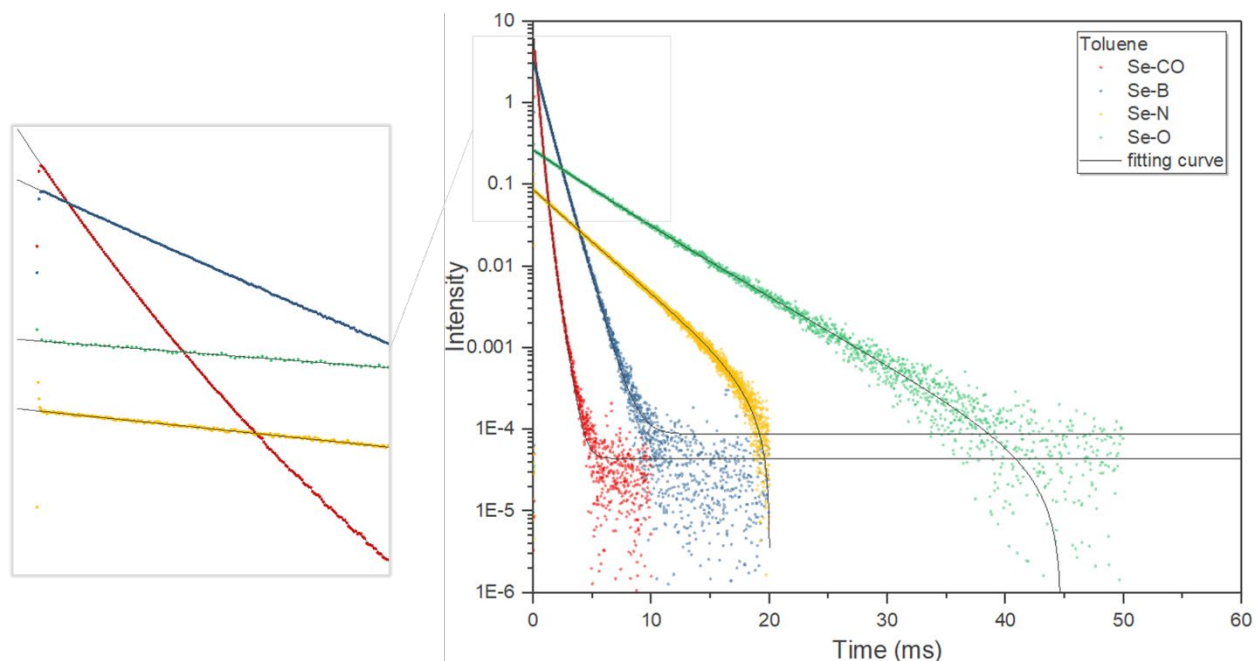


**Figure S5.14. Photoluminescence decay of Se-CO, Se-B, Se-N, and Se-O in toluene measured at 78K.** The fitting curve was included, which was done by Origin Lab software with its built-in exponential decay function. The raw decay data was recorded from 0 ms, while fitting was done using the data from 0.2 ms. The insets show the fitting in the head (0-2 ms). The head, body, and tail of the decay were all well-fitted, indicating good fitting quality.

## **CHAPTER VI**

### **Conclusions and Perspectives**

Designing purely organic phosphorescent materials with tailored properties is a demanding task requiring rational molecular design principles that accurately account for how all conceivable structural, electronic, chemical, compositional, and environmental factors affect material performance. This dissertation started from reviewing the past developments on metal-free purely organic phosphors to the present challenges towards the design of “fast and efficient” POPs. Subsequent in the following chapters, our recent research developments of POPs were discussed from a practical perspective in various modern applications including sensor and imaging, data encryption, display devices, and from a theoretical perspective by introducing our novel design concept of “Heavy atom oriented orbital angular momentum manipulation” targeting at fast POPs. In this last chapter, an overview summary is given for the presented developments on POPs in this dissertation and perspectives on the future directions.



## 6.1. Summary and Outlook

This dissertation begins with a thorough review on the molecular design factors affecting the internal and external efficiencies of POPs by connecting the theoretical descriptors influencing on SOC with the molecular orbitals and functional moieties. These foundational guidelines promoted the design of contemporary POP, POP-incorporated systems, and projected the futuristic “fast and efficient” POP design under the HAAM concept.

Contemporary developments of POPs have focused extensively on the activation of intrinsic SOC channels and the suppression of extrinsic non-radiatively decay pathways to incite efficient room-temperature phosphorescence from POPs. The employed strategies include the internal and external heavy atom effects, attachment of functional moieties to satisfy the El-Sayed rule by creating transitions exerting orbital angular momentum change mostly through  $(n, \pi^*) - (\pi, \pi^*)$  channels, and embedding POPs in tailor-designed matrices capable of establishing specific intermolecular interactions with POPs to suppress molecular motion. Remarkably bright RTP could be activated from POPs and POP-employed systems with quantum yield exceeding 10% and tunable lifetime in the millisecond to second regime, making them suitable candidates for modern anti-counterfeiting platforms, chemical and biosensors, bioimaging, and OLEDs.

Chapter II-IV discusses our recent developments on POPs from a practical engineering perspective in various modern applications including sensor, imaging, data encryption, display devices, as well as from a fundamental scientific perspective by addressing how molecular level manipulation affects the performance of POPs.

In detail, Chapter II explores the combined molecular design of purely organic triplet emission with the ESIPT phenomenon to create dual-emissive “ESIPT triplet emitters”. These ESIPT triplet emitters were designed from the simplest HBI structure and bright room-temperature triplet emission was successfully activated both in the keto and enol tautomers by incorporating aldehyde to generate efficient  $(n, \pi^*) - (\pi, \pi^*)$  SOC channels and Br to elevate the overall SOC efficiencies. Interestingly, the developed BrA-HBI was capable of emitting blue delayed fluorescence in its keto form with a high  $\Phi_d$  of 31% in PMMA, while enol-related green phosphorescence was detected in PAA with 26%  $\Phi_{ph}$ . Moreover, switching the matrix acidity could make the devised ESIPT triplet emitters undergo switching between their enol and keto forms. The effects of Br and aldehyde on triplet population and triplet emission were further evaluated. Results highlighted unexpected external boosting effects of PAA host on the

phosphorescence efficiency of the embedded brominated ESIPT chromophores. Surprisingly, enol-form Br-HBI exhibited 50%  $\Phi_{ph}$  in PAA matrix. To our best knowledge, BrA-HBI and Br-HBI were among the brightest ESIPT triplet emitters designed so far. Application merits of the prototype ESIPT triplet emitters were explored in the spirit of the keto-enol tautomerization. An on-off switchable system was developed which was responsive to acid vapor by reversibly protonating P4VP matrix. Photo-patterning systems were also developed by taking advantage of the triplet emission chromism of the devised ESIPT chromophores. Bright yellowish green emissive patterns were generated with high contrast.

Chapter III illustrates a new type of light-induced luminescence switching based on the triplet oxygen consumption by UV-light and consequent phosphorescence enhancement of POPs embedded in a-PMMA. Converting ground-state triplet oxygen to singlet oxygen mediated by UV-excited POPs was proposed as the origin of the UV-induced luminescence enhancement of the organic phosphors. Because phosphorescence of POPs with a long emission lifetime is quenched in the presence of oxygen, the observed UV-responsive phosphorescence enhancement is a unique phenomenon pertinent to purely organic phosphors when they are embedded in a polymer matrix having proper oxygen permeability. Visualization of concealed information on such an organic phosphor film by UV-irradiation was demonstrated toward novel secure information communication applications.

Chapter IV presents phosphorescent OLEDs employing a metal-free organic phosphor, BrPFL-TFK. The aromatic carbonyl, spiro-annulated phenyl moieties, and heavy atom effect from bromine in BrPFL-TFK synergistically facilitate efficient ISC and effectively prevent the concentration quenching, allowing bright phosphorescence emission. PPT was identified as the suitable OLED host material for BrPFL-TFK compared to CBP or mCP due to its suppression of exciplex formation and restriction of molecular motion, rendering good color purity and a high phosphorescence yield. OLEDs incorporating BrPFL-TFK and PPT host exhibited 2.5 % maximum EQE at 1 mA/cm<sup>2</sup>.

The millisecond or longer phosphorescence lifetime of POPs detrimentally limit their application for electroluminescence devices. Two major challenges identified are the deficient visualization rationales for molecular descriptors exerting orbital angular momentum and the insufficient interplay between orbital angular momentum manipulation and heavy atom effects. In this regard, the new HAAM molecular design concept is thoroughly discussed in Chapter V. The

HAAM concept enables strategical maximization of the intrinsic SOC of POPs, featuring a synergic interplay among various design descriptors and a more efficient usage of heavy atoms to directly stimulate orbital angular momentum change. The HAAM concept was verified and implemented in a series of prototype POPs capable of emitting “fast and efficient” room-temperature phosphorescence emission with intrinsic SOC efficiencies over  $200 \text{ cm}^{-1}$  and experimental  $\tau_{ph}$  approaching  $200 \mu\text{s}$ , while maintaining near-unity room-temperature  $\Phi_{ph}$ , implying the potential to have similar ISC and phosphorescence efficiencies to their organometallic counterparts. An expanded molecular library is proposed under the HAAM concept to guide the future developments of fast and efficient POPs.

The SOC efficiency of POPs should still be much further enhanced. On one hand, the library of organic heavy atom derivatives and moieties exerting  $\Delta L$  needs to be further expanded. On the other hand, external factors such as external heavy atom effects should be explored as well to build a hybrid system. To address these tasks requires synergetic cooperation among molecular design, chemical synthesis, photophysical analysis, and device physics.

## REFERENCES

- (1) Turro, N. J.; Ramamurthy, V.; Scaiano, J. C. *Modern Molecular Photochemistry of Organic Molecules*, First Indi.; University Science Books: Sausalito, CA, 2012; Vol. 88.
- (2) Schmidbauer, S.; Hohenleutner, A.; König, B. Chemical Degradation in Organic Light-Emitting Devices: Mechanisms and Implications for the Design of New Materials. *Advanced Materials* **2013**, *25* (15), 2114–2129.
- (3) Jeong, C.; Coburn, C.; Idris, M.; Li, Y.; Djurovich, P. I.; Thompson, M. E.; Forrest, S. R. Understanding Molecular Fragmentation in Blue Phosphorescent Organic Light-Emitting Devices. *Organic Electronics* **2019**, *64*, 15–21.
- (4) Mukherjee, S.; Thilagar, P. Recent Advances in Purely Organic Phosphorescent Materials. *Chemical Communications* **2015**, *51* (55), 10988–11003.
- (5) Ma, H.; Lv, A.; Fu, L.; Wang, S.; An, Z.; Shi, H.; Huang, W. Room-Temperature Phosphorescence in Metal-Free Organic Materials. *Annalen der Physik* **2019**, *531* (7), 1800482.
- (6) Nidhankar, A. D.; Goudappagouda; Wakchaure, V. C.; Babu, S. S. Efficient Metal-Free Organic Room Temperature Phosphors. *Chemical Science* **2021**, *12* (12), 4216–4236.
- (7) El-Sayed, M. A. Spin-Orbit Coupling and the Radiationless Processes in Nitrogen Heterocyclics. *The Journal of Chemical Physics* **1963**, *38* (12), 2834–2838.
- (8) Bolton, O.; Lee, K.; Kim, H. J.; Lin, K. Y.; Kim, J. Activating Efficient Phosphorescence from Purely Organic Materials by Crystal Design. *Nature Chemistry* **2011**, *3* (3), 205–210.
- (9) Mao, Z.; Yang, Z.; Mu, Y.; Zhang, Y.; Wang, Y. F.; Chi, Z.; Lo, C. C.; Liu, S.; Lien, A.; Xu, J. Linearly Tunable Emission Colors Obtained from a Fluorescent-Phosphorescent Dual-Emission Compound by Mechanical Stimuli. *Angewandte Chemie - International Edition* **2015**, *54* (21), 6270–6273.
- (10) Lee, D. R.; Lee, K. H.; Shao, W.; Kim, C. L.; Kim, J.; Lee, J. Y. Heavy Atom Effect of Selenium for Metal-Free Phosphorescent Light-Emitting Diodes. *Chemistry of Materials* **2020**, *32* (6), 2583–2592.

- (11) Shao, W.; Jiang, H.; Ansari, R.; Zimmerman, P.; Kim, J. Heavy Atom Oriented Orbital Angular Momentum Manipulation in Metal-Free Organic Phosphors. *Chemical Science* **2022**, *13*, 789–797.
- (12) Kwon, M. S.; Yu, Y.; Coburn, C.; Phillips, A. W.; Chung, K.; Shanker, A.; Jung, J.; Kim, G.; Pipe, K.; Forrest, S. R.; Youk, J. H.; Gierschner, J.; Kim, J. Suppressing Molecular Motions for Enhanced Room-Temperature Phosphorescence of Metal-Free Organic Materials. *Nature Communications* **2015**, *6* (8947).
- (13) Bolton, O.; Lee, D.; Jung, J.; Kim, J. Tuning the Photophysical Properties of Metal-Free Room Temperature Organic Phosphors via Compositional Variations in Bromobenzaldehyde/Dibromobenzene Mixed Crystals. *Chemistry of Materials* **2014**, *26* (22), 6644–6649.
- (14) Lee, D.; Bolton, O.; Kim, B. C.; Youk, J. H.; Takayama, S.; Kim, J. Room Temperature Phosphorescence of Metal-Free Organic Materials in Amorphous Polymer Matrices. *Journal of the American Chemical Society* **2013**, *135* (16), 6325–6329.
- (15) Kwon, M. S.; Lee, D.; Seo, S.; Jung, J.; Kim, J. Tailoring Intermolecular Interactions for Efficient Room-Temperature Phosphorescence from Purely Organic Materials in Amorphous Polymer Matrices. *Angewandte Chemie* **2014**, *126* (42), 11359–11363.
- (16) Murawski, C.; Leo, K.; Gather, M. C. Efficiency Roll-off in Organic Light-Emitting Diodes. *Advanced Materials* **2013**, *25* (47), 6801–6827.
- (17) Kasha, M. Characterization of Electronic Transitions in Complex Molecules. *Discussions of the Faraday Society* **1950**, *9*, 14–19.
- (18) Itoh, T. Fluorescence and Phosphorescence from Higher Excited States of Organic Molecules. *Chemical Reviews* **2012**, *112* (8), 4541–4568.
- (19) Forrest, S. R. *Organic Electronics: Foundations to Applications*; Oxford Scholarship Online, 2020.
- (20) McGlynn, S. P.; Azumi, T.; Kinoshita, M. *Molecular Spectroscopy of the Triplet State*; 1969.
- (21) Yarkony, D. R. Spin-Forbidden Chemistry within the Breit-Pauli Approximation. *International Reviews in Physical Chemistry* **1992**, *11* (2), 195–242.

- (22) Song, B.; Shao, W.; Jung, J.; Yoon, S. J.; Kim, J. Organic Light-Emitting Diode Employing Metal-Free Organic Phosphor. *ACS Applied Materials and Interfaces* **2020**, *12* (5), 6137–6143.
- (23) Dance, Z. E. X.; Mickley, S. M.; Wilson, T. M.; Ricks, A. B.; Scott, A. M.; Ratner, M. A.; Wasielewski, M. R. Intersystem Crossing Mediated by Photoinduced Intramolecular Charge Transfer: Julolidine - Anthracene Molecules with Perpendicular  $\pi$  Systems. *Journal of Physical Chemistry A* **2008**, *112* (18), 4194–4201.
- (24) Wang, J.; Gu, X.; Ma, H.; Peng, Q.; Huang, X.; Zheng, X.; Sung, S. H. P.; Shan, G.; Lam, J. W. Y.; Shuai, Z.; Tang, B. Z. A Facile Strategy for Realizing Room Temperature Phosphorescence and Single Molecule White Light Emission. *Nature Communications* **2018**, *9* (1), 1–9.
- (25) Yu, Y.; Kwon, M. S.; Jung, J.; Zeng, Y.; Kim, M.; Chung, K.; Gierschner, J.; Youk, J. H.; Borisov, S. M.; Kim, J. Room-Temperature-Phosphorescence-Based Dissolved Oxygen Detection by Core-Shell Polymer Nanoparticles Containing Metal-Free Organic Phosphors. *Angewandte Chemie* **2017**, *129* (51), 16425–16429.
- (26) Zhou, Y.; Qin, W.; Du, C.; Gao, H.; Zhu, F.; Liang, G. Long-Lived Room-Temperature Phosphorescence for Visual and Quantitative Detection of Oxygen. *Angewandte Chemie* **2019**, *131* (35), 12230–12234.
- (27) Zhang, G.; Palmer, G. M.; Dewhurst, M. W.; Fraser, C. L. A Dual-Emissive-Materials Design Concept Enables Tumour Hypoxia Imaging. *Nature Materials* **2009**, *8* (9), 747–751.
- (28) Reineke, S.; Baldo, M. A. Room Temperature Triplet State Spectroscopy of Organic Semiconductors. *Scientific Reports* **2014**, *4*.
- (29) Jaehun Jung. Enhancing Room Temperature Phosphorescence from Organic Molecules by Internal Heavy Atom Effect and External Agents, 2018.
- (30) Chen, X.; Xu, C.; Wang, T.; Zhou, C.; Du, J.; Wang, Z.; Xu, H.; Xie, T.; Bi, G.; Jiang, J.; Zhang, X.; Demas, J. N.; Trindle, C. O.; Luo, Y.; Zhang, G. Versatile Room-Temperature-Phosphorescent Materials Prepared from N-Substituted Naphthalimides: Emission Enhancement and Chemical Conjugation. *Angewandte Chemie - International Edition* **2016**, *55* (34), 9872–9876.
- (31) Lucenti, E.; Forni, A.; Botta, C.; Carlucci, L.; Giannini, C.; Marinotto, D.; Pavanello, A.; Previtali, A.; Righetto, S.; Cariati, E. Cyclic Triimidazole Derivatives: Intriguing Examples of

Multiple Emissions and Ultralong Phosphorescence at Room Temperature. *Angewandte Chemie - International Edition* **2017**, *56* (51), 16302–16307.

(32) An, Z.; Zheng, C.; Tao, Y.; Chen, R.; Shi, H.; Chen, T.; Wang, Z.; Li, H.; Deng, R.; Liu, X.; Huang, W. Stabilizing Triplet Excited States for Ultralong Organic Phosphorescence. *Nature Materials* **2015**, *14* (7), 685–690.

(33) Chen, C.; Chi, Z.; Chong, K. C.; Batsanov, A. S.; Yang, Z. Z. Z. Z. Z.; Mao, Z.; Yang, Z. Z. Z. Z. Z.; Liu, B. Carbazole Isomers Induce Ultralong Organic Phosphorescence. *Nature Materials* **2021**, *20* (2), 175–180.

(34) Yang, J.; Zhen, X.; Wang, B.; Gao, X.; Ren, Z.; Wang, J.; Xie, Y.; Li, J.; Peng, Q.; Pu, K.; Li, Z. The Influence of the Molecular Packing on the Room Temperature Phosphorescence of Purely Organic Luminogens. *Nature Communications* **2018**, *9* (1), 1–10.

(35) Xiao, L.; Wu, Y.; Chen, J.; Yu, Z.; Liu, Y.; Yao, J.; Fu, H. Highly Efficient Room-Temperature Phosphorescence from Halogen-Bonding-Assisted Doped Organic Crystals. *Journal of Physical Chemistry A* **2017**, *121* (45), 8652–8658.

(36) Zhang, Z. Y.; Chen, Y.; Liu, Y. Efficient Room-Temperature Phosphorescence of a Solid-State Supramolecule Enhanced by Cucurbit[6]Urils. *Angewandte Chemie - International Edition* **2019**, *58* (18), 6028–6032.

(37) Kremer, A.; Aurisicchio, C.; Deleo, F.; Ventura, B.; Wouters, J.; Armaroli, N.; Barbieri, A.; Bonifazi, D. Walking Down the Chalcogenic Group of the Periodic Table: From Singlet to Triplet Organic Emitters. *Chemistry - A European Journal* **2015**, *21* (43), 15377–15387.

(38) Acharya, R.; Cekli, S.; Zeman, C. J.; Altamimi, R. M.; Schanze, K. S. Effect of Selenium Substitution on Intersystem Crossing in  $\pi$ -Conjugated Donor-Acceptor-Donor Chromophores: The LUMO Matters the Most. *Journal of Physical Chemistry Letters* **2016**, *7* (4), 693–697.

(39) de Sa Pereira, D.; Lee, D. R.; Kukhta, N. A.; Lee, K. H.; Kim, C. L.; Batsanov, A. S.; Lee, J. Y.; Monkman, A. P. The Effect of a Heavy Atom on the Radiative Pathways of an Emitter with Dual Conformation, Thermally-Activated Delayed Fluorescence and Room Temperature Phosphorescence. *Journal of Materials Chemistry C* **2019**, *7* (34), 10481–10490.

(40) Wang, S.; Shu, H.; Han, X.; Wu, X.; Tong, H.; Wang, L.; Paper, S. I. of K.; Wang, S.; Shu, H.; Han, X.; Wu, X.; Tong, H.; Wang, L. A Highly Efficient Purely Organic

Roomtemperature Phosphorescence Film Based on a Selenium-Containing Emitter for Sensitive Oxygen Detection. *Journal of Materials Chemistry C* **2021**, *9* (31), 9907–9913.

(41) Weng, T.; Baryshnikov, G.; Deng, C.; Li, X.; Wu, B.; Wu, H.; Ågren, H.; Zou, Q.; Zeng, T.; Zhu, L. A Fluorescence–Phosphorescence–Phosphorescence Triple-Channel Emission Strategy for Full-Color Luminescence. *Small* **2020**, *1906475*, 1–6.

(42) Riebe, S.; Wölper, C.; Balszuweit, J.; Hayduk, M.; Gutierrez Suburu, M. E.; Strassert, C. A.; Doltsinis, N. L.; Voskuhl, J. Understanding the Role of Chalcogens in Ether-Based Luminophores with Aggregation-Induced Fluorescence and Phosphorescence. *ChemPhotoChem* **2020**, *4* (6), 398–406.

(43) Clark, T.; Hennemann, M.; Murray, J. S.; Politzer, P. Halogen Bonding: The  $\sigma$ -Hole: Proceedings of “Modeling Interactions in Biomolecules II”, Prague, September 5th–9th, 2005. *Journal of Molecular Modeling* **2007**, *13* (2), 291–296.

(44) Wang, W.; Zhang, Y.; Jin, W. J. Halogen Bonding in Room-Temperature Phosphorescent Materials. *Coordination Chemistry Reviews* **2020**, *404*, 213107.

(45) Zhou, B.; Yan, D. Hydrogen-Bonded Two-Component Ionic Crystals Showing Enhanced Long-Lived Room-Temperature Phosphorescence via TADF-Assisted Förster Resonance Energy Transfer. *Advanced Functional Materials* **2019**, *29* (4).

(46) Cheng, Z.; Shi, H.; Ma, H.; Bian, L.; Wu, Q.; Gu, L.; Cai, S.; Wang, X.; Xiong, W. W.; An, Z.; Huang, W. Ultralong Phosphorescence from Organic Ionic Crystals under Ambient Conditions. *Angewandte Chemie - International Edition* **2018**, *57* (3), 678–682.

(47) Yang, X.; Yan, D. Long-Afterglow Metal-Organic Frameworks: Reversible Guest-Induced Phosphorescence Tunability. *Chemical Science* **2016**, *7* (7), 4519–4526.

(48) Wang, Z.; Zhu, C. Y.; Wei, Z. W.; Fan, Y. N.; Pan, M. Breathing-Ignited Long Persistent Luminescence in a Resilient Metal-Organic Framework. *Chemistry of Materials* **2020**, *32* (2), 841–848.

(49) Hu, H.; Meier, F.; Zhao, D.; Abe, Y.; Gao, Y.; Chen, B.; Salim, T.; Chia, E. E. M.; Qiao, X.; Deibel, C.; Lam, Y. M. Efficient Room-Temperature Phosphorescence from Organic–Inorganic Hybrid Perovskites by Molecular Engineering. *Advanced Materials*. 2018.

(50) Yang, S.; Wu, D.; Gong, W.; Huang, Q.; Zhen, H.; Ling, Q.; Lin, Z. Highly Efficient Room-Temperature Phosphorescence and Afterglow Luminescence from Common Organic Fluorophores in 2D Hybrid Perovskites. *Chemical Science* **2018**, *9* (48), 8975–8981.



- (51) Hu, H.; Zhao, D.; Gao, Y.; Qiao, X.; Salim, T.; Chen, B.; Chia, E. E. M.; Grimsdale, A. C.; Lam, Y. M. Harvesting Triplet Excitons in Lead-Halide Perovskites for Room-temperature Phosphorescence. *Chemistry of Materials* **2019**, *31* (7), 2597–2602.
- (52) Feng, S.; Huang, Q.; Yang, S.; Lin, Z.; Ling, Q. A Metal-Free 2D Layered Organic Ammonium Halide Framework Realizing Full-Color Persistent Room-Temperature Phosphorescence. *Chemical Science* **2021**, *12* (43), 14451–14458.
- (53) Yang, S.; Zhou, B.; Huang, Q.; Wang, S.; Zhen, H.; Yan, D.; Lin, Z.; Ling, Q. Highly Efficient Organic Afterglow from a 2D Layered Lead-Free Metal Halide in Both Crystals and Thin Films under an Air Atmosphere. *ACS Applied Materials and Interfaces* **2020**, *12* (1), 1419–1426.
- (54) Mark, J. E. *Physical Properties of Polymers Handbook*; Springer: New York, 2007.
- (55) Ma, X. K.; Liu, Y. Supramolecular Purely Organic Room-Temperature Phosphorescence. *Accounts of Chemical Research* **2021**, *54* (17), 3403–3414.
- (56) Lee, D.; Jung, J.; Bilby, D.; Kwon, M. S.; Yun, J.; Kim, J. A Novel Optical Ozone Sensor Based on Purely Organic Phosphor. *ACS Applied Materials and Interfaces* **2015**, *7* (5), 2993–2997.
- (57) Zhan, G.; Liu, Z.; Bian, Z.; Huang, C. Recent Advances in Organic Light-Emitting Diodes Based on Pure Organic Room Temperature Phosphorescence Materials. *Frontiers in Chemistry* **2019**, *7* (MAY), 1–6.
- (58) Kwon, M. S.; Jordahl, J. H.; Phillips, A. W.; Chung, K.; Lee, S.; Gierschner, J.; Lahann, J.; Kim, J. Multi-Luminescent Switching of Metal-Free Organic Phosphors for Luminometric Detection of Organic Solvents. *Chemical Science* **2016**, *7* (3), 2359–2363.
- (59) Kang, D. H.; Zeng, Y.; Tewari, M.; Kim, J. Highly Sensitive and Quantitative Biodetection with Lipid-Polymer Hybrid Nanoparticles Having Organic Room-Temperature Phosphorescence. *Biosensors and Bioelectronics* **2022**, *199*, 113889.
- (60) Zeng, Y. Organic Room-Temperature Phosphorescence Materials: From Fundamental Triplet Exciton Modulations to Novel Applications in Biosensing and Bioimaging, 2021.
- (61) Gmelch, M.; Thomas, H.; Fries, F.; Reineke, S. Programmable Transparent Organic Luminescent Tags. *Science Advances* **2019**, *5* (2).

- (62) Zang, L.; Shao, W.; Kwon, M. S.; Zhang, Z.; Kim, J. Photoresponsive Luminescence Switching of Metal-Free Organic Phosphors Doped Polymer Matrices. *Advanced Optical Materials* **2020**, *8* (23), 2000654.
- (63) Shi, H.; Zou, L.; Huang, K.; Wang, H.; Sun, C.; Wang, S.; Ma, H.; He, Y.; Wang, J.; Yu, H.; Yao, W.; An, Z.; Zhao, Q.; Huang, W. A Highly Efficient Red Metal-Free Organic Phosphor for Time-Resolved Luminescence Imaging and Photodynamic Therapy. *ACS Applied Materials and Interfaces* **2019**, *11* (20), 18103–18110.
- (64) Jin, J.; Jiang, H.; Yang, Q.; Tang, L.; Tao, Y.; Li, Y.; Chen, R.; Zheng, C.; Fan, Q.; Zhang, K. Y.; Zhao, Q.; Huang, W. Thermally Activated Triplet Exciton Release for Highly Efficient Tri-Mode Organic Afterglow. *Nature Communications* **2020**, *11* (1), 1–9.
- (65) Rothberg, L. J.; Lovinger, A. J. Status of and Prospects for Organic Electroluminescence. *Journal of Materials Research* **1996**, *11* (12), 3174–3187.
- (66) Sarkar, S.; Hendrickson, H. P.; Lee, D.; Devine, F.; Jung, J.; Geva, E.; Kim, J.; Dunietz, B. D. Phosphorescence in Bromobenzaldehyde Can Be Enhanced through Intramolecular Heavy Atom Effect. *Journal of Physical Chemistry C* **2017**, *121* (7), 3771–3777.
- (67) Uoyama, H.; Goushi, K.; Shizu, K.; Nomura, H.; Adachi, C. Highly Efficient Organic Light-Emitting Diodes from Delayed Fluorescence. *Nature* **2012**, *492* (7428), 234–238.
- (68) Kukhta, N. A.; Bryce, M. R. Dual Emission in Purely Organic Materials for Optoelectronic Applications. *Materials Horizons* **2021**, *8* (1), 33–55.
- (69) Padalkar, V. S.; Seki, S. Excited-State Intramolecular Proton-Transfer (ESIPT)-Inspired Solid State Emitters. *Chemical Society Reviews* **2016**, *45* (1), 169–202.
- (70) McMorro, D.; Kasha, M. Proton-Transfer Spectroscopy of 3-Hydroxychromones. Extreme Sensitivity to Hydrogen-Bonding Perturbations. *Journal of the American Chemical Society* **1983**, *105* (15), 5133–5134.
- (71) Kasha, M. Proton-Transfer Spectroscopy. Perturbation of the Tautomerization Potential. *Journal of the Chemical Society, Faraday Transactions 2: Molecular and Chemical Physics* **1986**, *82* (12), 2379–2392.
- (72) van Benthem, M. H.; Gillispie, G. D. Intramolecular Hydrogen Bonding. 4. Dual Fluorescence and Excited-State Proton Transfer in 1,5-Dihydroxyanthraquinone. *Journal of Physical Chemistry* **1984**, *88* (14), 2954–2960.

- (73) Massue, J.; Jacquemin, D.; Ulrich, G. Molecular Engineering of Excited-State Intramolecular Proton Transfer (ESIPT) Dual and Triple Emitters. *Chemistry Letters* **2018**, *47* (9), 1083–1089.
- (74) Heyer, E.; Benelhadj, K.; Budzák, S.; Jacquemin, D.; Massue, J.; Ulrich, G. On the Fine-Tuning of the Excited-State Intramolecular Proton Transfer (ESIPT) Process in 2-(2'-Hydroxybenzofuran)Benzazole (HBBX) Dyes. *Chemistry - A European Journal* **2017**, *23* (30), 7324–7336.
- (75) Benelhadj, K.; Muzuzu, W.; Massue, J.; Retailleau, P.; Charaf-Eddin, A.; Laurent, A. D.; Jacquemin, D.; Ulrich, G.; Ziessel, R. White Emitters by Tuning the Excited-State Intramolecular Proton-Transfer Fluorescence Emission in 2-(2-Hydroxybenzofuran)Benzoxazole Dyes. *Chemistry - A European Journal* **2014**, *20* (40), 12843–12857.
- (76) Tang, K. C.; Chang, M. J.; Lin, T. Y.; Pan, H. A.; Fang, T. C.; Chen, K. Y.; Hung, W. Y.; Hsu, Y. H.; Chou, P. T. Fine Tuning the Energetics of Excited-State Intramolecular Proton Transfer (ESIPT): White Light Generation in a Single ESIPT System. *Journal of the American Chemical Society* **2011**, *133* (44), 17738–17745.
- (77) Halder, S.; Chakraborty, D.; Roy, B.; Banappanavar, G.; Rinku, K.; Mullangi, D.; Hazra, P.; Kabra, D.; Vaidhyanathan, R. Anthracene-Resorcinol Derived Covalent Organic Framework as Flexible White Light Emitter. *Journal of the American Chemical Society* **2018**, *140* (41), 13367–13374.
- (78) Wu, K.; Zhang, T.; Wang, Z.; Wang, L.; Zhan, L.; Gong, S.; Zhong, C.; Lu, Z. H.; Zhang, S.; Yang, C. De Novo Design of Excited-State Intramolecular Proton Transfer Emitters via a Thermally Activated Delayed Fluorescence Channel. *Journal of the American Chemical Society* **2018**, *140* (28), 8877–8886.
- (79) Mamada, M.; Inada, K.; Komino, T.; Potsavage, W. J.; Nakanotani, H.; Adachi, C. Highly Efficient Thermally Activated Delayed Fluorescence from an Excited-State Intramolecular Proton Transfer System. *ACS Central Science* **2017**, *3* (7), 769–777.
- (80) Gupta, A. K.; Li, W.; Ruseckas, A.; Lian, C.; Carpenter-Warren, C. L.; Cordes, D. B.; Slawin, A. M. Z.; Jacquemin, D.; Samuel, I. D. W.; Zysman-Colman, E. Thermally Activated Delayed Fluorescence Emitters with Intramolecular Proton Transfer for High Luminance Solution-Processed Organic Light-Emitting Diodes. *ACS Applied Materials and Interfaces* **2021**, *13* (13), 15459–15474.

- (81) Long, Y.; Mamada, M.; Li, C.; dos Santos, P. L.; Colella, M.; Danos, A.; Adachi, C.; Monkman, A. Excited State Dynamics of Thermally Activated Delayed Fluorescence from an Excited State Intramolecular Proton Transfer System. *Journal of Physical Chemistry Letters* **2020**, *11* (9), 3305–3312.
- (82) Berezin, A. S.; Vinogradova, K. A.; Krivopalov, V. P.; Nikolaenkova, E. B.; Plyusnin, V. F.; Kupryakov, A. S.; Pervukhina, N. v.; Naumov, D. Y.; Bushuev, M. B. Excitation-Wavelength-Dependent Emission and Delayed Fluorescence in a Proton-Transfer System. *Chemistry - A European Journal* **2018**, *24* (49), 12790–12795.
- (83) Cao, Y.; Eng, J.; Penfold, T. J. Excited State Intramolecular Proton Transfer Dynamics for Triplet Harvesting in Organic Molecules. *Journal of Physical Chemistry A* **2019**, *123* (13), 2640–2649.
- (84) Khisamov, R. M.; Ryadun, A. A.; Sukhikh, T. S.; Konchenko, S. N. Excitation Wavelength-Dependent Room-Temperature Phosphorescence: Unusual Properties of Novel Phosphinoamines. *Molecular Systems Design & Engineering* **2021**.
- (85) Liang, F.; Wang, L.; Ma, D.; Jing, X.; Wang, F. Oxadiazole-Containing Material with Intense Blue Phosphorescence Emission for Organic Light-Emitting Diodes. *Applied Physics Letters* **2002**, *81* (1), 4–6.
- (86) Sahoo, D.; Adhikary, T.; Chowdhury, P.; Roy, S. C.; Chakravorti, S. Understanding the Photophysics of 4-Nitro-1-Hydroxy-2-Naphthoic Acid: A Controlled Excited State Proton Transfer. *Chemical Physics* **2008**, *352* (1–3), 175–184.
- (87) Hagiri, M.; Ichinose, N.; Kinugasa, J. I.; Iwasa, T.; Nakayama, T. Excited-State Intramolecular Proton Transfer (ESIPT)-Type Phosphorescence of 2-Aminobenzophenone in 77 K Matrices. *Chemistry Letters* **2004**, *33* (3), 326–327.
- (88) Saigusa, H.; Azumi, T. Internal Heavy Atom Effect on the Triplet Spin Sublevels of the Lowest Triplet State of Naphthalene. I. Radiative and Nonradiative Decays of the Spin Sublevels of 1-Halonaphthalenes. *The Journal of Chemical Physics* **1979**, *71* (3), 1408–1413.
- (89) Chien, A. D.; Zimmerman, P. M. Recovering Dynamic Correlation in Spin Flip Configuration Interaction through a Difference Dedicated Approach. *Journal of Chemical Physics* **2017**, *146* (1), 014103.

- (90) Bell, F.; Zimmerman, P. M.; Casanova, D.; Goldey, M.; Head-Gordon, M. Restricted Active Space Spin-Flip (RAS-SF) with Arbitrary Number of Spin-Flips. *Physical Chemistry Chemical Physics* **2013**, *15* (1), 358–366.
- (91) Zimmerman, P. M.; Bell, F.; Goldey, M.; Bell, A. T.; Head-Gordon, M. Restricted Active Space Spin-Flip Configuration Interaction: Theory and Examples for Multiple Spin Flips with Odd Numbers of Electrons. *Journal of Chemical Physics* **2012**, *137* (16), 164110.
- (92) Jiang, H.; Zimmerman, P. M. Charge Transfer via Spin Flip Configuration Interaction: Benchmarks and Application to Singlet Fission. *Journal of Chemical Physics* **2020**, *153* (6), 064109.
- (93) Casanova, D.; Head-Gordon, M. Restricted Active Space Spin-Flip Configuration Interaction Approach: Theory, Implementation and Examples. *Physical Chemistry Chemical Physics* **2009**, *11* (42), 9779–9790.
- (94) Krylov, A. I. Size-Consistent Wave Functions for Bond-Breaking: The Equation-of-Motion Spin-Flip Model. *Chemical Physics Letters* **2001**, *338* (4–6), 375–384.
- (95) Krylov, A. I. Spin-Flip Configuration Interaction: An Electronic Structure Model That Is Both Variational and Size-Consistent. *Chemical Physics Letters* **2001**, *350* (5–6), 522–530.
- (96) Bolton, O.; Lee, K.; Kim, H. J.; Lin, K. Y.; Kim, J. Activating Efficient Phosphorescence from Purely Organic Materials by Crystal Design. *Nature Chemistry* **2011**, *3* (3), 205–210.
- (97) Ma, H.; Peng, Q.; An, Z.; Huang, W.; Shuai, Z. Efficient and Long-Lived Room-Temperature Organic Phosphorescence: Theoretical Descriptors for Molecular Designs. *Journal of the American Chemical Society* **2019**, *141* (2), 1010–1015.
- (98) Gibson, J.; Monkman, A. P.; Penfold, T. J. The Importance of Vibronic Coupling for Efficient Reverse Intersystem Crossing in Thermally Activated Delayed Fluorescence Molecules. *ChemPhysChem* **2016**, No. 1, 2956–2961.
- (99) Evans, E. W.; Olivier, Y.; Puttisong, Y.; Myers, W. K.; Hele, T. J. H.; Menke, S. M.; Thomas, T. H.; Credgington, D.; Beljonne, D.; Friend, R. H.; Greenham, N. C. Vibrationally Assisted Intersystem Crossing in Benchmark Thermally Activated Delayed Fluorescence Molecules. *Journal of Physical Chemistry Letters* **2018**, *9* (14), 4053–4058.

- (100) Gibson, J.; Penfold, T. J. Nonadiabatic Coupling Reduces the Activation Energy in Thermally Activated Delayed Fluorescence. *Physical Chemistry Chemical Physics* **2017**, *19* (12), 8428–8434.
- (101) Kim, I.; Jeon, S. O.; Jeong, D.; Choi, H.; Son, W. J.; Kim, D.; Rhee, Y. M.; Lee, H. S. Spin-Vibronic Model for Quantitative Prediction of Reverse Intersystem Crossing Rate in Thermally Activated Delayed Fluorescence Systems. *Journal of Chemical Theory and Computation*. 2020, pp 621–632.
- (102) Etherington, M. K.; Gibson, J.; Higginbotham, H. F.; Penfold, T. J.; Monkman, A. P. Revealing the Spin-Vibronic Coupling Mechanism of Thermally Activated Delayed Fluorescence. *Nature Communications* **2016**, *7*, 1–7.
- (103) Hosokai, T.; Noda, H.; Nakanotani, H.; Nawata, T.; Nakayama, Y.; Matsuzaki, H.; Adachi, C. Solvent-Dependent Investigation of Carbazole Benzonitrile Derivatives: Does the LE3–CT1 Energy Gap Facilitate Thermally Activated Delayed Fluorescence? *Journal of Photonics for Energy* **2018**, *8* (03), 1.
- (104) Zhu, Y.; Guan, Y.; Niu, Y.; Wang, P. P. P.; Chen, R.; Wang, Y.; Wang, P. P. P.; Xie, H. Iou. Ultralong Polymeric Room Temperature Phosphorescence Materials Fabricated by Multiple Hydrogen Bondings Resistant to Temperature and Humidity. *Advanced Optical Materials* **2021**, *2100782*, 1–9.
- (105) Ma, T.; Li, T.; Zhou, L.; Ma, X.; Yin, J.; Jiang, X. Dynamic Wrinkling Pattern Exhibiting Tunable Fluorescence for Anticounterfeiting Applications. *Nature Communications* **2020**, *11* (1), 1–8.
- (106) Zhao, S.; Ma, H.; Wang, M.; Cao, C.; Xiong, J.; Xu, Y.; Yao, S. Role of Primary Reaction Initiated by 254 Nm UV Light in the Degradation of P-Nitrophenol Attacked by Hydroxyl Radicals. *Photochemical and Photobiological Sciences* **2010**, *9* (5), 710–715.
- (107) Epifanovsky, E.; Gilbert, A. T. B.; Feng, X.; Lee, J.; Mao, Y.; Mardirossian, N.; Pokhilko, P.; White, A. F.; Coons, M. P.; Dempwolff, A. L.; Gan, Z.; Hait, D.; Horn, P. R.; Jacobson, L. D.; Kaliman, I.; Kussmann, J.; Lange, A. W.; Lao, K. U.; Levine, D. S.; Liu, J.; McKenzie, S. C.; Morrison, A. F.; Nanda, K. D.; Plasser, F.; Rehn, D. R.; Vidal, M. L.; You, Z. Q.; Zhu, Y.; Alam, B.; Albrecht, B. J.; Aldossary, A.; Alguire, E.; Andersen, J. H.; Athavale, V.; Barton, D.; Begam, K.; Behn, A.; Bellonzi, N.; Bernard, Y. A.; Berquist, E. J.; Burton, H. G. A.; Carreras, A.; Carter-Fenk, K.; Chakraborty, R.; Chien, A. D.; Closser, K. D.; Cofer-Shabica, V.; Dasgupta, S.; de

Wergifosse, M.; Deng, J.; Diedenhofen, M.; Do, H.; Ehlert, S.; Fang, P. T.; Fatehi, S.; Feng, Q.; Friedhoff, T.; Gayvert, J.; Ge, Q.; Gidofalvi, G.; Goldey, M.; Gomes, J.; González-Espinoza, C. E.; Gulania, S.; Gunina, A. O.; Hanson-Heine, M. W. D.; Harbach, P. H. P.; Hauser, A.; Herbst, M. F.; Hernández Vera, M.; Hodecker, M.; Holden, Z. C.; Houck, S.; Huang, X.; Hui, K.; Huynh, B. C.; Ivanov, M.; Jász, Á.; Ji, H.; Jiang, H.; Kaduk, B.; Kähler, S.; Khistyayev, K.; Kim, J.; Kis, G.; Klunzinger, P.; Koczor-Benda, Z.; Koh, J. H.; Kosenkov, D.; Koulias, L.; Kowalczyk, T.; Krauter, C. M.; Kue, K.; Kunitsa, A.; Kus, T.; Ladjánszki, I.; Landau, A.; Lawler, K. v.; Lefrancois, D.; Lehtola, S.; Li, R. R.; Li, Y. P.; Liang, J.; Liebenthal, M.; Lin, H. H.; Lin, Y. S.; Liu, F.; Liu, K. Y.; Loipersberger, M.; Luenser, A.; Manjanath, A.; Manohar, P.; Mansoor, E.; Manzer, S. F.; Mao, S. P.; Marenich, A. v.; Markovich, T.; Mason, S.; Maurer, S. A.; McLaughlin, P. F.; Menger, M. F. S. J.; Mewes, J. M.; Mewes, S. A.; Morgante, P.; Mullinax, J. W.; Oosterbaan, K. J.; Paran, G.; Paul, A. C.; Paul, S. K.; Pavošević, F.; Pei, Z.; Prager, S.; Proynov, E. I.; Rák, Á.; Ramos-Cordoba, E.; Rana, B.; Rask, A. E.; Rettig, A.; Richard, R. M.; Rob, F.; Rossomme, E.; Scheele, T.; Scheurer, M.; Schneider, M.; Sergueev, N.; Sharada, S. M.; Skomorowski, W.; Small, D. W.; Stein, C. J.; Su, Y. C.; Sundstrom, E. J.; Tao, Z.; Thirman, J.; Tornai, G. J.; Tsuchimochi, T.; Tubman, N. M.; Veccham, S. P.; Vydrov, O.; Wenzel, J.; Witte, J.; Yamada, A.; Yao, K.; Yeganeh, S.; Yost, S. R.; Zech, A.; Zhang, I. Y.; Zhang, X.; Zhang, Y.; Zuev, D.; Aspuru-Guzik, A.; Bell, A. T.; Besley, N. A.; Bravaya, K. B.; Brooks, B. R.; Casanova, D.; Chai, J. da; Coriani, S.; Cramer, C. J.; Cserey, G.; Deprince, A. E.; Distasio, R. A.; Dreuw, A.; Dunietz, B. D.; Furlani, T. R.; Goddard, W. A.; Hammes-Schiffer, S.; Head-Gordon, T.; Hehre, W. J.; Hsu, C. P.; Jagau, T. C.; Jung, Y.; Klamt, A.; Kong, J.; Lambrecht, D. S.; Liang, W.; Mayhall, N. J.; McCurdy, C. W.; Neaton, J. B.; Ochsenfeld, C.; Parkhill, J. A.; Peverati, R.; Rassolov, V. A.; Shao, Y.; Slipchenko, L. v.; Stauch, T.; Steele, R. P.; Subotnik, J. E.; Thom, A. J. W.; Tkatchenko, A.; Truhlar, D. G.; van Voorhis, T.; Wesolowski, T. A.; Whaley, K. B.; Woodcock, H. L.; Zimmerman, P. M.; Faraji, S.; Gill, P. M. W.; Head-Gordon, M.; Herbert, J. M.; Krylov, A. I.

Software for the Frontiers of Quantum Chemistry: An Overview of Developments in the Q-Chem 5 Package. *Journal of Chemical Physics* **2021**, *155* (8), 084801. (108)

Hariharan, P. C.; Pople, J. A. The Influence of Polarization Functions on Molecular Orbital Hydrogenation Energies. *Theoretica Chimica Acta* **1973**, *28* (3), 213–222.

- (109) Bernholdt, D. E.; Harrison, R. J. Fitting Basis Sets for the RI-MP2 Approximate Second-Order Many-Body Perturbation Theory Method. *Journal of Chemical Physics* **1998**, *109* (5), 1593–1600.
- (110) Grimme, S. Semiempirical GGA-Type Density Functional Constructed with a Long-Range Dispersion Correction. *Journal of Computational Chemistry* **2006**, *27* (15), 1787–1799.
- (111) Weigend, F.; Ahlrichs, R. Balanced Basis Sets of Split Valence, Triple Zeta Valence and Quadruple Zeta Valence Quality for H to Rn: Design and Assessment of Accuracy. *Physical Chemistry Chemical Physics* **2005**, *7* (18), 3297–3305.
- (112) Pokhilko, P.; Epifanovsky, E.; Krylov, A. I. General Framework for Calculating Spin-Orbit Couplings Using Spinless One-Particle Density Matrices: Theory and Application to the Equation-of-Motion Coupled-Cluster Wave Functions. *Journal of Chemical Physics* **2019**, *151* (3).
- (113) Plasser, F.; Wormit, M.; Dreuw, A. New Tools for the Systematic Analysis and Visualization of Electronic Excitations. I. Formalism. *Journal of Chemical Physics* **2014**, *141* (2), 024106.
- (114) Schaftenaar, G.; Noordik, J. H. Molden: A Pre- and Post-Processing Program for Molecular and Electronic Structures. *Journal of Computer-Aided Molecular Design* **2000**, *14* (2), 123–134.
- (115) Liang, F.; Wang, L.; Ma, D.; Jing, X.; Wang, F. Oxadiazole-Containing Material with Intense Blue Phosphorescence Emission for Organic Light-Emitting Diodes. *Applied Physics Letters* **2002**, *81* (1), 4–6.
- (116) Seo, J.; Kim, S.; Lee, Y. S.; Kwon, O. H.; Park, K. H.; Choi, S. Y.; Chung, Y. K.; Jang, D. J.; Park, S. Y. Enhanced Solid-State Fluorescence in the Oxadiazole-Based Excited-State Intramolecular Proton-Transfer (ESIPT) Material: Synthesis, Optical Property, and Crystal Structure. *Journal of Photochemistry and Photobiology A: Chemistry* **2007**, *191* (1), 51–58.
- (117) Park, S. S. Y. S.; Kwon, O. H.; Lee, Y. S.; Jang, D. J.; Park, S. S. Y. S. Imidazole-Based Excited-State Intramolecular Proton-Transfer (ESIPT) Materials: Observation of Thermally Activated Delayed Fluorescence (TDF). *Journal of Physical Chemistry A* **2007**, *111* (39), 9649–9653.
- (118) Wang, G.; Zhang, J. Photoresponsive Molecular Switches for Biotechnology. *Journal of Photochemistry and Photobiology C: Photochemistry Reviews* **2012**, *13* (4), 299–309.



- (119) Irie, M.; Fukaminato, T.; Matsuda, K.; Kobatake, S. Photochromism of Diarylethene Molecules and Crystals: Memories, Switches, and Actuators. *Chemical Reviews* **2014**, *114* (24), 12174–12277.
- (120) Nakagawa, T.; Hasegawa, Y.; Kawai, T. Photoresponsive Europium(III) Complex Based on Photochromic Reaction. *Journal of Physical Chemistry A* **2008**, *112* (23), 5096–5103.
- (121) Yildiz, I.; Deniz, E.; Raymo, F. M. Fluorescence Modulation with Photochromic Switches in Nanostructured Constructs. *Chemical Society Reviews* **2009**, *38* (7), 1859–1867.
- (122) Kuno, S.; Akeno, H.; Ohtani, H.; Yuasa, H. Visible Room-Temperature Phosphorescence of Pure Organic Crystals via a Radical-Ion-Pair Mechanism. *Physical Chemistry Chemical Physics* **2015**, *17* (24), 15989–15995.
- (123) Tan, W.; Zhang, Q.; Zhang, J.; Tian, H. Near-Infrared Photochromic Diarylethene Iridium (III) Complex. *Organic Letters* **2009**, *11* (1), 161–164.
- (124) Nakai, H.; Kitagawa, K.; Nakamori, H.; Tokunaga, T.; Matsumoto, T.; Nozaki, K.; Ogo, S. Reversible Switching of the Luminescence of a Photoresponsive Gadolinium(III) Complex. *Angewandte Chemie* **2013**, *125* (33), 8884–8887.
- (125) Wang, C.; Yuan, Y.; Li, S. Y.; Sun, Z. B.; Jiang, Z. Q.; Zhao, C. H. A Highly Twisted Triarylborane-Based Biphenyl as an Efficient Host for Blue and Green Phosphorescent OLEDs. *Journal of Materials Chemistry C* **2016**, *4* (32), 7607–7613.
- (126) Xu, W. J.; Liu, S. J.; Zhao, X.; Zhao, N.; Liu, Z. Q.; Xu, H.; Liang, H.; Zhao, Q.; Yu, X. Q.; Huang, W. Synthesis, One- and Two-Photon Photophysical and Excited-State Properties, and Sensing Application of a New Phosphorescent Dinuclear Cationic Iridium(III) Complex. *Chemistry - A European Journal* **2013**, *19* (2), 621–629.
- (127) Yuan, W. Z.; Shen, X. Y.; Zhao, H.; Lam, J. W. Y.; Tang, L.; Lu, P.; Wang, C.; Liu, Y.; Wang, Z.; Zheng, Q.; Sun, J. Z.; Ma, Y.; Tang, B. Z. Crystallization-Induced Phosphorescence of Pure Organic Luminogens at Room Temperature. *Journal of Physical Chemistry C* **2010**, *114* (13), 6090–6099.
- (128) Hirata, S. Recent Advances in Materials with Room-Temperature Phosphorescence: Photophysics for Triplet Exciton Stabilization. *Advanced Optical Materials* **2017**, *5* (17), 1700116.

- (129) Wang, H.; Wang, H.; Yang, X.; Wang, Q.; Yang, Y. Ion-Unquenchable and Thermally “on-Off” Reversible Room Temperature Phosphorescence of 3-Bromoquinoline Induced by Supramolecular Gels. *Langmuir* **2015**, *31* (1), 486–491.
- (130) Bergamini, G.; Fermi, A.; Botta, C.; Giovanella, U.; di Motta, S.; Negri, F.; Peresutti, R.; Gingras, M.; Ceroni, P. A Persulfurated Benzene Molecule Exhibits Outstanding Phosphorescence in Rigid Environments: From Computational Study to Organic Nanocrystals and OLED Applications. *Journal of Materials Chemistry C* **2013**, *1* (15), 2717–2724.
- (131) Hirata, S.; Vacha, M. Circularly Polarized Persistent Room-Temperature Phosphorescence from Metal-Free Chiral Aromatics in Air. *Journal of Physical Chemistry Letters* **2016**, *7* (8), 1539–1545.
- (132) Abrahamse, H.; Hamblin, M. R. New Photosensitizers for Photodynamic Therapy. *Biochemical Journal* **2016**, *473* (4), 347–364.
- (133) Kisku, S. K.; Swain, S. K. Study of Oxygen Permeability and Flame Retardancy Properties of Biodegradable Polymethylmethacrylate/Starch Composites. *Polymer Composites* **2012**, *33* (1), 79–84.
- (134) Allonas, X.; Fouassier, J. P.; Angiolini, L.; Caretti, D. Excited-State Properties of Camphorquinone Based Monomeric and Polymeric Photoinitiators. *Helvetica Chimica Acta* **2001**, *84* (9), 2577–2588.
- (135) Marsico, F.; Turshatov, A.; Peköz, R.; Avlasevich, Y.; Wagner, M.; Weber, K.; Donadio, D.; Landfester, K.; Balushev, S.; Wurm, F. R. Hyperbranched Unsaturated Polyphosphates as a Protective Matrix for Long-Term Photon Upconversion in Air. *Journal of the American Chemical Society* **2014**, *136* (31), 11057–11064.
- (136) Chirinos Padrón, A. J. Mechanistic Aspects of Polymer Photostabilization. *Journal of Photochemistry and Photobiology, A: Chemistry* **1989**, *49* (1–2), 1–39.
- (137) Bilen, C. S.; Morantz, D. J. Confirmation of the Role of Radicals in Energy Transfer Resulting in Induced Phosphorescence of Irradiated Doped Poly(Methyl Methacrylate). *Polymer* **1976**, *17* (12), 1091–1094.
- (138) Morantz, D. J.; Bilen, C. S. Thermoluminescence and Induced Phosphorescence in Irradiated Doped PMMA. *Polymer* **1975**, *16* (10), 745–748.
- (139) Peyrot, D. A.; Aptel, F.; Crotti, C.; Deloison, F.; Lemaire, S.; Marciano, T.; Bancelin, S.; Alahyane, F.; Kowalczyk, L.; Savoldelli, M.; Legeais, J. M.; Plamann, K. Effect of Incident

Light Wavelength and Corneal Edema on Light Scattering and Penetration: Laboratory Study of Human Corneas. *Journal of Refractive Surgery* **2010**, *26* (10), 786–795.

(140) Quaranta, M.; Borisov, S. M.; Klimant, I. Indicators for Optical Oxygen Sensors. *Bioanalytical Reviews* **2012**, *4* (2–4), 115–157.

(141) Pang, Y.; Cui, Y.; Ma, Y.; Qian, H.; Shen, X. Fluorescence Quenching of Cationic Organic Dye by Graphene: Interaction and Its Mechanism. *Micro and Nano Letters* **2012**, *7* (7), 608–612.

(142) Martínez, V. M.; Arbeloa, F. L.; Prieto, J. B.; Arbeloa, I. L. Characterization of Rhodamine 6G Aggregates Intercalated in Solid Thin Films of Laponite Clay. 2 Fluorescence Spectroscopy. *Journal of Physical Chemistry B* **2005**, *109* (15), 7443–7450.

(143) Shen, X.; Lu, W.; Feng, G.; Yao, Y.; Chen, W. Preparation and Photoactivity of a Novel Water-Soluble, Polymerizable Zinc Phthalocyanine. *Journal of Molecular Catalysis A: Chemical* **2009**, *298* (1–2), 17–22.

(144) Papkovsky, D. B.; Dmitriev, R. I. Biological Detection by Optical Oxygen Sensing. *Chemical Society Reviews* **2013**, *42* (22), 8700–8732.

(145) Xu, J.; Takai, A.; Kobayashi, Y.; Takeuchi, M. Phosphorescence From a Pure Organic Fluorene Derivative in Solution at Room Temperature. *Chemical Communications* **2013**, *49* (76), 8447–8449.

(146) Deng, H.; Yu, C.; Gong, L.; Zhu, X. Self-Restricted Green Fluorescent Protein Chromophore Analogues: Dramatic Emission Enhancement and Remarkable Solvatochromism. *Journal of Physical Chemistry Letters* **2016**, *7* (15), 2935–2944.

(147) Waser, R. *Nanoelectronics and Information Technology*; Wiley-VCH, 2012.

(148) Baldo, M. A.; Thompson, M. E.; Forrest, S. R. High-Efficiency Fluorescent Organic Light-Emitting Devices Using a Phosphorescent Sensitizer. *Nature* **2000**, *403* (6771), 750–753.

(149) Adachi, C.; Baldo, M. A.; Thompson, M. E.; Forrest, S. R. Nearly 100% Internal Phosphorescence Efficiency in an Organic Light Emitting Device. *Journal of Applied Physics* **2001**, *90* (10), 5048–5051.

(150) Baldo, M. A.; O'Brien, D. F.; You, Y.; Shoustikov, A.; Sibley, S.; Thompson, M. E.; Forrest, S. R. Highly Efficient Phosphorescent Emission from Organic Electroluminescent Devices. *Nature* **1998**, *395* (6698), 151–154.

- (151) Baranoff, E.; Curchod, B. F. E.; Frey, J.; Scopelliti, R.; Kessler, F.; Tavernelli, I.; Rothlisberger, U.; Grätzel, M.; Nazeeruddin, M. K. Acid-Induced Degradation of Phosphorescent Dopants for OLEDs and Its Application to the Synthesis of Tris-Heteroleptic Iridium(III) Bis-Cyclometalated Complexes. *Inorganic Chemistry* **2012**, *51* (1), 215–224.
- (152) Chaudhuri, D.; Wettach, H.; van Schooten, K. J.; Liu, S.; Sigmund, E.; Höger, S.; Lupton, J. M. Tuning the Singlet-Triplet Gap in Metal-Free Phosphorescent  $\pi$ -Conjugated Polymers. *Angewandte Chemie - International Edition* **2010**, *49* (42), 7714–7717.
- (153) Shen, Q. J.; Pang, X.; Zhao, X. R.; Gao, H. Y.; Sun, H. L.; Jin, W. J. Phosphorescent Cocrystals Constructed by 1,4-Diodotetrafluorobenzene and Polyaromatic Hydrocarbons Based on C-I $\cdots$  $\pi$  Halogen Bonding and Other Assisting Weak Interactions. *CrystEngComm* **2012**, *14* (15), 5027–5034.
- (154) Anzenbacher, P.; Pérez-Bolívar, C.; Takizawa, S. ya; Brega, V. Room-Temperature Electrophosphorescence from an All-Organic Material. *Journal of Luminescence* **2016**, *180*, 111–116.
- (155) Lower, S. K.; El-Sayed, M. A. The Triplet State and Molecular Electronic Processes in Organic Molecules. *Chemical Reviews* **1966**, *66* (2), 199–241.
- (156) El-Sayed, M. A. The Triplet State: Its Radiative and Nonradiative Properties. *Accounts of Chemical Research* **1968**, *1* (1), 8–16.
- (157) Baba, M. Intersystem Crossing in the  $1n\pi^*$  and  $1\pi\pi^*$  States. *Journal of Physical Chemistry A* **2011**, *115* (34), 9514–9519.
- (158) Ma, H.; Peng, Q.; An, Z.; Huang, W.; Shuai, Z. Efficient and Long-Lived Room-Temperature Organic Phosphorescence: Theoretical Descriptors for Molecular Designs. *Journal of the American Chemical Society* **2019**, *141* (2), 1010–1015.
- (159) Huang, W. Y.; Chang, M. Y.; Han, Y. K.; Huang, P. T. Sterically Encumbered Poly(Arylene Ether)s Containing Spiro-Annulated Substituents: Synthesis and Thermal Properties. *Journal of Polymer Science, Part A: Polymer Chemistry* **2010**, *48* (24), 5872–5884.
- (160) Al-Attar, H. A.; Monkman, A. P. Room-Temperature Phosphorescence from Films of Isolated Water-Soluble Conjugated Polymers in Hydrogen-Bonded Matrices. *Advanced Functional Materials* **2012**, *22* (18), 3824–3832.

- (161) Jeong, S. H.; Lee, J. Y. Dibenzothiophene Derivatives as Host Materials for High Efficiency in Deep Blue Phosphorescent Organic Light Emitting Diodes. *Journal of Materials Chemistry* **2011**, *21* (38), 14604–14609.
- (162) Gong, M. S.; Cha, J. R.; Lee, C. W. Synthesis and Device Properties of MCP Analogues Based on Fused-Ring Carbazole Moiety. *Organic Electronics* **2017**, *42*, 66–74.
- (163) Zhang, T.; Liang, Y.; Cheng, J.; Li, J. A CBP Derivative as Bipolar Host for Performance Enhancement in Phosphorescent Organic Light-Emitting Diodes. *Journal of Materials Chemistry C* **2013**, *1* (4), 757–764.
- (164) Kröger, M.; Hamwi, S.; Meyer, J.; Riedl, T.; Kowalsky, W.; Kahn, A. P-Type Doping of Organic Wide Band Gap Materials by Transition Metal Oxides: A Case-Study on Molybdenum Trioxide. *Organic Electronics* **2009**, *10* (5), 932–938.
- (165) Adachi, C.; Baldo, M. A.; Forrest, S. R. Electroluminescence Mechanisms in Organic Light Emitting Devices Employing a Europium Chelate Doped in a Wide Energy Gap Bipolar Conducting Host. *Journal of Applied Physics* **2000**, *87* (11), 8049–8055.
- (166) Frisch, M. J.; Trucks, G. W.; Schlegel, H. B.; Scuseria, G. E.; Robb, M. A.; Cheeseman, J. R.; Scalmani, G.; Barone, V.; Mennucci, B.; Petersson, G. A.; Nakatsuji, H.; Caricato, M.; Li, X.; Hratchian, H. P.; Izmaylov, A. F.; Bloino, J.; Zheng, G.; Sonnenberg, J. L.; Had, M.; Fox, D. J. Gaussian 09. Gaussian, Inc., Wallingford CT 2009.
- (167) Becke, A. D. Density-Functional Thermochemistry. III. The Role of Exact Exchange. *The Journal of Chemical Physics* **1993**, *98* (7), 5648–5652.
- (168) Stephens, P. J.; Devlin, F. J.; Chabalowski, C. F.; Frisch, M. J. Ab Initio Calculation of Vibrational Absorption and Circular Dichroism Spectra Using Density Functional Force Fields. *Journal of Physical Chemistry* **1994**, *98* (45), 11623–11627.
- (169) Dunning, T. H. Gaussian Basis Sets for Use in Correlated Molecular Calculations. I. The Atoms Boron through Neon and Hydrogen. *The Journal of Chemical Physics* **1989**, *90* (2), 1007–1023.
- (170) Aidas, K.; Angeli, C.; Bak, K. L.; Bakken, V.; Bast, R.; Boman, L.; Christiansen, O.; Cimiraglia, R.; Coriani, S.; Dahle, P.; Dalskov, E. K.; Ekström, U.; Enevoldsen, T.; Eriksen, J. J.; Ettenhuber, P.; Fernández, B.; Ferrighi, L.; Fliegl, H.; Frediani, L.; Hald, K.; Halkier, A.; Hättig, C.; Heiberg, H.; Helgaker, T.; Hennum, A. C.; Hetttema, H.; Hjertenæs, E.; Høst, S.; Høyvik, I. M.; Iozzi, M. F.; Jansík, B.; Jensen, H. J. A.; Jonsson, D.; Jørgensen, P.; Kauczor, J.; Kirpekar, S.;

- Kjærsgaard, T.; Klopper, W.; Knecht, S.; Kobayashi, R.; Koch, H.; Kongsted, J.; Krapp, A.; Kristensen, K.; Ligabue, A.; Lutnæs, O. B.; Melo, J. I.; Mikkelsen, K. v.; Myhre, R. H.; Neiss, C.; Nielsen, C. B.; Norman, P.; Olsen, J.; Olsen, J. M. H.; Osted, A.; Packer, M. J.; Pawlowski, F.; Pedersen, T. B.; Provasi, P. F.; Reine, S.; Rinkevicius, Z.; Ruden, T. A.; Ruud, K.; Rybkin, V. v.; Sałek, P.; Samson, C. C. M.; de Merás, A. S.; Saue, T.; Sauer, S. P. A.; Schimmelpfennig, B.; Sneskov, K.; Steindal, A. H.; Sylvester-Hvid, K. O.; Taylor, P. R.; Teale, A. M.; Tellgren, E. I.; Tew, D. P.; Thorvaldsen, A. J.; Thøgersen, L.; Vahtras, O.; Watson, M. A.; Wilson, D. J. D.; Ziolkowski, M.; Ågren, H. The Dalton Quantum Chemistry Program System. *Wiley Interdisciplinary Reviews: Computational Molecular Science* **2014**, *4* (3), 269–284.
- (171) Liu, Z.; Shi, E.; Wan, Y.; Li, N.; Chen, D.; Xu, Q.; Li, H.; Lu, J.; Zhang, K.; Wang, L. Effects of Gradual Oxidation of Aromatic Sulphur-Heterocycle Derivatives on Multilevel Memory Data Storage Performance. *Journal of Materials Chemistry C* **2015**, *3* (9), 2033–2039.
- (172) Forrest, S. R.; Bradley, D. D. C.; Thompson, M. E. Measuring the Efficiency of Organic Light-Emitting Devices. *Advanced Materials* **2003**, *15* (13), 1043–1048.
- (173) Gong, Y.; Chen, G.; Peng, Q.; Yuan, W. Z.; Xie, Y.; Li, S.; Zhang, Y.; Tang, B. Z. Achieving Persistent Room Temperature Phosphorescence and Remarkable Mechanochromism from Pure Organic Luminogens. *Advanced Materials* **2015**, *27* (40), 6195–6201.
- (174) Chen, X.; Xu, C.; Wang, T.; Zhou, C.; Du, J.; Wang, Z.; Xu, H.; Xie, T.; Bi, G.; Jiang, J.; Zhang, X.; Demas, J. N.; Trindle, C. O.; Luo, Y.; Zhang, G. Versatile Room-Temperature-Phosphorescent Materials Prepared from N-Substituted Naphthalimides: Emission Enhancement and Chemical Conjugation. *Angewandte Chemie - International Edition* **2016**, *55* (34), 9872–9876.
- (175) Ma, J. L.; Liu, H.; Li, S. Y.; Li, Z. Y.; Zhang, H. Y.; Wang, Y.; Zhao, C. H. Metal-Free Room-Temperature Phosphorescence from Amorphous Triarylborane-Based Biphenyl. *Organometallics* **2020**, *39* (23), 4153–4158.
- (176) Bolton, O.; Lee, K.; Kim, H. J.; Lin, K. Y.; Kim, J. Activating Efficient Phosphorescence from Purely Organic Materials by Crystal Design. *Nature Chemistry* **2011**, *3* (3), 205–210.

- (177) Song, B.; Shao, W.; Jung, J.; Yoon, S. J.; Kim, J. Organic Light-Emitting Diode Employing Metal-Free Organic Phosphor. *ACS Applied Materials and Interfaces* **2020**, *12* (5), 6137–6143.
- (178) Xu, J.; Takai, A.; Kobayashi, Y.; Takeuchi, M. Phosphorescence from a Pure Organic Fluorene Derivative in Solution at Room Temperature. *Chemical Communications* **2013**, *49* (76), 8447–8449.
- (179) She, P.; Yu, Y.; Qin, Y.; Zhang, Y.; Li, F.; Ma, Y.; Liu, S.; Huang, W.; Zhao, Q. Controlling Organic Room Temperature Phosphorescence through External Heavy-Atom Effect for White Light Emission and Luminescence Printing. *Advanced Optical Materials* **2020**, *8* (4), 1–7.
- (180) He, Z.; Zhao, W.; Lam, J. W. Y.; Peng, Q.; Ma, H.; Liang, G.; Shuai, Z.; Tang, B. Z. White Light Emission from a Single Organic Molecule with Dual Phosphorescence at Room Temperature. *Nature Communications* **2017**, *8* (1).
- (181) Chen, X.; Xu, C.; Wang, T.; Zhou, C.; Du, J.; Wang, Z.; Xu, H.; Xie, T.; Bi, G.; Jiang, J.; Zhang, X.; Demas, J. N.; Trindle, C. O.; Luo, Y.; Zhang, G. Versatile Room-Temperature-Phosphorescent Materials Prepared from N-Substituted Naphthalimides: Emission Enhancement and Chemical Conjugation. *Angewandte Chemie - International Edition* **2016**, *55* (34), 9872–9876.
- (182) Gong, Y.; Chen, G.; Peng, Q.; Yuan, W. Z.; Xie, Y.; Li, S.; Zhang, Y.; Tang, B. Z. Achieving Persistent Room Temperature Phosphorescence and Remarkable Mechanochromism from Pure Organic Luminogens. *Advanced Materials* **2015**, *27* (40), 6195–6201.
- (183) Yang, Z.; Mao, Z.; Zhang, X.; Ou, D.; Mu, Y.; Zhang, Y.; Zhao, C.; Liu, S.; Chi, Z.; Xu, J.; Wu, Y. C.; Lu, P. Y.; Lien, A.; Bryce, M. R. Intermolecular Electronic Coupling of Organic Units for Efficient Persistent Room-Temperature Phosphorescence. *Angewandte Chemie - International Edition* **2016**, *55* (6), 2181–2185.
- (184) Fateminia, S. M. A.; Mao, Z.; Xu, S.; Yang, Z.; Chi, Z.; Liu, B. Organic Nanocrystals with Bright Red Persistent Room-Temperature Phosphorescence for Biological Applications. *Angewandte Chemie - International Edition* **2017**, *56* (40), 12160–12164.

- (185) Gutierrez, G. D.; Sazama, G. T.; Wu, T.; Baldo, M. A.; Swager, T. M. Red Phosphorescence from Benzo[2,1,3]Thiadiazoles at Room Temperature. *Journal of Organic Chemistry* **2016**, *81* (11), 4789–4796.
- (186) Xiao, L.; Wu, Y.; Chen, J.; Yu, Z.; Liu, Y.; Yao, J.; Fu, H. Highly Efficient Room-Temperature Phosphorescence from Halogen-Bonding-Assisted Doped Organic Crystals. *Journal of Physical Chemistry A* **2017**, *121* (45), 8652–8658.
- (187) Kremer, A.; Aurisicchio, C.; Deleo, F.; Ventura, B.; Wouters, J.; Armaroli, N.; Barbieri, A.; Bonifazi, D. Walking Down the Chalcogenic Group of the Periodic Table: From Singlet to Triplet Organic Emitters. *Chemistry - A European Journal* **2015**, *21* (43), 15377–15387.
- (188) Wang, S.; Shu, H.; Han, X.; Wu, X.; Tong, H.; Wang, L.; Paper, S. I. of K.; Wang, S.; Shu, H.; Han, X.; Wu, X.; Tong, H.; Wang, L. A Highly Efficient Purely Organic Roomtemperature Phosphorescence Film Based on a Selenium-Containing Emitter for Sensitive Oxygen Detection. *Journal of Materials Chemistry C* **2021**, *9* (31), 9907–9913.
- (189) Weng, T.; Baryshnikov, G.; Deng, C.; Li, X.; Wu, B.; Wu, H.; Ågren, H.; Zou, Q.; Zeng, T.; Zhu, L. A Fluorescence–Phosphorescence–Phosphorescence Triple-Channel Emission Strategy for Full-Color Luminescence. *Small* **2020**, *1906475*, 1–6.
- (190) Jiang, M.; Guo, J.; Liu, B.; Tan, Q.; Xu, B. Synthesis of Tellurium-Containing  $\pi$ -Extended Aromatics with Room-Temperature Phosphorescence. *Organic Letters*. 2019, pp 8328–8333.
- (191) de Sa Pereira, D.; Lee, D. R.; Kukhta, N. A.; Lee, K. H.; Kim, C. L.; Batsanov, A. S.; Lee, J. Y.; Monkman, A. P. The Effect of a Heavy Atom on the Radiative Pathways of an Emitter with Dual Conformation, Thermally-Activated Delayed Fluorescence and Room Temperature Phosphorescence. *Journal of Materials Chemistry C* **2019**, *7* (34), 10481–10490.
- (192) An, Z.; Zheng, C.; Tao, Y.; Chen, R.; Shi, H.; Chen, T.; Wang, Z.; Li, H.; Deng, R.; Liu, X.; Huang, W. Stabilizing Triplet Excited States for Ultralong Organic Phosphorescence. *Nature Materials* **2015**, *14* (7), 685–690.
- (193) Lv, A.; Ye, W.; Jiang, X.; Gan, N.; Shi, H.; Yao, W.; Ma, H.; An, Z.; Huang, W. Room-Temperature Phosphorescence from Metal-Free Organic Materials in Solution: Origin and Molecular Design. *Journal of Physical Chemistry Letters* **2019**, *10* (5), 1037–1042.



- (194) Chen, C.; Chi, Z.; Chong, K. C.; Batsanov, A. S.; Yang, Z.; Mao, Z.; Yang, Z.; Liu, B. Carbazole Isomers Induce Ultralong Organic Phosphorescence. *Nature Materials* **2021**, *20* (2), 175–180.
- (195) Yang, J.; Zhen, X.; Wang, B.; Gao, X.; Ren, Z.; Wang, J.; Xie, Y.; Li, J.; Peng, Q.; Pu, K.; Li, Z. The Influence of the Molecular Packing on the Room Temperature Phosphorescence of Purely Organic Luminogens. *Nature Communications* **2018**, *9* (1), 1–10.
- (196) Song, B.; Shao, W.; Jung, J.; Yoon, S. J.; Kim, J. Organic Light-Emitting Diode Employing Metal-Free Organic Phosphor. *ACS Applied Materials and Interfaces* **2020**, *12* (5), 6137–6143.
- (197) Kim, H.; Keller, B.; Ho-Wu, R.; Abeyasinghe, N.; Vázquez, R. J.; Goodson, T.; Zimmerman, P. M. Enacting Two-Electron Transfer from a Double-Triplet State of Intramolecular Singlet Fission. *Journal of the American Chemical Society* **2018**, *140* (25), 7760–7763.
- (198) Kim, H.; Zimmerman, P. M. Coupled Double Triplet State in Singlet Fission. *Physical Chemistry Chemical Physics*. Royal Society of Chemistry 2018, pp 30083–30094.
- (199) Zimmerman, P. M.; Bell, F.; Casanova, D.; Head-Gordon, M. Mechanism for Singlet Fission in Pentacene and Tetracene: From Single Exciton to Two Triplets. *Journal of the American Chemical Society* **2011**, *133* (49), 19944–19952.
- (200) Chien, A. D.; Molina, A. R.; Abeyasinghe, N.; Varnavski, O. P.; Goodson, T.; Zimmerman, P. M. Structure and Dynamics of the 1(TT) State in a Quinoidal Bithiophene: Characterizing a Promising Intramolecular Singlet Fission Candidate. *Journal of Physical Chemistry C* **2015**, *119* (51), 28258–28268.
- (201) Rudenko, A. E.; Clayman, N. E.; Walker, K. L.; Maclaren, J. K.; Zimmerman, P. M.; Waymouth, R. M. Ligand-Induced Reductive Elimination of Ethane from Azopyridine Palladium Dimethyl Complexes. *Journal of the American Chemical Society* **2018**, *140* (36), 11408–11415.
- (202) Pokhilko, P.; Krylov, A. I. Quantitative El-Sayed Rules for Many-Body Wave Functions from Spinless Transition Density Matrices. *Journal of Physical Chemistry Letters* **2019**, *10* (17), 4857–4862.

- (203) Xiao, L.; Chen, Z.; Qu, B.; Luo, J.; Kong, S.; Gong, Q.; Kido, J. Recent Progresses on Materials for Electrophosphorescent Organic Light-Emitting Devices. *Advanced Materials*. February 22, 2011, pp 926–952.
- (204) Mori, K.; Goumans, T. P. M.; van Lenthe, E.; Wang, F. Predicting Phosphorescent Lifetimes and Zero-Field Splitting of Organometallic Complexes with Time-Dependent Density Functional Theory Including Spin-Orbit Coupling. *Physical Chemistry Chemical Physics* **2014**, *16* (28), 14523–14530.
- (205) Kolek, M.; Otteny, F.; Schmidt, P.; Mück-Lichtenfeld, C.; Einholz, C.; Becking, J.; Schleicher, E.; Winter, M.; Bieker, P.; Esser, B. Ultra-High Cycling Stability of Poly(Vinylphenothiazine) as a Battery Cathode Material Resulting from  $\pi$ - $\pi$  Interactions. *Energy and Environmental Science* **2017**, *10* (11), 2334–2341.
- (206) Kobayashi, J.; Kato, K.; Agou, T.; Kawashima, T. Synthesis of Dibenzochalcogenaborins and Systematic Comparisons of Their Optical Properties by Changing a Bridging Chalcogen Atom. *Chemistry - An Asian Journal* **2009**, *4* (1), 42–49.
- (207) Toma, A. M.; Nicoarǎ, A.; Silvestru, A.; Ruffer, T.; Lang, H.; Mehring, M. Bis(2-Phenoxyphenyl)Dichalcogenides and Their Chemical Reactivity. *Journal of Organometallic Chemistry* **2016**, *810*, 33–39.
- (208) Ansari, R.; Shao, W.; Yoon, S. J.; Kim, J.; Kieffer, J. Charge Transfer as the Key Parameter Affecting the Color Purity of Thermally Activated Delayed Fluorescence Emitters. *ACS Applied Materials and Interfaces* **2021**, *13* (24), 28529–28537.
- (209) Knöller, J. A.; Meng, G.; Wang, X.; Hall, D.; Pershin, A.; Beljonne, D.; Olivier, Y.; Laschat, S.; Zysman-Colman, E.; Wang, S. Intramolecular Borylation via Sequential B–Mes Bond Cleavage for the Divergent Synthesis of B,N,B-Doped Benzo[4]Helicenes. *Angewandte Chemie - International Edition* **2020**, *59* (8), 3156–3160.
- (210) Li, C.; Mellerup, S. K.; Wang, X.; Wang, S. Accessing Two-Stage Regioselective Photoisomerization in Unsymmetrical N,C-Chelate Organoboron Compounds: Reactivity of B(Ppz)(Mes)Ar. *Organometallics* **2018**, *37* (19), 3360–3367.
- (211) Yaqoob Bhat, M.; Kumar, A.; Naveed Ahmed, Q. Selenium Dioxide Promoted Dinitrogen Extrusion/Direct Selenation of Arylhydrazines and Anilines. *Tetrahedron* **2020**, *76* (16), 131105.

- (212) Li, Y.; Nie, C.; Wang, H.; Li, X.; Verpoort, F.; Duan, C. A Highly Efficient Method for the Copper-Catalyzed Selective Synthesis of Diaryl Chalcogenides from Easily Available Chalcogen Sources. *European Journal of Organic Chemistry* **2011**, 2011 (36), 7331–7338.
- (213) Shao, Y.; Gan, Z.; Epifanovsky, E.; Gilbert, A. T. B.; Wormit, M.; Kussmann, J.; Lange, A. W.; Behn, A.; Deng, J.; Feng, X.; Ghosh, D.; Goldey, M.; Horn, P. R.; Jacobson, L. D.; Kaliman, I.; Khaliullin, R. Z.; Kuš, T.; Landau, A.; Liu, J.; Proynov, E. I.; Rhee, Y. M.; Richard, R. M.; Rohrdanz, M. A.; Steele, R. P.; Sundstrom, E. J.; Woodcock, H. L.; Zimmerman, P. M.; Zuev, D.; Albrecht, B.; Alguire, E.; Austin, B.; Beran, G. J. O.; Bernard, Y. A.; Berquist, E.; Brandhorst, K.; Bravaya, K. B.; Brown, S. T.; Casanova, D.; Chang, C. M.; Chen, Y.; Chien, S. H.; Closser, K. D.; Crittenden, D. L.; Diedenhofen, M.; Distasio, R. A.; Do, H.; Dutoi, A. D.; Edgar, R. G.; Fatehi, S.; Fusti-Molnar, L.; Ghysels, A.; Golubeva-Zadorozhnaya, A.; Gomes, J.; Hanson-Heine, M. W. D.; Harbach, P. H. P.; Hauser, A. W.; Hohenstein, E. G.; Holden, Z. C.; Jagau, T. C.; Ji, H.; Kaduk, B.; Khistyayev, K.; Kim, J.; Kim, J.; King, R. A.; Klunzinger, P.; Kosenkov, D.; Kowalczyk, T.; Krauter, C. M.; Lao, K. U.; Laurent, A. D.; Lawler, K. v.; Levchenko, S. v.; Lin, C. Y.; Liu, F.; Livshits, E.; Lochan, R. C.; Luenser, A.; Manohar, P.; Manzer, S. F.; Mao, S. P.; Mardirossian, N.; Marenich, A. v.; Maurer, S. A.; Mayhall, N. J.; Neuscammann, E.; Oana, C. M.; Olivares-Amaya, R.; Oneill, D. P.; Parkhill, J. A.; Perrine, T. M.; Peverati, R.; Prociuk, A.; Rehn, D. R.; Rosta, E.; Russ, N. J.; Sharada, S. M.; Sharma, S.; Small, D. W.; Sodt, A.; Stein, T.; Stück, D.; Su, Y. C.; Thom, A. J. W.; Tsuchimochi, T.; Vanovschi, V.; Vogt, L.; Vydrov, O.; Wang, T.; Watson, M. A.; Wenzel, J.; White, A.; Williams, C. F.; Yang, J.; Yeganeh, S.; Yost, S. R.; You, Z. Q.; Zhang, I. Y.; Zhang, X.; Zhao, Y.; Brooks, B. R.; Chan, G. K. L.; Chipman, D. M.; Cramer, C. J.; Goddard, W. A.; Gordon, M. S.; Hehre, W. J.; Klamt, A.; Schaefer, H. F.; Schmidt, M. W.; Sherrill, C. D.; Truhlar, D. G.; Warshel, A.; Xu, X.; Aspuru-Guzik, A.; Baer, R.; Bell, A. T.; Besley, N. A.; Chai, J. da; Dreuw, A.; Dunietz, B. D.; Furlani, T. R.; Gwaltney, S. R.; Hsu, C. P.; Jung, Y.; Kong, J.; Lambrecht, D. S.; Liang, W.; Ochsenfeld, C.; Rassolov, V. A.; Slipchenko, L. v.; Subotnik, J. E.; van Voorhis, T.; Herbert, J. M.; Krylov, A. I.; Gill, P. M. W.; Head-Gordon, M. Advances in Molecular Quantum Chemistry Contained in the Q-Chem 4 Program Package. *Molecular Physics* **2015**, 113 (2), 184–215.
- (214) Weigend, F. Accurate Coulomb-Fitting Basis Sets for H to Rn. *Physical Chemistry Chemical Physics* **2006**, 8 (9), 1057–1065.

- (215) Chai, J. da; Head-Gordon, M. Systematic Optimization of Long-Range Corrected Hybrid Density Functionals. *Journal of Chemical Physics* **2008**, *128* (8), 84106.
- (216) Chai, J. da; Head-Gordon, M. Long-Range Corrected Hybrid Density Functionals with Damped Atom-Atom Dispersion Corrections. *Physical Chemistry Chemical Physics* **2008**, *10* (44), 6615–6620.
- (217) Allouche, A. R. Gabedita - A Graphical User Interface for Computational Chemistry Softwares. *Journal of Computational Chemistry* **2011**, *32* (1), 174–182.